

Ministry of Education and Science of the Russian Federation
Saint Petersburg National Research University of Information
Technologies, Mechanics, and Optics

NANOSYSTEMS:
PHYSICS, CHEMISTRY, MATHEMATICS

2020, volume 11(1)

Наносистемы: физика, химия, математика

2020, том 11, № 1



NANOSYSTEMS:

PHYSICS, CHEMISTRY, MATHEMATICS

ADVISORY BOARD MEMBERS

Chairman: V.N. Vasiliev (*St. Petersburg, Russia*),
V.M. Buznik (*Moscow, Russia*); V.M. Ievlev (*Voronezh, Russia*), P.S. Kop'ev (*St. Petersburg, Russia*), N.F. Morozov (*St. Petersburg, Russia*), V.N. Parmon (*Novosibirsk, Russia*),
A.I. Rusanov (*St. Petersburg, Russia*),

EDITORIAL BOARD

Editor-in-Chief: I.Yu. Popov (*St. Petersburg, Russia*)

Section Co-Editors:

Physics – V.M. Uzdin (*St. Petersburg, Russia*),
Chemistry, material science – V.V. Gusarov (*St. Petersburg, Russia*),
Mathematics – I.Yu. Popov (*St. Petersburg, Russia*).

Editorial Board Members:

V.V.M. Adamyan (*Odessa, Ukraine*); O.V. Al'myasheva (*St. Petersburg, Russia*);
A.P. Alodjants (*Vladimir, Russia*); S. Bechta (*Stockholm, Sweden*); J. Behrndt (*Graz, Austria*);
M.B. Belonenko (*Volgograd, Russia*); A. Chatterjee (*Hyderabad, India*); S.A. Chivilikhin
(*St. Petersburg, Russia*); A.V. Chizhov (*Dubna, Russia*); A.N. Enyashin (*Ekaterinburg, Russia*),
P.P. Fedorov (*Moscow, Russia*); E.A. Gudilin (*Moscow, Russia*); V.K. Ivanov
(*Moscow, Russia*), H. Jónsson (*Reykjavik, Iceland*); A.A. Kiselev (*Durham, USA*);
Yu.S. Kivshar (*Canberra, Australia*); S.A. Kozlov (*St. Petersburg, Russia*); P.A. Kurasov
(*Stockholm, Sweden*); A.V. Lukashin (*Moscow, Russia*); I.V. Melikhov (*Moscow, Russia*);
G.P. Miroshnichenko (*St. Petersburg, Russia*); I.Ya. Mittova (*Voronezh, Russia*); Nguyen
Anh Tien (*Ho Chi Minh, Vietnam*); V.V. Pankov (*Minsk, Belarus*); K. Pankrashkin (*Orsay, France*);
A.V. Ragulya (*Kiev, Ukraine*); V. Rajendran (*Tamil Nadu, India*); A.A. Rempel
(*Ekaterinburg, Russia*); V.Ya. Rudyak (*Novosibirsk, Russia*); D Shoikhet (*Karmiel, Israel*);
P Stovicek (*Prague, Czech Republic*); V.M. Talanov (*Novocherkassk, Russia*); A.Ya. Vul'
(*St. Petersburg, Russia*); A.V. Yakimansky (*St. Petersburg, Russia*), V.A. Zagrebnev
(*Marseille, France*).

Editors:

I.V. Blinova; A.I. Popov; A.I. Trifanov; E.S. Trifanova (*St. Petersburg, Russia*),
R. Simoneaux (*Philadelphia, Pennsylvania, USA*).

Address: University ITMO, Kronverkskiy pr., 49, St. Petersburg 197101, Russia.

Phone: +7(812)312-61-31, **Journal site:** <http://nanojournal.ifmo.ru/>,

E-mail: popov1955@gmail.com

AIM AND SCOPE

The scope of the journal includes all areas of nano-sciences. Papers devoted to basic problems of physics, chemistry, material science and mathematics inspired by nanosystems investigations are welcomed. Both theoretical and experimental works concerning the properties and behavior of nanosystems, problems of its creation and application, mathematical methods of nanosystem studies are considered.

The journal publishes scientific reviews (up to 30 journal pages), research papers (up to 15 pages) and letters (up to 5 pages). All manuscripts are peer-reviewed. Authors are informed about the referee opinion and the Editorial decision.

CONTENT

MATHEMATICS

Jyoti Kori, Pratibha, Mohammad Junaid Abbasi
**A mathematical study of the flow of nanoparticles
inside periodic permeable and viscoelastic lung** 5

S. Mondal, A. Bhosale, N. De, A. Pal
Topological properties of some nanostructures 14

A.S. Mikhaylov, V.S. Mikhaylov
Finite Toda lattice and classical moment problem 25

PHYSICS

W. Florek, A. Marlewski, G. Kamieniarz, M. Antkowiak
**The Lagrange variety approach applied to frustrated
classical wheels** 30

V. Sajfert, N. Pop, D. Popov
Geometrical analyses of nanostructures 36

F. Iacob
**Electron transport through nanosystems driven
by pseudo-Gaussian well scattering** 44

S. Leble
**Magnetoelectric effects theory by Heisenberg method
based on permutation group symmetry of nanoparticles** 50

A.V. Ivanov, P.F. Bessarab, H. Jónsson, V.M. Uzdin
**Fully self-consistent calculations of magnetic structure
within non-collinear Alexander-Anderson model** 65

CHEMISTRY AND MATERIAL SCIENCE

V. Gupta, V. Kant, A.K. Sharma, M. Sharma
**Comparative assessment of antibacterial efficacy
for cobalt nanoparticles, bulk cobalt and standard
antibiotics: A concentration dependant study** 78

S. Saravanan	
Optical pathlength enhancement in ultrathin silicon solar cell using decorated silver nanoparticles on aluminium grating	86
H. Sharma, Y.C. Sharma	
Synthesis and characterization of bismuth selenide thin films by thermal evaporation technique	92
N.R. Popova, V.V. Andreeva, N.V. Khohlov, A.L. Popov, V.K. Ivanov	
Fabrication of CeO₂ nanoparticles embedded in polysaccharide hydrogel and their application in skin wound healing	99
I.Ya. Mittova, V.F. Kostyukov, N.A. Ilyasova, B.V. Sladkopevtsev, A.A. Samsonov	
Modification of nanoscale thermal oxide films formed on indium phosphide under the influence of tin dioxide	110
Sidheshwar G. Gaurkhede	
Microwave synthesis and studies room temperature optical properties of LaF₃: Ce³⁺, Pr³⁺, Nd³⁺ nanocrystals	117
Information for authors	123

A mathematical study of the flow of nanoparticles inside periodic permeable and viscoelastic lung

Jyoti Kori*, Pratibha, Mohammad Junaid Abbasi

Department of Mathematics, Indian Institute of Technology Roorkee, Roorkee-247667, Uttarakhand, India

*jyotikorii@gmail.com

DOI 10.17586/2220-8054-2020-11-1-5-13

Smoking and pollution are highly hazardous to human health. Most of the environmental particles are very small in size i.e. micro or nanoparticles. When these particles are inhaled, they enter from the nose and flow with the air stream into various portions of the lungs. The alveolar region, a porous media due to number of alveoli, serves as an internal biofilter medium to filter deposited particles. To analyze the behavior of this biofilter medium, we considered the periodic permeability of lungs (due to periodic breathing) together with the viscoelasticity of the lung tissues. The flow of viscous air through the porous media is modeled by using one dimensional momentum equation with Darcy's law and the velocity of particles by second law of Newton. To model the viscoelasticity, we used Kelvin-Voigt model. The finite difference method is used to solve the governing equations and MATLAB is used to solve the computational problem. The effects of various parameters, such as the Darcy number, porosity, and the breathing frequency are analyzed for flow of air, particle and viscoelasticity of lung graphically. Results show that by increasing the breathing frequency, decreasing the porosity, and decreasing the Darcy number, the viscoelastic stress increases.

Keywords: Breathing frequency, Darcy number, lungs tissue, periodic permeability, porous media, viscoelasticity.

Received: 23 October 2019

Revised: 10 December 2019

1. Introduction

Various literature have been presented on lungs and on its parts [1, 2], few of them considered lungs as a porous media, because there were many alveoli and multiple bifurcations and some of the literature [3, 4] considered lung airways as a permeable tube [5, 6]. Alveoli lie at the last division of the lungs, and their work is to exchange the oxygen and carbon dioxide from air to blood and vice-versa. They are little balloon shaped air sacs and are clustered together throughout the lungs. Hazardous nanoparticles may get deposited in the alveoli and cause various lung diseases.

The toxicity of nanoparticles is right now of major concern, due to fast evolution and growth of nanotechnology [7, 8]. To date, the interactions of nanoparticles with human body are not completely understood, while an epidemiological study noted surplus incidence from fine particles derived from air pollution affects several cities of the United States [9]. When nanoparticles are merged or joined, their performance varies from larger particles. They create an extraordinarily huge risk to health, as they are assumed to be more reactive and toxic as compared to larger particles. Depending on the field of implementation, nanoparticles have various ways to enter the body, via inhalation, dermal, oral or injection exposure. Carbon nanotubes have aspect ratios which are comparable to asbestos fibers. If inhaled, then the nanotubes can probably move effortlessly through the airways down to the alveoli, where they might get stuck and can commence different diseases like asthma, COPD, emphysema, fibrosis [10, 11] etc.

Biofiltration is a transpiring technology used for pollution control. It can be used for both water purification as well as air purification, with a comprehensive range of adulterants. Biofiltration uses biological means for the deterioration of pollutants in either air or water stream. It has been applied to rectify contaminated air with volatile organic compounds (VOCs) and other gases [10, 12–14]. This technology is favored as a pollutant removal technique, as it has low investment and operating cost, high efficiency, reliable operating stability and low aggregate of secondary pollution [4]. Biofilters are generally porous media, i.e., a material that contains pores or voids in it. The pores are ordinarily filled with a fluid (liquid or gas) [11]. Generally, fluids flowing through the biofilter media can be exactly calculated by the accustomed models, such as the Darcy's model [7]. Darcy's law enables the analysis of laminar flow of a fluid through a porous media. The lower limit of sustainability of Darcy's law is a threshold gradient that can be required to start the flow. Darcy's law was productively used to model the flow of gas through the various mixtures. The media must have a high porosity for minimization of the pressure drop across the biofilter, quality moisture holding capacity, and a sufficiently long usage life [2]. In human lung alveolar sacs can be reviewed as a biofilter, which removes the particles from the in-breathed air.

The objective of this study is to analyze the behavior of biofilter media (alveolar sac) with respect to Darcy number, elasticity of lungs and breathe frequency. We considered in this study the periodic permeability of lungs (due to periodic breathing) together with the viscoelasticity of the lung tissues.

2. Mathematical modeling

2.1. Governing equations for viscous air flowing through airway tube

We assumed the duct of alveolar region as a circular tube of radius a as shown in Fig. 1. The motion of dusty air is along the axial direction of tube and there is no flow in radial direction. The fluid is incompressible, viscous and flow is laminar Newtonian under the time dependent pressure gradient.

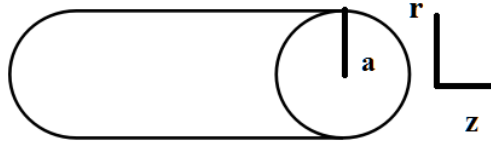


FIG. 1. Alveolar region as circular tube, where r is the radial direction and z is the axial direction of viscous air flow

To analyze the behavior of viscous air through the alveolar region (internal biofilter and also a porous media) Darcy law for porous media is used in one dimensional momentum equation and flow of particle is analyzed by Newton second law of motion. In our previous work [5] we focused on the effect of periodic permeability of lung. We extended our previous work by including viscoelastic property of human lung and aimed to analyze the flow behavior of air and nanoparticles inside periodically permeable human lung.

To observe the effects of lung tissue viscoelasticity, we considered human lung as a Voigt body and extended Kelvin-Voigt model by including periodic permeability of lung. So, the flow governing equations in cylindrical polar coordinate system are defined as follows [5, 15, 16]:

$$\frac{\partial u}{\partial t} + \frac{u}{\epsilon} \frac{\partial u}{\partial r} = -\frac{\epsilon}{\rho} \frac{\partial p}{\partial r} + \nu \left(\frac{\partial^2 u}{\partial r^2} + \frac{1}{r} \frac{\partial u}{\partial r} \right) + F, \quad (1)$$

$$m \frac{\partial v}{\partial t} = k(u - v), \quad (2)$$

$$\sigma_f = \left(B + \frac{4\phi}{3} \right) \frac{\partial u}{\partial r} + \left(\zeta + \frac{4\eta}{3} \right) \left(\frac{\partial^2 u}{\partial t \partial r} \right), \quad (3)$$

where u and v are the velocity of air flow and dust particles respectively, ρ is the air density, ϵ is the porosity, ν is the kinematic viscosity parameter, p is the fluid pressure, m is the mass concentration of dust particles, k is the Stokes resistance coefficient, which is equal to $6\mu a$ for spherical particles, μ being the coefficient of viscosity of the air and a is the radius of the particles. B and ϕ are bulk compression; ζ and η are shear and bulk coefficients of viscosity. F stands for the entire body force because of the existence of porous media and additional external force fields, and is formulated as:

$$F = \left(-\frac{\epsilon\nu}{K} u + k \frac{N_0}{\rho} (v - u) \right), \quad (4)$$

where K is the periodic permeability [17], which is different from permeability. We are using periodic permeability because our breathe changes with time or we can say that our breath is periodic and the permeability of the porous medium need not to be constant. Recently, Singh et al. [19] studied buoyancy-driven free convective flow through a porous medium with periodic permeability variation. The problem becomes three-dimensional due to such a variation of permeability. The permeability of the porous medium and the free air flow velocity are assumed to be of the following forms respectively:

$$K = \frac{K_0}{1 - a_0 \cos(\pi r/a)}, \quad (5)$$

k_0 is the mean permeability of porous medium, and a_0 is the amplitude of oscillation.

2.2. Initial and boundary conditions

All the initial conditions are at $t = 0$:

$$u = 0, \quad v = 0. \quad (6)$$

The boundary conditions for the fluid are same as those for classical fluid and no particle boundary conditions are required. The air velocity is set to be zero on the walls.

$$u = 0, \quad v = 0, \quad \frac{\partial u}{\partial r} = 0. \quad (7)$$

2.3. Transformation of the governing equations

In order to solve the equations numerically, we choose the physical effects which are important for us and correspondingly make the above equations dimensionless as follows:

$$x^* = \frac{r}{a}, \quad P^* = \frac{pa^2}{\rho w_0^2}, \quad T^* = \frac{t\nu}{a^2}, \quad U^* = \frac{au}{\nu}, \quad V^* = \frac{av}{\nu}, \quad \sigma_{F^*} = \frac{\sigma_f a^2}{\rho \nu^2}.$$

By using above quantities, we obtained the following equations ¹,

$$\frac{\partial U}{\partial T} + \frac{U}{\epsilon} \frac{\partial U}{\partial x} = -\epsilon \frac{\partial P}{\partial x} + \left(\frac{\partial^2 U}{\partial x^2} + \frac{1}{x} \frac{\partial U}{\partial x} \right) + L(V - U) - \frac{\epsilon}{Da} U, \quad (8)$$

$$\frac{\partial V}{\partial T} = \frac{(U - V)}{\tau}, \quad (9)$$

where:

$$Da = \frac{K}{a^2}, \quad L = \frac{M}{\tau} = \frac{N_0 k a^2}{\mu}, \quad M = \frac{N_0 a m}{\rho}, \quad \tau = \frac{m \nu}{a^2 k},$$

$$\sigma_F = \frac{\rho \nu^3}{a^3} \left[\left(B + 4 \frac{\phi}{3} \right) \frac{\partial U}{\partial X} + \left(\zeta + \frac{4\eta}{3} \right) \frac{\partial^2 U}{\partial X^2} \right]. \quad (10)$$

Due to smoking a person faces a breathing problem, therefore, we assumed the pressure gradient of air as a function of exponent:

$$-\frac{\partial P}{\partial x} = P_0 e^{-ft}, \quad (11)$$

where, f is the breathing frequency per minute.

3. Methodology

The governing transformed equation is solved using finite difference method and used central difference approximation for the radial derivatives [14] and after discretization, we used MATLAB to solve computational problem. The result seemed to be converged with an accuracy on the order the time step which was chosen $\Delta t = 0.00001$ and $\Delta x = 0.01$ along the axial directions.

4. Discretization of components

For discretization of velocity $u(x, T)$ or $u(x_i, T_j)$ or $u(i, j)$, we used following step sizes:

$$x_i = i \Delta x, \quad (i = 0, 1, 2, 3, \dots, N),$$

where

$$x_N = 1.0, \quad T_j = (j - 1) \Delta t, \quad (j = 1, 2, \dots).$$

Additionally, at $x = 0$, following approximation is applicable in equation (8), When $x \rightarrow 0$, we found that the denominator is also approaching to zero and make the term indeterminate, which is inappropriate for the physical state of the respiratory system. Therefore, to remove this kind of inconsistency we used L'Hôpital's rule of limit here:

$$\lim_{x \rightarrow 0} \frac{1}{x} \frac{\partial U}{\partial x} = \lim_{x \rightarrow 0} \frac{\partial^2 U}{\partial x^2}, \quad (12)$$

¹For simplicity we drop the asterisk in all the dimensionless equations.

so, the equation 8 at $x = 0$ becomes:

$$U_{i,j+1} = \left(1 - L\Delta t - \left(\frac{\epsilon}{Da}\right) \Delta t - 4r_1\right) U_{i,j} + \left(2r_1 - \frac{U_{i,j}r_1\Delta x}{2\epsilon}\right) U_{i+1,j} + \left(2r_1 + \frac{U_{i,j}r_1\Delta x}{2\epsilon}\right) U_{i-1,j} + L\Delta t V_{i,j} + P_0 e^{-fj\Delta t} \epsilon \Delta t, \quad (13)$$

and at $0 < x \leq 1$:

$$U_{i,j+1} = \left(1 - L\Delta t - \left(\frac{\epsilon}{Da}\right) \Delta t - 2r_1\right) U_{i,j} + \left(r_1 - r_1\Delta x \frac{U_{i,j}}{2\epsilon} + \frac{r_1}{2i}\right) U_{i+1,j} + \left(r_1 + \frac{r_1\Delta x U_{i,j}}{2\epsilon} - \frac{r_1}{2i}\right) U_{i-1,j} + L\Delta t V_{i,j} + P_0 e^{-fj\Delta t} \epsilon \Delta t, \quad (14)$$

where $\left(\frac{\Delta t}{\Delta x^2}\right) = r_1$.

The equation (9) transforms as:

$$V_{i,j+1} = \left(1 - \frac{\Delta t}{\tau}\right) V_{i,j} + \frac{\Delta t}{\tau} U_{i,j}, \quad (15)$$

$$(\sigma_F)_{i,j} = \frac{\rho\nu^3}{a^3} \left[\left(B + 4\frac{\phi}{3}\right) - \left(\left(\zeta + \frac{4\eta}{3}\right) \frac{1}{\Delta t}\right) \frac{U_{i+1,j}}{2\Delta r} \right] + \frac{\rho\nu^3}{a^3} \left[\left(\left(\zeta + \frac{4\eta}{3}\right) \frac{1}{\Delta t} - \left(B + 4\frac{\phi}{3}\right)\right) \frac{U_{i+1,j}}{2\Delta r} + \left(\zeta + \frac{4\mu}{3}\right) \left(\frac{u_{i+1,j+1} - u_{i-1,j+1}}{2\Delta t\Delta r}\right) \right]. \quad (16)$$

The initial and boundary conditions in discretized form are as follows:

$$U_{i,1} = V_{i,1} = 0, \quad U_{2,j} = U_{0,j}; \quad U_{N+1,j} = 0. \quad (17)$$

5. Results and Discussion

Numerical computations have been carried out using the following parameter values [1, 9, 18]:

$$\begin{aligned} P_0 &= 101.325 \text{ kPa}, \quad m = 0.0002 \text{ kg/l}, \quad d_p = 100 \text{ nm}, \quad \rho = 1.185 \text{ kg/m}^3, \quad \nu = 1.52 \text{ s}^{-1}, \\ N_0 &= 0.02504 \cdot 10^{12} / \text{m}^3, \quad a = 0.5 \text{ } \mu\text{m}, \quad \epsilon = 0.6, \quad B = 3000 \text{ kg}/(\text{m sec}^2), \quad \phi = 400 \text{ kg}/(\text{m sec}), \\ \zeta &= 10 \text{ kg}/(\text{m sec}), \quad f = 0.2 \text{ to } 0.3 \text{ per sec (for diseased, 0.2 to 0.5 per sec)}. \end{aligned} \quad (18)$$

Velocities of air and dust particles on the wall have been represented graphically with variable axial positions, time, and porosity and Darcy number.

5.1. Effect of porosity on internal biofilter

We defined void ratio as the ratio of free space volume in the biofilter to the total volume of biofilter. There are voids in a biofilter which are not filled by any medium. If the void ratios are high then it reduces the clogging and allow the air to move freely in biofilter.

From Fig. 2(a) it is clear that at porosity $\epsilon = 0.6$, and Darcy number = 0.01 the velocity of the air increases with time. It has attained maximum velocity at the center of the tube at $x = 0$ and occupied maximum value earlier at $t = 0.1$. After that, the velocity of air decreases simultaneously as time increases and became zero on the tube wall. Due to classical flow, initially the effects of particles are almost negligible, therefore the highest velocity is attained. Later the particle hinders the flow and the subsequent velocity reduces:

In Fig. 2(b) at porosity $\epsilon = 0.9$, the velocity of the air increases with time. It obtains maximum velocity at $t = 0.2$ at the center of the tube and after that decreases as time increases. The velocity depends on the porosity. From Figs. 2(a) and 2(b) it is quite clear that at porosity $\epsilon = 0.9$, the velocity profiles for the air flow are significantly more than that at porosity $\epsilon = 0.6$. Figs. 3(a) and 3(b) show the velocities for the dust particles near the starting point of the tube with the time at porosity (ϵ) 0.6 and 0.9 respectively. Velocities of the dust particles increase when radial distance increases and increasing values of time. From the figures, we can see that the radial parameter works gradually to exhibit its effect, i.e. velocity of the dust particles increases frequently with time. From Figs. 3(a) and 3(b) it is clear that at porosity $\epsilon = 0.9$, the velocity profiles for the dust particles increase more than that at porosity $\epsilon = 0.6$.

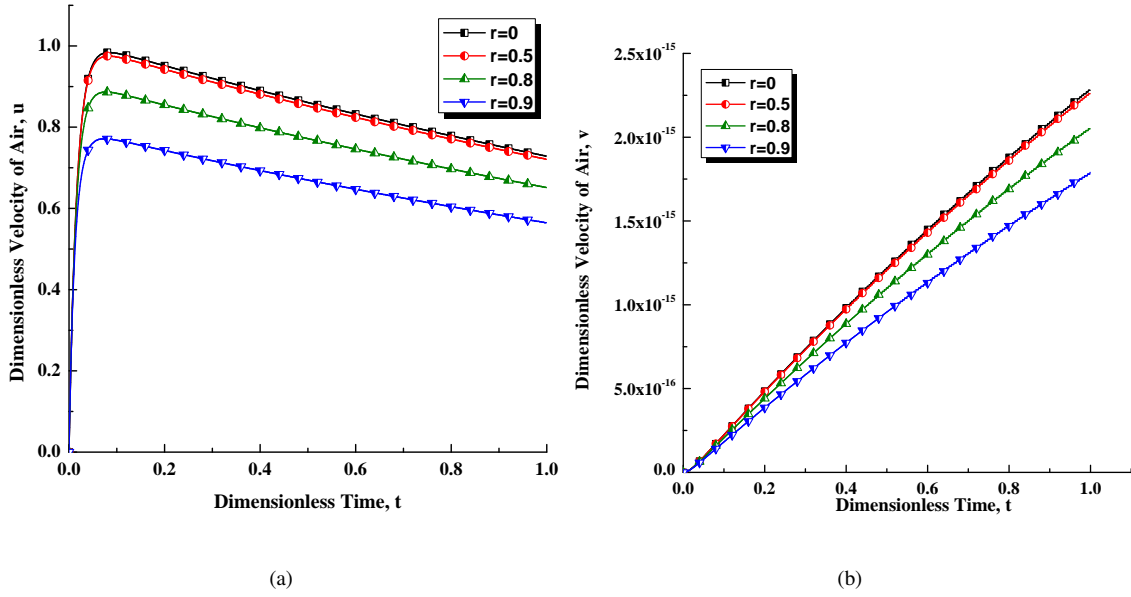


FIG. 2. Velocity profile at $K_0 = 0.1$, $d = 100$ nm, $\epsilon = 0.6$, and $f = 0.2$ per sec for different radial positions of (a) air and (b) particle flows

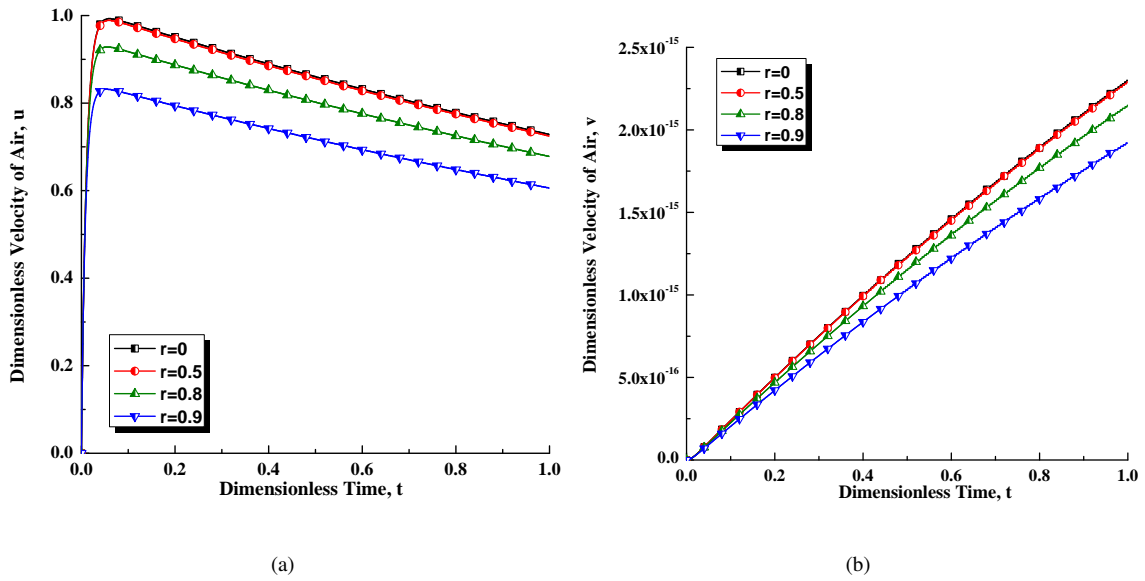


FIG. 3. Velocity profiles at $K_0 = 0.1$, $d = 100$ nm, $\epsilon = 0.9$, and $f = 0.2$ per sec for different radial positions of (a) air and (b) particle flows

5.2. Effect of Darcy number on internal biofilter

Figures 4 and 5 are shown the variations of velocity for the fluid for different values of radial positions (x with time). As x increases, the velocity decreases for the fluid. Velocity of the fluid at Darcy number 10^{-1} is greater than at Darcy number 10^{-2} for fixed axial position: From Figs. 4(a) and 4(b), it is clear that the velocity of the air increases regularly as value of time increases. As well as we found from Figs. 5(a) and 5(b) velocity of particle at Darcy number 10^{-1} is greater than at Darcy number 10^{-2} for fixed axial position.

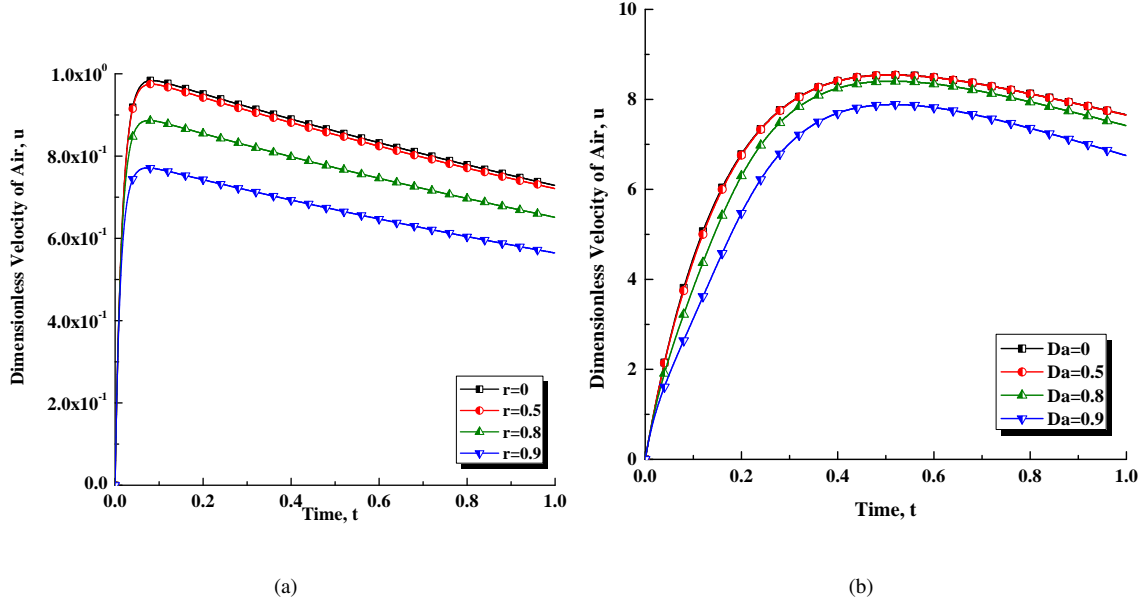


FIG. 4. Velocity profiles for different radial positions of air for (a) $Da = 10^{-2}$, and (b) $Da = 10^{-1}$ at $K_0 = 0.1$, $d = 100$ nm, $\epsilon = 0.6$, and $f = 0.3$ per sec.

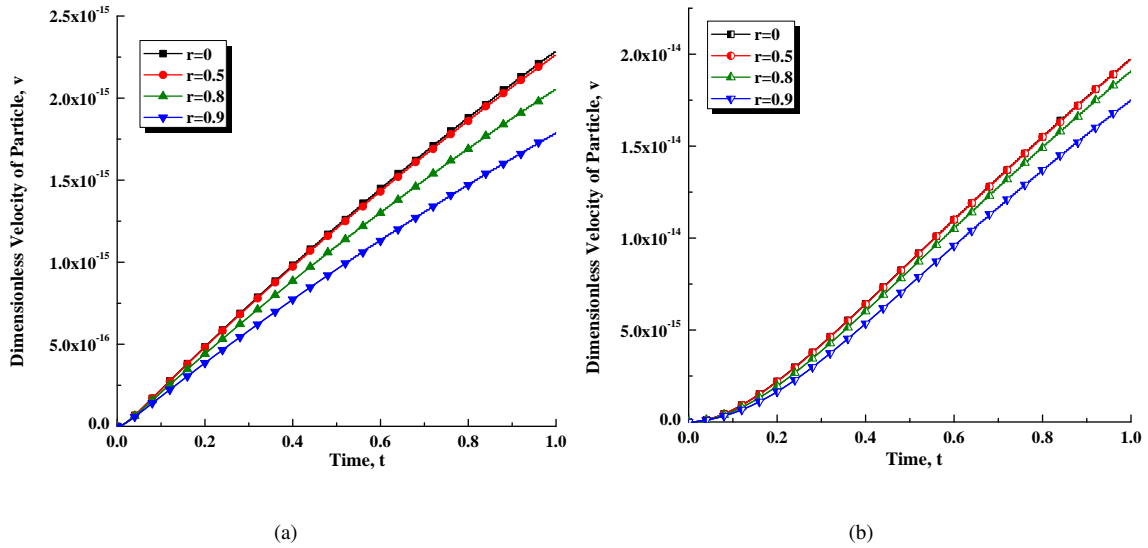


FIG. 5. Velocity profiles for different radial positions of particle for (a) $Da = 10^{-2}$, and (b) $Da = 10^{-1}$ at $K_0 = 0.1$, $d = 100$ nm, $\epsilon = 0.6$, and $f = 0.3$ per sec.

5.3. Effect of breathing frequency on viscoelastic stress

Figure 6 shows how increasing value of breathing frequency increases the viscoelastic stress, when we take Darcy number as 0.01, porosity 0.9 and varies the breathing frequency from $f = 0.2$ to 0.5 per sec. At $f = 0.2$, value of viscoelastic stress is very low and by increasing value of f from 0.2 to 0.5 we found increment in the viscoelastic stress. Due to an increase in breathing frequency, which can be caused by any lung disease such as COPD or asthma, the velocity of air as well as particles increases. Due to increment in the fluid velocity the pressure in alveolar section increases, which causes increment in the viscoelastic stress.

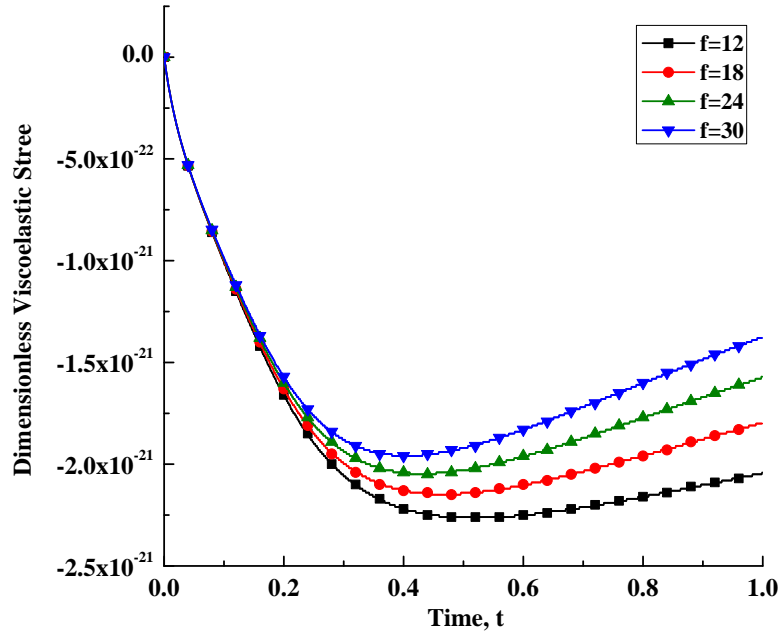


FIG. 6. Effect of breathing frequencies from 0.2 – 0.5 per sec on viscoelastic stress at $Da = 10^{-2}$, $K_0 = 0.1$, $d = 100$ nm, and $\epsilon = 0.6$.

5.4. Effect of porosity on viscoelastic stress

In Fig. 7, we have plotted viscoelastic stress with different values of porosity (0.6 & 0.9) at Darcy number 0.01 and breathing frequency at 0.26 per sec.

From Fig. 7, we found by increasing porosity from 0.6 to 0.9, the viscoelastic stress first decreases then increases. By increasing the porosity from 0.6 to 0.9, the number of alveoli increases which allow flow of air very freely and caused reduction in the stress of lung tissue in some extent.

5.5. Effect of Darcy number on viscoelastic stress

Darcy number is calculated using permeability of medium which depends on porosity of medium, so it is safe to say that Darcy number depends on porosity of medium. So, if Darcy number increases media becomes more fluidic. We have plotted the stress vs Darcy number varying from 0.1 to 0.001 with keeping breathing frequency at 0.26 per sec and porosity at 0.6. From Fig. 8, we can see that as the Darcy number increases the value of viscoelastic stress decreases. The value of stress at Darcy number 0.001 is not quite zero but it has comparatively very small value. The minimum value is obtained for Darcy number 0.1 at $x = 0.5$. From that, we can see that viscoelastic stress decreases as we increases value of Darcy number, which make the flow more fluidic.

6. Conclusion

In this study, to analyze the behavior of biofilter media, we considered the periodic permeability of lungs (due to periodic breathing) together with the viscoelasticity of the lung tissues. Mathematical modeling is used to model the problem and MATLAB is used to solve the problem computationally. The effects of various parameters, such as Darcy number, porosity, and breathing frequency are calculated on flow of air and particles. Additionally, effects of breathing frequency, porosity, Darcy number are found on viscoelastic stress for diseased lung (such as COPD, Asthma). After performing the numerical computation we found that by increasing the media porosity velocity of air and particle increases. By increasing the Darcy number, the velocity of air and particle increases. By increasing the breathing frequency, decreasing the porosity and decreasing the Darcy number viscoelastic stress increases. Hence, we can conclude from this study that Darcy number, elasticity of lungs and breathing frequency affect the flow of air and particles inside internal biofilter media (alveolar sac) of lung.

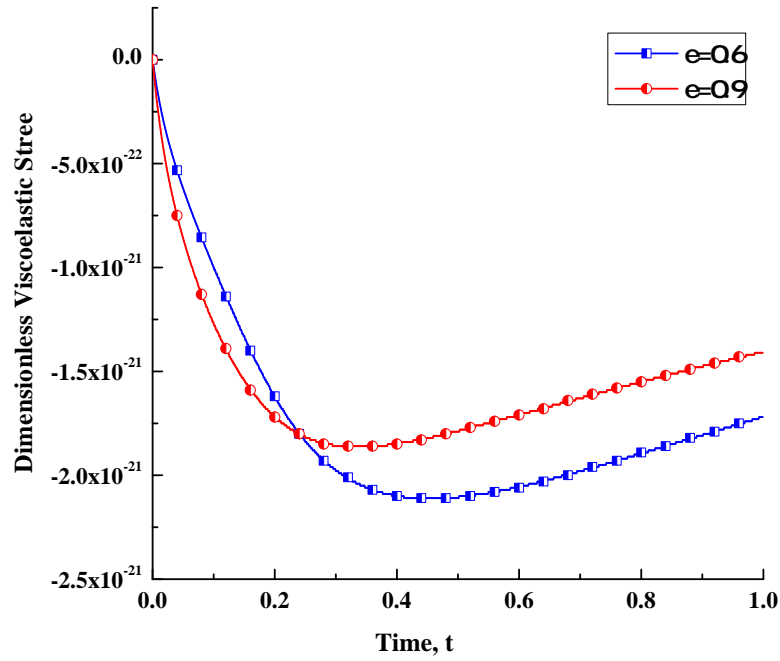


FIG. 7. Effect of porosity ($\epsilon = 0.6$ and 0.9) of biofilter media on viscoelastic stress at $Da = 10^{-2}$, $K_0 = 0.1$, $d = 100$ nm, and $f = 0.26$ per sec.

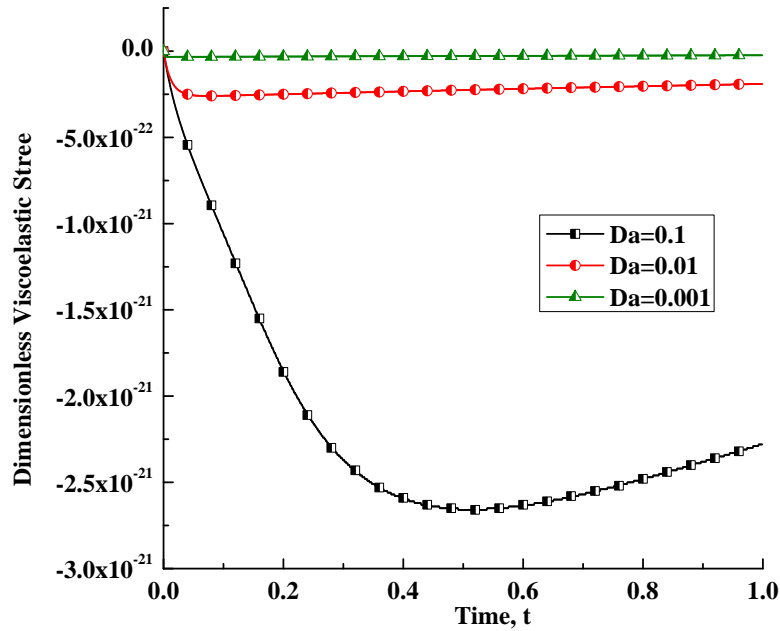


FIG. 8. Effect of Darcy number for 0.1 and 0.01 on viscoelastic stress at $\epsilon = 0.6$, $K_0 = 0.1$, $d = 100$ nm, and $f = 0.26$ per sec.

Acknowledgements

One of the authors, Jyoti Kori, is thankful to Ministry of Human Resource Development India (Grant Code: MHR-02-23-200-44) for providing fund and support while writing this manuscript.

Conflict of Interest

No conflict of interest.

References

- [1] Cengel Y., Cimbala J. *Solutions manual for fluid mechanics: Fundamentals and applications*. Bukupedia, McGraw-Hill Companies, Incorporation, New York, 2006.
- [2] Kafle G., Chen L., et al. Field evaluation of wood bark-based down-flow biofilters for mitigation of odor, ammonia, and hydrogen sulfide emissions from confined swine nursery barns. *Journal of environmental management*, 2015, **147**, P. 164–174.
- [3] Wei Z., Liu X., et al. Gas dimethyl sulfide removal in biotrickling filtration. *Open Access Scientific Reports*, 2013, **2** (702).
- [4] Zhang Y., Finlay W.H. Measurement of the effect of cartilaginous rings on particle deposition in a proximal lung bifurcation model. *Aerosol Science and Technology*, 2005, **39**, P. 394–399.
- [5] Kori J., Pratibha. Effect of periodic permeability of lung airways on the flow dynamics of viscous fluid. *Nanosystems: Physics, Chemistry, Mathematics*, 2019, **10** (3), P. 235–242.
- [6] Kori J., Pratibha. Effect of Periodic Permeability of Lung Tissue on Fluid, Velocity and Nonspherical Nanoparticle Filtration. *International Journal of Applied and Computational Mathematics*, 2019, **5** (49), P. 1–15.
- [7] Darcy H. *Les fontaines publiques de la ville de Dijon*. Dijon, Vector Dalmont, Paris, 1856.
- [8] Nel A., Xia T., et al. Toxic potential of materials at the nanolevel. *Science*, 2006, **311** (5761), P. 622–627.
- [9] Hoet P., Hohlfeld I., Salata O. Nanoparticles-known and unknown health risks. *Journal of Nanobiotechnology*, 2004, **2** (12), P. 1–15.
- [10] Sharma P. Free convection effects on the low past a porous medium bounded by a vertical infinite surface with constant suction and constant heat flux. *Journal of physics D – Applied physics*, 1992, **25**, P. 162–166.
- [11] Siddiqui A.M., Siddiqua S., Naqvi A.S. Effect of constant wall permeability and porous media on the creeping flow through round vessel. *Journal of Applied and Computational Mathematics*, 2018, **7** (2), P. 1–6.
- [12] Anet B., Lemasle M., et al. Characterization of gaseous odor emissions from a rendering plant by gc/ms and treatment by biofiltration. *Journal of Environmental Management*, 2013, **128**, P. 981–987.
- [13] Malhautier L., Cariou S., et al. Treatment of complex gaseous emissions emitted by a rendering facility using a semi-industrial biofilter. *Journal of Chemical Technology and Biotechnology*, 2014, **11** (21), P. 426–430.
- [14] Smith G. *Numerical Solution of Partial Differential Equations*, Oxford University Press, New York, 1985.
- [15] Nithiarasu P., Ravindran K. A new semi-implicit time stepping procedure for buoyancy driven flow in a fluid saturated porous medium. *Computer methods in applied mechanics and engineering*, 1998, **165** (1), P. 147–154.
- [16] Saini A., Katiyar V.K., Pratibha. Numerical simulation of gas flow through a biofilter in lung tissue. *World Journal of Modelling and Simulation*, 2015, **11** (1), P. 33–42.
- [17] Meyers, Chawla. Section 13.10 of Mechanical Behaviors of Materials, *Mechanical behavior of Materials*, Cambridge University Press, 1999, P. 570–580. Prentice Hall, Inc.
- [18] Flora J., Hargis R., et al. The role of pressure drop and flow redistribution on modeling mercury control using sorbent injection in baghouse filters. *Journal of the Air & Waste Management Association*, 2006, **56** (3), P. 343–349.
- [19] Singh P., Mishra J.K., Narayan K.A. Free convection along a vertical wall in a porous medium with periodic permeability variation. *Int. J. Numer. Anal. Methods Geomech.*, 1989, **13**, P. 443–450.

Topological properties of some nanostructures

S. Mondal¹, A. Bhosale¹, N. De², A. Pal¹

¹Department of mathematics, NIT Durgapur, India,

²Department of Basic Sciences and Humanities (Mathematics),
Calcutta Institute of Engineering and Management, Kolkata, India

souravmath94@gmail.com, bhosaleakshay78@gmail.com, de.nilanjan@rediffmail.com, anita.buie@gmail.com

DOI 10.17586/2220-8054-2020-11-1-14-24

Topological indices are numerical values associated with chemical constitution describing the structures of chemical compounds and helping to predict different physicochemical properties. In this report, some newly designed topological descriptors, namely, neighborhood Zagreb index (M_N), neighborhood version of Forgotten topological index (F_N), modified neighborhood version of Forgotten topological index (F_N^*), neighborhood version of second Zagreb index (M_2^*), neighborhood version of hyper Zagreb index (HM_N) are obtained for the $TURC_4C_8(S)$, armchair nanotube $TUAC_6$, V-phenylenic nanotube $VPHX[m, n]$, and V-phenylenic nanotori $VPHY[m, n]$.

Keywords: Topological indices, $TURC_4C_8(S)$, armchair nanotube ($TUAC_6$), V-phenylenic nanotube ($VPHX[m, n]$), V-phenylenic nanotori ($VPHY[m, n]$).

Received: 30 December 2019

Revised: 3 January 2020

1. Introduction

We consider only molecular graphs throughout this article. By molecular graph [1–3], we mean a simple connected graph in which nodes are supposed to be atoms and edges are chemical bonds. The vertex and edge sets of a graph G are represented here by $V(G)$ and $E(G)$, respectively. The degree of a vertex v on a graph G , denoted by $d_G(v)$, is the total number of edges associated with v . Moreover, we define

$$\delta_G(v) = \sum_{u \in N_G(v)} deg_G(u),$$

where

$$N_G(v) = \{u \in V(G) : uv \in E(G)\}.$$

The chemical graph theory has a significant impact on the chemical science development. Chemical graph theory is a part of mathematical chemistry that uses graph theory for mathematically modeling chemical phenomena. In this field, a leading tool is topological index. A real valued mapping considering graphs as arguments is called a graph invariant if it gives same value to isomorphic graphs. In chemical graph theory, the graph invariants are named as topological indices. Topological indices play key role in QSPR/QSAR study. Topological indices interpret chemical compound structures and help to predict certain physicochemical properties such as entropy, boiling point, acentric factor, vaporization enthalpy, etc. Among different types of topological indices, degree based topological indices have prominent role in this research area. For some well-known degree based topological indices, readers are referred to [4–8]. In [9, 10], some new neighborhood degree based indices are presented having good correlations with entropy and acentric factor. They are defined as follows.

The neighborhood Zagreb index is denoted by $M_N(G)$ and is defined as:

$$M_N(G) = \sum_{v \in V(G)} \delta_G(v)^2.$$

Neighborhood version of Forgotten topological index is denoted by $F_N(G)$ and is defined as:

$$F_N(G) = \sum_{v \in V(G)} \delta_G(v)^3.$$

Modified neighborhood version of Forgotten topological index is denoted by $F_N^*(G)$ and is defined as:

$$F_N^*(G) = \sum_{uv \in E(G)} [\delta_G(u)^2 + \delta_G(v)^2].$$

Neighborhood version of second Zagreb index is denoted by $M_2^*(G)$ and is defined by:

$$M_2^*(G) = \sum_{uv \in E(G)} [\delta_G(u)\delta_G(v)].$$

Neighborhood version of hyper Zagreb index is denoted by $HM_N(G)$ and is defined by:

$$HM_N(G) = \sum_{uv \in E(G)} [\delta_G(u) + \delta_G(v)]^2.$$

A nanostructure is an intermediate object between microscopic and molecular structures. It is a molecular-scale product obtained from engineering. The most important class of such materials is the carbon nanotubes. Carbon nanotubes (CNTs) are carbon allotropes with cylindrical molecular structures, having diameters ranging from a few nanometers and lengths to several millimeters. Nanotubes are categorized as single-walled (SWNTs) and multi-walled (MWNTs) nanotubes. Researchers have found topological descriptors for various nanotube and nanotori. In [11], topological properties of $TURC_4C_8(S)$ are investigated. Jiang et al. determined topological index of V-phenylenic nanotubes and V-phenylenic nanotori in [12]. Topological properties of armchair polyhex nanotube are discussed in [13]. For more discussion on this topic, readers are referred to [14–21]. Inspired by these works, we have derived M_N , F_N , F_N^* , M_2^* , and HM_N indices for $TURC_4C_8(S)$, armchair polyhex nanotube $TUAC_6$, V-phenylenic nanotube $VPHX[m, n]$, and V-phenylenic nanotori $VPHY[m, n]$. Moreover, we have compared these indices graphically.

2. Motivation

The correlation coefficient (r) of topological indices with different physicochemical properties for a benchmark data set is determined to check the utility of the indices in QSPR/QSAR analysis. According to the International Academy of Mathematical chemistry, an index is considered to be useful if $r^2 \geq 0.8$. In [9, 10], the chemical applicability of the indices M_N , F_N , F_N^* , M_2^* , and HM_N are studied taking octane isomers as data set. The r^2 values of those indices with entropy are 0.907, 0.88, 0.868, 0.899 and 0.88, respectively. The r^2 values of those indices with acentric factor are 0.989, 0.989, 0.952, 0.971 and 0.961, respectively. The aforesaid indices are therefore effective in QSPR/QSAR analysis with powerful accuracy. In addition, their isomer discrimination ability also remarkable [9, 10] in comparison with the other degree based indices. With the help of nanotechnology, many new materials and devices are in progress with a wide range of applications in medicine, electronics and computers. Motivated by the importance of topological indices and the nanotechnology, we intend to compute the aforementioned indices for some nanostructures which are described in the next section.

3. Preliminaries

The 2D and 3D lattice of $TURC_4C_8(S)$ nanotube are shown in Fig. 1. We consider mn numbers of C_8 and C_4 cycles in the 2D lattice of $TURC_4C_8(S)$ nanotube. We denote this graph by $TUC_4C_8[m, n]$. From Fig. 1, it is clear that this graph has $8mn + 2m$ nodes and $12mn + m$ edges.

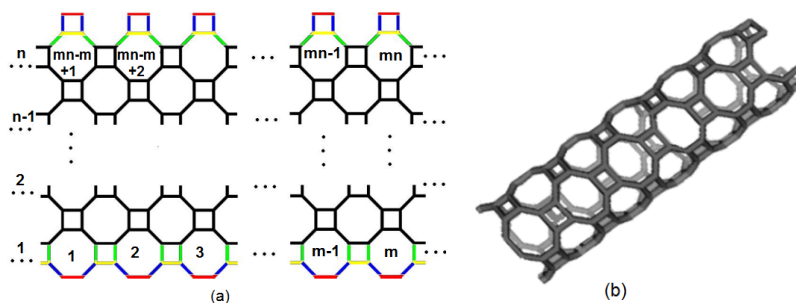


FIG. 1. (a) The 2D and (b) the 3D lattice of $TUC_4C_8[m, n]$ nanotube

We consider a class of armchair polyhex nano tubes $TUAC_6[m, n]$ having m and n numbers of hexagons in each rows and columns, respectively. The molecular graph of $TUAC_6[m, n]$ is depicted in the Fig. 2. We can say from Fig. 2, that m is even for all $n \in N$. This nanotube has $2mn + 2m$ and $3mn + 2m$ numbers of nodes and edges respectively.

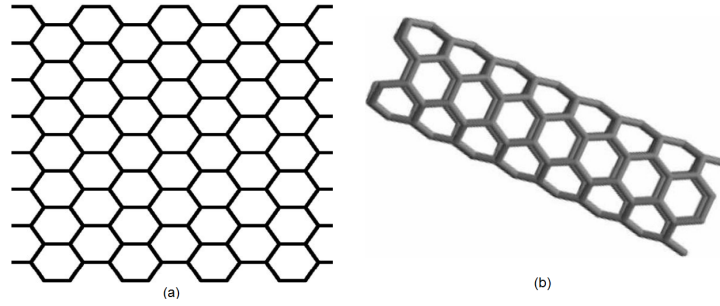


FIG. 2. (a) The 2D and (b) the 3D lattice of Armchair polyhex nanotubes $TUAC_6$

Also we consider V-phenylenic nanotube and V-phenylenic nanotori whose 2D lattices are depicted in Figs. 3 and 4. Phenylenes are polycyclic conjugated molecules, made of C_4 and C_6 such that every C_4 is adjacent to two C_6 and lies between two C_6 . No two C_6 are mutually adjacent. Each C_6 is adjacent to only two C_4 cycles.

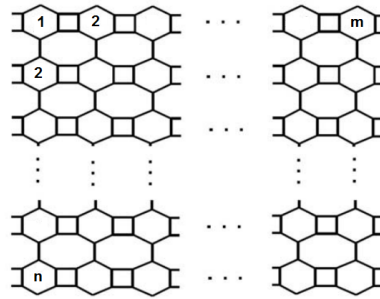


FIG. 3. The molecular graph of V-phenylenic nanotube $VPHX[m, n]$

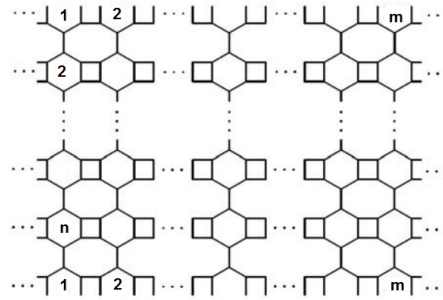


FIG. 4. The molecular graph of V-phenylenic nanotori $VPHY[m, n]$

4. Main results

In this section, our goal is to compute aforesaid indices for $TUC_4C_8[m, n]$, armchair polyhex nanotube $TUAC_6$, V-phenylenic nanotube $VPHX[m, n]$, and V-phenylenic nanotori $VPHY[m, n]$. Following Figs. 1, 2, 3, and 4, first we obtain vertex and edge partitions of nanotubes and nanotori discussed above and then proceed for main theorems.

The vertex and edge partitions for $TUC_4C_8[m, n]$ nanotube are given in Table 1 and 2, respectively. The vertex and edge partitions for $TUAC_6[m, n]$ nanotube are given in Table 3 and 4, respectively. The vertex and edge partitions for $VPHX[m, n]$ nanotube are given in Table 5 and 6, respectively.

TABLE 1. Vertex partition of $TUC_4C_8[m, n]$

$\delta_G(u)$	5	8	9
Frequency	$4m$	$4m$	$8mn - 6m$

TABLE 2. Edge partition of $TUC_4C_8[m, n]$

$(\delta_G(u), \delta_G(v))$	(5, 5)	(5, 8)	(8, 8)	(8, 9)	(9, 9)
Frequency	$2m$	$4m$	$2m$	$4m$	$12mn - 11m$

TABLE 3. Vertex partition of $TUAC_6[m, n]$

$\delta_G(u)$	5	8	9
Frequency	$2m$	$2m$	$2m(n - 1)$

TABLE 4. Edge partition of $TUAC_6[m, n]$

$(\delta_G(u), \delta_G(v))$	(5, 5)	(5, 8)	(8, 8)	(8, 9)	(9, 9)
Frequency	m	$2m$	m	$2m$	$m(3n - 4m)$

TABLE 5. Vertex partition of $VPHX[m, n]$

$\delta_G(u)$	6	8	9
Frequency	$2m$	$4m$	$6mn - 6m$

TABLE 6. Edge partition of $VPHX[m, n]$

$(\delta_G(u), \delta_G(v))$	(6, 8)	(8, 8)	(8, 9)	(9, 9)
Frequency	$4m$	$2m$	$2m$	$9m(n - 1)$

Theorem 1. The neighborhood Zagreb index M_N of $TUC_4C_8[m, n]$ ($m, n \geq 2$), $TUAC_6[m, n]$, $VPHX[m, n]$, and $VPHY[m, n]$ nanotubes are given by:

- (i) $M_N(TUC_4C_8[m, n]) = 648mn - 130m$,
- (ii) $M_N(TUAC_6[m, n]) = 162mn - 16m$,
- (iii) $M_N(VPHX[m, n]) = 486mn - 158m$,
- (iv) $M_N(VPHY[m, n]) = 486mn$.

Proof. The general formula of neighborhood Zagreb index M_N is given by:

$$M_N(G) = \sum_{v \in V(G)} \delta_G(v)^2.$$

- (i) Let G be the $TUC_4C_8[m, n]$ nanotube for ($m, n \geq 2$). Then applying the Table 1 on the definition of neighborhood Zagreb index, we obtain:

$$\begin{aligned} M_N(G) &= \sum_{v \in V_5} \delta_G(v)^2 + \sum_{v \in V_8} \delta_G(v)^2 + \sum_{v \in V_9} \delta_G(v)^2 \\ &= |V_5|(5^2) + |V_8|(8^2) + |V_9|(9^2) \\ &= 4m(5^2) + 4m(8^2) + (8mn - 6m)(9^2) \\ &= 648mn - 130m. \end{aligned}$$

- (ii) Let G be the V-phenylenic nanotube ($TUAC_6[m, n]$). Then applying the Table 3 on the general formula of neighborhood Zagreb index, we have:

$$\begin{aligned} M_N(G) &= \sum_{v \in V_5} \delta_G(v)^2 + \sum_{v \in V_8} \delta_G(v)^2 + \sum_{v \in V_9} \delta_G(v)^2 \\ &= |V_5|(5^2) + |V_8|(8^2) + |V_9|(9^2) \\ &= 2m(6^2) + 2m(8^2) + 2m(n-1)(9^2) \\ &= 486mn - 158m. \end{aligned}$$

- (iii) Let G be the V-phenylenic nanotube ($VPHX[m, n]$). Then applying the Table 5 on the general formula of neighborhood Zagreb index, we have:

$$\begin{aligned} M_N(G) &= \sum_{v \in V_6} \delta_G(v)^2 + \sum_{v \in V_8} \delta_G(v)^2 + \sum_{v \in V_9} \delta_G(v)^2 \\ &= |V_6|(6^2) + |V_8|(8^2) + |V_9|(9^2) \\ &= 2m(6^2) + 4m(8^2) + (6mn - 6m)(9^2) \\ &= 486mn - 158m. \end{aligned}$$

- (iv) Let G be the V-phenylenic nanotube ($VPHY[m, n]$). Its clear from Fig. 3 that $V(G) = V_9$ and $|V_9| = 6mn$. The required result follows clearly from the definition of neighborhood Zagreb index. \square

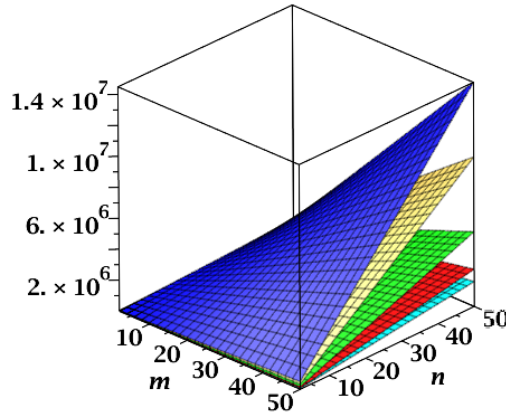


FIG. 5. Topological indices for $TUC_4C_8[m, n]$ nanotube

Theorem 2. The neighborhood version of Forgotten topological index F_N of $TUC_4C_8[m, n]$ ($m, n \geq 2$), $TUAC_6[m, n]$, $VPHX[m, n]$, and $VPHY[m, n]$ nanotubes are given by:

- (i) $F_N(TUC_4C_8[m, n]) = 5832mn - 1826m$,
- (ii) $F_N(TUAC_6[m, n]) = 1458mn - 184m$,
- (iii) $F_N(VPHX[m, n]) = 4374mn - 1894m$,
- (iv) $F_N(VPHY[m, n]) = 4374mn$,

Proof. The general formula of neighborhood version of Forgotten topological index F_N is given by:

$$F_N(G) = \sum_{v \in V(G)} \delta_G(v)^3.$$

- (i) Let G be the $TUC_4C_8[m, n]$ nanotube for ($m, n \geq 2$). Then applying the Table 1 on the definition of neighborhood version of Forgotten topological index, we obtain:

$$\begin{aligned} F_N(G) &= \sum_{v \in V_5} \delta_G(v)^3 + \sum_{v \in V_8} \delta_G(v)^3 + \sum_{v \in V_9} \delta_G(v)^3 \\ &= |V_5|(5^3) + |V_8|(8^3) + |V_9|(9^3) \\ &= 4m(5^3) + 4m(8^3) + (8mn - 6m)(9^3) \\ &= 5832mn - 1826m. \end{aligned}$$

(ii) Let G be the V-phenylenic nanotube ($TUAC_6[m, n]$). Then applying the Table 3 on the general formula of neighborhood version of Forgotten topological index, we have:

$$\begin{aligned} F_N(G) &= \sum_{v \in V_5} \delta_G(v)^3 + \sum_{v \in V_8} \delta_G(v)^3 + \sum_{v \in V_9} \delta_G(v)^3 \\ &= |V_5|(5^3) + |V_8|(8^3) + |V_9|(9^3) \\ &= 2m(5^3) + 2m(8^3) + 2m(n-1)(9^3) \\ &= 1458mn - 184m. \end{aligned}$$

(iii) Let G be the V-phenylenic nanotube ($VPHX[m, n]$). Then applying the Table 5 on the general formula of neighborhood version of Forgotten topological index, we have:

$$\begin{aligned} F_N(G) &= \sum_{v \in V_6} \delta_G(v)^3 + \sum_{v \in V_8} \delta_G(v)^3 + \sum_{v \in V_9} \delta_G(v)^3 \\ &= |V_6|(6^3) + |V_8|(8^3) + |V_9|(9^3) \\ &= 2m(6^3) + 4m(8^3) + (6mn - 6m)(9^3) \\ &= 4374mn - 1894m. \end{aligned}$$

(iv) Let G be the V-phenylenic nanotori ($VPHY[m, n]$). From Fig. 3, we have, $V(G) = V_9$ and $|V_9| = 6mn$. Using the definition of neighborhood version of Forgotten topological index, the desired result can be obtained easily.

□

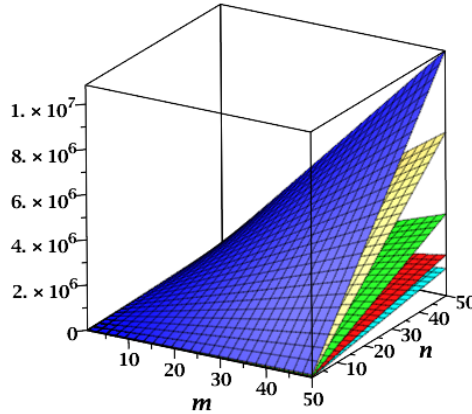


FIG. 6. Topological indices for $VPHX[m, n]$ nanotube.

Theorem 3. The modified neighborhood version of Forgotten topological index F_N^* of $TUC_4C_8[m, n]$ ($m, n \geq 2$), $TUAC_6[m, n]$, $VPHX[m, n]$, and $VPHY[m, n]$ nanotubes are given by:

- (i) $F_N^*(TUC_4C_8[m, n]) = 1944mn - 490m$,
- (ii) $F_N^*(TUAC_6[m, n]) = 486mn - 2m$,
- (iii) $F_N^*(VPHX[m, n]) = 1458mn - 512m$,
- (iv) $F_N^*(VPHY[m, n]) = 1458mn$.

Proof. The general formula of modified neighborhood version of Forgotten topological index F_N^* is given by:

$$F_N^*(G) = \sum_{uv \in E(G)} [\delta_G(u)^2 + \delta_G(v)^2].$$

(i) Let G be the $TUC_4C_8[m, n]$ nanotube for ($m, n \geq 2$). Then applying the Table 2 on the definition of modified neighborhood version of Forgotten topological index, we obtain:

$$\begin{aligned}
F_N^*(G) &= \sum_{uv \in E_{(5,5)}} [\delta_G(u)^2 + \delta_G(v)^2] + \sum_{uv \in E_{(5,8)}} [\delta_G(u)^2 + \delta_G(v)^2] + \sum_{uv \in E_{(8,8)}} [\delta_G(u)^2 + \delta_G(v)^2] \\
&+ \sum_{uv \in E_{(8,9)}} [\delta_G(u)^2 + \delta_G(v)^2] + \sum_{uv \in E_{(9,9)}} [\delta_G(u)^2 + \delta_G(v)^2] \\
&= |E_{(5,5)}|(5^2 + 5^2) + |E_{(5,8)}|(5^2 + 8^2) + |E_{(8,8)}|(8^2 + 8^2) + |E_{(8,9)}|(8^2 + 9^2) \\
&+ |E_{(9,9)}|(9^2 + 9^2) \\
&= 2m(5^2 + 5^2) + 4m(5^2 + 8^2) + 2m(8^2 + 8^2) + 4m(8^2 + 9^2) + m(12n - 11)(9^2 + 9^2).
\end{aligned}$$

After simplification the desired result can be obtained easily.

- (ii) Let G be the $TUAC_6[m, n]$ nanotube. Then applying the Table 4 on the definition of modified neighborhood version of Forgotten topological index, we obtain:

$$\begin{aligned}
F_N^*(G) &= \sum_{uv \in E_{(5,5)}} [\delta_G(u)^2 + \delta_G(v)^2] + \sum_{uv \in E_{(5,8)}} [\delta_G(u)^2 + \delta_G(v)^2] + \sum_{uv \in E_{(8,8)}} [\delta_G(u)^2 + \delta_G(v)^2] \\
&+ \sum_{uv \in E_{(8,9)}} [\delta_G(u)^2 + \delta_G(v)^2] + \sum_{uv \in E_{(9,9)}} [\delta_G(u)^2 + \delta_G(v)^2] \\
&= |E_{(5,5)}|(5^2 + 5^2) + |E_{(5,8)}|(5^2 + 8^2) + |E_{(8,8)}|(8^2 + 8^2) + |E_{(8,9)}|(8^2 + 9^2) \\
&+ |E_{(9,9)}|(9^2 + 9^2) \\
&= m(5^2 + 5^2) + 2m(5^2 + 8^2) + m(8^2 + 8^2) + 2m(8^2 + 9^2) + m(3n - 4)(9^2 + 9^2).
\end{aligned}$$

After simplification the required result can be obtained easily.

- (iii) Let G be the $VPHX[m, n]$ nanotube. Then applying the Table 6 on the definition of modified neighborhood version of Forgotten topological index, we obtain:

$$\begin{aligned}
F_N^*(G) &= \sum_{uv \in E_{(6,8)}} [\delta_G(u)^2 + \delta_G(v)^2] + \sum_{uv \in E_{(8,8)}} [\delta_G(u)^2 + \delta_G(v)^2] \\
&+ \sum_{uv \in E_{(8,9)}} [\delta_G(u)^2 + \delta_G(v)^2] + \sum_{uv \in E_{(9,9)}} [\delta_G(u)^2 + \delta_G(v)^2] \\
&= |E_{(6,8)}|(6^2 + 8^2) + |E_{(8,8)}|(8^2 + 8^2) + |E_{(8,9)}|(8^2 + 9^2) + |E_{(9,9)}|(9^2 + 9^2) \\
&= 4m(6^2 + 8^2) + 2m(8^2 + 8^2) + 2m(8^2 + 9^2) + 9m(n - 1)(9^2 + 9^2).
\end{aligned}$$

After simplification the required result can be obtained easily.

- (iv) Let G be the $VPHY[m, n]$ nanotube. From Fig. 3, it is clear that $E(G) = E_{(9,9)}$ and $|E_{(9,9)}| = 9mn$. Thus, we have $F_N^*(G) = 9mn(9^2 + 9^2) = 1458mn$

Hence the proof. □

Theorem 4. The neighborhood version of second Zagreb index M_2^* of $TUC_4C_8[m, n]$ ($m, n \geq 2$), $TUAC_6[m, n]$, $VPHX[m, n]$, and $VPHY[m, n]$ nanotubes are given by:

- (i) $M_2^*(TUC_4C_8[m, n]) = 972mn - 265m$,
- (ii) $M_2^*(TUAC_6[m, n]) = 243mn - 11m$,
- (iii) $M_2^*(VPHX[m, n]) = 729mn - 265m$,
- (iv) $M_2^*(VPHY[m, n]) = 729mn$.

Proof. The general formula of neighborhood version of second Zagreb index M_2^* is given by:

$$M_2^*(G) = \sum_{uv \in E(G)} [\delta_G(u)\delta_G(v)].$$

- (i) Let G be the $TUC_4C_8[m, n]$ nanotube for ($m, n \geq 2$). Then applying the Table 2 on the general form of neighborhood version of second Zagreb index, we obtain the following computation.

$$\begin{aligned}
 M_2^*(G) &= \sum_{uv \in E_{(5,5)}} [\delta_G(u) \cdot \delta_G(v)] + \sum_{uv \in E_{(5,8)}} [\delta_G(u) \cdot \delta_G(v)] + \sum_{uv \in E_{(8,8)}} [\delta_G(u) \cdot \delta_G(v)] \\
 &+ \sum_{uv \in E_{(8,9)}} [\delta_G(u) \cdot \delta_G(v)] + \sum_{uv \in E_{(9,9)}} [\delta_G(u) \cdot \delta_G(v)] \\
 &= |E_{(5,5)}|(5.5) + |E_{(5,8)}|(5.8) + |E_{(8,8)}|(8.8) + |E_{(8,9)}|(8.9) + |E_{(9,9)}|(9.9) \\
 &= 2m(5.5) + 4m(5.8) + 2m(8.8) + 4m(8.9) + (12mn - 11m)(9.9).
 \end{aligned}$$

After simplification, the desired result can be easily obtained.

(ii) Let G be the $TUAC_6[m, n]$ nanotube. Then, applying the Table 4 on the definition of neighborhood version of second Zagreb index, we get the following derivation:

$$\begin{aligned}
 M_2^*(G) &= \sum_{uv \in E_{(5,5)}} [\delta_G(u) \cdot \delta_G(v)] + \sum_{uv \in E_{(5,8)}} [\delta_G(u) \cdot \delta_G(v)] + \sum_{uv \in E_{(8,8)}} [\delta_G(u) \cdot \delta_G(v)] \\
 &+ \sum_{uv \in E_{(8,9)}} [\delta_G(u) \cdot \delta_G(v)] + \sum_{uv \in E_{(9,9)}} [\delta_G(u) \cdot \delta_G(v)] \\
 &= |E_{(5,5)}|(5.5) + |E_{(5,8)}|(5.8) + |E_{(8,8)}|(8.8) + |E_{(8,9)}|(8.9) + |E_{(9,9)}|(9.9) \\
 &= 4m(6.8) + 2m(8.8) + 2m(8.9) + 9m(n - 1)(9.9) \\
 &= 243mn - 11m.
 \end{aligned}$$

(iii) Let G be the $VPHX[m, n]$ nanotube. Then, applying the Table 6 on the definition of neighborhood version of second Zagreb index, we get the following derivation:

$$\begin{aligned}
 M_2^*(G) &= \sum_{uv \in E_{(6,8)}} [\delta_G(u) \cdot \delta_G(v)] + \sum_{uv \in E_{(8,8)}} [\delta_G(u) \cdot \delta_G(v)] \\
 &+ \sum_{uv \in E_{(8,9)}} [\delta_G(u) \cdot \delta_G(v)] + \sum_{uv \in E_{(9,9)}} [\delta_G(u) \cdot \delta_G(v)] \\
 &= |E_{(6,8)}|(6.8) + |E_{(8,8)}|(8.8) + |E_{(8,9)}|(8.9) + |E_{(9,9)}|(9.9) \\
 &= 4m(6.8) + 2m(8.8) + 2m(8.9) + 9m(n - 1)(9.9) \\
 &= 729mn - 265m.
 \end{aligned}$$

(iv) Let G be the $VPHY[m, n]$ nanotube. From Fig. 3, it is clear that $E(G) = E_{(9,9)}$ and $|E_{(9,9)}| = 9mn$. Thus, we have $F_N^*(G) = 9mn(9.9) = 729mn$.

Hence the proof. □

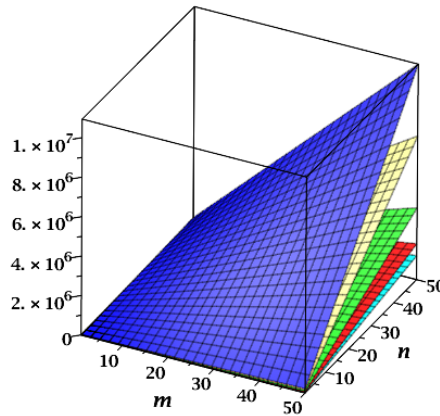


FIG. 7. Topological indices for $VPHY[m, n]$ nanotori.

Theorem 5. The neighborhood version of hyper Zagreb index HM_N of $TUC_4C_8[m, n]$ ($m, n \geq 2$), $TUAC_6[m, n]$, $VPHX[m, n]$, and $VPHY[m, n]$ nanotubes are given by:

- (i) $HM_N(TUC_4C_8[m, n]) = 3888mn - 1020m$,
- (ii) $HM_N(TUAC_6[m, n]) = 972mn - 24m$,
- (iii) $HM_N(VPHX[m, n]) = 2916mn - 1042m$,
- (iv) $HM_N(VPHY[m, n]) = 2916mn$.

Proof. The general formula of neighborhood version of hyper Zagreb index HM_N is given by:

$$HM_N(G) = \sum_{uv \in E(G)} [\delta_G(u) + \delta_G(v)]^2.$$

- (i) Let G be the $TUC_4C_8[m, n]$ nanotube for ($m, n \geq 2$). Then applying Table 2 on the general form of neighborhood version of hyper Zagreb index, we obtain the following computation:

$$\begin{aligned} HM_N(G) &= \sum_{uv \in E_{(5,5)}} [\delta_G(u) + \delta_G(v)]^2 + \sum_{uv \in E_{(5,8)}} [\delta_G(u) + \delta_G(v)]^2 + \sum_{uv \in E_{(8,8)}} [\delta_G(u) + \delta_G(v)]^2 \\ &\quad + \sum_{uv \in E_{(8,9)}} [\delta_G(u) + \delta_G(v)]^2 + \sum_{uv \in E_{(9,9)}} [\delta_G(u) + \delta_G(v)]^2 \\ &= |E_{(5,5)}|(5+5)^2 + |E_{(5,8)}|(5+8)^2 + |E_{(8,8)}|(8+8)^2 + |E_{(8,9)}|(8+9)^2 \\ &\quad + |E_{(9,9)}|(9+9)^2 \\ &= 2m(5+5)^2 + 4m(5+8)^2 + 2m(8+8)^2 + 4m(8+9)^2 + (12mn - 11m)(9+9)^2. \end{aligned}$$

After simplification the desired result can be obtained easily.

- (ii) Let G be the $TUAC_6[m, n]$ nanotube. Then applying the Table 4 on the definition of neighborhood version of second Zagreb index, we get the following derivation:

$$\begin{aligned} HM_N(G) &= \sum_{uv \in E_{(5,5)}} [\delta_G(u) + \delta_G(v)]^2 + \sum_{uv \in E_{(5,8)}} [\delta_G(u) + \delta_G(v)]^2 + \sum_{uv \in E_{(8,8)}} [\delta_G(u) + \delta_G(v)]^2 \\ &\quad + \sum_{uv \in E_{(8,9)}} [\delta_G(u) + \delta_G(v)]^2 + \sum_{uv \in E_{(9,9)}} [\delta_G(u) + \delta_G(v)]^2 \\ &= |E_{(5,5)}|(5+5)^2 + |E_{(5,8)}|(5+8)^2 + |E_{(8,8)}|(8+8)^2 + |E_{(8,9)}|(8+9)^2 + |E_{(9,9)}|(9+9)^2 \\ &= 4m(5+5)^2 + 4m(5+8)^2 + 2m(8.8) + 2m(8+9)^2 + 9m(n-1)(9+9)^2 \\ &= 972mn - 24m. \end{aligned}$$

- (iii) Let G be the $VPHX[m, n]$ nanotube. Then applying the Table 6 on the definition of neighborhood version of second Zagreb index, we get the following derivation:

$$\begin{aligned} HM_N(G) &= \sum_{uv \in E_{(6,8)}} [\delta_G(u) + \delta_G(v)]^2 + \sum_{uv \in E_{(8,8)}} [\delta_G(u) + \delta_G(v)]^2 + \sum_{uv \in E_{(8,9)}} [\delta_G(u) + \delta_G(v)]^2 \\ &\quad + \sum_{uv \in E_{(9,9)}} [\delta_G(u) + \delta_G(v)]^2 \\ &= |E_{(6,8)}|(6+8)^2 + |E_{(8,8)}|(8+8)^2 + |E_{(8,9)}|(8+9)^2 + |E_{(9,9)}|(9+9)^2 \\ &= 4m(6+8)^2 + 2m(8.8) + 2m(8+9)^2 + 9m(n-1)(9+9)^2 \\ &= 2916mn - 1042m. \end{aligned}$$

- (iv) Let G be the $VPHY[m, n]$ nanotube. From Fig. 3, it is clear that $E(G) = E_{(9,9)}$ and $|E_{(9,9)}| = 9mn$. Thus, we have $F_N^*(G) = 9mn(9+9)^2 = 2916mn$

Hence the proof. □

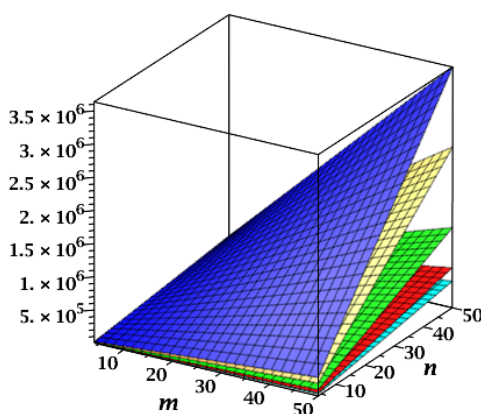


FIG. 8. Topological indices for $TUAC_6[m, n]$ nanotube.

The surface plotting of topological indices for the nanotubes and nanotori are shown in the Figs. 5, 6, 7, and 8. We have built the figures using Maple 2015.1 software taking the parametric values (m, n) in $[2, 50]$. For different indices, different colors are used. We put cyan, blue, green, red and gold colors for M_N , F_N , F_N^* , M_2^* , and HM_N indices respectively.

5. Remarks and conclusion

In this article, the structures of $TURC_4C_8(S)$, armchair polyhex nanotube $TUAC_6$, V-phenylenic nanotube $VPHX[m, n]$, and V-phenylenic nanotori $VPHY[m, n]$ are discussed and explicit expressions of M_N , F_N , F_N^* , M_2^* , and HM_N are derived for them. In fact, comparison among these indices for the considered nanotubes and nanotori are shown in the Figs. 5,6,7, and 8. Clearly, the indices for different nanotubes and nanotori are growing in the following order.

$$TUAC_6[m, n] < VPHY[m, n] < VPHX[m, n] < TURC_4C_8(S),$$

where in each case, indices have following order.

$$M_N < M_2^* < F_N^* < HM_N < F_N.$$

Thus, for each structure discussed above, the indices behave somewhat differently. The formulas obtained here enable the chemical structure of nano structures to be correlated with a large amount of information about their physicochemical characteristics.

Acknowledgments

The first author is very obliged to the Department of Science and Technology (DST), Government of India for the Inspire Fellowship [IF170148].

References

- [1] Trinajstić N. *Chemical Graph Theory*. CRC Press, Boca Raton, 1983.
- [2] Gutman I. Polansky O.E. *Mathematical Concepts in Organic Chemistry*. Springer, Berlin, 1986.
- [3] Diudea M.V., Gutman I., Lorentz J. *Molecular Topology*. Romania: Babes-Bolyai University, 2001.
- [4] Gutman I. Degreebased topological indices. *Croat. Chem. Acta*, 2013, **86** (4), P. 351–361.
- [5] Gutman I., Trinajstić N. Graph theory and molecular orbitals. Total π -electron energy of alternate hydrocarbons. *Chem. Phys. Lett.*, 1972, **17**, P. 535–538.
- [6] Gutman I., Das K.C. The first Zagreb index 30 years after. *MATCH Commun. Math. Comput. Chem.*, 2004, **50**, P. 83–92.
- [7] Furtula B., Gutman I. A forgotten topological index. *J. Math. Chem.*, 2015, **53** (4), P. 1184–1190.
- [8] Shirdeh G.H., Rezapour H., Sayadi A.M. The hyper Zagreb index of graph operations. *Iran. J. Math. Chem.*, 2013, **4** (2), P. 213–220.
- [9] Mondal S., De N., Pal A. On neighbourhood zagreb index of product graphs. *arXiv:1805.05273*, 2018.
- [10] Mondal S., De N., Pal A. On some new neighbourhood degree based indices. *Acta Chemica Iasi*, 2019, **27** (1), P. 31–46.
- [11] Gao Y.Y., Sardar M.S., Hosamani S.M., Farahani M.R. Computing sanskruti index of $TURC_4C_8(s)$ nanotube. *Int. J. Pharm. Sci. Res.*, 2017, **8** (10), P. 4423–4425.
- [12] Jiang H., Sardar M.S., et al. Computing sanskruti index V-phenylenic nanotube and nanotori. *Int. J. Pure Appl. Math.*, 2017, **115** (4), P. 859–865.
- [13] Farahani M.R. Computing GA_5 index of armchair polyhex nanotube. *Le Matematiche*, 2014, **LXIX**, P. 69–76.

- [14] Mondal S., De N., Pal A. On Some New Neighborhood Degree-Based Indices for Some Oxide and Silicate Networks. *J. Multidisciplinary Scientific Journal*, 2019, **2** (3), P. 384–409.
- [15] Kawun Y.C., Munir M., et al. Computational Analysis of topological indices of two Boron Nanotubes. *Scientific Reports*, 2018, **8** (1), 14843.
- [16] Kawun Y.C., Munir M., et al. M-Polynomials and topological indices of V-Phenylenic Nanotubes and Nanotori. *Scientific Reports*, 2017, **7** (1), 8756.
- [17] Farahani M. R. On the fourth atom bond connectivity index of armchair polyhex nanotube. *Proc. Rom. Acad., Series B*, 2013, **15** (1), P. 3–6.
- [18] Ashrafi A.R., Doslic T., Saheli M. The eccentric connectivity index of $TUC_4C_8(R)$ nanotubes. *MATCH Commun. Math. Comput. Chem.*, 2011, **65**, P. 221–230.
- [19] Farahani M.R. Fifth Geometric-Arithmetic Index of $TURC_4C_8(S)$ Nanotubes. *J. Chem. Acta*, 2013, **2** (1), P. 62–64.
- [20] De N., Nayeem S.M.A. Computing the F-index of nanostar dendrimers. *Pacific Science Review A: Natural Science and Engineering*, 2016, 10.1016/j.psra.2016.06.001.
- [21] Gao W., Siddiqui M.K. Molecular Descriptors of Nanotube, Oxide, Silicate, and Triangulene Networks. *J. Chem.*, 2017, 6540754.

Finite Toda lattice and classical moment problem

A. S. Mikhaylov^{1,2}, V. S. Mikhaylov¹

¹Saint Petersburg Department of V. A. Steklov Institute of Mathematics of the Russian Academy of Sciences,
7, Fontanka, 191023 Saint Petersburg, Russia

²Saint Petersburg State University, Saint Petersburg State University, 7/9 Universitetskaya nab.,
Saint Petersburg, 199034 Russia

mikhaylov@pdmi.ras.ru, vsmikhaylov@pdmi.ras.ru

DOI 10.17586/2220-8054-2020-11-1-25-29

We study the problem of computing the solution to finite Toda lattice. Specifically, we describe the evolution of moments of the spectral measure of a Jacobi matrix entering in the Lax pair.

Keywords: Toda lattice, moment problem, Jacobi matrices.

Received: 13 January 2020

Revised: 16 January 2020

1. Introduction

The semi-infinite or finite Toda lattice can be written in the following way:

$$\begin{cases} \dot{a}_n(t) = a_n(t) (b_{n+1}(t) - b_n(t)), \\ \dot{b}_n(t) = 2 (a_n^2(t) - a_{n-1}^2(t)), \quad t \geq 0, n = 1, 2, \dots, N, \end{cases} \quad (1)$$

where $N \in \mathbb{N}$ or $N = \infty$, and one looks for a solution satisfying the initial conditions:

$$a_n(0) = a_n^0, \quad b_n(0) = b_n^0, \quad n = 1, \dots, N, \quad (2)$$

where a_n^0, b_n^0 are real and $a_n^0 > 0$. Toda lattices are used for modeling of nanosystems and macromolecules [1–3]. Methods of computing of functions $a_n(t), b_n(t)$ are subject of many investigations, see for example [4–6] and references therein. In the present paper, we restrict ourselves to the case of finite N , this situation was studied in [7].

We define two operators acting in \mathbb{R}^N , $f \in \mathbb{R}^N$, $f = (f_1, f_2, \dots, f_N)$ by rules:

$$H(t) : f \mapsto \begin{cases} a_1(t)f_2 + b_1(t)f_1, \\ a_n(t)f_{n+1} + a_{n-1}f_{n-1} + b_n(t)f_n, \quad n = 2, \dots, N-1, \\ a_{N-1}(t)f_{N-1} + b_N(t)f_N, \end{cases}$$

$$P(t) : f \mapsto \begin{cases} a_1(t)f_2, \\ a_n(t)f_{n+1} - a_{n-1}(t)f_{n-1}, \quad n = 2, \dots, N-1, \\ a_{N-1}f_{N-1}. \end{cases}$$

Note that the operator $H(t)$ is given by the Jacobi matrix (we keep the same notation for it):

$$H(t) = \begin{pmatrix} b_1(t) & a_1(t) & 0 & 0 & 0 \\ a_1(t) & b_2(t) & a_2(t) & 0 & 0 \\ 0 & a_2(t) & b_3(t) & a_3(t) & 0 \\ \cdot & \cdot & \cdot & \cdot & \cdot \\ 0 & 0 & 0 & a_{N-1}(t) & b_N(t) \end{pmatrix}. \quad (3)$$

It is a well known fact [5, 6] that the system (1) is equivalent to the following operator equation:

$$\frac{dH}{dt} = PH - HP. \quad (4)$$

By $d\rho^t(\lambda)$, we denote the spectral measure of operator $H(t)$. Being a spectral measure of a bounded operator in \mathbb{R}^N , it has the form:

$$d\rho^t(\lambda) = \sum_{k=1}^N \sigma_k^2(t) \delta(\lambda - \lambda_k(t)), \quad (5)$$

where $\lambda_k(t)$, $k = 1, \dots, N$ is a spectrum of $H(t)$. The moments of $d\rho^t(\lambda)$ are introduced by the rule:

$$s_k(t) = \int_{-\infty}^{\infty} \lambda^k d\rho^t(\lambda), \quad k = 0, 1, 2, \dots \quad (6)$$

It is well-known fact that the set of moments determines the semi-infinite Jacobi operator (but not necessarily in the unique way!), see [8, 9] and [10, 11] for dynamic approach.

For infinite Toda lattices, people are interested in the evolution of scattering data for operator $H(t)$ [4, 5, 7]. In the finite case in [7] the author studied the evolution of $\sigma_k(t)$ (it happens that λ_k do not depend on t). In the present paper, we investigate the evolution of moments $s_k(t)$ under Toda flow. The authors are planning to use the obtained results for studying the semi-infinite Toda lattices, which will be the subject of forthcoming publications.

In the second section, we provide the necessary information on Toda lattices and adopt and rewrite some of results from [7] in a form, convenient for our purposes. In the last section, we remind the reader some basic facts on moment problem and derive the evolution equation for moments under the Toda flow.

2. Finite Toda lattice, Moser formula.

Here, we adapt some of results from [7] to the convenient forms for our use. For simplicity we usually omit the argument t .

Proposition 1. *The eigenvalues of the matrix $H(t)$ do not depend on t : $\lambda_j(t) = \lambda_j(0)$.*

This fact follows from the representation $\frac{dH}{dt} = i(HiP - (iP)H) = \{-iP, H\}$, and thus $H(t) = e^{Pt}H(0)e^{-Pt}$. Let (\cdot, \cdot) denotes the scalar product in \mathbb{R}^N . The Weyl function [12, 13] is introduced by the rule:

$$m(\lambda) := (R(\lambda)e_1, e_1),$$

where:

$$R(\lambda) = (H(t) - \lambda I)^{-1}, \quad e_i = (0, \dots, 0, 1, 0, \dots, 0),$$

with 1 being at i -th place.

Proposition 2. *The following relation holds:*

$$\frac{d}{dt}m(\lambda) = 2a_1R_{21}(\lambda). \quad (7)$$

Proof. We can evaluate:

$$\frac{dR}{dt} = -R\frac{dH}{dt}R = -RPHR + RHPR = -RP(I + \lambda R) + (I + \lambda R)PR = PR - RP.$$

Then, using this relation, we have that:

$$\frac{d}{dt}m(\lambda) = ((PR - RP)e_1, e_1) = -2(RPe_1, e_1) = 2a_1R_{21}.$$

□

We introduce the matrix:

$$B_N = H - \lambda I = \begin{pmatrix} b_1 - \lambda & a_1 & 0 & 0 & 0 \\ a_1 & b_2 - \lambda & a_2 & 0 & 0 \\ 0 & a_2 & b_3 - \lambda & a_3 & 0 \\ \cdot & \cdot & \cdot & \cdot & \cdot \\ 0 & 0 & 0 & a_{N-1} & b_N - \lambda \end{pmatrix}$$

and minors B_k , $1 \leq k < N$ of B_N , where B_k are given by the intersection of k rows $N - k + 1, \dots, N - 1, N$ and k columns $N - k + 1, \dots, N - 1, N$. Denote $\Delta_k := \det B_k$. Then, simple algebra shows that:

$$m(\lambda) = R_{11} = \frac{\Delta_{N-1}}{\Delta_N},$$

$$R_{21}(\lambda) = R_{12}(\lambda) = (R(\lambda)e_1, e_2) = -\frac{a_1\Delta_{N-2}}{\Delta_N}.$$

Using these equalities we can rewrite (7) in the following form:

$$\frac{d}{dt}m(\lambda) = 2(1 - (b_1 - \lambda)m(\lambda)). \quad (8)$$

Representations of a Weyl function [12, 13] and a spectral measure (5) imply that:

$$m(\lambda) = \int_R \frac{1}{\lambda - z} d\rho(z) = \sum_{k=1}^N \frac{\sigma_k^2(t)}{\lambda - \lambda_k}.$$

Plugging the latter representation into (8) we have that:

$$\sum_{k=1}^N \frac{2\dot{\sigma}_k \sigma_k}{\lambda - \lambda_k} = 2 \left(1 - (b_1 - \lambda) \sum_{k=1}^N \frac{\sigma_k^2}{\lambda - \lambda_k} \right),$$

where by dot we denote the differentiation with respect to t . Multiplying the last equality by $(\lambda - \lambda_k)$ and setting $\lambda = \lambda_k$, we come to the following system:

$$\dot{\sigma}_k(t) = -(b_1 - \lambda_k)\sigma_k(t), \quad k = 1, \dots, N. \quad (9)$$

By $\|\cdot\|$ we denote the standard norm in \mathbb{R}^N .

Proposition 3. *The coefficient b_1 admits the representation:*

$$b_1 = \sum_{k=1}^N \lambda_k \sigma_k^2.$$

Proof. Denote by C_k the eigenvectors of H :

$$HC^k = \lambda_k C^k, \quad C^k = \begin{pmatrix} C_1^k \\ C_2^k \\ \dots \\ C_N^k \end{pmatrix}, \quad k = 1, \dots, N,$$

such that $\|C^k\| = 1$, $k = 1, \dots, N$. Then, by the spectral theorem:

$$C^* H C = \begin{pmatrix} \lambda_1 & 0 & 0 & \dots & 0 \\ 0 & \lambda_2 & 0 & \dots & 0 \\ \dots & \dots & \dots & \dots & \dots \\ 0 & 0 & 0 & \dots & \lambda_N \end{pmatrix}, \quad \text{where } C = (C^1 | C^2 | \dots | C^N),$$

i.e., the matrix C is constructed from columns C^k , $k = 1, \dots, N$. Then:

$$H = C \begin{pmatrix} \lambda_1 & 0 & 0 & \dots & 0 \\ 0 & \lambda_2 & 0 & \dots & 0 \\ \dots & \dots & \dots & \dots & \dots \\ 0 & 0 & 0 & \dots & \lambda_N \end{pmatrix} C^*,$$

from where and (3) we have that:

$$b_1 = H_{11} = \sum_{k=1}^N \lambda_k (C_1^k)^2 = \sum_{k=1}^N \lambda_k (\sigma_k)^2.$$

□

The above proposition allows us to rewrite the system (9) in a more convenient form:

$$\dot{\sigma}_k(t) = - \left(\sum_{j=1}^N \lambda_j \sigma_j^2(t) - \lambda_k \right) \sigma_k(t), \quad k = 1, \dots, N. \quad (10)$$

Solution of (10) is given by the *Moser formula*:

$$\sigma_k^2(t) = \frac{\sigma_k^2(0) e^{2\lambda_k t}}{\sum_{j=1}^N \sigma_j^2(0) e^{2\lambda_j t}}. \quad (11)$$

3. Moment problem. Evolution of moments under the Toda flow.

We denote by $C_N[X]$ the set of polynomials of order less than N . The set of moments $\{s_k\}_{k=0}^{2N-2}$ determines on $C_N[X]$ the bilinear form by the rule: for $F, G \in C_N[X]$, $F(\lambda) = \sum_{n=0}^{N-1} \alpha_n \lambda^n$, $G(\lambda) = \sum_{n=0}^{N-1} \beta_n \lambda^n$, one defines:

$$\langle F, G \rangle = \sum_{n,m=0}^{N-1} s_{n+m} \alpha_n \beta_m. \quad (12)$$

Thus this quadratic form is determined by the following Hankel matrix:

$$S = \begin{pmatrix} s_0 & s_1 & s_2 & \dots & s_{N-1} \\ s_1 & s_2 & \dots & \dots & \dots \\ s_2 & \dots & \dots & \dots & \dots \\ \dots & \dots & \dots & \dots & s_{2N-1} \\ s_{N-1} & \dots & \dots & s_{2N-1} & s_{2N-2} \end{pmatrix} \quad (13)$$

In [10, 11] it is shown that $C_N[X]$ is in fact a de Branges space (we denote it here by $B^N(t)$), related to the dynamical system with discrete time associated with Jacobi matrix (3), see also [14, 15]. The scalar product in $B^N(t)$ is given by $[F, G]_{B^N(t)} = \langle F, G \rangle$.

By $\|\cdot\|$ we denote the standard norm in \mathbb{R}^N . We introduce the vector:

$$\tilde{\sigma}(t) = \begin{pmatrix} \tilde{\sigma}_1(t) \\ \tilde{\sigma}_2(t) \\ \dots \\ \tilde{\sigma}_N(t) \end{pmatrix} = \begin{pmatrix} \sigma_1(0)e^{\lambda_1 t} \\ \sigma_2(0)e^{\lambda_2 t} \\ \dots \\ \sigma_N(0)e^{\lambda_N t} \end{pmatrix}. \quad (14)$$

Then (11) and (14) implies that:

$$\sigma_k(t) = \frac{\tilde{\sigma}_k(t)}{\|\tilde{\sigma}(t)\|},$$

where

$$\|\tilde{\sigma}(t)\| = \sqrt{\sum_{j=1}^N \sigma_j^2(0)e^{2\lambda_j t}}.$$

For $k = 1, \dots, N$ we have that:

$$s_k(t) = \int_{\mathbb{R}} \lambda^k d\rho^t(\lambda) = \sum_{j=1}^N \lambda_j^k \sigma_j^2(t) = \sum_{j=1}^N \lambda_j^k \frac{\tilde{\sigma}_j^2(t)}{\|\tilde{\sigma}(t)\|^2}. \quad (15)$$

Then on introducing the notation

$$\tilde{s}_k(t) = s_k(t) \|\tilde{\sigma}(t)\|^2,$$

and using (15) we see that

$$\dot{\tilde{s}}_k(t) = \sum_{j=1}^N \lambda_j^k 2\dot{\tilde{\sigma}}_j(t) \tilde{\sigma}_j(t) = \sum_{j=1}^N \lambda_j^{k+1} 2\tilde{\sigma}_j^2(t) = 2\tilde{s}_{k+1}(t). \quad (16)$$

We take $F, G \in C_N[X]$, $F(\lambda) = \sum_{n=0}^{N-1} \alpha_n \lambda^n$, $G(\lambda) = \sum_{n=0}^{N-1} \beta_n \lambda^n$, then the scalar product in $B^N(t)$ has the form:

$$[F, G]_{B^N(t)} = \sum_{n,m=0}^{N-1} s_{n+m}(t) \alpha_n \beta_m.$$

We multiply both sides of the above equality by $\|\tilde{\sigma}(t)\|^2$ and differentiate:

$$\begin{aligned} \left([F, G]_{B^N(t)} \|\tilde{\sigma}(t)\|^2 \right)' &= \sum_{n,m=0}^{N-1} \left(\|\tilde{\sigma}(t)\|^2 s_{n+m}(t) \right)' \alpha_n \beta_m \\ &= \sum_{n,m=0}^{N-1} (\tilde{s}_{n+m}(t))' \alpha_n \beta_m = \sum_{n,m=0}^{N-1} 2\tilde{s}_{n+m+1}(t) \alpha_n \beta_m = 2\|\tilde{\sigma}(t)\|^2 \sum_{n,m=0}^{N-1} s_{n+m+1}(t) \alpha_n \beta_m. \end{aligned} \quad (17)$$

Differentiating the left hand side of the above equality, we have that:

$$\left([F, G]_{B^N(t)} \|\tilde{\sigma}(t)\|^2\right)' = (\|\tilde{\sigma}(t)\|^2)' \sum_{n,m=0}^{N-1} s_{n+m}(t) \alpha_n \beta_m + \|\tilde{\sigma}(t)\|^2 \sum_{n,m=0}^{N-1} \dot{s}_{n+m}(t) \alpha_n \beta_m. \quad (18)$$

On equating (18) and the right and side of (17), we come to the relation:

$$\frac{(\|\tilde{\sigma}(t)\|^2)'}{\|\tilde{\sigma}(t)\|^2} \sum_{n,m=0}^{N-1} s_{n+m}(t) \alpha_n \beta_m + \sum_{n,m=0}^{N-1} \dot{s}_{n+m}(t) \alpha_n \beta_m = 2 \sum_{n,m=0}^{N-1} s_{n+m+1}(t) \alpha_n \beta_m.$$

Due to the arbitrariness of F, G the last equality implies that for moments s_k the following system holds:

$$\dot{s}_k(t) + (\ln \{\|\tilde{\sigma}(t)\|^2\})' s_k(t) = 2s_{k+1}(t), \quad k = 0, \dots, 2N - 2. \quad (19)$$

Since we know that $s_0(t) = 1$ for all t , then (19) allows us to determine $s_1(t), s_2(t), \dots, s_{2N-2}(t)$ recursively. Then, we use the fact that the set of moments $s_k(t), k = 0, \dots, 2N - 2$ determines $N \times N$ Jacobi matrix (3) and thus coefficients $a_k(t), b_k(t), a_N(t), k = 1, \dots, N - 1$. Formulas for the reconstruction of entries of Jacobi matrix from moments are given in [8, 14, 16]

Analysis of the solution to (19) as well as an application of the results of the present paper and of [11, 16] to the case of semi-infinite Toda lattices will be the subject of forthcoming publications.

Acknowledgements

A. S. Mikhaylov and V. S. Mikhaylov were partially supported by RFBR 18-01-00269 and by the Ministry of Education and Science of Republic of Kazakhstan under grant AP05136197 and by Volkswagen Foundation project ‘‘From Modeling and Analysis to Approximation’’.

References

- [1] Cho K. *Optical Response of Nanostructures.: Microscopic Nonlocal Theory*. Springer Science & Business Media, Berlin, 2003.
- [2] Muto V., Scott A.C., Christiansen P.L. A Toda lattice model for DNA: Thermally generated solitons. *Physica D: Nonlinear Phenomena*, 1990, **44**(1-2), P. 75–91.
- [3] Tsen K.-T. (Ed.) *Non-Equilibrium Dynamics of Semiconductors and Nanostructures*. CRC Press, 2018.
- [4] Faddeev L.D., Takhtajan L.A. *Hamiltonian Methods in the Theory of Solitons*. Springer-Verlag Berlin Heidelberg, 2007.
- [5] Teschl G. *Jacobi operator and completely integrable nonlinear lattices*. Providence: Amer. Math. Soc., 2001.
- [6] Toda M. *Theory of Nonlinear Lattices*. Springer Series in Solid-State Sciences, 20 (2 ed.), Berlin: Springer, 1989.
- [7] Moser J. Finitely many mass points on the line under the influence of an exponential potential – an integrable system. *Dynamical Systems, Theory and Applications, Lecture Notes in Physics*, 1975, **38**, P. 67–497.
- [8] Akhiezer N.I. *The classical moment problem and some related questions in analysis*. Edinburgh, Oliver and Boyd, 1965.
- [9] Simon B. The classical moment problem as a self-adjoint finite difference operator. *Advances in Math.*, 1998, **137**, P. 82–203.
- [10] Mikhaylov A.S., Mikhaylov V.S. On application of the Boundary control method to classical moment problems. *Journal of Physics: Conference Series - IOPscience*.
- [11] Mikhaylov A.S., Mikhaylov V.S. *Inverse problem for dynamical system associated with Jacobi matrices and classical moment problems*. <https://arxiv.org/abs/1907.11153>
- [12] Gesztesy F., Simon B. m -functions and inverse spectral analysis for finite and semi-infinite Jacobi matrices, *J. d'Analyse Math.*, 1997, **73**, P. 267–297.
- [13] Mikhaylov A.S., Mikhaylov V.S., Simonov S.A. On the relationship between Weyl functions of Jacobi matrices and response vectors for special dynamical systems with discrete time. *Mathematical Methods in the Applied Sciences*, 2018, **41**(16), P. 6401–6408.
- [14] Mikhaylov A.S., Mikhaylov V.S. Inverse dynamic problems for canonical systems and de Branges spaces. *Nanosystems: Physics, Chemistry, Mathematics*, 2018, **9**(2), P. 215–224.
- [15] Mikhaylov A.S., Mikhaylov V.S. Boundary Control method and de Branges spaces. Schrödinger operator, Dirac system, discrete Schrödinger operator. *Journal of Mathematical Analysis and Applications*, 2018, **460**(2), P. 927–953.
- [16] Mikhaylov A.S., Mikhaylov V.S. Dynamic inverse problem for Jacobi matrices. *Inverse Problems and Imaging*, 2019, **13**(3), P. 431–447.

The Lagrange variety approach applied to frustrated classical wheels

W. Florek¹, A. Marlewski², G. Kamieniarz¹, M. Antkowiak¹

¹Adam Mickiewicz University, Faculty of Physics,
ul. Uniwersytetu Poznańskiego 2, 61-614 Poznań, Poland

²Poznań University of Technology, Institute of Mathematics,
ul. Piotrowo 3A, 60-965 Poznań, Poland

wojciech.florek@amu.edu.pl

PACS 75.10.Hk, 75.50.Ee, 75.50.Xx, 02.40.Re

DOI 10.17586/2220-8054-2020-11-1-30-35

The Lagrange variety approach introduced by Schmidt and Luban [J. Phys. A: Math. Gen. **36**, 6351 (2003)] is applied to geometrically frustrated wheels (centered regular polygons). It is shown that the lowest energy configurations are planar or collinear. The latter one, characteristic for non-frustrated classical systems, is also observed in the presence of competing interactions in a well-determined range $(0, \alpha_c)$ of the energy function parameter α . The ‘critical’ value $\alpha_c = 1/4$ is universal, i.e., it does not depend on a system size. In this domain, the geometric frustration is present, but there is no non-trivial degeneracy.

Keywords: frustration, classical spin models, magnetic molecules, Lagrange variety.

Received: 29 December 2019

1. Introduction

Ring-shaped magnetic molecules play an important role due to possible realization of single molecule magnets or molecular qubits [1–6]. Moreover, these, with an odd number of spins and dominant antiferromagnetic couplings, are interesting subjects in the study of the spin frustration [7–14]. In this work, we focus on the classical counterparts of rings with an extra spin placed at its center (see Fig. 1) [13–18]. In general, heterometallic systems may be considered [19], but this short paper is limited to homogeneous ones. To avoid frustration in a peripheral ring only centered polygons XY_{2q} (corresponding to wheel graphs W_{2q+1} [20]) are investigated. The aim of this paper is to determine the lowest energy configuration (LEC) for a system of classical spin vectors coupled by the isotropic Heisenberg interactions with two exchange integrals J and J_0 for the nearest-neighbor spins s_j , $1 \leq j \leq N$, in the peripheral ring and for their couplings with the central spin s_0 , respectively; competing interactions are present for antiferromagnetic couplings J , despite the value of J_0 .

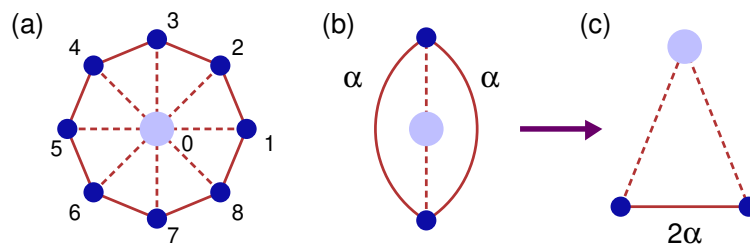


FIG. 1. (a) A centered octagon (the wheel W_9) and (b) a centred regular digon (the ‘wheel’ W_3) transformed to an isosceles triangle; the weight of the edge (1, 2) is doubled to mimic two pairs in the original system. The edges correspond to couplings J and J_0 (solid and dashed lines, respectively).

Such a system is another example of models in which the collinear LEC is ‘retained’ when competing interactions are ‘turned on’ by a relatively weak antiferromagnetic coupling(s) [13, 14, 21]. This feature can be considered as the classical counterpart of the third type frustration according to the classification scheme recently proposed [8]. To clarify relations among the notions of ‘frustration’, ‘degeneracy’, and ‘competing interactions’, a short resume is given in the next section.

To determine LECs one has to find the global local minimum of energy function, which is a real-valued function of many variables. This is very challenging task and it is difficult to obtain some general results (cf. [22–24]). An efficient method based on the Lagrange variety has been proposed [25] and extensively discussed in a series of papers [26]. This technique enables precise determination of the global minimum and the corresponding LEC considering a general

form of the energy function for any system size [27]. Such approach has been successfully applied to heterometallic wheels [19] and some of the results obtained are shortly presented below.

This work starts with a short discussion on the frustration and degeneracy. A model considered and solutions obtained are presented in Sec. 3. In the last section the most important conclusions and some challenges are gathered.

2. Frustration and degeneracy

The term ‘frustration’ was introduced by Toulouse [28,29], though spin glasses and other systems with frustration (competing interactions) had been investigated many years earlier [30,31]. Toulouse considered the standard Ising model, i.e., spins $S_j = \pm 1$ and exchange integrals $J = \pm 1$. He introduced the frustration function as a product of exchange integrals over a contour c ($J = 1$ corresponds to antiferromagnetic couplings)

$$\Phi(c) = \prod_{\text{contour } c} (-J_{jj'}), \quad (1)$$

where j and j' are labels of neighbouring nodes in the contour considered – the frustration is present if $\Phi(c) = -1$ [28]. Four obvious facts may be established:

- This property characterises a cycle (a system), not an individual spin.
- Antiferromagnetic couplings must be present. To be more precise – the considered cycle has to comprise an odd number of them.
- The ground state (GS) of a system is degenerated.
- Competing interactions are present, i.e., not all bonds (terms in the energy function) are ‘satisfied’: The GS energy is greater than a sum of the minimum energies of individual bonds (terms).

When more general cases of spin glasses have been considered (e.g., these with random values of $J_{jj'} \in \mathbb{R}$), another characteristic has been introduced (cf., e.g., [32]):

$$P(c) = (-1)^{N_{\text{AFM}}}, \quad (2)$$

where N_{AFM} denotes a number of antiferromagnetic couplings in the contour c . Its advantage is to give values restricted to ± 1 , though, in general, $|J_{jj'}| \neq 1$. However, it ‘predicts’ frustration ($P(c) = -1$) in the presence of competing interactions but without the degeneracy (cf. [33]). It can be easily seen in the classical example of an antiferromagnetic triangle ($S_j = \pm 1$) with the energy function

$$E = S_2(S_1 + S_3) + \alpha S_1 S_3. \quad (3)$$

According to the rule ‘The enemy of my enemy is my ally’, in the GS configuration there is $S_1 = S_3$ if $0 < \alpha < 1$, though these spins are ‘enemies’ for positive α . Note, that this configuration is identical to that of the non-frustrated system with $\alpha < 0$ (when S_1 and S_3 are in fact ‘allies’). The GS degeneracy is present for $\alpha \geq 1$ only. Hence, in the range $0 < \alpha < 1$ there are merely competing interactions (the term $\alpha S_1 S_3$ is not satisfied), but the degeneracy is absent. This feature can be considered as a counterpart of the third type frustration [8, 13, 14] for the Ising model.

This phenomenon is absent in some systems. For example, considering the Ising antiferromagnetic pentagon with the energy function (cf. Fig. 2):

$$E = S_3(S_2 + S_4) + \alpha(S_1 S_2 + S_4 S_5 + S_1 S_5), \quad (4)$$

one obtains that the GS configuration changes at $\alpha = 0$ and $\alpha = 1$ (cf. Fig. 2) and for all $\alpha > 0$ the competing interactions and the degeneracy are present simultaneously.

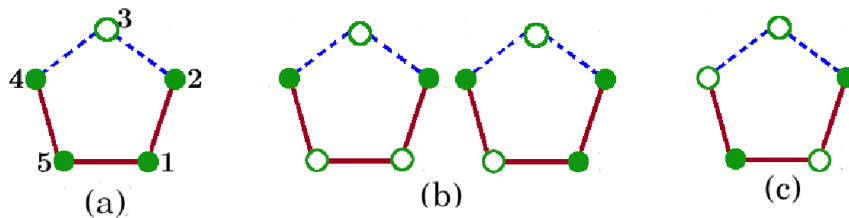


FIG. 2. The GS configurations for the energy functions given in Eq. (4). The exchange integrals are $J = 1$ (dashed lines) or $J = \alpha$ (solid ones); $S = \pm 1$ are denoted by full and empty symbols, respectively. The GS configurations for (a) $\alpha < 0$, (b) $0 \leq \alpha < 1$, and (c) $\alpha \geq 1$ are presented. Due to lack of the reflection symmetry the two right-most configurations are doubly degenerate.

3. Model and its solution

3.1. General remarks

When lengths of spin vectors are fixed (a constraint $|\mathbf{s}_j| = 1$ for $0 \leq j \leq N$ is assumed in this work), the energy is a real-valued of angles determining positions of vectors \mathbf{s}_j in \mathbb{R}^3 . The first two vectors ($j = 0, 1$) can be fixed to lie in the xy plane, so it is assumed that

$$\mathbf{s}_0 = [1, 0, 0], \quad \mathbf{s}_1 = [\cos \varphi_1, \sin \varphi_1, 0]. \quad (5)$$

For the others ($2 \leq j \leq N$) one may put

$$\mathbf{s}_j = [\sin \vartheta_j \cos \varphi_j, \sin \vartheta_j \sin \varphi_j, \cos \vartheta_j]. \quad (6)$$

Hence, in a general case the energy depends on $2N - 1$ variables.

The LEC is collinear for non-frustrated systems [34]. Hence, if the LEC is planar or even spatial then competing interactions are certainly present [25, 34]. However, these statements do not exclude the special case when competing interactions are present but there is no degeneracy and the LEC is collinear, what can be considered as an analog of the third type frustration in quantum systems.

This possibility is realised in an isosceles antiferromagnetic triangle presented in Fig. 1(b) with the energy function:

$$E(\varphi_1, \varphi_2) = \cos \varphi_1 + \cos \varphi_2 + 2\alpha \cos(\varphi_2 - \varphi_1), \quad (7)$$

where it is assumed that the LEC is planar (cf. [13, 14, 19, 34]). It is easy to show that:

- For $\alpha \leq 1/4$ the LEC is collinear with $\varphi_1 = \varphi_2 = \pi$ and $E_1 = 2(\alpha - 1)$;
- For $\alpha \geq 1/4$ the LEC is planar with $\varphi_2 = -\varphi_1$, $\cos \varphi_1 = -1/4\alpha$ (so for increasing α the angle φ_1 increases from π to $3\pi/2$ or decreases to $\pi/2$), and $E_2 = -(1 + 8\alpha^2)/(4\alpha)$.

Therefore, in a range $0 < \alpha < 1/4$ the LEC is collinear in the presence of competing interactions ($\mathbf{s}_1 = \mathbf{s}_2$ despite antiferromagnetic coupling).

3.2. The Lagrange variety approach

This approach has been extensively discussed in Schmidt's works [26] and its application to heterogeneous systems have been recently presented [19], so only some important points are mentioned below. In a present version this approach can be applied to isotropic bilinear interactions when a general form of the energy function is given as:

$$\mathcal{E} = \frac{1}{2} \sum_{(j,k)} J_{jk} \mathbf{s}_j \cdot \mathbf{s}_k, \quad J_{jj} = 0. \quad (8)$$

Exchange integrals J_{jk} , $j \neq k$, are considered as off-diagonal elements of the so-called 'dressed matrix' $\mathbb{J}(\boldsymbol{\lambda})$. Its diagonal elements are determined by a gauge vector:

$$\boldsymbol{\lambda} = [\lambda_0, \lambda_1, \dots, \lambda_N], \quad (9)$$

with the constraint $\sum_j \lambda_j = 0$. To determine the LEC the least eigenvalue of $\mathbb{J}(\boldsymbol{\lambda})$ has to be found and expressed as a function in $N + 1$ variables λ_j . At first glance it seems that this approach is even more difficult than standard analytical methods. However, the gauge vector coefficients have to obey the symmetry of the original problem, so a number of independent parameters is significantly reduced [19, 25, 26].

The lowest energy and the corresponding LEC (or LECs) of a given system are determined in three steps:

- (1) Solve the eigenproblem for the matrix \mathbb{J} .
- (2) Determine the function $j_{\min}(\boldsymbol{\lambda})$: a dependence of the minimum eigenvalue with respect to the gauge vector $\boldsymbol{\lambda}$.
- (3) The *maximum* of this function, $\bar{j} = \max_{\boldsymbol{\lambda}} j_{\min}(\boldsymbol{\lambda})$, determines the appropriate gauge vector $\bar{\boldsymbol{\lambda}}$, i.e., $\bar{j} = j_{\min}(\bar{\boldsymbol{\lambda}})$.

This specific eigenvalue \bar{j} of $\mathbb{J}(\boldsymbol{\lambda})$ is used to calculate $E_{\text{LEC}} = (N + 1)\bar{j}/2$ [19, 25]. Some important notes have to be made

- This solution is *unique*, i.e., there is only one global maximum of j_{\min} , but the corresponding eigenvalue may be degenerate.
- This degeneracy d determines a spatial dimension of the LEC: $d = 1$ means collinear one, if $d = 2$ then the LEC is coplanar etc; with *nonphysical* solutions for $d > 3$ [26].
- In a simplified approach presented here eigenvectors of \mathbb{J} are not necessary and the LECs can be determined solving a system of linear equations [19].

3.3. Classical wheels

The original energy function (cf. Fig. 1(a)) is given as: ($N + 1 \equiv 1$)

$$\mathcal{E} = J \sum_{j=1}^N \mathbf{s}_j \cdot \mathbf{s}_{j+1} + J_0 \mathbf{s}_0 \cdot \sum_{j=1}^N \mathbf{s}_j, \quad (10)$$

can be rewritten as:

$$E(\alpha) = \frac{\mathcal{E}}{|J_0|} = \alpha \sum_{j=1}^N \mathbf{s}_j \cdot \mathbf{s}_{j+1} + \varepsilon \mathbf{s}_0 \cdot \sum_{j=1}^N \mathbf{s}_j, \quad \alpha = \frac{J}{|J_0|}, \quad \varepsilon = \frac{J_0}{|J_0|} = \pm 1. \quad (11)$$

The cyclic symmetry demands $\lambda_j = \lambda$ for $1 \leq j \leq N$, so a traceless matrix is obtained if $\lambda_0 = -N\lambda$. Therefore, the dressed matrix \mathbb{J} is a regular arrow-bordered circulant one [27]:

$$\mathbb{J} = \left(\begin{array}{c|cccccc} -N\lambda & \varepsilon & \varepsilon & \cdots & \varepsilon & \varepsilon \\ \hline \varepsilon & \lambda & \alpha & \cdots & 0 & \alpha \\ \varepsilon & \alpha & \lambda & \cdots & 0 & 0 \\ \cdots & \cdots & \cdots & \cdots & \cdots & \cdots \\ \varepsilon & \alpha & 0 & \cdots & \alpha & \lambda \end{array} \right). \quad (12)$$

Its eigenvalues do not depend on ε and are given as [27]:

$$j_{\pm} = (2\alpha - (N-1)\lambda \pm \sqrt{\Delta})/2, \quad (13)$$

$$j_k = \lambda + 2\alpha \cos(k\psi), \quad k = 1, 2, \dots, N-1, \quad (14)$$

where

$$\Delta = (2\alpha + (N+1)\lambda)^2 + 4N, \quad \text{and} \quad \psi = 2\pi/N. \quad (15)$$

The minimum function $j_{\min}(\lambda)$ is constructed from two of them: $j_-(\lambda)$ and $j_{N/2}(\lambda)$, which have the same value at

$$j_{\text{cross}}(\alpha) = j_{N/2}(\lambda_{\text{cross}}) = -\frac{N(8\alpha^2 + 1)}{4(N+1)\alpha}. \quad (16)$$

Hence, one obtains that $j_{\min}(\lambda) = j_-(\lambda)$ for $\lambda \leq \lambda_{\text{cross}}$ and $j_{\min}(\lambda) = j_{N/2}(\lambda)$ otherwise. The maximum, $\max_{\lambda} j_{\min}(\lambda)$ (and its abscissa) depends on relation between λ_{cross} and λ_{max} , where $j_-(\lambda)$ reaches its maximum. It can be shown that [27]:

$$\lambda_{\text{max}}(\alpha) = -\frac{(N-1) + 2\alpha}{N+1} = -1 - \frac{2(\alpha-1)}{N+1}, \quad (17)$$

$$\max_{\lambda} j_-(\lambda) = \frac{2N}{N+1}(\alpha-1) = -N(\lambda_{\text{max}} + 1). \quad (18)$$

Simple algebra shows that $\lambda_{\text{cross}} = \lambda_{\text{max}}$ for $\alpha = 1/4$, so the final result is

$$\bar{j} = \begin{cases} \max_{\lambda} j_-(\lambda) = \frac{2N}{N+1}(\alpha-1), & \text{for } \alpha \leq 1/4, \\ j_{\text{cross}}(\alpha) = -\frac{2N}{N+1} \frac{8\alpha^2 + 1}{8\alpha}, & \text{for } \alpha \geq 1/4. \end{cases} \quad (19)$$

The corresponding abscissa is given as:

$$\bar{\lambda} = \begin{cases} \lambda_{\text{max}} = -1 - \frac{2(\alpha-1)}{N+1}, & \text{for } \alpha \leq 1/4, \\ \lambda_{\text{cross}} = \frac{8\alpha^2 - N}{4(N+1)\alpha}, & \text{for } \alpha \geq 1/4. \end{cases} \quad (20)$$

It has to be emphasised that the ‘critical’ value $\alpha_{\text{crit}} = 1/4$ is universal – it does not depend on the system size N and a type of couplings with the central spin determined by the sign of J_0 , i.e., by the parameter ε .

3.4. The lowest energy configurations

Since there are N bonds in the outer ring and the same number of couplings between the peripheral spins and the central one (the first and the second term in Eq. (10) or (11), respectively), then it is convenient to divide E_{LEC} by N and to consider energy density. According to the relation between E_{LEC} and the eigenvalue \bar{j} (see Sec. 3.2) one obtains:

$$\frac{E_{\text{LEC}}}{N} = \begin{cases} \alpha - 1, & \text{for } \alpha \leq 1/4, \\ -\left(\alpha + \frac{1}{8\alpha}\right), & \text{for } \alpha \geq 1/4. \end{cases} \quad (21)$$

The first formula immediately confirms that for $\alpha < 1/4$ the peripheral spins are ordered ferromagnetically (despite antiferromagnetic couplings for $0 < \alpha < 1/4$) and they are antiparallel (parallel) to the central spin s_0 for $\varepsilon = \pm 1$, respectively. Therefore, the collinear LEC, characteristic for non-frustrated systems, retains for relatively weak antiferromagnetic couplings which yield competing interaction, but without non-trivial degeneracy.

In the second range antiferromagnetic ordering of the peripheral spins is preferred: $E_{\text{LEC}}/(N\alpha) \rightarrow -1$ when $\alpha \rightarrow \infty$. For finite $\alpha > 1/4$ spin vectors with odd (even) indices are rotated by an angle φ ($-\varphi$, respectively) in the same way as it has been given in Sec. 3.1 for $N = 2$, i.e., $\cos \varphi = -\varepsilon/(4\alpha)$. Exchange of spins with odd and even indices (or, equivalently, reversing the sign of φ) yields another LEC for $0 < \varphi < \pi$ (see Fig. 3).

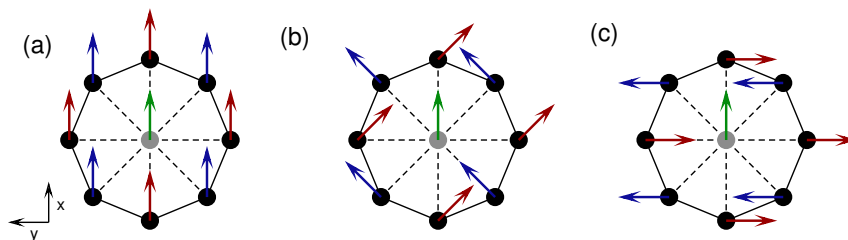


FIG. 3. The LECs for the centred octagon (the wheel W_9) for $\varepsilon = -1$ and (a) $\alpha < 1/4$, (b) $\alpha = 1/\sqrt{8}$, and (c) $\alpha \rightarrow \infty$. If φ is not a multiplicity of π (the later two cases) another two LECs are obtained changing sign of the angle φ . In the case (b) presented LEC corresponds to $\alpha = 1/\sqrt{8}$ and $\varphi = \pm\pi/4$, when the nearest neighbours are orthogonal.

4. Conclusions and challenges

The systems considered in this paper reveal the classical counterpart of the third type frustration defined for quantum systems – in the well-determined range $0 < \alpha < 1/4$ the unique collinear LEC, characteristic for non-frustrated systems, is observed. Therefore, there exists nontrivial range of the energy function parameter α , at which competing interactions are not accompanied by degeneracy. Note that in some approaches frustration is present only in systems with non-trivial degeneracy of the ground state.

The second important phenomenon is universality of the critical value $\alpha_{\text{crit}} = 1/4$ (cf. [19]) and, moreover, it is also valid in the case of quantum systems [14, 15, 35]. Above this value, the angle φ is a continuous function of the parameter α .

It should be also emphasized that such general results can be obtained owing to the powerful and efficient approach worked out by Schmidt and Luban. It is a challenging task to apply this method to heterogeneous and/or less symmetric systems. Some initial considerations, including classical analogs of the Ising system with energy function (4), have indicated two facts. At first, in some systems, there is an abrupt change in the LEC, when very weak competing interactions are ‘turned on’. Secondly, in the case of rings with antiferromagnetic couplings of the second neighbors the LEC does not change continuously for increasing α , but a series of abrupt changes is rather observed.

References

- [1] Furrer A., Waldmann O. Magnetic cluster excitations. *Rev. Mod. Phys.*, 2013, **85** (1), P. 367–420.
- [2] Timco G.A., McInnes E.J.L., Winpenny R.E.P. Physical studies of heterometallic rings: An ideal system for studying magnetically-coupled systems. *Chem. Soc. Rev.*, 2013, **42** (4), P. 1796–1806.
- [3] McInnes E.J.L., Timco G.A., Whitehead G.F.S., Winpenny R.E.P. Heterometallic rings: Their physics and use as supramolecular building blocks. *Angew. Chem. Int. Ed.*, 2015, **54** (48), 14244.
- [4] Ghirri A., Chiesa A., et al. Coherent spin dynamics in molecular Cr_8Zn wheels. *The J. Phys. Chem. Lett.*, 2015, **6** (24), 5062.
- [5] Baker M.L., Lancaster T., et al. Studies of a large odd-numbered odd-electron metal ring: Inelastic neutron scattering and muon spin relaxation spectroscopy of Cr_8Mn . *Chemistry – A European Journal*, 2016, **22** (5), P. 1779–1788.

- [6] Woolfson R.J., Timco G.A., et al. [CrF(O₂CtBu)₂]₉: Synthesis and characterization of a regular homometallic ring with an odd number of metal centers and electrons. *Angew. Chem. Int. Ed.*, 2016, **55** (31), 8856.
- [7] Furukawa Y., Kiuchi K., et al. Evidence of spin singlet ground state in the frustrated antiferromagnetic ring Cr₈Ni. *Phys. Rev. B*, 2009, **79** (13), 134416.
- [8] Baker M.L., Timco G.A., et al. A classification of spin frustration in molecular magnets from a physical study of large odd-numbered-metal, odd electron rings. *Proc. Nat. Acad. Sci. USA*, 2012, **109**, P. 19113–19118.
- [9] Antkowiak M., Kozłowski P., et al. Detection of ground states in frustrated molecular rings by in-field local magnetization profiles. *Phys. Rev. B*, 2013, **87** (18), 184430.
- [10] Kozłowski P. Frustration and quantum entanglement in odd-membered ring-shaped chromium nanomagnets. *Phys. Rev. B*, 2015, **91** (17), 174432.
- [11] Owerre S.A., Nsofini J. Antiferromagnetic molecular nanomagnets with odd-numbered coupled spins. *Europhys. Lett. (EPL)*, 2015, **110** (4), 47002.
- [12] Garlatti E., Bordignon S., et al. Relaxation dynamics in the frustrated Cr₉ antiferromagnetic ring probed by NMR. *Phys. Rev. B*, 2016, **93** (2), 024424.
- [13] Kamieniarz G., Florek W., Antkowiak M. Universal sequence of ground states validating the classification of frustration in antiferromagnetic rings with a single bond defect. *Phys. Rev. B*, 2015, **92** (14), 140411(R).
- [14] Florek W., Antkowiak M., Kamieniarz G. Sequences of ground states and classification of frustration in odd-numbered antiferromagnetic rings. *Phys. Rev. B*, 2016, **94** (22), 224421.
- [15] Ako A.M., Waldmann O., et al. Odd-numbered Fe(III) complexes: Synthesis, molecular structure, reactivity, and magnetic properties. *Inorg. Chem.*, 2007, **46** (3), P. 756–766.
- [16] Garlatti E., Carretta S., et al. Theoretical design of molecular nanomagnets for magnetic refrigeration. *Appl. Phys. Lett.*, 2013, **103**, 202410.
- [17] Sharples J.W., Collison D., et al. Quantum signatures of a molecular nanomagnet in direct magnetocaloric measurements. *Nature Commun.*, 2014, **5**, 5321.
- [18] Kakaroni F.E., Collet A., et al. Constructing CrIII-centered heterometallic complexes: [NiII6CrIII] and [CoII6CrIII] wheels. *Dalton Trans.*, 2018, **47** (1), P. 58–61.
- [19] Florek W., Kamieniarz G., Marlewski A. Universal lowest energy configurations in a classical Heisenberg model describing frustrated systems with wheel geometry. *Phys. Rev. B*, 2019, **100** (5), 054434.
- [20] Wilson R.J. *Introduction to Graph Theory*. Addison Wesley Longman Ltd., London, 1996.
- [21] Grajek M., Kopyciuk T., Florek W., Marlewski A. Collinear and non-collinear configurations in classical geometrically frustrated ring-shaped systems. *Acta Phys. Pol. A*, 2018, **133** (3), P. 417–419.
- [22] Popov A.P., Anisimov A.V., Eriksson O., Skorodumova N.V. Metastable noncollinear canted states from a phenomenological model of a symmetric ferromagnetic film. *Phys. Rev. B*, 2010, **81** (5), 054440.
- [23] Popov A.P., Rettori A., Pini M.G. Discovery of metastable states in a finite-size classical one-dimensional planar spin chain with competing nearest- and next-nearest-neighbor exchange couplings. *Phys. Rev. B*, 2014, **90** (13), 134418.
- [24] Popov A.P., Rettori A., Pini M.G. Spectrum of noncollinear metastable configurations of a finite-size discrete planar spin chain with a collinear ferromagnetic ground state. *Phys. Rev. B*, 2015, **92** (2), 024414.
- [25] Schmidt H.-J., Luban M. Classical ground states of symmetric Heisenberg spin systems. *Journal of Physics A: Math. Gen.*, 2003, **36** (23), P. 6351–6378.
- [26] Schmidt H.-J. Theory of ground states for classical Heisenberg spin systems. Parts I–IV. 2017, arXiv: <https://arxiv.org/abs/1701.02489>, 1707.02859, 1707.06512, 1710.00318.
- [27] Florek W., Marlewski A. Spectrum of some arrow-bordered circulant matrix. 2019, arXiv: <https://arxiv.org/abs/1905.04807>.
- [28] Toulouse G. Theory of the frustration effect in spin glasses: I. In Mézard M., Parisi G., Virasoro M. A. *Spin Glass Theory and Beyond*. World Scientific, Singapore: 1987, P. 99–103. Reprinted form: Toulouse G. *Communications de Physique*. 1977, **2**, P. 115–119.
- [29] Vannimenus J., Toulouse G. Theory of the frustration effect: II. Ising spins on a square lattice. *J. Phys. C: Solid State Phys.*, 1977, **10** (18), P. L537–L542.
- [30] Pauling L. The structure and entropy of ice and of other crystals with some randomness of atomic arrangement. *J. Am. Chem. Soc.*, 1935, **57** (12), P. 2680–2684.
- [31] Wannier G.H. Antiferromagnetism. The triangular Ising net. *Phys. Rev.*, 1950, **79** (2), P. 357–364.
- [32] Giampaolo S.M., Gualdi G., Monras A., Illuminati F. Characterizing and quantifying frustration in quantum many-body systems. *Phys. Rev. Lett.*, 2011, **107** (26), 260602.
- [33] Binder K., Young A.P. Spin glasses: Experimental facts, theoretical concepts, and open questions. *Rev. Mod. Phys.*, 1986, **58**, P. 801–967.
- [34] Lacorre P. The constraint functions: an attempt to evaluate the constraint rate inside structures that undergo ordered magnetic frustration. *J. Phys. C: Solid State Phys.*, 1987, **20** (29), P. L775–L781.
- [35] Florek W., Antkowiak M., Kamieniarz G. The Kahn degenerate frustration points and the Lieb-Mattis level order in heterometallic wheel molecules with competing interactions. *J. Mag. Mag. Mater.*, 2019, **487**, 165326.

Geometrical analyses of nanostructures

V. Sajfert¹, N. Pop², D. Popov²

¹Technical Faculty “Mihajlo Pupin” Zrenjanin, Djure Djakovica Street bb, 23000 Zrenjanin, Serbia

²Department of Physical Foundations of Engineering, Politehnica University of Timișoara,

V. Parvan. No.2, 300223, Timisoara, România

nicolina.pop@upt.ro

PACS 81.07.b, 81.07.D, 62.23.St, 61.50.Ah

DOI 10.17586/2220-8054-2020-11-1-36-43

In this paper, the statistical and dynamical equivalence between rectangular cell and lower symmetry cell is presented. The achievement of this equivalence will improve theoretical investigations of nanostructures as thin film or quantum rods.

Keywords: Nanostructures, triclinic cell, cubic cell, thin film.

Received: 29 December 2019

1. Introduction

Nanotechnology has had much progress recently and produces different rectangular and cylindrical structures [1, 2]. The main problem of theoretical investigations of nanostructures is correct inclusion of boundary conditions into physical behavior of nanostructures. The importance of studying nanostructures is that their properties and behavior are different in comparison with the bulk structures.

The geometrical form of produced nanostructures is rectangular (thin films, quantum rods and quantum parallelepiped) or cylindrical (cylinders with nanocross-section and macroscopic height and cylinders having nanoheight and nanocross-section). Mentioned geometrical forms enable correct inclusion of boundary conditions into evaluations [3–10].

Taking into account of boundary conditions for the structure of lower symmetry (monoclinic, triclinic, tetragonal and others), we will try, in the first part of this paper, to achieve statistical equivalence between rectangular cell and lower symmetry cell. The statistical equivalence means equating of momentum volumes for the mentioned cells since statistical averages are usually calculated in momentum space.

In the second part, the rectangular cell will be reduced to simple cubic one which has the same momentum volume as lower symmetry one. After this, we can try to achieve the dynamical equivalence, too. In the nearest neighbors approximation, the dynamics of simple cubic cell is defined by six nearest neighbors. For lower symmetry cell the dynamics is defined by six or more neighbors. The last is dependent on angles between vectors of lower symmetry cell. If some of angles are less than 90° , then the interactions between ends of corresponding vectors have to be included into total interactions of atoms of lower symmetry cells. The achievement of described equivalence will noticeably accelerate theoretical investigations of nanostructures.

2. Preliminaries: Statistical equivalence

An elementary cell of triclinic crystal structure [11–13] has lattice constants: A , B and C . The lengths of these lattice constants are different and the angles between vectors \vec{A} , \vec{B} and \vec{C} are different: $\angle(\vec{A}, \vec{B}) = \alpha$, $\angle(\vec{B}, \vec{C}) = \beta$ and $\angle(\vec{C}, \vec{A}) = \gamma$. The notations used are: $|\vec{A}| = A$, $|\vec{B}| = B$ and $|\vec{C}| = C$.

The lattice constant of rectangular structure will be denoted with a , b and c . Their lengths are different in general case. The angles between vectors \vec{a} , \vec{b} and \vec{c} are 90° . The notations used are $|\vec{a}| = a$, $|\vec{b}| = b$ and $|\vec{c}| = c$.

The elementary cells introduced are presented on Fig. 1 and Fig. 2.

The phase volume Φ is the product of configuration volume V and momentum volume W and, for crystals with simple lattice is equal to h^3 [14], where h is Planck’s constant.

If configurationally, the volume of triclinic cell is denoted with V_T and the momentum cell volume with W_T , that results in the following:

$$V_T W_T = \Phi_T = h^3. \quad (1)$$

For rectangular structure we have the relation:

$$V_C W_C = \Phi_C = h^3, \quad (2)$$

where V_C is configurationally volume and W_C is momentum cell volume.

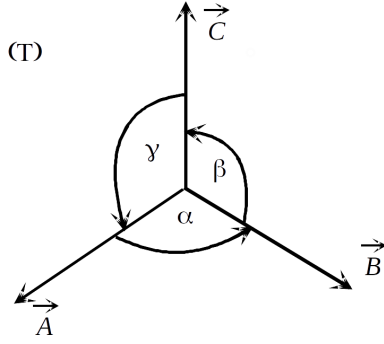


FIG. 1. Elementary cell of triclinic structure

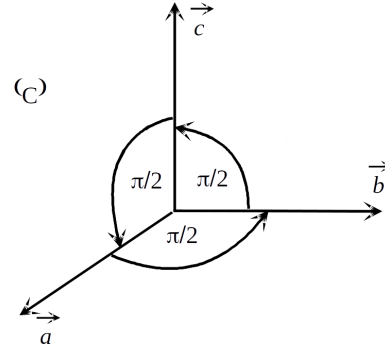


FIG. 2. Elementary cell of rectangular structure

In order to achieve equality:

$$V_C = V_T, \quad (3)$$

the rectangular vector \vec{c} is chosen in the direction of vector \vec{C} of triclinic cell and both of them, into direction of z -axis:

$$\vec{C} = C\vec{k}; \quad \vec{c} = c\vec{k}. \quad (4)$$

Vectors \vec{a} and \vec{b} of rectangular cell will be put in directions of x -axis and y -axis, respectively. In this way for rectangular structure can be written as:

$$\vec{a} = a\vec{i}; \quad \vec{b} = b\vec{j}; \quad \vec{c} = c\vec{k}, \quad (5)$$

where \vec{i} , \vec{j} and \vec{k} are vectors of Descartes coordinate system. Therefore, the expression for configurationally volume of rectangular structure is:

$$V_C = \vec{a} \left(\vec{b} \times \vec{c} \right) = \begin{vmatrix} a & 0 & 0 \\ 0 & b & 0 \\ 0 & 0 & c \end{vmatrix} = abc. \quad (6)$$

On the basis of (4), the configurational volume of the triclinic structure is given by:

$$V_T = \vec{A} \left(\vec{B} \times \vec{C} \right) = \begin{vmatrix} A_x & A_y & A_z \\ B_x & B_y & B_z \\ 0 & 0 & C \end{vmatrix} = C (A_x B_y - A_y B_x). \quad (7)$$

Using (6) and (7) the equality (3) becomes:

$$abc = (A_x B_y - A_y B_x) C. \quad (8)$$

From Fig. 3, in spherical coordinates, the projectors from (8) are:

$$\begin{aligned} A_x &= A \sin \gamma \cos \varphi_A; & B_x &= B \sin \beta \cos \varphi_B; \\ A_y &= A \sin \gamma \sin \varphi_A; & B_y &= B \sin \beta \sin \varphi_B; \\ A_z &= A \cos \gamma; & B_z &= B \cos \beta \end{aligned} \quad (9)$$

and obtain:

$$A_x B_y - A_y B_x = AB \sin \beta \sin \gamma \sin (\varphi_B - \varphi_A). \quad (10)$$

Since

$$\vec{A} \circ \vec{B} = A_x B_x + A_y B_y + A_z B_z \quad (11)$$

the substitution of (9) leads to:

$$AB \cos \alpha = AB \sin \beta \sin \gamma \cos (\varphi_B - \varphi_A) + AB \cos \beta \cos \gamma. \quad (12)$$

Combining (12) and (10) results in the following:

$$\cos (\varphi_B - \varphi_A) = \frac{\cos \alpha - \cos \beta \cos \gamma}{\sin \beta \sin \gamma}. \quad (13)$$

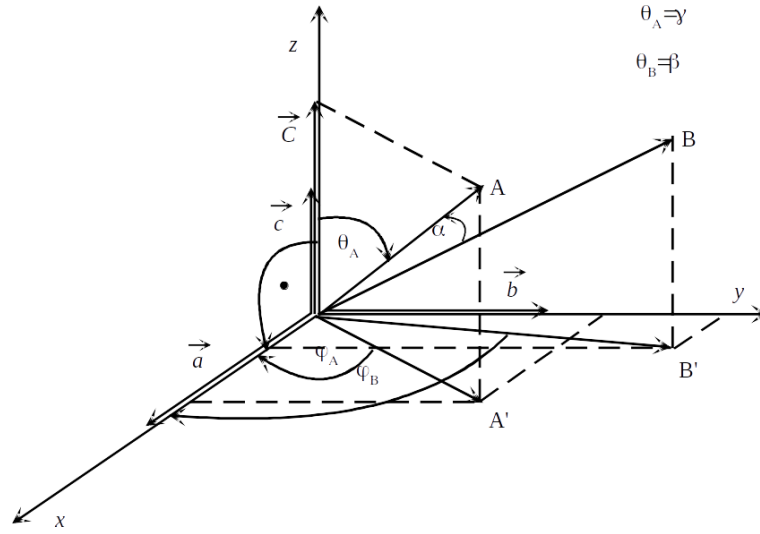


FIG. 3. Triclinic rectangular lattice vectors in spherical coordinates

Substituting (10) and (13) into (8), we finally obtain the connection between configurationally volumes of triclinic and rectangular cell:

$$abc = XABC, \quad (14)$$

where

$$X = \sqrt{1 + 2 \cos \alpha \cos \beta \cos \gamma - \cos^2 \alpha - \cos^2 \beta - \cos^2 \gamma}. \quad (15)$$

The formula (14) can be applied only if $X > 0$. In some cases the equivalence cannot be achieved. As an illustration if $\alpha = 90^\circ$, $\beta = 60^\circ$ and $\gamma = 30^\circ$, in accordance with (15), one obtains $X = 0$. For $\alpha = 150^\circ$, $\beta = 90^\circ$ and $\gamma = 30^\circ$ it follows from (15) that $X = -0.5$. In both cases the equivalence cannot be achieved. The cases when the exposed procedure gives satisfactory result are for example $\alpha = \beta = \gamma = 1^\circ$ with $X = 6.9 \cdot 10^{-8}$, $\alpha = 70^\circ$, $\beta = 50^\circ$ and $\gamma = 30^\circ$ with $X = 0.312$, $\alpha = 110^\circ$, $\beta = 100^\circ$ and $\gamma = 80^\circ$ with $X = 0.843$ etc. For $\alpha = 125.9^\circ$, $\beta = 115.3^\circ$ and $\gamma = 115.1^\circ$ results $X = 0.081$, i.e. this has equivalent cubic cell.

It should be pointed out that transition to statistically equivalent cell is possible for all monoclinic structures [15]. In these structures, two angles are equal 90° and in accordance with (14) it follows $X = 1 - \cos^2 \beta$, where $\beta \neq 90^\circ$, i.e. we always have that $X > 0$.

It is clear, also, that the equivalence conditions are not uniquely defined.

Momentum cell volume is defined as product of reciprocal configurationally cell and factor $(h/2\pi)^3$. The vectors \vec{k}_a , \vec{k}_b and \vec{k}_c are defined as follows:

$$\vec{k}_a = 2\pi \frac{\vec{a} \times \vec{c}}{\vec{a} \cdot (\vec{b} \times \vec{c})} = \frac{2\pi}{a} \vec{i}; \quad \vec{k}_b = 2\pi \frac{\vec{c} \times \vec{a}}{\vec{b} \cdot (\vec{c} \times \vec{a})} = \frac{2\pi}{b} \vec{j}; \quad \vec{k}_c = 2\pi \frac{\vec{a} \times \vec{b}}{\vec{c} \cdot (\vec{a} \times \vec{b})} = \frac{2\pi}{c} \vec{k}. \quad (16)$$

Taking into account formula (6) we easily conclude on the basis of (16) that the volume of reciprocal cell is:

$$R = \frac{(2\pi)^3}{abc}. \quad (17)$$

Multiplying (17) with we obtain volume of momentum cell for rectangular structure:

$$W_C = \frac{h^3}{abc} = W_T. \quad (18)$$

The last equality sign follows from the fact that equality of configurationally cells V_C and V_T has been achieved. If one considers:

$$a = X^p A; \quad b = X^q B; \quad c = X^r C, \quad (19)$$

where p , q and r are arbitrary constants, (14) gives

$$p + q + r = \frac{1}{2}. \quad (20)$$

In order to obtain equivalent simple cubic cell, one takes

$$\frac{a}{b} = X^{p-q} \frac{A}{B} = 1. \quad (21)$$

$$\frac{a}{c} = X^{p-r} \frac{A}{C} = 1. \quad (22)$$

Combining (20), (21) and (22) we find

$$p = \frac{1}{6} - \frac{2 \ln A - \ln B - \ln C}{3 \ln X}. \quad (23)$$

Taking $\frac{b}{a} = X^{q-p} \frac{B}{A}$, $\frac{b}{c} = X^{q-r} \frac{B}{C}$, we have:

$$q = \frac{1}{6} - \frac{2 \ln B - \ln A - \ln C}{3 \ln X}. \quad (24)$$

Finally taking $\frac{c}{a} = X^{r-p} \frac{C}{A}$, $\frac{c}{b} = X^{r-q} \frac{C}{B}$, we get:

$$r = \frac{1}{6} - \frac{2 \ln C - \ln A - \ln B}{3 \ln X}. \quad (25)$$

Substituting (23), (24) and (25) into (14) it obtain the constant of simple cubic lattice which is statistically equivalent to triclinic one with lattice constants A , B and C .

$$d = X^p A = X^q B = X^r C. \quad (26)$$

For the angles $\alpha = 125.9^\circ$, $\beta = 115.3^\circ$ and $\gamma = 115.1^\circ$, while the lattice constants are $A = 0.942$, $B = 1.264$ and $C = 0.573$ nm the value of d , is calculated by means of (23), (24) and (25) is $d = 0.839$ nm.

3. Results: Dynamical equivalence of triclinic cell and simple cubic cell

The achievement of this equivalence requires knowing of interactions between atoms (molecules) of triclinic cell. Using Landau's estimate [16] of intermolecular interactions, i.e. we assume that interaction between two atoms is of the form:

$$I(l) = \begin{cases} \frac{\varphi}{l^\eta}; & l > 1 \text{ nm}; \\ \frac{\varphi}{l^{-\eta}}; & l < 1 \text{ nm}; \end{cases} \quad \eta > 0, \quad (27)$$

where φ is interaction constant expressed in $J \times (10^{-9} \text{ m})^{\pm\eta}$, while l is distance between nearest neighbors expressed in 10^{-9} m .

The total interaction energy of triclinic cell is given as:

$$J_T = 2\varphi \left(\frac{1}{A^{-\eta}} + \frac{1}{B^{-\eta}} + \frac{1}{C^{-\eta}} + \frac{1}{(AB)^{-\eta}} + \frac{1}{(AC)^{-\eta}} + \frac{1}{(BC)^{-\eta}} \right), \quad (28)$$

since all lengths are less than 1 nm. The formula is valid if $A \geq B, C, AB, AC, BC$. If some of lengths AB, AC and BC is higher than A , this term has to be omitted from (28).

The total interaction energy of the equivalent simple cubic cell is given by:

$$J_{SC} = \frac{6\Phi}{d^{-\eta}}, \quad d < 1 \text{ nm}, \quad (29)$$

where Φ is interaction constant of equivalent simple cubic cell.

It is obvious that the structures will be dynamically equivalent if

$$\Phi = \frac{\varphi}{3} d^\eta \left(\frac{1}{A^{-\eta}} + \frac{1}{B^{-\eta}} + \frac{1}{C^{-\eta}} + \frac{1}{(AB)^{-\eta}} + \frac{1}{(AC)^{-\eta}} + \frac{1}{(BC)^{-\eta}} \right). \quad (30)$$

For calculation of some physical characteristics of simple cubic lattice, the interaction between two neighbors is most often used. This interaction is $j_{CE} = \frac{\Phi}{d^{-\eta}}$, i.e. in accordance with (30):

$$j_{CE} = \frac{\varphi}{3} \left(\frac{1}{A^{-\eta}} + \frac{1}{B^{-\eta}} + \frac{1}{C^{-\eta}} + \frac{1}{(AB)^{-\eta}} + \frac{1}{(AC)^{-\eta}} + \frac{1}{(BC)^{-\eta}} \right). \quad (31)$$

An illustrative example is the ideal Heisenberg ferromagnet with spin $S = 1/2$ in Bloch's approximation. The exchange interactions are, in accordance with general opinion, of exponential type [14]. It means that in formula (31) every of terms have to be prescribed in following way

$$\frac{1}{L^{-\eta}} = e^{\ln \frac{1}{L^{-\eta}}} = e^{\eta \ln L} \quad (l < 1).$$

The Hamiltonian of this system in nearest neighbour's approximation [8] is:

$$H = 3j_{CE} \sum_{n_x, n_y, n_z} B_{n_x, n_y, n_z}^+ B_{n_x, n_y, n_z} - \frac{1}{2} j_{CE} \sum_{n_x, n_y, n_z} B_{n_x, n_y, n_z}^+ \left(B_{n_x+1, n_y, n_z} + B_{n_x-1, n_y, n_z} + B_{n_x, n_y+1, n_z} + B_{n_x, n_y-1, n_z} + B_{n_x, n_y, n_z+1} + B_{n_x, n_y, n_z-1} \right) \quad (32)$$

with B_{n_x, n_y, n_z} Bose operators.

The dispersion law of spin waves is:

$$E_{k_x, k_y, k_z} = (3 - \cos k_x d - \cos k_y d - \cos k_z d) j_{CE} \approx \frac{1}{2} j_{CE} k^2 d^2. \quad (33)$$

The ordering parameter in Bloch's approximation is given by:

$$\sigma = 1 - 2\langle B^+ B \rangle = 1 - 2\zeta_{3/2} \tau^{3/2}, \quad (34)$$

where

$$\zeta_{3/2} = \sum_{n=1}^{\infty} \frac{1}{n^{3/2}} \quad (35)$$

is Riemann's function [14], while:

$$\tau = \frac{k_B T}{2\pi j_{CE}}. \quad (36)$$

As it is seen, the value j_{CE} is expressed in parameters of triclinic structure (see formula (31) and, consequently, the result (34) with τ expressed by (36) represents ordering parameter of ferromagnet with triclinic lattice which is evaluated by means of equivalent simple cubic lattice.

The given example demonstrates the advantages of translation the lower symmetry structure into equivalent simple cubic one. The statistical averages can be evaluated without mathematical complication and by means of standard and well developed approaches.

The more complicated problem is determining of ordering parameter of thin film cut off from triclinic crystal. In this case we immediately go over to thin film of statistically and dynamically equivalent simple cubic structure. The interactions j_{CE} are given by (31).

The Hamiltonian of equivalent film in nearest neighbor's approximation [5] is given by:

$$H = \frac{1}{2} \sum_{n_x, n_y, n_z} \left(j_{n_x+1, n_y, n_z; n_x, n_y, n_z} + j_{n_x-1, n_y, n_z; n_x, n_y, n_z} + j_{n_x, n_y+1, n_z; n_x, n_y, n_z} + j_{n_x, n_y-1, n_z; n_x, n_y, n_z} + j_{n_x, n_y, n_z+1; n_x, n_y, n_z} + j_{n_x, n_y, n_z-1; n_x, n_y, n_z} \right) B_{n_x, n_y, n_z}^+ B_{n_x, n_y, n_z} - j_{n_x, n_y, n_z-1; n_x, n_y, n_z} B_{n_x, n_y, n_z}^+ B_{n_x, n_y, n_z} - \frac{1}{2} \sum_{n_x, n_y, n_z} B_{n_x, n_y, n_z}^+ \left(j_{n_x+1, n_y, n_z; n_x, n_y, n_z} B_{n_x+1, n_y, n_z}^+ + j_{n_x-1, n_y, n_z; n_x, n_y, n_z} B_{n_x-1, n_y, n_z}^+ + j_{n_x, n_y+1, n_z; n_x, n_y, n_z} B_{n_x, n_y+1, n_z}^+ + j_{n_x, n_y-1, n_z; n_x, n_y, n_z} B_{n_x, n_y-1, n_z}^+ + j_{n_x, n_y, n_z+1; n_x, n_y, n_z} B_{n_x, n_y, n_z+1}^+ + j_{n_x, n_y, n_z-1; n_x, n_y, n_z} B_{n_x, n_y, n_z-1}^+ \right). \quad (37)$$

For functions j the following is valid:

$$j_{n_x \pm 1, n_y, n_z; n_x, n_y, n_z} = j_{n_x, n_y \pm 1, n_z; n_x, n_y, n_z} = j_{n_x, n_y, n_z \pm 1; n_x, n_y, n_z} = j_{CE}. \quad (38)$$

The cut off in z direction leads to the following boundary conditions:

$$j_{n_x, n_y, -1; n_x, n_y, 0} = j_{n_x, n_y, N_z+1; n_x, n_y, N_z} = 0. \quad (39)$$

The film will be analysed by means of Green's function:

$$G_{n_x, n_y, n_z; m_x, m_y, m_z}(t) = \left\langle \left\langle B_{n_x, n_y, n_z}(t) \left| B_{n_x, n_y, n_z}^+(0) \right. \right\rangle \right\rangle = \Theta(t) \left\langle \left[B_{n_x, n_y, n_z}(t), B_{n_x, n_y, n_z}^+(0) \right] \right\rangle; \quad (40)$$

where $\Theta(t) = \begin{cases} 1, & t > 0; \\ 0, & t < 0; \end{cases}$ is the Heaviside step function.

Fourier transformations are:

$$G_{n_x, n_y, n_z; m_x, m_y, m_z}(t) = \int_{-\infty}^{+\infty} d\omega e^{-i\omega t} G_{n_x, n_y, n_z; m_x, m_y, m_z}(\omega); \quad \delta(t) = \frac{1}{2\pi} \int_{-\infty}^{+\infty} d\omega e^{-i\omega t}. \quad (41)$$

In order to use translational invariance in x, y planes the following transformation is used [17, 18]

$$G_{n_x, n_y, n_z; m_x, m_y, m_z}(\omega) = \frac{1}{N_x N_y} \sum_{k_x, k_y} e^{ik_x(n_x - m_x) + ik_y(n_y - m_y)} \Gamma(k_x, k_y, \omega). \quad (42)$$

The quoted procedure gives the system of three different equations:

$$\frac{1}{2} j_{CE} (\Gamma_{n_z+1, m_z} + \Gamma_{n_z-1, m_z}) + \rho \Gamma_{n_z, m_z} = \frac{i\hbar}{2\pi} \delta_{n_z, m_z}; \quad 1 \leq n_z \leq N_z - 1, \quad (43)$$

$$\frac{1}{2} j_{CE} \Gamma_{1, m_z} + \left(\rho + \frac{1}{2} j_{CE} \right) \Gamma_{0, m_z} = \frac{i\hbar}{2\pi} \delta_{0, m_z}, \quad (44)$$

$$\frac{1}{2} j_{CE} \Gamma_{N_z-1, m_z} + \left(\rho + \frac{1}{2} j_{CE} \right) \Gamma_{N_z, m_z} = \frac{i\hbar}{2\pi} \delta_{N_z, m_z}; \quad n_z = N_z, \quad (45)$$

where

$$\rho = E - 3j_{CE} + j_{CE} (\cos dk_x + \cos dk_y). \quad (46)$$

It can be easily shown that by the substitution:

$$\Gamma_{n_z, m_z}(\omega) = \sum_{\lambda=1}^{N_z} g(k_x, k_y, \lambda; \omega) \Omega_\lambda(m_z) F_\lambda(n_z), \quad (47)$$

where Ω are undetermined functions and F is given by:

$$F_\lambda(n_z) = \sin(n_z + 1) \frac{\pi\lambda}{N_z + 1} - \sin n_z \frac{\pi\lambda}{N_z + 1}; \quad \lambda = 1, 2, 3, \dots, N_z, \quad (48)$$

the system of equations (43), (44) and (45) reduces into one equation of the form

$$\sum_{\lambda=1}^{N_z} g(k_x, k_y, \lambda; \omega) \left(j_{CE} \cos \frac{\pi\lambda}{N_z + 1} + \rho \right) \Omega_\lambda(m_z) F_\lambda(n_z) = \frac{i\hbar}{2\pi} \delta_{n_z, m_z}; \quad n_z = 0, 1, 2, \dots, N_z. \quad (49)$$

Kronecker symbol will be taken in the form

$$\delta_{n_z, m_z} = \sum_{\lambda=1}^{N_z} \Omega_\lambda(m_z) F_\lambda(n_z). \quad (50)$$

Using the properties of Kronecker symbol $\delta_{n_z, n_z} = 1$ and $\delta_{n_z, m_z} = 0, n_z \neq m_z$, we obtain the system of n_z^2 algebraic equations determining unknown functions Ω .

$$g(k_x, k_y, \lambda; \omega) = \frac{i\hbar}{2\pi} \frac{1}{j_{CE} \cos \frac{\pi\lambda}{N_z + 1} + \rho} = \frac{i\hbar}{2\pi} \frac{1}{E - E_{k_x, k_y}}, \quad (51)$$

where

$$E_{k_x, k_y, \lambda} = 3j_{CE} - j_{CE} \left(\cos k_x d + \cos k_y d + \cos \frac{\pi\lambda}{N_z + 1} \right). \quad (52)$$

Substituting (51) into (47) and including obtained result into (42) we get final result for Green's function:

$$G_{n_x, n_y, n_z; m_x, m_y, m_z}(\omega) = \frac{i}{2\pi} \frac{1}{N_x N_y} \sum_{k_x, k_y} e^{ik_x(n_x - m_x) + ik_y(n_y - m_y)} \sum_{\lambda=1}^{N_z} \frac{\Omega_\lambda(m_z) F_\lambda(n_z)}{\omega - \omega_{k_x, k_y, \lambda}}, \quad (53)$$

where

$$\omega = \frac{E}{\hbar}, \quad \omega_{k_x, k_y, \lambda} = \frac{E_{k_x, k_y, \lambda}}{\hbar}. \quad (54)$$

The expression for concentration is:

$$\left\langle B_{n_x, n_y, n_z}^+(0) B_{n_x, n_y, n_z}(t) \right\rangle = \frac{1}{N_x N_y} \sum_{k_x, k_y} \sum_{\lambda=1}^{N_z} \frac{\Omega_\lambda(m_z) F_\lambda(n_z)}{\omega - \omega_{k_x, k_y, \lambda}}. \quad (55)$$

It is very important to note that the transformation from configurational space to momentum space is not isomorphic one. It is transition of the type $n \rightarrow n - 1$ [8]. It is seen that for $N_z + 1$ values of index n_z the momentum index λ takes N_z values. It practically means that in one of layers of the film there are not spin waves. In further we shall consider three layer films. Due to the mentioned reduction it goes over to three subfilms containing two layers.

For subfilm 0–1 from Fig. 4, the solutions of the equation:

$$\delta_{m_z, n_z} = \sum_{\lambda=1}^2 \Omega_{\lambda}(m_z) F_{\lambda}(m_z); \quad n_z, m_z \in (0, 1), \quad (56)$$

are

$$\Omega_1(0) = 2\frac{\sqrt{3}}{3}; \quad \Omega_2(0) = 0; \quad \Omega_1(1) = \frac{\sqrt{3}}{3}; \quad \Omega_2(1) = -\frac{\sqrt{3}}{3}. \quad (57)$$

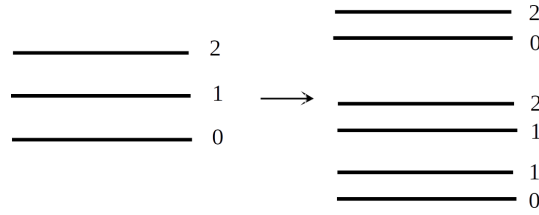


FIG. 4. The Autoreduction in three layer film

Substituting (57) into (55) it obtain concentrations:

$$\langle B^+ B \rangle_{n_z=0} = \frac{1}{4\sqrt{\pi}} \frac{\theta}{j_{CE}} \sum_{n=1}^{\infty} \frac{1}{n} e^{-\frac{j_{CE}}{2\theta} n}; \quad \langle B^+ B \rangle_{n_z=1} = \frac{1}{4\sqrt{\pi}} \frac{\theta}{j_{CE}} \sum_{n=1}^{\infty} \frac{1}{n} e^{-\frac{3j_{CE}}{2\theta} n}, \quad (58)$$

where $\theta = k_B T$.

It is seen that concentration of the layers 0 and 1 differ. It is the consequence of broken symmetry. The corresponding ordering parameters are:

$$\sigma_{n_z=0} = 1 - \frac{1}{2\sqrt{\pi}} \frac{\theta}{j_{CE}} \sum_{n=1}^{\infty} \frac{1}{n} e^{-\frac{j_{CE}}{2\theta} n}; \quad \sigma_{n_z=1} = 1 - \frac{1}{2\sqrt{\pi}} \frac{\theta}{j_{CE}} \sum_{n=1}^{\infty} \frac{1}{n} e^{-\frac{3j_{CE}}{2\theta} n}. \quad (59)$$

The last result shows that the layer $n_z = 1$ is better ordered. It is physically understandable since to spin in layer $n_z = 1$ act exchange forces from two sides, while to spins of layer $n_z = 0$ act exchange forces from one side, only. In the same way for subfilm 1–2 we have:

$$\langle B^+ B \rangle_{n_z=2} = \frac{1}{4\sqrt{\pi}} \frac{\theta}{j_{CE}} \sum_{n=1}^{\infty} \frac{1}{n} e^{-\frac{j_{CE}}{2\theta} n}; \quad \langle B^+ B \rangle_{n_z=1} = \frac{1}{4\sqrt{\pi}} \frac{\theta}{j_{CE}} \sum_{n=1}^{\infty} \frac{1}{n} e^{-\frac{3j_{CE}}{2\theta} n}, \quad (60)$$

$$\sigma_{n_z=2} = 1 - \frac{1}{2\sqrt{\pi}} \frac{\theta}{j_{CE}} \sum_{n=1}^{\infty} \frac{1}{n} e^{-\frac{j_{CE}}{2\theta} n}; \quad \sigma_{n_z=1} = 1 - \frac{1}{2\sqrt{\pi}} \frac{\theta}{j_{CE}} \sum_{n=1}^{\infty} \frac{1}{n} e^{-\frac{3j_{CE}}{2\theta} n}. \quad (61)$$

Finally for subfilm 0–2 we have:

$$\langle B^+ B \rangle_{n_z=0} = \langle B^+ B \rangle_{n_z=2} = \frac{1}{8\sqrt{\pi}} \frac{\theta}{j_{CE}} \left(\sum_{n=1}^{\infty} \frac{1}{n} e^{-\frac{j_{CE}}{2\theta} n} + \sum_{n=1}^{\infty} \frac{1}{n} e^{-\frac{3j_{CE}}{2\theta} n} \right); \quad (62)$$

$$\sigma_{n_z=0} = \sigma_{n_z=2} = 1 - \frac{1}{4\sqrt{\pi}} \frac{\theta}{j_{CE}} \left(\sum_{n=1}^{\infty} \frac{1}{n} e^{-\frac{j_{CE}}{2\theta} n} + \sum_{n=1}^{\infty} \frac{1}{n} e^{-\frac{3j_{CE}}{2\theta} n} \right). \quad (63)$$

The obtained results are in full accordance with symmetry of structure.

4. Conclusions

The recovery of equivalence between rectangular structures and the structures of lower symmetry (triclinic, monoclinic, etc.) is one of the most important necessities the theory of nanostructures. The theoretical analysis of nanostructures is developed for rectangular and cylindrical ones. In this work, the concept of statistical and dynamical equivalence between structures of higher and lower symmetry was introduced.

The proposed method is not universal, unfortunately. As it was seen for some triclinic structures the equivalent rectangular one does not exist. Nevertheless, in many actual cases method of equivalence can be applied. Concerning the monoclinic structure this method is always successful.

Acknowledgements

This work was supported by a grant of the Romanian Ministry of Research and Innovation, project number 10PFE/16.10.2018, PERFORM-TECH-UPT – The increasing of the institutional performance of the Polytechnic University of Timișoara by strengthening the research, development and technological transfer capacity in the field of “Energy, Environment and Climate Change”, within Program 1 – Development of the national system of Research and Development, Subprogram 1.2 – Institutional Performance – Institutional Development Projects – Excellence Funding Projects in RDI, PNCDI III.

References

- [1] Kittel Ch. *Introduction to Solid State Physics*, 7th ed., New York, Wiley, 1995.
- [2] Siegel R.W., Hu E., Roko M.C. (eds.) *Nanostructure Science and Technology A Worldwide Study Prepared under the guidance of the IWGN, NSTC, WTEC, Loyola College in Maryland, 2004*, URL: <http://www.whitehouse.gov/WH/EOP/OSTP/NSTC>.
- [3] Sajfert V., Đajić R., Četković M., Tošić B. Cylindrical quantum dots with hydrogen-bonded materials. *Nanotechnology*, 2003, **14**, P. 358–365.
- [4] Sajfert V., Đajić R., Tošić B.S., Hydrogen-Bonded Nanotubes as a Model for DNA Transcription. *J. Nanosci. Nanotech.*, 2004, **4** (7), P. 886–890.
- [5] Sajfert V., Štrajčić J., Tošić B., Đajić R. Excitonic Diffusion in Thin Molecular films. *Czechoslovak Journal of Physics*, 2004, **54** (9), P. 975–988.
- [6] Sajfert V., Tošić B. Conductance Properties of Cylindrical Quantum Nano Dots. *Journal of Computational and Theoretical Nanoscience*, 2005, **2** (1) P. 148–153.
- [7] Sajfert V., Štrajčić J.P., Jačimovski S., Tošić B. Thermodynamic and Kinetic Properties of Cylindrical Quantum dots. *Physica E: Low-dimensional Systems and Nanostructures*, 2005, **25** (4), P. 479–491.
- [8] Backović D., Sajfert V., Štrajčić J., Tošić B. Magnetic Nanorod in the Transition Temperature Vicinity. *Journal of Computational and Theoretical Nanoscience*, 2005, **2** (3), P. 448–455.
- [9] Popov D., Dong S.H., et al. Construction of the Barut-Girardello quasi coherent states for the Morse potential. *Annals of Physics*, 2013, **339**, P. 122–134.
- [10] Smolkina M.O., Popov I.Y., Blinova I.V., Milakis E. On the metric graph model for flows in tubular nanostructures. *Nanosystems: Physics, Chemistry, Mathematics*, 2019, **10** (1), P. 6–11.
- [11] Ziman J.M. *Principles of the Theory of Solids*, Cambridge University Press, 1972.
- [12] Puta M., Iacob F. Geometric prequantization of the symmetric rigid body. *Differential Geometry and Its Applications*, 2001, **39**, P. 385–390.
- [13] Ibach H., Lüth H. *Solid State Physics, An Introduction to Principles of Material Science*, 3rd edition, Springer-Verlag, Berlin, Heidelberg, New York, 2003.
- [14] Zubarev D. *Statistical Mechanics of Nonequilibrium Processes, Basic Concepts, Kinetic Theory*, Wiley, New York, 1997.
- [15] Chaikin P.B., Lubensky T.C. *Principles of Condensed Matter Physics*, Cambridge University Press, 1995.
- [16] Yablikov S.V. *Methods in the Quantum Theory in Magnetism*, Plenum Press, New York, 1967.
- [17] Gradshteyn I.S., Ryzhik I.M. *Table of Integrals, Series, and Products*, Academic Press, New York, London, 1965.
- [18] Sajfert V., Bucalović N., Mašković Lj., Tošić B. Electrons in thin films. *Czechoslovak Journal of Physics*, 2006, **56**, P. 253–266.

Electron transport through nanosystems driven by pseudo-Gaussian well scattering

Felix Iacob

West University of Timișoara, 300223 V. Pârvan 4, Timișoara, Romania

felix.iacob@gmail.com

PACS 61.46.w, 34.80.i

DOI 10.17586/2220-8054-2020-11-1-44-49

Electron transmission through nanosystems encounter different scattering processes. We focus on the scattering by impurities, which were implemented by considering a model based on the pseudo-Gaussian well. We discuss typical signatures of this phenomenon.

Keywords: Structure of nanoscale materials, electron scatter.

Received: 12 January 2020

1. Introduction

Particle scattering outside the target has been one of the most important applications of quantum mechanics. Probably, it is the most efficient way to study the structure of matter at short distances. A high-momentum scattering is required, by uncertainty principle, in order to achieve better resolutions. However, a low energy study reveals the excitation spectrum of a system, the resonances. Particle scattering is of great interest in disruptive technologies, as it critically depends on the dissipationless transport of electrons. It is of great interests about electron mobility calculation as well as the specific equations for the different scattering mechanisms [1]. This allows the evaluation of properties at the macro level, as well as the evaluation of measure at the nanoscale voltage drop caused by the scattering was previously reported [2].

In this work we, investigate the electrons coming in and getting scattered by a short-ranged potential, namely, the pseudo-Gaussian potential [3–5] considered to be located around the origin. Nanosystems having size approaching the fundamental scale of microscopic length have fundamentally demonstrated new physical phenomena. New advances have been made in many basic and modified fields of nanophysics, including diluted cold gases, carbon nanotubes, graphene, magnetic nanostructures, composite nanoparticles, transport through coupled quantum dots, spin-dependent electron transport phenomena, optical arrays with doped nanoparticles, and electronic, molecular, and quantum information processing. The pseudo-Gaussian potential proves to be a reliable model for defects in nanostructures or a bulk material itself. It can easily model the vibrational levels of such a nanostructure based on the fact it has a finite levels of energies, as shown in different papers as [6,7], despite of harmonic oscillator with an infinite one. Moreover, change of number of levels is possible by manipulation of some parameters, and also it permits dissociation with the energy in the continuum. Heterostructures can be used for advanced electronic devices (for example, modulated field effect transistors, heterojunction bipolar transistors, and resonant tunneling devices), optical components (e.g., waveguides, mirrors) and optoelectronic devices and structures (for example, laser diodes, photodetectors). These are also crucial in many optoelectronic devices (e.g., lasers). Perhaps their most important technological aspect may be that they can be used for all these electronic, optical and optoelectronic purposes and, therefore, can allow the integration of all of them. The scattering method of investigation can be found in any area of physics even in astrophysics [8].

2. Pseudo-Gaussian oscillator model

The computation of the scattering data for a given potential requires the construction of the regular solution of the radial equation. We, shortly, introduce some aspects of the pseudo-Gaussian oscillator (PGO) model. The central real valued potential:

$$V_{\lambda,\mu}^s(r) = \left(\lambda + \sum_{k=1}^s C_k r^{2k} \right) \exp(-\mu r^2), \quad (1)$$

is fixed by the coefficients C_k :

$$C_k = \frac{(\lambda + k)\mu^k}{k!}, \quad (2)$$

and its properties are completely determined by the dimensionless parameters $\lambda \in \mathbb{R}$, $\mu \in \mathbb{R}_+$ and the positive integer $s = 1, 2, \dots$, named the *order* of PGO. The potentials defined by the Eqs. (1) and (2) have the property to approach to the HO potential when $r \rightarrow 0$ together with Gaussian asymptotic behavior, i.e. $\lim_{r \rightarrow \infty} V_{\lambda,\mu}^s(r) = 0$. The plot from

Fig. 1, shows the shape of PGO potential. A last observation on the potential is that the Taylor expansion does not have terms proportional with r^4, r^6, \dots, r^{2s} , for a fixed s ,

$$V_{\lambda,\mu}^s(r) = \lambda + \mu r^2 + \sum_{k=s+1} \hat{C}_k r^{2k}. \quad (3)$$

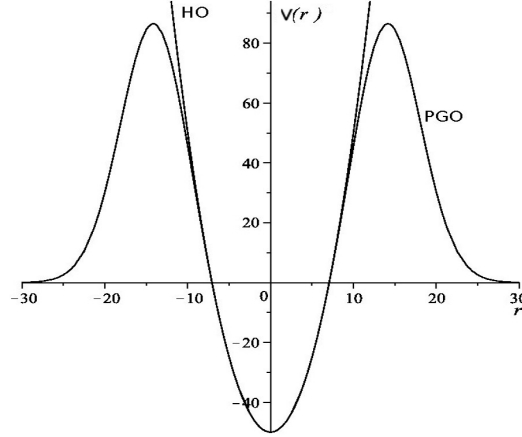


FIG. 1. The pseudo-Gaussian oscillator potential graph ($s = 3$) compared with harmonic oscillator potential one

The evolution in this potential is given by Schrödinger equation:

$$\left[\frac{d^2}{dr^2} + (E - V(r)) - \frac{l(l+1)}{r^2} \right] R(r, t) = -\frac{i\hbar}{2\pi} \frac{\partial R(r, t)}{\partial t}, \quad (4)$$

where $\psi(r, t) \equiv r^{-1}R(r, t)$ eliminates the first derivative. It was shown [4] that the time independent equation of (4) generates a stationary states in the pseudo-Gaussian well,

$$R(r) = \exp[p(r)] \sum_{n=0} a_n r^{2n+\tau}, \quad (5)$$

the polynomial $p(r)$ has the form:

$$p(r) = \sum_{n=1}^{s+1} \frac{1}{2n} \alpha_{2n} r^{2n}, \quad (6)$$

where α_{2n} are parameters. The analytic expression of ground state looks like:

$$\psi_0(r) = a_0 \exp[0.638r^2 - 0.039r^4 + 0.0034r^6 - 0.0029r^8]. \quad (7)$$

A plot of wave eigenfunctions for $n \in \{0, 1, 2, 3\}$ is shown in Fig. 2.

To evaluate the transport of electron through a nanostructure where impurities are supposed to be modeled with PG potential, we notice that it is independent on the polar and azimuth coordinate (θ, ϕ). The probability of current $J(r, t)$:

$$J(r, t) = \frac{i}{2m} \left(\psi \frac{\partial \psi^*}{\partial r} - \psi^* \frac{\partial \psi}{\partial r} \right), \quad (8)$$

is defined:

$$\frac{dP_{ab}(t)}{dt} = J(a, t) - J(b, t), \quad (9)$$

such that describes the change in the probability of finding a particle in the region bordered by a and b at the time t. In order to overcome the problems caused due to the centrifugal barrier we organize ourselves completing a procedure regarding the scattering amplitude. The scattering amplitude $f(k, k')$ solution of the time independent equation (4), corresponding to the particle incident on the scattering centre in the solid angle $\Omega(\theta, \phi)$, has the form, [9]:

$$f(k, k') = -\frac{m}{\sqrt{2\pi}} \int dr' e^{-ikr'} V(r') \psi_n(r') \quad (10)$$

where a Born approximation is not required, due to the wave function which has the known expression (5).

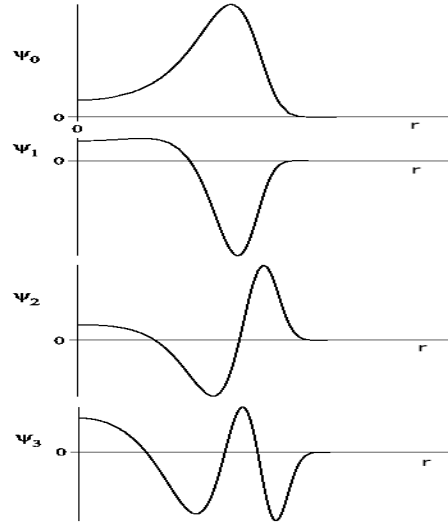


FIG. 2. The first four eigenfunctions for pseudo-Gaussian oscillator, $N = 7$, $\lambda = -5.6$, $\mu = 0.2$ and $l = 0$

The current (8) has the form:

$$J_{scat} = \frac{r^2}{2mi(2\pi)^3} |f(k, k')|^2 \left[\frac{e^{-ikr}}{r} \partial_r \frac{e^{ikr}}{r} + c.c. \right] \quad (11)$$

Finally, we get that the cross section has the expression,

$$\frac{d\sigma}{d\Omega} = |f(k, k')|^2, \quad (12)$$

knowing that the probability flux associated with the incident wavefunction is $j_{inc} = \frac{\hbar}{m(2\pi)^3} k$ [13].

3. Results of calculations and discussion

Based on the previous section were performed calculations of electron scattered on the PGO structure, which simulates conduction resistivity in nanostructure. The explicit formulae calculation ia given in Appendix (A). The main difficulties that had to be overcome were due to centrifugal barrier and the fact that even if equation (4) is solvable the potential is an infinite series, thus just an formal solution of (4) can be given. In order to obtain specific computation firstly the potential have to be finite, i.e. to specify the depth of the well. We performed our computation with the potential (13), by setting $s = 4$, similar computation can be made for any s , as was shown [4]. This is straightforward due to the Gaussian integrals, (17), that are generated by the infinite series of potential and which can be solved for each term taken as a sum of integrals. This observation facilitates a direct calculation of the scattering amplitude, the cross-section and so on. The calculation considers the following constant values: Planck constant $\hbar = 4.13566766$ eV·s, electron mass $m = 0.511$ MeV, and provides a treatment for an electron collisions with PGO scattering potential. Fig. 3, schematically represents the associated plane wave, the free particle wave function can

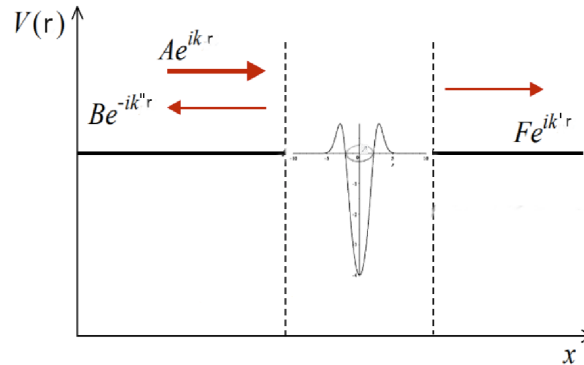


FIG. 3. Plan wave scatter on pseudo-Gaussian oscillator, $N = 4$, $\lambda = -4$, $\mu = 0.2$

be represented by a superposition of momentum eigenfunctions, with coefficients given by the Fourier transform of the plane wave, representing the wave packet. The interaction in the potential region is given by a series of Gaussian integrals. The work is facilitated by the fact that the PGO potential has the Taylor expansion simplified by the fact that the terms proportional with r^4, r^6, \dots, r^{2s} , are missing for a given s , as (3) shows. Making use of Gaussian integral properties, appendix relations (16) and (17), the scattering amplitude, (10), was obtained as it is given in the appendix expression (14). With the use of latter mentioned expression, it was given the expression to the cross section (15).

In the Fig. 4, one can see different cross sections calculated for certain particular cases of potentials. In all cases, it can be observed a resonant state given by the oscillatory structure. As one can compare with the resonance disposal in works like ([10–12]), it not belongs to the outer-well resonances. For a shallow deep potential endowed with high barriers, Fig. 4(b), extra resonances can be observed with a low probability, Fig. 4(a). As the potential gets deeper and barriers decrease, Fig. 4(d), the extra resonances reduces, Fig. 4(c). Finally, for a well without barrier, Fig. 4(f), the cross section, Fig. 4(e), does not exhibit resonant states. In this way, a model with a barriers can be used to explain the electronic conductance through nanostructure. The resistive transition is caused due to the resonant capture of passing

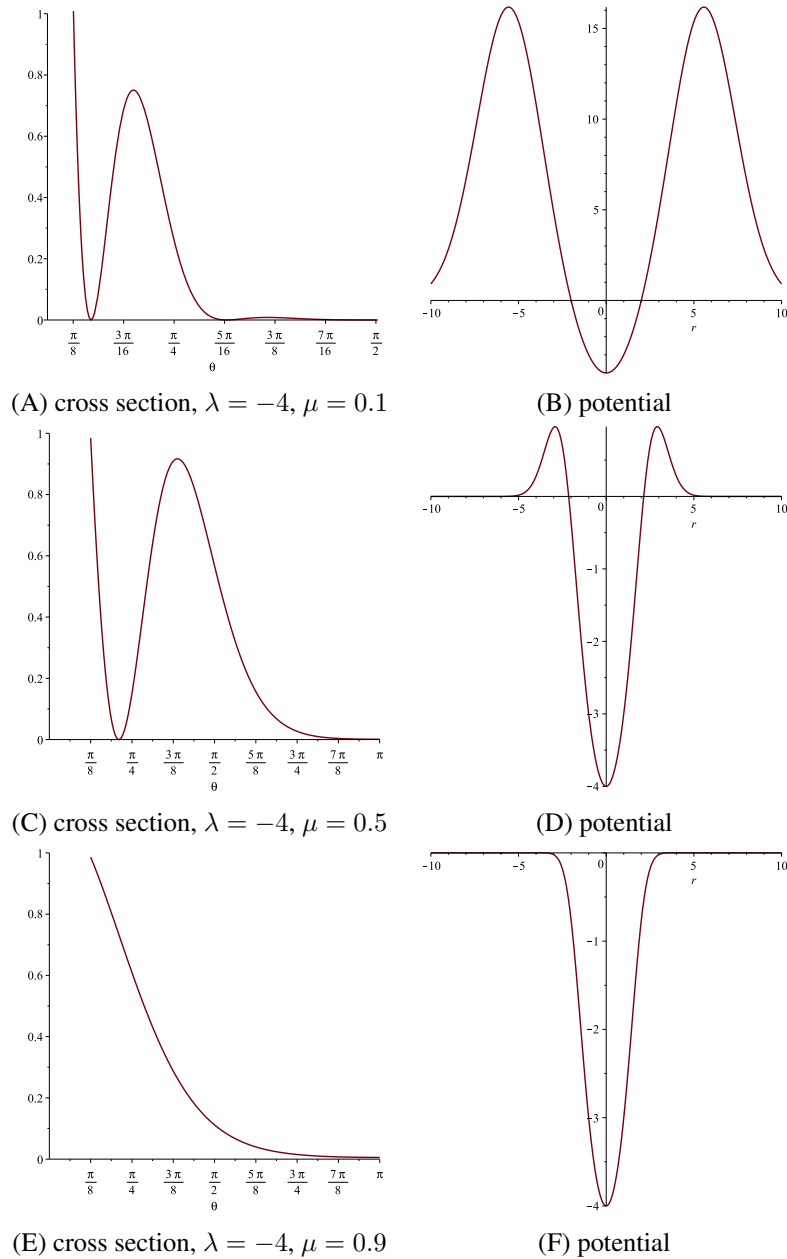


FIG. 4. The cross section, on left, vs. shape of potential corresponds to, on right

electron along the impurity described by the PGO. Our calculation shows that Rydberg states cannot be formed, being in the case of Fig. 4(e).

In conclusion the PGO model applied to electronic transport in nanostructure confirm that a part of resistivity is given by scattering on impurity centers, described by PGO potential, caused by capture of electron in a resonant state. The resonant state is confirmed on a narrow potential center, $\mu = 0.1$, and barriers whose size is comparable to the wavelength of the electron and disappears with increasing of the potential size.

Acknowledgements

The author like to acknowledge the COST Action CA17126, Towards understanding and modelling intense electronic excitation, part of this is due to the support for collaboration and discussions established with other scientists through the network.

References

- [1] Sadi T., Medina-Bailon C., et al. Simulation of the Impact of Ionized Impurity Scattering on the Total Mobility in Si Nanowire Transistors. *Materials*, 2019, **12** (1), 124.
- [2] Bauer S., Bobisch C.A. Nanoscale electron transport at the surface of a topological insulator. *Nat. Commun.*, 2016, **7**, 11381.
- [3] Iacob F. Relativistic pseudo-Gaussian oscillators. *Phys. Lett. A*, 2010, **374** (11–12), P. 1332–1335.
- [4] Iacob F., Lute M. Exact solution to the Schrodingers equation with pseudo-Gaussian potential. *J. Math. Phys.*, 2015, **56**, 121501.
- [5] Iacob F. Spectral Characterization Of Hydrogen-Like Atoms Confined By Oscillating Systems. *Centr. Eur. J. Phys.*, 2014, **12** (9), P. 628–636.
- [6] Kuemmeth F., Bolotin K.I., Shi S.-F., Ralph D.C. Measurement of discrete energy-level spectra in individual chemically synthesized gold nanoparticles. *Nano Lett.*, 2008, **8**, 4506.
- [7] Popov D., Dong S.H., et al. Construction of the Barut–Girardello quasi coherent states for the Morse potential. *Annals of Physics*, 2013, **339**, P. 122–134.
- [8] Coțăescu I.I., Sporea C.A. Scattering of Dirac fermions by spherical massive bodies. *Eur. Phys. J. C*, 2019, **79** (1), 15.
- [9] Johnson C.W. *A practical introduction to quantum scattering theory, and beyond*, 2017.
- [10] Niyonzima S., Pop N., et al. Low-energy collisions between electrons and BeD+. *Plasma Sources Science and Technology*, 2018, **27** (2), 025015.
- [11] Iacob F., Pop N., et al. Recombination and excitation of molecular cations with electrons: Application to BeD+ and BeT+. *AIP Conference Proceedings*, 2019, **2071** (1), 020007.
- [12] Pop N., Iacob F., et al. Reactive collisions of electrons with HD+, BeH+, BeD+ and SH+. *AIP Conference Proceedings*, 2017, **1916** (1), 020013.
- [13] Fitzpatrick R. Scattering Theory. URL: <https://farside.ph.utexas.edu/teaching/qm/lectures/node82.html>.

Appendix

A. The scattered amplitude and cross section expressions

In our calculations we consider the potential (1) having the depth given by the chosen value of $s = 4$,

$$V(r) = [\lambda + (\lambda \mu + 1) r^2 + (1/2 \lambda \mu + 1) \mu r^4 + (1/6 \lambda \mu + 1/2) \mu^2 r^6 + (1/24 \lambda \mu + 1/6) \mu^3 r^8] e^{-\mu r^{2'}}, \quad (13)$$

which gives the scattered amplitude,

$$f(q) = -7.76 \times 10^{20} \frac{\sqrt{2\pi}}{q} \left(e^{1/4 \frac{q^2}{\mu}} \right)^{-1} \left[\begin{aligned} & 1/4 \frac{\lambda \sqrt{2} q}{\sqrt{\pi} \mu} \sqrt{\frac{\pi}{\mu}} - 1/16 \frac{\lambda \sqrt{2} q (q^2 - 6 \mu)}{\mu^{5/2}} 1/16 \frac{\sqrt{2} q (q^2 - 6 \mu)}{\mu^{7/2}} \\ & + \frac{\lambda \sqrt{2} q (q^4 - 20 \mu q^2 + 60 \mu^2)}{128 \mu^{7/2}} + \frac{\sqrt{2} q (q^4 - 20 \mu q^2 + 60 \mu^2)}{64 \mu^{9/2}} \\ & - \frac{\lambda \sqrt{2} q (q^6 - 42 \mu q^4 + 420 \mu^2 q^2 - 840 \mu^3)}{1536 \mu^{9/2}} - \frac{\sqrt{2} q (q^6 - 42 \mu q^4 + 420 \mu^2 q^2 - 840 \mu^3)}{512 \mu^{11/2}} \\ & + \frac{\lambda \sqrt{2} q (q^8 - 72 \mu q^6 + 1512 \mu^2 q^4 - 10080 \mu^3 q^2 + 15120 \mu^4)}{24576 \mu^{11/2}} \\ & + \frac{\sqrt{2} q (q^8 - 72 \mu q^6 + 1512 \mu^2 q^4 - 10080 \mu^3 q^2 + 15120 \mu^4)}{6144 \mu^{13/2}} \end{aligned} \right] \quad (14)$$

conversion to wave vectors $\sqrt{2k^2(1-\cos(\theta))}$ cross section $(|f(q)|)^2$ gives

$$\begin{aligned} \frac{d\sigma}{d\Omega} = & 3.21 \times 10^{36} \frac{1}{\mu^{13}} \left(e^{1/2 \frac{k^2(-1+\cos(\theta))}{\mu}} \right)^{-2} \\ & C^2 \left| -8712.0 k^2 \mu^3 - 168.0 k^6 \mu + 2112.0 k^4 \mu^2 + 4.0 k^8 (\cos(\theta))^4 \right. \\ & - 16.0 k^8 (\cos(\theta))^3 + 24.0 k^8 (\cos(\theta))^2 - 16.0 k^8 \cos(\theta) + 3465.0 \lambda \mu^5 \\ & + 168.0 k^6 (\cos(\theta))^3 \mu - 504.0 k^6 (\cos(\theta))^2 \mu + 2112.0 k^4 (\cos(\theta))^2 \mu^2 \\ & + 504.0 k^6 \cos(\theta) \mu - 4224.0 k^4 \cos(\theta) \mu^2 + 8712.0 k^2 \cos(\theta) \mu^3 + k^8 \lambda \mu \\ & - 2772.0 \lambda k^2 \mu^4 + 594.0 \lambda k^4 \mu^3 - 44.0 \lambda k^6 \mu^2 + \lambda k^8 (\cos(\theta))^4 \mu \\ & - 4.0 \lambda k^8 (\cos(\theta))^3 \mu + 44.0 \lambda k^6 (\cos(\theta))^3 \mu^2 + 6.0 \lambda k^8 (\cos(\theta))^2 \mu \\ & - 132.0 \lambda k^6 (\cos(\theta))^2 \mu^2 - 4.0 \lambda k^8 \cos(\theta) \mu + 594.0 \lambda k^4 (\cos(\theta))^2 \mu^3 \\ & + 132.0 \lambda k^6 \cos(\theta) \mu^2 - 1188.0 \lambda k^4 \cos(\theta) \mu^3 + 2772.0 \lambda k^2 \cos(\theta) \mu^4 \\ & \left. + 4.0 k^8 + 8316.0 \mu^4 \right|^2 \end{aligned} \quad (15)$$

substitution ($\lambda = -4, \mu = 0.5, C = 1.5 \times 10^{-44}, k = 2$).

B. Gaussian integrals

$$\int_0^{\infty} r \sin(qr) \left(r^2 e^{-\mu r^2} \right) dr \quad (16)$$

gives

$$-1/16 \frac{\sqrt{\pi} q^3}{m u^{7/2}} \frac{1}{\sqrt[4]{e^{\frac{q^2}{\mu}}}} + 3/8 \frac{\sqrt{\pi} q}{m u^{5/2}} \frac{1}{\sqrt[4]{e^{\frac{q^2}{\mu}}}}. \quad (17)$$

The influence of the centrifugal barrier:

$$\lim_{n \rightarrow \infty} \int_0^n \frac{\sin(qr) l(l+1) e^{-0.5 r^2}}{r} dr \quad (18)$$

is an amortized oscillation as increasing the integration domain.

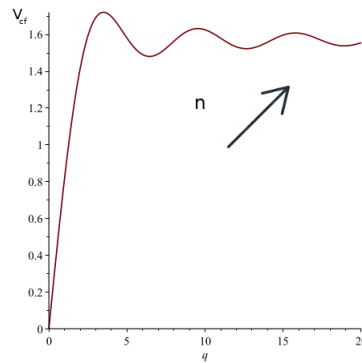


FIG. 5. The dependence on centrifugal barrier. As n , the domain, extends upwards the sinusoids become dense

Magnetoelectric effects theory by Heisenberg method based on permutation group symmetry of nanoparticles

S. Leble

Immanuel Kant Baltic Federal University, Institute of Physics,
Mathematics and Informational Technology, Russia, Kaliningrad 236000
lebleu@mail.ru

PACS 75.70.Cn, 05.30.d, 02.20.a

DOI 10.17586/2220-8054-2020-11-1-50-64

The Heisenberg theory of ferromagnetism is widened to include external electric field action. The material relations are derived by means of differentiation of logarithm of partition function with respect to the magnetic and electric fields. The mean energy coefficients as the exchange integrals combinations are expressed via characters of irreducible representations of corresponding permutation groups by the Heitler method. The thermodynamic equations of state for polarization and magnetization, as functions of the electric and magnetic fields, are derived and illustrated by figures. The magnetization and hysteresis curves in magnetization – magnetic field components plane are built. The theory is applied to nanoparticles, the particle partition function is modeled as the product of the surface and bulk parts. The statistical sum is constructed having explicit expressions for the mean energy in terms of exchange integrals and number of closest neighbors for surface and bulk atoms. The relative contribution of the surface and bulk terms is evaluated.

Keywords: multielectron states, permutation group symmetry, mean energy, Gauss distribution, Heisenberg chain, electric field, nanoparticles, multiferroics.

Received: 20 January 2020

Revised: 10 February 2020

1. Introduction

1.1. General remarks

An exchange integral for electron pair interaction enters the theory of magnetic phenomena as a basic notion from times of pioneer paper of Heisenberg [1]. In majority of papers on magnetic phenomena applications it is used as a unique parameter, conventionally established by experiments for a given class of matter [2]. A main result of the Heisenberg work is the relation that includes the matter parameters, temperature and magnetic field. It contains information of the distribution of atoms in space via number of closest neighbors z . This relation is a transcendental equation for the magnetization vector component, that, dependent on the matter parameters values, has one or two solutions. The last is identified with ferro-magnetism existence. Its estimation by the Heitler-London model approximation, as it is made in [1] can be improved by Fockian eigenfunctions [3], which, however, is a complicated numerical task.

This seminal paper [1] theory exhibits the next important ingredient of the multi-electrons' system natural symmetry, with respect to the permutation group. Following [4], it uses evaluation of mean energy for a given irreducible representation of this group, expressing it explicitly via exchange integrals. On same platform, explicit formulas for mean quadratic deviations of the energy is derived by Heisenberg [1] and used for energy distribution modeling in Gaussian form. Some natural critics of this theory is published in [5] with respect to its applicability to the case of 8 nearest neighbors case (Fe), but exhibits a good physical realization for a 12 neighbors matter (Ni,Co), illustrated by comparison with experiments [6, 7].

The *ab initio* models such as Brillouin or Langevin ones developed by Weiss either in a framework of molecular theory, or in combination with the phenomenology of Landau, improves paramagnetic domain description for a ferromagnetic matter, but not so good in a hysteresis curves production [8, 9]. It also do not take into account the fundamental permutation group symmetry.

In [10] Nakano represents the results with the lower (compared to Heisenbergs') minimal number of closest neighbors $z = 6$, that opens a possibility of using this model for Iron. Next, W. Heisenberg [11] develops the theory with the domain walls account. The whole story of the ferromagnetism theory, related to Heisenberg contributions, is outlined in [12].

According to Kondorsky classification [13], there are three main causes of hysteresis: 1) Hysteresis due to a delay in the displacement of boundaries between domains. 2) Hysteresis due to growth retardation of the magnetization reversal of nucleation. 3) Hysteresis due to irreversible rotation.

It is known that the continuous version of Heisenberg chain equation with Gilbert term account [14] may explain existence of domain walls (DW). An energy of a DW and conditions of its creation may be estimated in terms of exchange integral and anisotropy coefficient. The first is proportional to the so-called exchange stiffness and the second is related to a distribution of atoms in space [15].

The hysteresis curve for nanocrystallized soft magnetic systems was extracted from the intrinsic switching field distribution of the sample, as it is simulated with a combination of a Gaussian distributions [16], that has an intersection of ideas with [11]; other approach is based on the solid base of Landau-Lifshitz-Gilbert equations [17].

The model we presented recently is a generalization of Heitler-Heisenberg method of energy mean values and mean quadratic deviations of the energy derivation by explicit formulas via characters of irreducible representation of permutation group. The generalizations widen the symmetry group including space transformation and external electric field [3]. As a consequence of a difference between the nearest neighbors relative distance, fixed by positions in an atomic net, two kinds of the exchange integrals were introduced.

In this work, going down with dimension of objects under consideration from macroscopic to mesoscopic such as “fine particles” or “nanoparticles”, we should take into account a relative weight of surface atoms in the whole object description [18]. There is important direction of the Barium titanate (BTO) nanoparticles investigations [19] related to the ferroelectricity phenomenon, known from times of [20].

The magnetoelectric effect has tremendous potential applications. Transition metal oxides provide a fertile playground for such phenomena. First-principles methods to study magnetoelectric phenomena are reviewed in the present text.

The search for materials displaying a large magnetoelectric effect has occupied researchers for many decades [21]. The rewards could include not only advanced electronics technologies, but also fundamental insights concerning the dielectric and magnetic properties of condensed matter. In this article, we focus on the magnetoelectric effect (e.g. in transition metal oxides) and review the manner in which first-principles calculations have helped guide the search for (and increasingly, predicted) new materials and shed light on the microscopic mechanisms responsible for magnetoelectric phenomena [22].

In this paper, we plan to go by the second way, introducing three kinds of the parameters (integrals) that link atoms as 1) bulk-bulk; 2) surface-surface; 3) bulk-surface.

The Heisenberg sum by atoms in such division would be shared to three subsums, with corresponding factors J_1, J_2, J_3 . The statistical sum is correspondingly factorized. In this note, to show the principle, we restrict ourselves by two terms, unifying the last two parts, deriving and illustrating matter relations, including hysteresis curves for the simplest bulk case and bulk-surface.

1.2. Notations. Partition function. Thermodynamics

Let a Hamiltonian \hat{H} be a function of external thermodynamic parameter a , which is conjugate to the internal parameter B , so that the elementary work is equal to Bda . Within the framework of the equilibrium quantum statistical physics, for given Boltzmann constant k and temperature T , the Gibbs operator [23]

$$\hat{f} = \frac{1}{Z} \exp\left[-\frac{\hat{H}}{kT}\right],$$

contains the normalization constant,

$$Z = \text{Tr} \left[\exp\left[\frac{-\hat{H}}{kT}\right] \right], \quad (1)$$

called a statistical sum (partition function). Then

$$B = -kT \frac{\partial \ln Z}{\partial a}. \quad (2)$$

In this text we shall consider two pairs of the parameters: $a, B \rightarrow H, M; E, P$, these are the component of magnetic field versus component of magnetization vector; the component of electric field versus component of polarization vector. For the sake of clarity, we act in a projection of all fields to one direction, so the Hamiltonian is a function of the magnetic and electric fields components along the marked direction $\hat{H} = \hat{H}(H, E)$. If the Hamiltonian is divided in few terms as $\hat{H} = \hat{H}_1 + \hat{H}_2$, the partition function is factorized as $Z = Z_1 Z_2$, hence the thermodynamic variable

$$-\frac{B}{kT} = \frac{\partial \ln Z_1 Z_2}{\partial a} = \frac{\partial \ln Z_1}{\partial a} + \frac{\partial \ln Z_2}{\partial a} \quad (3)$$

correspondingly splits.

2. Heisenberg relation and hysteresis existence condition

2.1. Origin of the Heisenberg relation

We start with the bulk case. After transformations, described in [24] (some explanations are given in subsequent sections) the partition function Z , defined by (1), is the following function of most probable magnetization M per electron:

$$Z = F \left[2 \cosh \frac{\omega}{2} \right]^{2n}, \quad (4)$$

where:

$$\omega = \alpha + \beta M - \beta^2 \frac{M}{z} + \beta^2 \frac{M^3}{2z}, \quad \alpha = \frac{e\hbar}{mkT} H, \quad \beta = \frac{zJ}{kT}, \quad (5)$$

z – number of closest neighbors, e , m – electron charge and mass, n – number of electrons, \hbar – Plank constant, J – exchange integral.

The value of magnetization as thermodynamic variable is determined by (2) and (4) as [23]:

$$M = \frac{1}{n} \frac{\partial \ln Z}{\partial \alpha} = \tanh \frac{\omega}{2}. \quad (6)$$

Finally, the Heisenberg relation appears as:

$$M = \tanh \frac{\alpha + \left(1 - \frac{\beta}{z}\right)\beta M + \beta^2 \frac{M^3}{2z}}{2}, \quad (7)$$

the l.h.s. of (7) we would note as $y_1(M) = M$ and the r.h.s. as $y_2(M, \alpha)$.

2.2. On Heisenberg relation solution

The number of intersections of the straight line $y_1 = M$ and the curve $y_2 = y_2(M, \alpha)$ for given α depends on the curve inclination in the origin. Let us illustrate it by plots, taking the closest neighbors number $z = 12$ as for nickel and cobalt. At the Fig. 1 plots of the y_1 and three curves y_2 with different values of α are shown for the paramagnetic case $\beta = 1$.

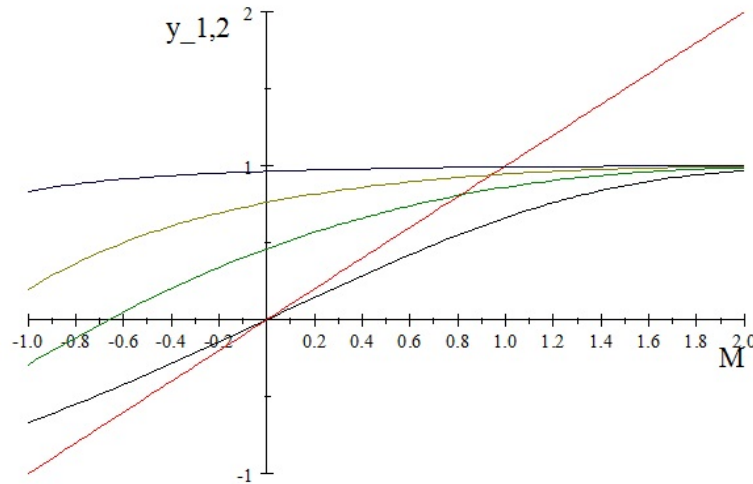


FIG. 1. $\beta = 1$. The straight line (red) is $y_1=M$. The curves from lower to upper $y_2(M, 0)$ – black – 4, $y_2(M, 0.5)$ – green – 3, $y_2(M, 1.0)$ – brown – 2, $y_2(M, 2.0)$ – navy – 1, with numbers at left

The intersection points for a sequence of unique values of α (proportional to the magnetic field, see (5)) lie on the magnetization curve, the phenomenon of saturation is quite visible. So, the intersection points form the magnetization curve.

2.3. Critical curve of ferromagnetism existence

As it is seen from the graphical view, for the ferro-magnetism in the present condition, the curve $y_2(M, \alpha)$ inclination at $M = 0$ is less than one for y_1 , or

$$\beta\left(1 - \frac{\beta}{z}\right) \geq 2. \quad (8)$$

At critical point of transition from unique to double solution, the inclinations at origin for both $y_{1,2}$ coincide, whence the derivative of the function $y_2(M, 0)$ should be equal to 1:

$$\left. \frac{\partial y_2(M, 0)}{\partial M} \right|_{M=0} = \frac{1}{2}\left(1 - \frac{\beta}{z}\right)\beta = z\frac{J}{2kT}\left(1 - \frac{J}{2kT}\right) = 1. \quad (9)$$

The curve of critical values of nearest neighbors $z\left(\frac{kT}{J}\right)$ as the inverse function of exchange integral per electron in kT units is shown at the Fig. 2.

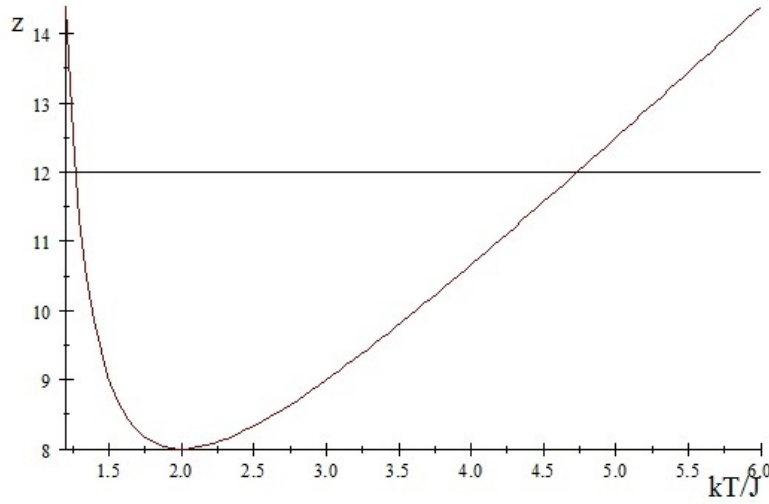


FIG. 2. The plot of the function $z = \frac{2x^2}{x-1}$, $x = \frac{kT}{J}$. The straight horizontal line marks $z = 12$. The Boltzmann constant is marked as k at the abscissa label

The solution of the quadratic equation $\left(1 - \frac{\beta}{z}\right)\beta = 2$ gives the roots:

$$\beta_{1,2} = \frac{z}{2} \pm \sqrt{\frac{z^2}{4} - 2z}, \quad (10)$$

the minimal temperature yields for the case:

$$\beta_{\max} = \frac{zJ}{kT_{\min}}, \quad T_{\min} = \frac{zJ}{k\beta_{\max}}, \quad (11)$$

and the maximum is equal to:

$$\beta_{\min} = \frac{zJ}{kT_{\max}}, \quad T_{\max} = \frac{zJ}{k\beta_{\min}}. \quad (12)$$

For the minimal case of $z = 8$, (iron) a direct application of the theory is impossible, because of the ferromagnetic range is restricted by one point, look e.g. [5, 6]. Outside the range, the magnetization curve shows the behavior typical for a paramagnetic material.

For the case, marked at the Fig. 2, $z = 12$, we obtain $\beta = 6 \pm 2\sqrt{3}$, hence the minimal temperature yields for the case:

$$T_{\min} = \frac{12J_{12}}{k(6 + 2\sqrt{3})}, \quad (13)$$

and the maximum

$$T_{\max} = \frac{12J_{12}}{k(6 - 2\sqrt{3})}. \quad (14)$$

We would estimate the exchange integral from (15) for Ni , having:

$$J_{Ni} = \frac{T_{\max Ni} k (6 - 2\sqrt{3})}{12}. \tag{15}$$

Plugging the result into (16) we compute the critical temperature:

$$T_{\min} = \frac{12 J_{Ni}}{k(6 + 2\sqrt{3})}, \tag{16}$$

This case, valid for Ni, Co, is described in [5], where the curve of magnetization as function of temperature is shown and close to experiments of [6, 7].

Then, the hysteresis phenomenon exists at $z \geq 8$. For a simulation of the effect we take $\beta = 10$, see Fig. 3.

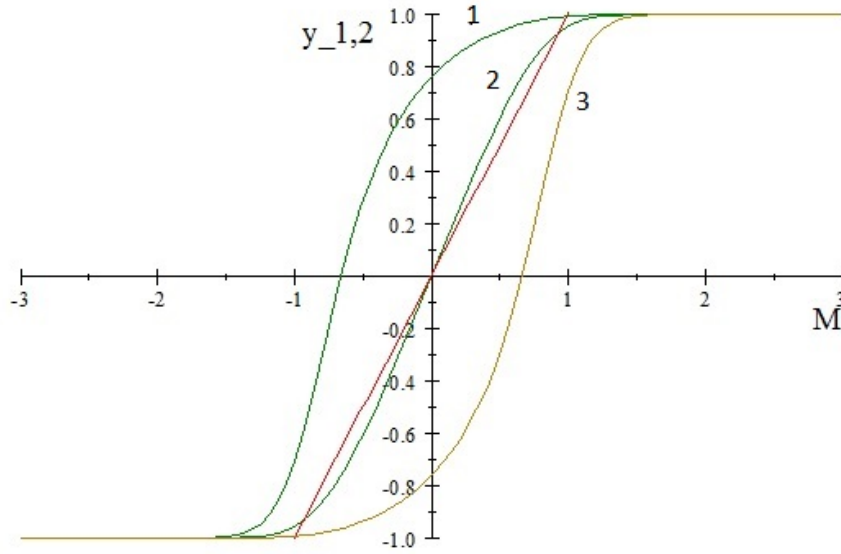


FIG. 3. The straight line (red) is $y_1 = M$. The curves from upper to lower, numbers at the top: $y_2(M, -1)$ – green – 1, $y_2(M, 0)$ – navy – 2, $y_2(M, 1)$ – sienna – 3

The double intersection of the curves $y_1 = M$ and $y_2(M, \alpha)$ are demonstrated by Fig. 4.

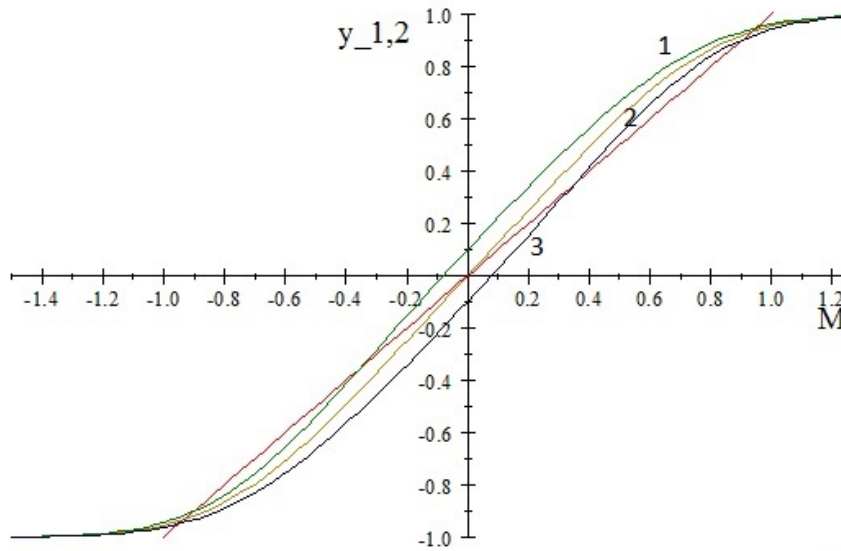


FIG. 4. The straight line (red) is $y_1 = M$. The curves from upper to lower $y_2(M, -0.2)$ – green – 1, $y_2(M, 0)$ – navy – 2, $y_2(M, 0.2)$ – sienna – 3

Generally, it is convenient to use the inverse to $M = \tanh \frac{x}{2}$ function:

$$x = \ln \frac{1+M}{1-M}, \quad M \in (-1, 1), \quad (17)$$

which has double intersections with the curve (see (7))

$$\omega = \alpha + \beta M - \beta^2 \frac{M}{z} + \beta^2 \frac{M^3}{2z}, \quad (18)$$

giving the hysteresis curve, as it is shown at the Fig. 5.

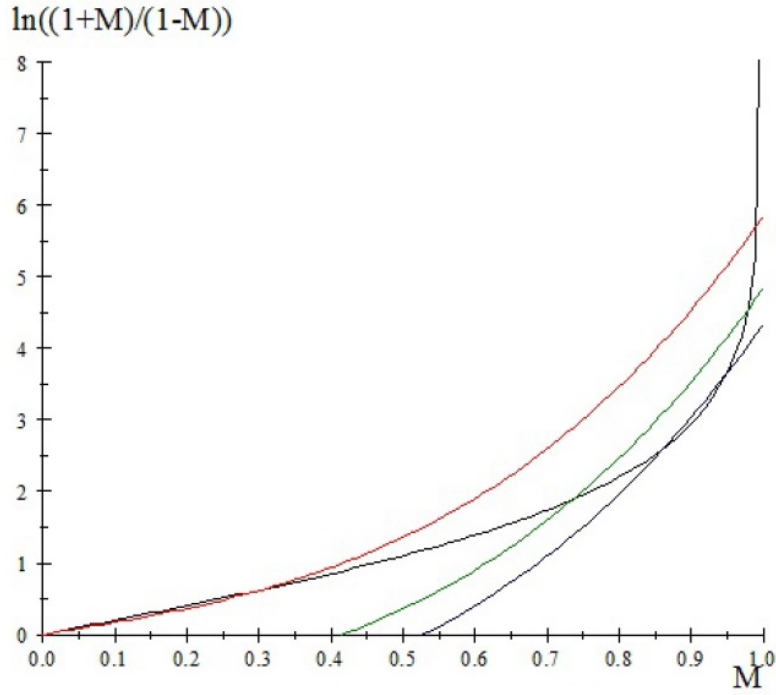


FIG. 5. The black curve shows the function marked at the ordinate. The colored curves shows the r.h.s. of the function (56) with $\beta = 10$, $\alpha = 0$ (red - 1), $\alpha = -1$ (green - 2), $\alpha = -1.5$ (navy - 3), numbers mark the curves

3. Fine particles case

3.1. Back to partition function, surface-bulk division

Figure 6 presents a nanoparticle cross-section schematically, that allows to estimate the number of atoms at the surface layer and under the surface (bulk) layers.

Let the nanoparticle radius be Nd , with N – number of layers and d is the atom diameter, then the number of “surface” particles is estimated as:

$$n_a = \frac{4}{3}\pi(N^3 - (N-1)^3) = 4\pi(3N^2 - 3N + 1), \quad (19)$$

the number of “bulk” particles is equal to:

$$n_b = \frac{4}{3}\pi(N-1)^3. \quad (20)$$

Let m be the spin projection quantum number. The partition function of states is built as in [1], taking as density of states the product of Gauss distribution and the distribution with mean energy for given spin s via evaluation for

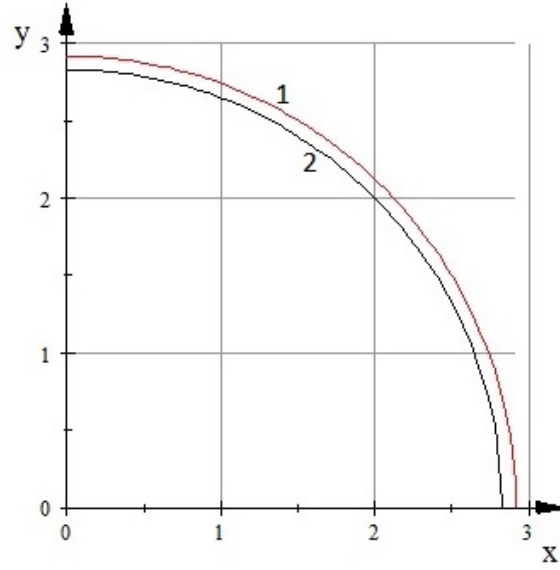


FIG. 6. The plot represents the cross-section of a nanoparticle, approximated by a sphere of radius Nd , where N is the number of layers and d is the atom diameter. E.g. for Ni it is $d = 1.49 \cdot 10^{-10} [m]$. The space between black curve (2) with radius $(N - 1)d$ and the red curve (1) with radius Nd shows the surface monoatomic layer. Numbers of curves are in the parenthesis

irreducible representation (n_ν its dimension) for electrons' permutations group; we keep the author's notations:

$$\sum_{s=0, m=-s}^{n, s} \int_{-\infty}^{\infty} d\Delta E \frac{n_\nu}{\sqrt{2\pi(\Delta E^\nu)^2}} \exp \left\{ \alpha m + \beta \frac{s^2}{2n} - \frac{\Delta E}{kT} - \frac{\Delta E^2}{2(\Delta E^\nu)^2} \right\} = \sum_{s=0}^n \sum_{m=-s}^s n_\nu \exp \left\{ \alpha m + \beta \frac{s^2}{2n} + \frac{\overline{\Delta(E^\nu)^2}}{2k^2T^2} \right\}. \quad (21)$$

After the principal bulk model simplification $J_g = J$ and some algebra we arrive at (4).

3.2. Energy distribution for a tiny particle

Now, let us take into account the difference between exchange integrals for surface and bulk atoms. Such division is stressed in [18]. We take, that the values of $J_{a,b}$ are the same for pairs bulk-bulk (J_b); while surface-surface; and bulk-surface are denoted as J_a . The energy E^ν and the Gauss distribution parameter ΔE^ν , that is also expressed in terms of the symmetry group characters [3]. The result of Heitler for the energy is expressed as the sum by n-particle permutation group $g \in P$ [4], the exchange integrals are marked by group elements:

$$E^\nu = \frac{1}{n_\nu} \sum_{g \in P} \chi^\nu(g) J_g. \quad (22)$$

Here, $\chi^\nu(g) = D_{ii}^\nu(g)$ is the character of the symmetry group irreducible representation (number ν , the representation dimension is n_ν), that numerates the energy terms of multielectron system. The characters of the permutation group are listed in [4], corrected in [1].

For the case with absence of space symmetry, as e.g. for amorphous matter, one has only the mentioned surface-bulk division of exchange integrals and the subgroups $G_a \in P$ that contains only permutations between electrons of surface-surface and bulk-surface atoms, while $G_b \in P$ contains the permutations only between bulk-bulk atoms, electrons. Both groups are the permutation ones of the corresponding orders. For clarity, we left only two different exchange integrals, marked by indices a, b ; b for bulk and a for surface. Then the mean energy reads:

$$E^{\nu, \nu'} = \frac{J_a}{n_{\nu'}} \sum_{g \in G_a} \chi^{\nu'}(g) + \frac{J_b}{n_\nu} \sum_{g' \in G_b} \chi^\nu(g'), \quad (23)$$

we keep the number ν for the irreducible representation of the “bulk” subgroup $G_b \in P$. To explain the modification of the statistical sum with the surface-bulk subdivision we return to its origin. The sum by Heisenberg includes the terms with an energy and its Gauss distribution parameter, i.e. the mean square deviation of energy distribution.

The $\sum \Delta E_n = 0$, as well as due to $\chi^\nu(e) = n_\nu$, again in terms of the characters, we derive, finally the mean square deviation from the mean value E^ν with more details compared with one from [3]:

$$\overline{(\Delta E_n)^2} = \frac{J_a^2}{n_{\nu'}^2} \sum_{g', g \in G_a} (\chi^{\nu'}(gg') - \chi^{\nu'}(g)\chi^{\nu'}(g')) + \frac{J_b^2}{n_\nu^2} \sum_{g', g \in G_b} (\chi^\nu(gg') - \chi^\nu(g)\chi^\nu(g')), \quad (24)$$

where the sums run the subgroups of the complete permutation group.

The energy (23) and the distribution parameter (24) enter the partition function exponent (21) linearly, hence the exponential property admits that the statistical may be factorized as in (3).

3.3. Partition functions for a tiny particle

The modification of the whole construction could be similarly done for Z^a and Z^b partition functions:

$$M^{a+b} = \frac{\partial \ln(Z_a Z_b)}{\partial \alpha} = \frac{\partial \ln(Z_a)}{\partial \alpha} + \frac{\partial \ln(Z_b)}{\partial \alpha} = \quad (25)$$

$$\frac{\partial \ln([2 \cosh \frac{\omega_a}{2}]^{2n_a})}{\partial \alpha} + \frac{\partial \ln([2 \cosh \frac{\omega_b}{2}]^{2n_b})}{\partial \alpha} = \quad (26)$$

$$\frac{n_a}{n} \tanh \frac{\omega_a}{2} + \frac{n_b}{n} \tanh \frac{\omega_b}{2}. \quad (27)$$

where n_a is given by (19) and n_b by (20) correspondingly, so that:

$$\frac{n_a}{n} = \frac{4\pi(3N^2 - 3N + 1)}{4\pi N^3} = \frac{3N^2 - 3N + 1}{N^3}, \quad (28)$$

similarly, the relative number of “bulk” particles is equal to:

$$\frac{n_b}{n} = \frac{(N-1)^3}{N^3}. \quad (29)$$

Look the plots at Fig. 7

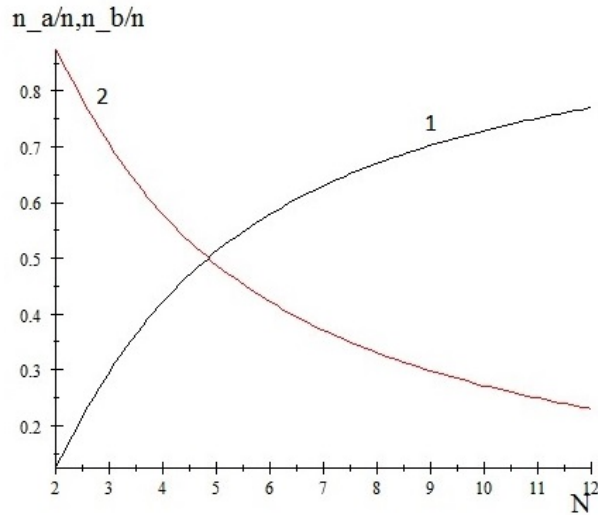


FIG. 7. The relative number of atoms in bulk (black – 1) and surface (red – 2) layers as the function of atomic layers N

$M^{a+b} = M_a + M_b$ is a most probable value of magnetic quantum number projection per electron for a joint bulk and a surface parts. The functions $\omega_{a,b}$ are described by:

$$\omega_a = \alpha + \beta_a M_a - \beta_a^2 \frac{M_a}{z_a} \left(1 - \frac{M_a^2}{2}\right). \quad (30)$$

similarly for b case. The parameters $\beta_{a,b} = \frac{z_{a,b} J_{a,b}}{kT}$ depend on exchange integrals. The bulk one may be defined via Curie point temperature.

3.4. Numerical experiments

For the numeric estimations let us choose the number of layers $N = 5$ for Ni nanoparticle. For such layers number we have equal number of atoms. The parameters we have chosen are the following: the bulk exchange integral, evaluated via Curie temperature value ($\theta_{Ni} = 627K$) $J_{Ni} = 1.8 \cdot 10^{-21} J$ [25]. The parameter $\beta_b = \frac{12J_{Ni}}{k_B T} = 2$ for $T = 795K$ outside the ferromagnetic range. For the surface condition we take $z = 8$, $\beta_a = \frac{8 \cdot 1, 15J_{Ni}}{k_B T} = 1.53$; the exchange integral corrected up 15%, for the minor distance between the surface and bulk atoms.

The magnetization of the surface layer is presented at Fig. 8. The corresponding bulk magnetization is superposed at the Fig. 9.

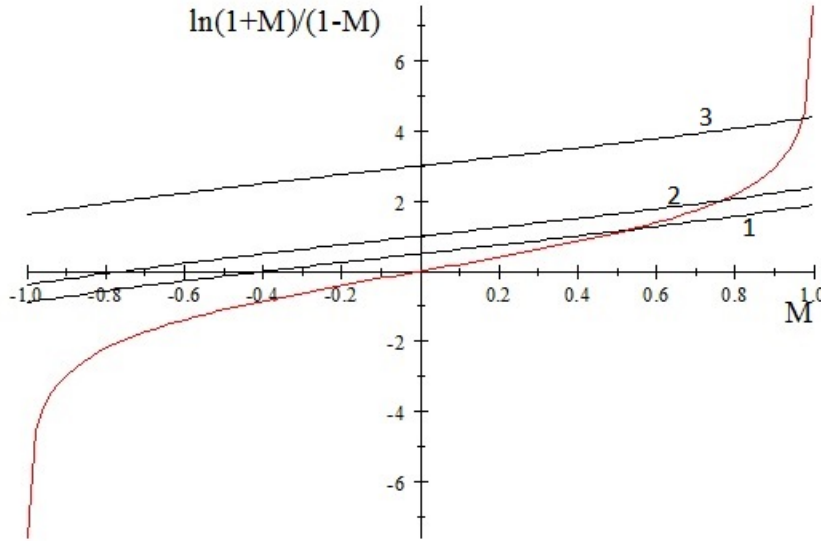


FIG. 8. The surface layer contribution to magnetization of a nanoparticle model. The three points of intersections of the inverse tanh function (red line) and ω_a black lines are shown for $\alpha = 0.5, 1.0, 3.0$ growth up (0.5 – 1, 0.3 – 2). The last point $\alpha = 3$ (3) stands close to magnetization saturation

4. Electric field action

4.1. Polarisation, Stark effect

A theory of perturbation of atoms by the external electric field \vec{E} is based on the perturbed Fockian action [3]:

$$H\phi = (H_F + V)\phi. \quad (31)$$

There are two possibilities for the field account: if a medium unit, e.g. – molecule, has constant dipole momentum $\vec{p} = e\vec{d}$, where $V = eE(x + d_x)$, \vec{E} applied along x , reads as the conventional expansion by small parameter ϵ , $\epsilon = eE$:

$$\phi = \phi_0 + \epsilon\phi^{(1)} + \dots \quad (32)$$

In the first order it gives the following expression for an eigen function perturbation, evaluated as sum by $m \neq n$

$$\phi_p^{(1)} = \sum_m \frac{x_{mp} + (d_x)_{mp}}{E_m - E_p} \phi_{0m}, \quad (33)$$

where x_{mn} are matrix elements of the Cartesian coordinate x and $(d_x)_{mn}$ are proportional to the matrix elements projection of the constant dipole momentum \vec{p}/e in non-perturbed states, between the eigenfunctions ϕ_{0m} of the Fockian H_F . Note, that a stability of similar perturbations is studied in [26].

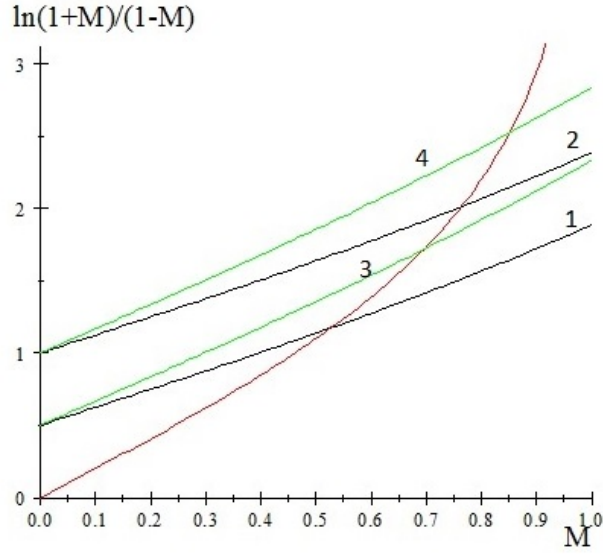


FIG. 9. The superposed layers contribution to magnetization of a nanoparticle model. The points of intersections of the inverse tanh function (red line) and $\omega_{a,b}$ black lines – 1, 2 for surface and green – 3, 4 for bulk are shown for $\alpha = 0.5, 1.0$. For $\alpha = 0.5$, the curves 1,3. The sum of magnetization contributions of the same order is quite visible with both values of α with the natural bulk prevails

4.2. Exchange integrals perturbation

Plugging (32) into exchange integrals J_{ik} , defined for the electrons coupled to the centers i, k , by the expression:

$$J_{ik} = \frac{e^2}{2} \iint \frac{\rho_{ik}(\vec{r}, \vec{r}')}{|\vec{r} - \vec{r}'|} d\vec{r} d\vec{r}', \quad (34)$$

where, in a spirit of the Fock paper [27], it may include all interacting electrons of the closest neighbors, as equal ones, hence indices omitted, reproducing [3]:

$$\begin{aligned} \rho(\vec{r}, \vec{r}') &= \sum_p \phi_p^*(\vec{r}) \phi_p(\vec{r}') = \sum_p \left(\phi_{0p}^*(\vec{r}) + \epsilon \phi_p^{(1)*}(\vec{r}) \right) \left(\phi_{0p}(\vec{r}') + \epsilon \phi_p^{(1)}(\vec{r}') \right) = \\ &= \sum_p \phi_{0p}^*(\vec{r}) \phi_{0p}(\vec{r}') + \epsilon \sum_p \left[\phi_p^{(1)*}(\vec{r}) \phi_{0p}(\vec{r}') + \phi_{0p}^*(\vec{r}) \phi_p^{(1)}(\vec{r}') \right] + o(\epsilon^2) = \rho_0(\vec{r}, \vec{r}') + \epsilon \rho_1(\vec{r}, \vec{r}') + \dots \end{aligned} \quad (35)$$

The electric field perturbs the exchange integral as it is prescribed by (35) with:

$$J_0 = \frac{e^2}{2} \iint \frac{\rho_0(\vec{r}, \vec{r}')}{|\vec{r} - \vec{r}'|} d\vec{r} d\vec{r}', \quad (36)$$

$$J_1 = \frac{e^2}{2} \iint \frac{\rho_1(\vec{r}, \vec{r}')}{|\vec{r} - \vec{r}'|} d\vec{r} d\vec{r}', \quad (37)$$

whence:

$$\beta = \frac{z(J_0 + \epsilon J_1)}{kT} = \beta_0 + \epsilon \beta_1. \quad (38)$$

More details for J_1 gives:

$$J_1 = \frac{e^2}{2} \sum_{p,m} \frac{(x_{mp} + (d_x)_{mp}) J_{mp}^0}{E_m - E_p}, \quad (39)$$

with the notation for $J_{pm}^0 = \int \frac{\phi_{0m}^*(\vec{r}) \phi_{0p}(\vec{r}')}{|\vec{r} - \vec{r}'|} d\vec{r} d\vec{r}'$.

The matrix elements J_{pm}^0 are evaluated between the unperturbed Fockian eigenfunction, that yields (39). In the phenomenologic theory we consider J_0 and J_1 as parameters.

5. Magneto-electric effect

5.1. Material equation of state

First-principles methods to study magnetoelectric phenomena are reviewed as follows. Plugging (38) into (4) yields:

$$\frac{Z}{F} = \left[2 \cosh \left(\frac{\alpha + \beta_0 M - \beta_0^2 \frac{M}{z} + \beta_0^2 \frac{M^3}{2z} + \epsilon \beta_1 M \left(1 - \frac{2}{z} \beta_0 + \frac{M^2}{2z} \beta_0\right) + \epsilon^2 \beta_1^2 \left(\frac{M^3}{2z} - \frac{M}{z}\right)}{2} \right) \right]^{2n}, \quad (40)$$

being the base for the partition function expression with the electric field account.

The mean (most probable) value of the magnetization per electron is defined by the Heisenberg relation (7):

$$M(\alpha, \epsilon) = \tanh \frac{\alpha + \left(1 - \frac{\beta(\epsilon)}{z}\right) \beta(\epsilon) M + \beta(\epsilon)^2 \frac{M^3}{2z}}{2}, \quad (41)$$

that now includes not only magnetic field H as the parameter, but also the electric field E via ϵ . It constitutes the magnetic material relation in implicit form.

Let us illustrate the solution of the transcendent equation (41) by the Fig. 10. It shows that there is a minimal value of ϵ for a solution existence.

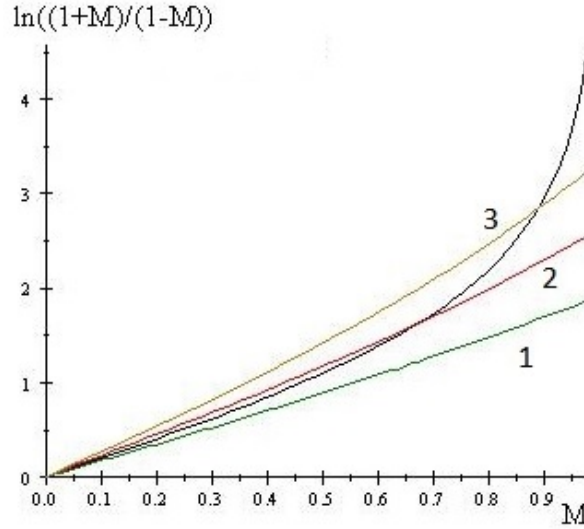


FIG. 10. The points of intersections of the inverse tanh function (black line) and $\omega(M)$, green line – 1 for $\epsilon = 0.1$, the red one – 2 for $\epsilon = 1$ and the sienna – 3 for $\epsilon = 2$ are shown for $\alpha = 0$. The case of $\epsilon = 0.1$ is out of a solution range

The derivative of $\ln Z$ by ϵ gives the polarization on electron as:

$$P = \frac{p_0}{n} = e \frac{\partial \ln Z}{n \partial \epsilon} = e \frac{\partial \omega}{\partial \epsilon} \tanh \frac{\omega}{2}, \quad \frac{\partial \omega}{\partial \epsilon} = \beta_1 M - 2\beta \frac{\beta_1}{z} M + 2\beta \beta_1 \frac{M^3}{2z} + \beta \left[\left(1 - \frac{\beta}{z}\right) + \frac{3M^2}{2z} \beta \right] \frac{\partial M}{\partial \epsilon}, \quad (42)$$

or, in alternative form,

$$P = e \left(\beta_1 M \left(1 - \frac{2}{z} \beta_0 + \frac{M^2}{2z} \beta_0\right) + 2\epsilon \beta_1^2 \frac{M}{z} \left(\frac{1}{2} M^2 - 1\right) \right) \tanh \left(\frac{\alpha + \beta_0 M - \beta_0^2 \frac{M}{z} + \beta_0^2 \frac{M^3}{2z} + A}{2} \right) + e \frac{\partial \ln Z}{n \partial M} \frac{\partial M}{\partial \epsilon}, \quad (43)$$

where

$$A = \left(\frac{1}{2} \frac{M^3}{z} \beta_1^2 - \frac{M}{z} \beta_1^2 \right) \epsilon^2 + \left(M \beta_1 + \frac{M^3}{z} \beta_0 \beta_1 - 2 \frac{M}{z} \beta_0 \beta_1 \right) \epsilon. \quad (44)$$

The second term in (42), $\frac{\partial M}{\partial \epsilon}$ should be evaluated along the solution of (41) path. The condition of a solution existence repeats the inequality (8) but now it should be solved with respect to ϵ , or for the boundary,

$$-\frac{1}{z} (\beta_0 + \epsilon \beta_1) (\beta_0 - z + \epsilon \beta_1) = \beta_0 - \frac{1}{z} \beta_0^2 + \epsilon \beta_1 - \frac{1}{z} \epsilon^2 \beta_1^2 - \frac{2}{z} \epsilon \beta_0 \beta_1 = 2.$$

The range of interest lies between the roots of this equations:

$$-\frac{1}{2\beta_1} \left(-z + 2\beta_0 + z\sqrt{\frac{1}{z}(z-8)} \right), \quad \frac{1}{2\beta_1} \left(z - 2\beta_0 + z\sqrt{\frac{1}{z}(z-8)} \right),$$

for $z = 12$ it gives $\frac{1}{2\beta_1} (4\sqrt{3} - 2\beta_0 + 12)$, $-\frac{1}{2\beta_1} (2\beta_0 + 4\sqrt{3} - 12)$.

To evaluate the derivative $\frac{\partial M}{\partial \epsilon}$, we use the approximate expansion of the both sides of (41), as is demonstrated by the plot Fig. 11. Algebraically it appears as:

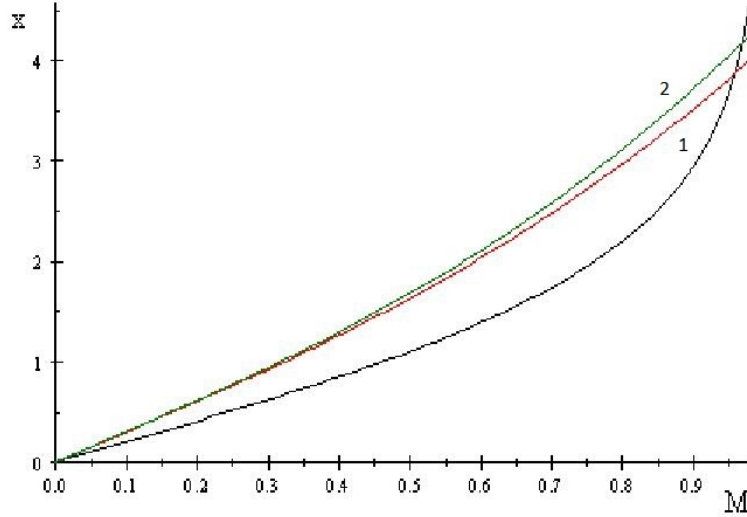


FIG. 11. The small variation of a solution of (41) by the change of β , for $z = 12$, $\beta_0 = 5.3$, red – 1, $\epsilon\beta_1 = 0.3$, $\beta = 5.6$ – green – 2

for the r.h.s. $\alpha + (\beta + x)(M + y) - (\beta + x)^2 \frac{M + y}{z} + (\beta + x)^2 \frac{(M + y)^3}{2z}$ and for the left one,

$$\ln \frac{1 + (M + y)}{1 - (M + y)} = \ln \left(-\frac{1}{M - 1} (M + 1) \right) - y \left(\frac{1}{(M - 1)^2} (M + 1) - \frac{1}{M - 1} \right) \frac{M - 1}{M + 1} + O(y^2).$$

The linear in y term is equal to:

$$\frac{1}{2} y \frac{4z - 5M^2\beta^2 + 3M^4\beta^2 - 2z\beta + 2\beta^2 + 2M^2z\beta}{z(M - 1)(M + 1)},$$

It contains the factor $4z - 5M^2\beta^2 + 3M^4\beta^2 - 2z\beta + 2\beta^2 + 2M^2z\beta$, that can be zero when:

$$M_r^2 = \pm \frac{1}{6\beta} \left(5\beta + \sqrt{\beta^2 + 48\beta - 24} \right). \quad (45)$$

In such points a solution of the equation for y does not exist. Hence, far enough of these points, equalizing the linear in x, y parts with $\alpha = 0$, we arrive at:

$$\frac{\partial M}{\partial \epsilon} \approx \frac{y}{x} = \frac{2M(z - 2\beta + M^2\beta)(M - 1)(M + 1)}{4z - 5M^2\beta^2 + 3M^4\beta^2 - 2z\beta + 2\beta^2 + 2M^2z\beta}. \quad (46)$$

Plugging it into (43) yields:

$$\frac{\partial \omega}{\partial \epsilon} = \beta_1 M - 2\beta \frac{\beta_1}{z} M + 2\beta \beta_1 \frac{M^3}{2z} + \beta \left[\left(1 - \frac{\beta}{z} \right) + \frac{3M^2}{2z} \beta \right] \frac{2M(z - 2\beta + M^2\beta)(M - 1)(M + 1)}{4z - 5M^2\beta^2 + 3M^4\beta^2 - 2z\beta + 2\beta^2 + 2M^2z\beta}. \quad (47)$$

That gives explicit form for the polarization $P(E)$ as function of electric field, see the Fig. 12.

If to write the material relations in approximation of Taylor expansion of both P, M in $\alpha\epsilon$ plane up to the first order, we arrive at:

$$P = P_0 + \epsilon P_1 + \alpha P^1, \quad M = M_0 + \alpha M_1 + \epsilon M^1, \quad (48)$$

where:

$$P_0 = e \frac{\partial \omega}{\partial \epsilon} \tanh \frac{\omega}{2} \Big|_{\epsilon, \alpha=0} = e \left(\beta_1 M - 2\beta_0 \frac{\beta_1}{z} M + 2\beta_0 \beta_1 \frac{M^3}{2z} + \beta_0 \left[\left(1 - \frac{\beta_0}{z}\right) + \frac{3M^2}{2z} \beta_0 \right] \frac{\partial M}{\partial \epsilon} \Big|_{\epsilon=0} \right) \mathcal{T},$$

$$P_1 = \frac{\partial P}{\partial \epsilon} \Big|_{\alpha, \epsilon=0} = e \left[\frac{\partial^2 \omega}{\partial \epsilon^2} \tanh \frac{\omega}{2} + \left(\frac{\partial \omega}{\partial \epsilon} \right)^2 \frac{1}{2} (1 - \mathcal{T}^2) \right] \Big|_{\epsilon=0}, \quad P^1 = \frac{\partial P}{\partial \alpha} \Big|_{\alpha, \epsilon=0} = \frac{e}{2} \frac{\partial \omega}{\partial \epsilon} (1 - \mathcal{T}^2), \quad (49)$$

$$M_0 = \mathcal{T}, \quad M_1 = \frac{1}{2} (1 - \mathcal{T}^2), \quad M^1 = \frac{\partial M}{\partial \epsilon} \Big|_{\alpha, \epsilon=0},$$

with $\mathcal{T} = \tanh \frac{\beta_0 M}{4z} (M^2 \beta_0 - 2\beta_0 + 2z)$. $u = -\frac{1}{2} M^2 \beta_1^2 \frac{(z - 2\beta_0 + M^2 \beta_0)^2}{z^2}$, $v = -\frac{M}{z} \beta_1^2 (2 - M^2)$, that demonstrates magneto-electric effects as in [28].

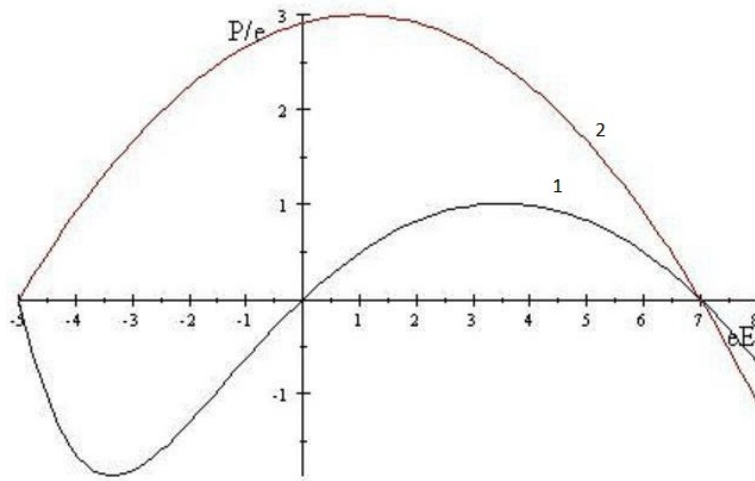


FIG. 12. The dependence the polarization P on field E – curve 1. The range of a solution of (41) existence lies between the red parabola (curve 2) roots, for $z = 12$, $\beta_0 = 5$, $\beta_1 = 1$

As we see, the argument of the hyperbolic tangent function in the r.h.s. of (42), contains the quadratic polynomial in the electric field ϵ . We observe the nonlinear dependence of $P(\epsilon)$. The key cross-terms of the polarization P^1 and magnetization M^1 material equations expansion coefficients in (49) are shown at the Fig. 13 as function of the background magnetization.

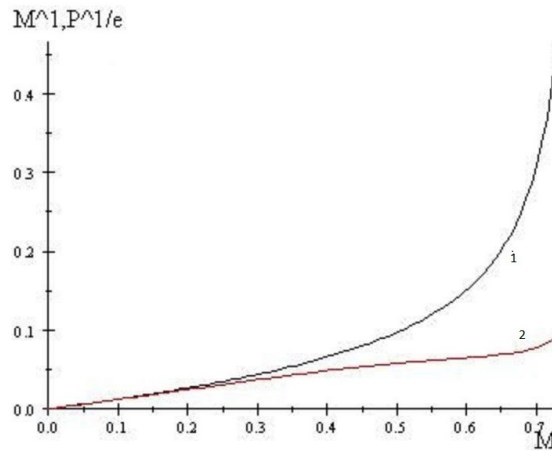


FIG. 13. The $M^1(M)$ – black – 1 and $P^1(M)$ – red – 2 are plotted within the range restricted by (45)

5.2. Magnetoelectric phenomena for nanoparticles

The consideration of magnetoelectric effects may be done along the lines of the Sec. 3.3. We base on the equation (25) while the functions (56) contain the parameters, $\beta_{a,b}$, “splitted” by the electric field action as, for example $\beta_a = \beta_a^0 + \epsilon\beta_a^1$ in direct analogy with (38). So, the basic equations for magnetization and polarization are

$$M^{a+b} = \frac{\partial \ln(Z_a)}{\partial \alpha} + \frac{\partial \ln(Z_b)}{\partial \alpha} = \quad (50)$$

$$\frac{\partial \ln([2 \cosh \frac{\omega_a^e}{2}]^{2n_a})}{\partial \alpha} + \frac{\partial \ln([2 \cosh \frac{\omega_b^e}{2}]^{2n_b})}{\partial \alpha} = \quad (51)$$

$$\frac{n_a}{n} \tanh \frac{\omega_a^e}{2} + \frac{n_b}{n} \tanh \frac{\omega_b^e}{2}, \quad (52)$$

and, for the polarization:

$$P^{a+b} = e \frac{\partial \ln(Z_a)}{\partial \epsilon} + e \frac{\partial \ln(Z_b)}{\partial \epsilon} = \quad (53)$$

$$e \frac{\partial \ln([2 \cosh \frac{\omega_a^e}{2}]^{2n_a})}{\partial \epsilon} + e \frac{\partial \ln([2 \cosh \frac{\omega_b^e}{2}]^{2n_b})}{\partial \epsilon} = \quad (54)$$

$$e \frac{n_a}{n} \frac{\partial \omega_a^e}{\partial \epsilon} \tanh \frac{\omega_a^e}{2} + e \frac{n_b}{n} \frac{\partial \omega_b^e}{\partial \epsilon} \tanh \frac{\omega_b^e}{2}. \quad (55)$$

where, plugging $\beta_a = \beta_a^0 + \epsilon\beta_a^1$, we write:

$$\omega_a^e = \alpha + (\beta_a^0 + \epsilon\beta_a^1)M_a \left(1 - \beta_a \frac{(1 - \frac{M_a^2}{2})}{z_a}\right), \quad (56)$$

and, quite similar for ω_b^e .

Let us plot the scheme of the equations (50) solution, again for the case, as for the Nickel, for magnetic properties see [29]. Taking the same values for the bulk contribution as at Fig. 14, and for the surface as in the Table 1:

TABLE 1. Nanoparticle parameters

Atom place	β^0	β^1	z
surface(a)	1.53	1	8
bulk(b)	2	1	12

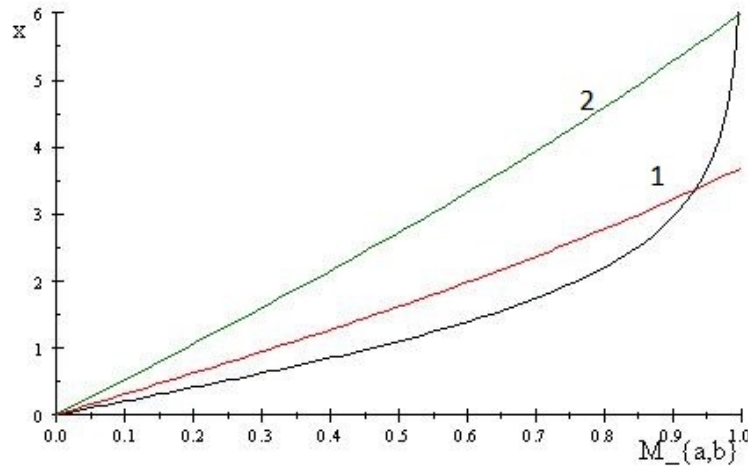


FIG. 14. The superposed layers contribution to magnetisation of a nanoparticle in the field with $\epsilon = 1$. The points of intersections of the inverse tanh function (black line) $x = \ln \frac{1+M}{1-M}$ and $\omega_{a,b}$ red – 1 line for surface and green – 2 for bulk are shown for $\alpha = 0$. The sum of magnetization contributions of the same order is quite visible with both values of β_a, z_a and β_b, z_b with the natural bulk prevails

6. Conclusion

We do understand, that the theory has model restrictions that are discussed in the Heisenberg papers, that do not allow literal application of the model, for example to Fe-based magnetics.

However, the use of a generalized Heisenberg theory allows one to classify matters in respect to matter relations and existence of ferro- properties of nanoparticles at least for the number of closest neighbors $z > 8$. It also allows one to construct the hysteresis curves for given values of the structure and electron states parameters. Modifications for nanotubes naturally introduce the closest neighbors exchange integrals defined by the nano-object symmetry and position of them in bulk or surface of it. This gives a model thermodynamic description on the basis of the Heisenberg model of the partition function, which allows natural modifications.

Acknowledgements

The author acknowledges discussions with V. Rodionova.

References

- [1] Heisenberg W. Zur Theorie des Ferromagnetismus. *Zs. Phys.*, 1928, **49**, P. 619–636. Zur Quantentheorie des Ferromagnetismus. *Probleme der Modernen Physik*, A. Sommerfeld Festschrift, Leipzig, 1928, P. 114–122.
- [2] Vázquez M. *Magnetic Nano- and Microwires: Design, Synthesis, Properties and Applications*. Woodhead Publishing Series in Electronic and Optical Materials. Elsevier Science, 2015, 314 p.
- [3] Leble S. Heisenberg chain equations in terms of Fockian covariance with electric field account and multiferroics in nanoscale. *Nanosystems: Physics, Chemistry, Mathematics*, 2019, **10**(1), P. 18–30.
- [4] Heitler W. Störungsenergie und Austausch beim Mehrkörperproblem. *Zs. Phys.* 1927, **46**, P. 47. Zur Gruppentheorie der homöopolaren chemischen Bindung, 1928, 835 p.
- [5] Inglis D.R. The Heisenberg Theory of Ferromagnetism. *Phys. Rev.*, 1932, **42**, P. 442.
- [6] Bitter F. On the Interpretation of Some Ferromagnetic Phenomena, *Phys. Rev.*, 1932, **39**, P. 337–345.
- [7] Tyler F. The magnetization-temperature curves of iron, cobalt and nickel. *Phil. Mag.*, 1931, **11**, P. 596.
- [8] Coey J.M.D. *Magnetism and magnetic materials*. Cambridge University Press, Cambridge, 2009.
- [9] Aharoni A. Introduction to the Theory of Ferromagnetism, Clarendon Press, Oxford, 1996, 192 p.
- [10] Nakano F. The Heisenberg Theory of Ferromagnetism of the Crystal constituted by the Atoms with Spin One. *Progress of Theoretical Physics*, 1953, **9**(4), P. 403–413.
- [11] Heisenberg W. Zur Theorie des Magnetpstriktin und der Magnetisierungskurve. *Zs. Phys.*, 1931, **69**, P. 287–297.
- [12] Singh N. The story of magnetism: from Heisenberg, Slater, and Stoner to Van Vleck, and the issues of exchange and correlation. arXiv:1807.11291 [cond-mat.str-el], 2018.
- [13] Borovik E.S., Eremenko V.V., Milner A.S. Lectures on magnetism. 3-rd ed. Revised. and add. M.: Fizmatlit, 2005. (In Russian)
- [14] Lakshmanan M. The fascinating world of the Landau–Lifshitz–Gilbert equation: an overview. *Phil. Trans. R. Soc. A*, 2011, **369**, P. 1280–1300.
- [15] Schollwöck U., Richter J., Farnell D.J.J., Bishop R.F. *Quantum Magnetism*, Lecture Notes in Physics, **645**, Springer-Verlag, Berlin, 2004, 381 p.
- [16] Martínez-García J.C., Rivas M., Lago-Cachón D., García J.A. First-order reversal curves analysis in nanocrystalline ribbons. *J. Phys. D: Appl. Phys.*, 2014, **47**, P. 015001.
- [17] Martínez-García J.C., Rivas M., García J.A. Induced ferro-ferromagnetic exchange bias in nanocrystalline systems. *Journal of Magnetism and Magnetic Materials*, 2015, **377**, P. 424.
- [18] Klaus D. Sattler-Ed. Handbook of Nanophysics: *Nanoparticles and Quantum Dots*, CRC press, 2011.
- [19] Gaikwad A.S., More S.S., et al. *Int. Res. J. of Science and Engineering*, 2018, **A5**, P. 41–44.
- [20] Valasek J. Piezo-electric and allied phenomena in Rochelle salt. *Phys. Rev.*, 1921, **17**, P. 475–481.
- [21] Spaldin, Nicola A., Fiebig, Manfred. The renaissance of magnetoelectric multiferroics. *Science*, 2005, **309**(5733), P. 391–392.
- [22] Birola T., Benedek N.A., et al. The magnetoelectric effect in transition metal oxides: Insights and the rational design of new materials from first principles Current Opinion. *Solid State and Materials Science*, 2012, **16**(5), P. 227–242.
- [23] Reichl L.E. *A Modern Course in Statistical Physics*, 2-nd Edition. A Wiley-interscience publication, John Wiley and Sons, inc., New York, Chichester, Weinheim, Brisbane, Singapore, Toronto, 1998, 822 p.
- [24] Heisenberg W. Zur Quantentheorie des Ferromagnetismus. *Probleme der Modernen Physik*, A. Sommerfeld Festschrift, Leipzig, 1928, P. 114–122.
- [25] Jössang P., Jössang A.C., Pouillet S.M. member of the French Academy of Sciences, discovered the “Curie” point in ... 1832. *Science Tribune*, January 1997, URL: <http://www.tribunes.com/tribune/art97/jos2e.htm>.
- [26] Popov I.Yu. Hydrodynamic stability and perturbation of the Schrodinger operator. *Lett. Math. Phys.*, 1995, **35**(2), P. 155–161.
- [27] Fock V. An Approximate Method for Solving the Quantum Many-Body Problem. *Zs. Phys.*, 1930, **61**, P. 126–148; TOI 1931, **5**, 51, 1; UFN 1967, **93**, 2, 342.
- [28] Dzyaloshinskii I.E. On the magneto-electrical effect in antiferromagnets. *J. Exp. Theor. Phys.*, 1959, **37**, P. 881–882.
- [29] Nasirpour F., Barzegar S., et al. Mesophase micelle-assisted electrodeposition and magnetisation behavior of meso-porous nickel films for efficient electrochemical energy and magnetic device applications. *Applied Surface Science*, 2019, **471**, P. 776–785.

Fully self-consistent calculations of magnetic structure within non-collinear Alexander–Anderson model

A. V. Ivanov^{1,2}, P. F. Bessarab^{2,3}, H. Jónsson^{2,4}, V. M. Uzdin³

¹Saint Petersburg State University, 199034, Saint Petersburg, Russia

²Science Institute and Faculty of Physical Sciences, U. of Iceland, 107 Reykjavík, Iceland

³ITMO University, 197101 Saint Petersburg, Russia

⁴Department of Applied Physics, Aalto University, FI-00076 Espoo, Finland

ali5@hi.is

PACS 05.20.Dd,75.10.-b

DOI 10.17586/2220-8054-2020-11-1-65-77

An implementation of the non-collinear Alexander–Anderson model for itinerant electrons in magnetic systems is presented where self-consistency is reached for specified directions of the magnetic moments. This is achieved by means of Lagrange multipliers and a variational principle for determining the transverse and longitudinal components of the magnetic moments as well as the average number of *d*-electrons using direct optimisation. Various optimisation algorithms are compared and the limited memory Broyden–Fletcher–Goldfarb–Shanno algorithm is found to give the best performance. An application to antiferromagnetic Cr crystal is presented where spin-dynamics and curvature of the energy surface are calculated to compare results obtained with and without the constraints on the orientation of the magnetic moments.

Keywords: itinerant magnetism, Alexander–Anderson model, non-stationary configurations, constraints.

Received: 10 February 2020

1. Introduction

A model for the description of a magnetic impurity in a non-magnetic metal was presented by Anderson [1] and later extended to describe the interaction between two magnetic atoms by Alexander and Anderson [2]. A multi-impurity extension of this model, allowing for arbitrary orientation of the spins and referred to as non-collinear Alexander–Anderson (NCAA) model [3–5] has been developed and used in studies of various systems of first row transition metals, for example spin-density waves [6, 7], magnetic nano-islands [8], and tip/surface interactions [9]. The calculations involve iterative self-consistency evaluations of the number of *d*-electrons and the magnetic moments.

An adiabatic separation of slow and fast degrees of freedom is assumed in NCAA calculations: the angles defining the orientation of the magnetic moments are treated as slow degrees of freedom, while the longitudinal components of the magnetic moments are treated as fast degrees of freedom [10–12]. This means that for a given set of angles, the length of the magnetic moments is found in a self-consistent manner. This adiabatic approximation is typically also used in density functional theory (DFT) [13] and tight binding calculations [14] of magnetic systems. It is analogous to the Born–Oppenheimer approximation in electronic structure calculations, where the electronic wave function is calculated for a fixed position of the nuclei. When stationary states are found, such as local minima corresponding to (meta)stable states or first order saddle points corresponding to transition states of magnetic transitions, some optimization algorithm is used to find orientations where the gradient of energy vanishes with respect to angles. Full self-consistency is then reached at the stationary points. However, when calculations of dynamics are carried out or the energy surface characterising the system explored in regions of non-stationary points, then the self-consistency calculation should be formulated in such a way as to keep the desired values of the angular variables fixed. This has, for example been emphasised in the context of the evaluation of exchange parameters [15].

Several methods for finding self-consistent solutions of non-stable magnetic states using tight-binding Hamiltonians or DFT have been presented [16–18]. These methods are based on the introduction of local magnetic fields to force the local magnetic moments to be pointing in the desired directions. Dederichs *et al.* [16] developed a general formalism for such constrained self-consistency calculations based on Lagrange multipliers. Various implementations of this general approach have been used [19–23] involving different algorithms for finding the optimal values of the Lagrange multipliers. A rigorous formulation based on a variational principle for such self-consistency calculations has been presented in the context of constrained DFT, primarily in the context of excited state electronic structure calculations [24–26]. A formulation in terms of a variational principle has the advantage that efficient and systematic optimisation methods can be employed to enforce the constraints and the optimisation can be carried out with respect to all degrees of freedom on an equal footing.

In this article, an implementation of the NCAA model is presented where constraints on the directions of the magnetic moments are included in the self-consistency calculations by use of a variational principle and the performance of various direct optimization algorithms tested. The article is organised as follows: In section 2, the NCAA model is reviewed and the inclusion of angular constraints presented. Numerical tests are presented in section 3 and the performance of the limited memory Broyden–Fletcher–Goldfarb–Shanno (L-BFGS) [27], conjugate gradient and fixed point mixing methods compared. Section 4 presents applications of the method to calculations of spin dynamics and curvature of the energy surface for Cr crystal.

2. Methodology

2.1. NCAA model

The NCAA model is based on the separation of electrons into conduction 4s(p)-electrons and quasi-localised 3d-electrons. The basic Hamiltonian is [2]:

$$\hat{H} = \sum_{i\alpha} \epsilon_i^0 \hat{n}_{i\alpha} + \sum_{i \neq j, \alpha} v_{ij} \hat{d}_{i\alpha}^\dagger \hat{d}_{j\alpha} + \frac{1}{2} \sum_{i, \alpha \neq \beta} U_i \hat{n}_{i\alpha} \hat{n}_{i\beta} + \sum_{\mathbf{k}\alpha} \epsilon_{\mathbf{k}} \hat{n}_{\mathbf{k}\alpha} + \sum_{\mathbf{k}, i, \alpha} \left(v_{i\mathbf{k}} \hat{d}_{i\alpha}^\dagger \hat{c}_{\mathbf{k}\alpha} + v_{\mathbf{k}i} \hat{c}_{\mathbf{k}\alpha}^\dagger \hat{d}_{i\alpha} \right), \quad (1)$$

where: $\hat{d}_{i\alpha}$, $\hat{d}_{i\alpha}^\dagger$ are annihilation and creation operators for d -electrons with spin α on i -th site, respectively, $\hat{c}_{\mathbf{k}\alpha}$, $\hat{c}_{\mathbf{k}\alpha}^\dagger$ are annihilation and creation operators of $s(p)$ -electrons with spin α and momentum \mathbf{k} , respectively, $\hat{n}_{i\alpha} = \hat{d}_{i\alpha}^\dagger \hat{d}_{i\alpha}$ and $\hat{n}_{\mathbf{k}\alpha} = \hat{c}_{\mathbf{k}\alpha}^\dagger \hat{c}_{\mathbf{k}\alpha}$ are number operators, ϵ_i^0 energy level of quasi-localised d -electrons at site i , $\epsilon_{\mathbf{k}}$ energy of $s(p)$ states with momentum \mathbf{k} , v_{ij} are hopping parameters for d -electrons on sites i and j , $v_{i\mathbf{k}}$ are parameters corresponding to hybridisation of d - and $s(p)$ electrons, U_i Coulomb repulsion between quasi-localised electrons on site i . The first three terms describe the subsystem of quasi-localised electrons. A Hamiltonian consisting only of these three terms is referred to as the single-band Hubbard model [28]. The fourth term in Eq. (1) describes the conduction band, and the last term describes coupling between electrons in quasi-localised states and electrons in the conduction band.

Many magnetic systems can be modelled accurately enough within the mean field approximation. The mean field approximation of Coulomb interaction is applied to each site in the local coordinate frame chosen in such a way that the z -axis points in the same direction as the expectation value of the magnetic moment operator [3]. The procedure is illustrated in Fig. 1. Within this approximation, the Coulomb interaction is approximated according to following equation in the laboratory coordinate frame:

$$U_i \hat{n}_{i\alpha} \hat{n}_{i\beta} \rightarrow \frac{U_i N_i}{2} (\hat{n}_{i\alpha} + \hat{n}_{i\beta}) - \frac{U_i M_i}{2} \hat{\mathbf{M}}_i \cdot \mathbf{e}_i - \frac{1}{4} U_i (N_i^2 - M_i^2), \quad (2)$$

where N_i is the average number of d -electrons at site i , M_i the magnitude of the magnetic moment of spins at site i , and $\mathbf{e}_i = (\sin \theta_i \cos \phi_i, \cos \theta_i \sin \phi_i, \cos \theta_i)$ the unit vector defining the direction of the magnetic moment at site i . The magnetic moment operator is:

$$\hat{\mathbf{M}}_i = \left(\hat{M}_{ix}, \hat{M}_{iy}, \hat{M}_{iz} \right)^T, \quad (3)$$

$$\hat{M}_{iq} = \sum_{\alpha\beta} \hat{d}_{i\alpha}^\dagger \sigma_{\alpha\beta}^q \hat{d}_{i\beta}, \quad q = x, y, z \quad (4)$$

where σ^q denotes the Pauli matrices.

In order to describe magnetic properties of itinerant magnets, the $s(p)$ -electrons are taken into account through the renormalisation of the parameters in the Hamiltonian and hybridisation of the d -level [1]. The effective Hamiltonian for non-collinear magnetism can be written as [5]:

$$\hat{H}^{NCAA} = \sum_{i\alpha} \left(E_i^0 + \frac{U_i N_i}{2} + i\Gamma \right) \hat{n}_{i\alpha} + \sum_i -\frac{U_i M_i}{2} \hat{\mathbf{M}}_i \cdot \mathbf{e}_i + \sum_i -\frac{1}{4} U_i (N_i^2 - M_i^2) + \sum_{i \neq j, \alpha} v_{ij} \hat{d}_{i\alpha}^\dagger \hat{d}_{j\alpha}, \quad (5)$$

where:

$$E_i^0 = \epsilon_i^0 + \text{Re} \sum_{\mathbf{k}} \frac{v_{i\mathbf{k}} v_{\mathbf{k}i}}{\omega - \epsilon_{\mathbf{k}}}, \quad (6)$$

$$\Gamma = \text{Im} \sum_{\mathbf{k}} \frac{v_{i\mathbf{k}} v_{\mathbf{k}i}}{\omega - \epsilon_{\mathbf{k}}}, \quad (7)$$

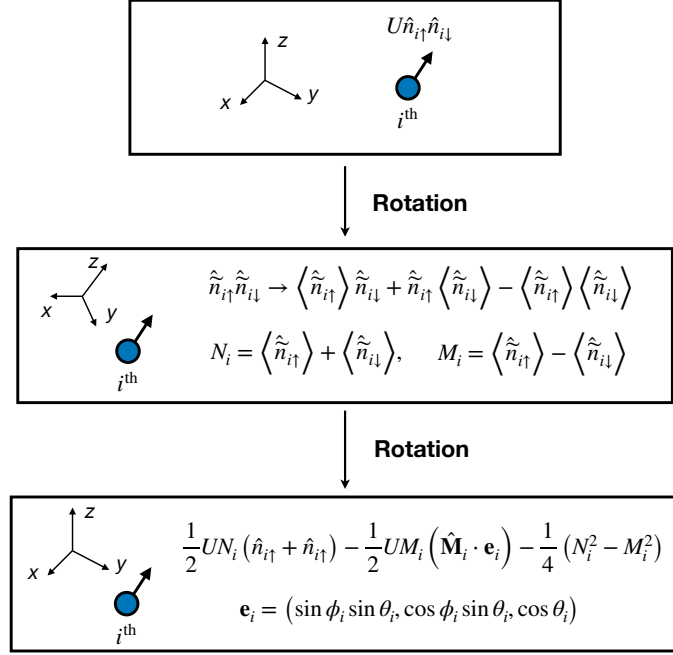


FIG. 1. Illustration of the implementation of the mean field approximation for non-collinear magnetism. Atoms i is denoted by the blue disk and the arrow indicates its average magnetic moment. First, the laboratory coordinate frame is rotated into the local coordinate frame so that the z axis points along the magnetic moment of the atom. Then, the mean field approximation for $\hat{n}_{i\alpha}\hat{n}_{i\beta}$ is applied in this local coordinate frame, and the number of d-electrons N_i and magnetic moment M_i evaluated. Then, the local coordinate frame is rotated back into the laboratory coordinate frame. This two step procedure is applied to all atoms in the system.

$$V_{ij} = v_{ij} + \sum_{\mathbf{k}} \frac{v_{i\mathbf{k}}v_{\mathbf{k}j}}{\omega - \epsilon_{\mathbf{k}}}. \quad (8)$$

This Hamiltonian is reminiscent of the Hubbard model with renormalised parameters ϵ_i^0 and v_{ij} within a mean field approximation, generalised for non-collinear alignment of the magnetic moments. For a more detailed discussion of the NCAA Hamiltonian, see Ref. [4, 5].

In order to calculate the expectation values of operators, the Green function formalism is used. As the NCAA model in the mean field approximation is quadratic with respect to fermion operators, the Green function is a resolvent of the NCAA Hamiltonian:

$$(\omega - \hat{H}^{NCAA}) \hat{G} = I. \quad (9)$$

In previous implementations, the Green function was calculated iteratively using the continued fraction approach [5]. However, we find that for small enough systems a direct solution in terms of eigenvalue decomposition of the NCAA Hamiltonian is a more efficient way to calculate the Green function. After the eigenvalues and eigenvectors has been found, the expectation values of interest can be calculated as shown in Appendix A.

The unit vectors $\{\mathbf{e}_i\}$ in the NCAA Hamiltonian should by definition point in the same direction as the magnetic moment operators. However, this will in general not be the case at a non-stationary point because there will, by definition, be a non-zero torque acting on the magnetic moments

$$\mathbf{T}_i^{NCAA} = -\mathbf{M}_i \times \mathbf{H}_i^{\text{eff}} = \mathbf{e}_i \times \frac{\partial E^{NCAA}}{\partial \mathbf{e}_i} = \frac{U_i}{2} \mathbf{M}_i \times \langle \hat{\mathbf{M}}_i \rangle. \quad (10)$$

Therefore, $\mathbf{M}_i \nparallel \langle \hat{\mathbf{M}}_i \rangle$, where $\mathbf{M}_i = M_i \mathbf{e}_i$. In order to enforce the expectation value of a magnetic moment to be aligned along the direction \mathbf{e}_i , the following constraint needs to be added: A projection of the expectation value of the

magnetic moment on the tangent space to the direction \mathbf{e}_i equals to zero, i.e.:

$$\langle \hat{\mathbf{M}}_i \rangle \cdot \mathbf{e}_{\theta_i} = 0 \quad (11)$$

$$\langle \hat{\mathbf{M}}_i \rangle \cdot \mathbf{e}_{\phi_i} = 0. \quad (12)$$

Here, $\mathbf{e}_{\phi_i} = (-\sin \phi_i, \cos \phi_i, 0)^T$, $\mathbf{e}_{\theta_i} = (\cos \theta_i \cos \phi_i, \cos \theta_i \sin \phi_i, -\sin \theta_i)^T$ are the local orthogonal unit vectors in the tangent space of \mathbf{e}_i . These constraints can be written formally in various forms, for example: $[\langle \hat{\mathbf{M}}_i \rangle, \mathbf{e}_i] = 0$ [19] or: $\langle \hat{\mathbf{M}}_i \rangle - (\langle \hat{\mathbf{M}}_i \rangle \cdot \mathbf{e}_i) \mathbf{e}_i = 0$ [20]. In either case, the constraint ensures that the projection of the magnetic moment on the local tangent space equals zero. We will proceed with Eqs. (11) and (12). The algorithm described in the following sections can be generalised to other formulations of the constraints in a straight-forward way.

The constraints can be satisfied by means of Lagrange multipliers [16]:

$$\begin{aligned} \hat{H} &= \hat{H}^{NCAA} - \sum_{i=1..P} \lambda_1^i \hat{\mathbf{M}}_i \cdot \mathbf{e}_{\theta_i} - \sum_{i=1..P} \lambda_2^i \hat{\mathbf{M}}_i \cdot \mathbf{e}_{\phi_i} = \\ &= \hat{H}^{NCAA} - \sum_{i=1..P} \tilde{\mathbf{M}}_i \cdot \mathbf{h}_i^c, \end{aligned} \quad (13)$$

The last term describes the interaction of a magnetic moment with a local magnetic field acting perpendicular to the magnetic moment. As a result, a revised torque acting on the magnetic moment in such a way as to satisfy the constraints is:

$$\mathbf{T}_i = -\mathbf{M}_i \times \mathbf{H}_i^{\text{eff}} = \mathbf{e}_i \times \mathbf{h}_i^c. \quad (14)$$

The energy of the system given by the NCAA model is a function of N_i , M_i , λ_1^i and λ_2^i . The optimal values of these parameters correspond to an extremum of the energy and can be determined through the implementation of a variation principle [26]. Energy gradients with respect to N_i , M_i , λ_1^i and λ_2^i , as well as optimisation algorithms for finding the optimal values are given below. First, the case of a non-stationary state where the orientation of the magnetic moments is fixed is discussed. Then, the case of a stationary state is discussed, where an optimisation of the energy with respect to angles is carried out.

2.2. Calculation of non-stationary states

In order to find a self-consistent solution at a non-stationary configuration of the magnetic moments, one needs to find the extremum of the energy with respect to N_i , M_i , λ_1^i and λ_2^i . Analysis of constrained DFT has shown that the extremum with respect to λ_1^i and λ_2^i corresponds to a maximum of the energy [26]. The same is true for the NCAA model. Also, the extremum of the energy with respect to N_i corresponds to a maximum of the energy within the mean field approximation. The non-zero magnetic moment can be considered as an additional constraint on the occupation numbers. The partial derivatives can be evaluated analytically:

$$\frac{\partial E}{\partial N_i} = \frac{U_i}{2} [\langle \hat{n}_i \rangle - N_i], \quad (15)$$

$$\frac{\partial E}{\partial M_i} = \frac{U_i}{2} [M_i - \langle \hat{\mathbf{M}}_i \rangle \cdot \mathbf{e}_i], \quad (16)$$

$$\frac{\partial E}{\partial \lambda_1^i} = -\langle \hat{\mathbf{M}}_i \rangle \cdot \mathbf{e}_{\theta_i}, \quad (17)$$

$$\frac{\partial E}{\partial \lambda_2^i} = -\langle \hat{\mathbf{M}}_i \rangle \cdot \mathbf{e}_{\phi_i}, \quad \forall i = 1 \dots P. \quad (18)$$

When the gradient given by the first expression is zero, a self-consistent value for the number of d -electrons has been reached. The second gradient vanishes when a self-consistent value has been obtained for the longitudinal component of the magnetic moments. The last two gradients give self-consistent equations for Lagrange multipliers that adjust the perpendicular component of magnetic moments. When they are zero, the expectation values of the magnetic moment operators point in the predefined directions, i.e. $\langle \hat{\mathbf{M}}_i \rangle \parallel \mathbf{e}_i$.

The most commonly used and simplest method for solving self-consistency equations is the fixed point iteration method with simple mixing:

$$M^{(k)} = \alpha \langle \hat{\mathbf{M}}^{(k-1)} \rangle \cdot \mathbf{e} + (1 - \alpha) M^{(k-1)}, \quad (19)$$

$$N^{(k)} = \alpha \langle \hat{n}^{(k-1)} \rangle + (1 - \alpha) N^{(k-1)}, \quad (20)$$

$$\lambda_1^{(k)} = \alpha [\lambda_1^{k-1} - \langle \hat{\mathbf{M}}^{(k-1)} \rangle \cdot \mathbf{e}_{\theta}] + (1 - \alpha) \lambda_1^{(k-1)} \quad (21)$$

where k is an iteration counter and α is a mixing parameter chosen in such a way as to give a balance between stability and rate of convergence. However, by formulating the equations in terms of partial derivatives and a variational principle, more efficient optimisation methods, such as the conjugate gradient algorithms and quasi-Newton algorithms, can be used. The fixed point iteration method Eq. (19) is effectively a steepest-descent algorithm:

$$\begin{aligned} M^{(k)} &= M^{(k-1)} + \alpha \left[\left\langle \hat{\mathbf{M}}^{(k-1)} \right\rangle \cdot \mathbf{e} - M^{(k-1)} \right] = \\ &= M^{(k-1)} - \alpha \frac{2}{U} \left(\frac{\partial E}{\partial M} \right)^{(k-1)}, \end{aligned} \quad (22)$$

$$\begin{aligned} N^{(k)} &= N^{(k-1)} + \alpha \left[\left\langle \hat{n}^{(k-1)} \right\rangle - N^{(k-1)} \right] = \\ &= N^{(k-1)} + \alpha \frac{2}{U} \left(\frac{\partial E}{\partial N} \right)^{(k-1)}, \end{aligned} \quad (23)$$

$$\lambda^{(k)} = \lambda^{(k-1)} + \alpha \left(\frac{\partial E}{\partial \lambda} \right)^{(k-1)} \quad (24)$$

Note that a descent direction is used for M_i and an ascent direction for n_i , λ_i^1 and λ_i^2 . This is due to the fact that the self-consistent solution for the NCAA model correspond to a saddle point in the parameter space.

In order to find the extremum of energy one can carry out optimisation with respect to all degrees of freedom. The algorithm is presented below:

Algorithm for Non-stationary States:

- (1) Given initial values of the variables that need to be determined self-consistently

$$\vec{x}^{(0)} = (N_1 \dots N_P, M_1 \dots M_P, \lambda_1^1 \dots \lambda_1^P, \lambda_2^1 \dots \lambda_2^P)^T, \quad (25)$$

the corresponding scaled derivatives of the energy

$$\vec{g}^{(0)} = \alpha \left(-\frac{2}{U} \frac{\partial E}{\partial N_1} \dots, \frac{2}{U} \frac{\partial E}{\partial M_1}, -\frac{\partial E}{\partial \lambda_1^1} \dots, -\frac{\partial E}{\partial \lambda_2^1} \dots - \frac{\partial E}{\partial \lambda_2^P} \right)^T \quad (26)$$

and a value of the scaling parameter α

- (2) Let $\Theta = \max_i \left\{ \left| \frac{2}{U} \frac{\partial E}{\partial N_i} \right|, \left| \frac{2}{U} \frac{\partial E}{\partial M_i} \right| \right\}$, $\Delta = \max_i |\mathbf{T}_i^{NCAA}|$; ϵ , δ are convergence tolerance, l is a parameter which controls the size of the step along the search direction and $k = 0$ is iteration counter
- (3) Calculate the search direction according to a given minimisation algorithm.
For example, $\vec{p}^{(k)} = -\vec{g}^{(k)}$ for gradient descent
- (4) While $\Theta > \epsilon$ and $\Delta > \delta$:
- $d = \|\vec{p}^{(k)}\|_{\text{inf}}$. If $d > l$ then $\vec{p}^{(k)} \leftarrow \vec{p}^{(k)} l/d$
 - $\vec{x}^{(k+1)} = \vec{x}^{(k)} + \vec{p}^{(k)}$
 - Calculate new gradient $\vec{g}^{(k+1)}$ and new search direction $\vec{p}^{(k+1)}$
 - $k \leftarrow k + 1$
- (5) End.

Typical values of the parameters are $\alpha = 0.7$, $\epsilon = 10^{-7}$, $\delta = 10^{-7}$, Γ , $l = 0.04$. If the algorithm does not converge, then the values of the parameters α and/or l should be reduced. As the extremum of energy that corresponds to the solution is not a minimum, a line search procedure cannot be applied in this case.

2.3. Calculations of stationary states

In order to find stationary states, i.e. configurations of the magnetic moments that correspond to a local minimum or a saddle point on the energy surface, the function that gives the energy of the system with respect to all the degrees of freedom, one can use the NCAA Hamiltonian without constraints because the Lagrange multipliers vanish at these points. Therefore, one needs to find the extremum of the energy with respect to N_i , M_i and \mathbf{e}_i . In order to find energy minima, the energy minimisation can be carried out in two different ways: Either the degrees of freedom are separated into fast and slow variables and the minimisation performed with an inner loop for the former and an outer loop for the latter or all degrees of freedom are treated on an equal footing. We will refer to the first option as algorithm M1, and the second option as algorithm M2. The motivation for M1 is that a deviation of N_i or M_i from the optimal values leads to larger change in the energy than a deviation in the angular variables, θ_i and ϕ_i . This, for example, leads to the separation of the dynamics into fast and slow degrees of freedom [12]: slow degrees of freedom are directions of magnetic moments obeying classical Landau–Lifshitz equations of motion while the fast degrees of freedom are

the longitudinal components of the magnetic moments found using self-consistency calculations for given directions. Similarly, one can separate the minimisation into two nested loops, where for each value of the slow degrees of freedom, the fast degrees of freedom are adjusted according to the self-consistency equations. The orthogonal spin optimisation (OSO) method [29] is used here for the slow degrees of freedom, \mathbf{e}_i . The inner loop finds optimal values of N_i and M_i , and the outer loop performs rotations of the magnetic moments towards the energy minimum:

Algorithm M1:

Inner loop for finding optimal values of N_i and M_i .

(1) Let

$$\vec{x} = (N_1 \dots N_P, M_1 \dots M_P)^T \quad (27)$$

be the vector consisting of variables that need to be found self-consistently,

$$\vec{g} = \alpha \left(-\frac{2}{U} \frac{\partial E}{\partial N_1}, \dots, \frac{2}{U} \frac{\partial E}{\partial M_1} \right)^T \quad (28)$$

the vector consisting of the corresponding energy derivatives, and α a scaling parameter.

- (2) Let $\Theta = \max_i \left\{ \left| \frac{2}{U} \frac{\partial E}{\partial N_i} \right|, \left| \frac{2}{U} \frac{\partial E}{\partial M_i} \right| \right\}$ be convergence tolerances, l a parameter controlling the size of the step along the search direction and $k_{in} = 0$ an iteration counter.
- (3) Calculate the search direction according to a given minimisation algorithm. For example, $\vec{p}^{(k_{in})} = -\vec{g}^{(k_{in})}$ for gradient descent algorithm.
- (4) While $\Theta > \epsilon$:
- $d = \|\vec{p}^{(k_{in})}\|_{\text{inf}}$. If $d > l$ then $\vec{p}^{(k_{in})} \leftarrow \vec{p}^{(k_{in})} l/d$.
 - $\vec{x}^{(k_{in}+1)} = \vec{x}^{(k_{in})} + \vec{p}^{(k_{in})}$
 - Calculate new gradient $\vec{g}^{(k_{in}+1)}$ and new search direction $\vec{p}^{(k_{in}+1)}$.
 - $k_{in} \leftarrow k_{in} + 1$.

End of inner loop.

Outer loop:

- (1) Let $k = 0$ be iteration counter. Let δ be a convergence tolerance for the maximum torque in the system. Call **Inner loop** to calculate optimal values $N_i^{(k)}, M_i^{(k)}$ for given initial directions of the magnetic moments: $\{\mathbf{e}_i^{(k)}\}_{i=1..N}$. Using this optimal values calculate the torques

$$\mathbf{T}_i^{(k)} = \frac{U_i M_i^{(k)}}{2} \mathbf{e}_i \times \langle \hat{\mathbf{M}}_i \rangle^{(k)}.$$

- (2) While $\max_i |\mathbf{T}_i^{(k)}| \geq \delta$ repeat the the following steps:
- Perform rotation of the magnetic moments towards the minimum of energy:

$$\mathbf{e}_i^{(k+1)} = \exp(-P_i) \mathbf{e}_i^{(k)}, \quad i = 1..N \quad (29)$$

where P is a skew-symmetric matrix. For gradient descent algorithm it is:

$$P_i = \begin{pmatrix} 0 & -t_{iz} & t_{iy} \\ t_{iz} & 0 & -t_{ix} \\ -t_{iy} & t_{ix} & 0 \end{pmatrix}, \quad \mathbf{t}_i \equiv \mathbf{T}_i^{(k)}. \quad (30)$$

- Call **Inner loop** to calculate optimal values $N_i^{(k+1)}, M_i^{(k+1)}$ for a new directions of magnetic moments $\{\mathbf{e}_i^{(k+1)}\}_{i=1..N}$.
- Calculate the torques,

$$\mathbf{T}_i^{(k)} = \frac{U_i M_i^{(k)}}{2} \mathbf{e}_i \times \langle \hat{\mathbf{M}}_i \rangle^{(k)}.$$

using the optimal values $N_i^{(k+1)}, M_i^{(k+1)}$.

- Set $k \leftarrow k + 1$.

End of outer loop

End of M1

While the expression given here for the matrices P_i in Eq. (30) are for gradient descent algorithm, it is more efficient to use the L-BFGS in the outer loop, as shown below. The relevant expressions for the P_i matrices in that case and detail on the implementation of the L-BFGS can be found in Ref. [29].

The second algorithm, M2, where all degrees of freedom are treated on an equal footing is given below.

Algorithm M2:

(1) Let

$$\vec{x} = (N_1 \dots N_P, M_1 \dots M_P, \theta_1, \dots, \theta_P, \phi_1, \dots, \phi_P)^T \quad (31)$$

be a vector consisting of the variables that need to be found self-consistently,

$$\vec{g} = \alpha \left(-\frac{2}{U} \frac{\partial E}{\partial N_1} \dots, \frac{2}{U} \frac{\partial E}{\partial M_1} \dots, \frac{2}{U M_i} \frac{\partial E}{\partial \theta_1} \dots, \frac{2}{U M_i \sin \theta_i} \frac{\partial E}{\partial \phi_1} \dots \right)^T \quad (32)$$

the vector consisting of corresponding derivatives of the energy, and α the scaling parameter.

- (2) Let $\Theta = \max_i \left\{ \left| \frac{2}{U} \frac{\partial E}{\partial N_i} \right|, \left| \frac{2}{U} \frac{\partial E}{\partial M_i} \right| \right\}$, $\Delta = \max_i |\mathbf{T}_i^{NCAA}|$; ϵ, δ be convergence tolerances, l a parameter controlling the size of steps along the search direction and $k = 0$ an iteration counter.
- (3) Calculate the search direction according to the given minimisation algorithm. For example, $\vec{p}^{(k)} = -\vec{g}^{(k)}$ for a gradient descent algorithm.
- (4) While $\Theta > \epsilon$ and $\Delta > \delta$:
 - (a) $d = \|\vec{p}^{(k)}\|_{\text{inf}}$. If $d > l$ then $\vec{p}^{(k)} \leftarrow \vec{p}^{(k)} l/d$.
 - (b) $\vec{x}^{(k+1)} = \vec{x}^{(k)} + \vec{p}^{(k)}$
 - (c) Calculate new gradient $\vec{g}^{(k+1)}$ and new search direction $\vec{p}^{(k+1)}$.
 - (d) $k \leftarrow k + 1$.

End of M2

Algorithm M2 is efficient when the system is far from the energy minimum and the gradients for all degrees of freedom are large. But, near a minimum it can be unstable. The reason is that it mixes slow and fast degrees of freedom. If one needs to converge N_i and M_i to a small tolerance then it is difficult to converge angles ϕ_i, θ_i to the same accuracy. Changes in M_i and N_i have large effect on the energy while changes in the angular variables do not affect the energy as strongly. In practice, it is better to use algorithm M2 in the beginning and start with relatively large tolerances for N_i and M_i , for example $\epsilon = 10^{-3}$, and then reduce ϵ to a smaller number so that the error in the torque due to deviations from self-consistency are smaller than the magnitude of the torque. Near the minimum it is usually enough to perform 1 to 3 iteration steps for N_i and M_i to reach good convergence.

Saddle points on the energy surface can be found using the geodesic nudged elastic band method [30] where a climbing image converges onto the saddle point. While constraints on the orientation of the magnetic moments should in principle be applied to images that are in between the endpoint minima and the climbing image, this turns out not to be important for convergence onto the saddle point. The intermediate images are needed to estimate the tangent along the path, and they can reveal the presence of intermediate minima, but it is not so critical that they lie exactly on the minimum energy path.

3. Numerical tests

The performance of three different optimisation algorithms: L-BFGS, Fletcher–Revere conjugate gradients (FR) and steepest-descent (SD) was tested in calculations of non-stationary states. Then, algorithms M1 and M2 as well as mixed M1+M2 algorithms were tested and compared in calculations of stationary states. The test system consists of either 400 or 196 atoms in a hexagonal two-dimensional lattice subject to periodic boundary conditions. The NCAA model parameters are $E_0 = -12 \Gamma$, $U = 13 \Gamma$, and $V = 0.5 \Gamma$.

The most demanding computational part of NCAA calculations is the diagonalisation of the Hamiltonian. The comparison of the performance of the various optimisation algorithms is, therefore, measured in terms of the number of diagonalisations which in the present case, equals the number of iterations needed in order to reach convergence.

3.1. Calculations of non-stationary states

The non-stationary states are a tilted spin spirals:

$$\mathbf{e}_i = \begin{pmatrix} \sin(\psi) \cos(\mathbf{q} \cdot \mathbf{r}_i) \\ \sin(\psi) \sin(\mathbf{q} \cdot \mathbf{r}_i) \\ \cos(\psi) \end{pmatrix} \quad (33)$$

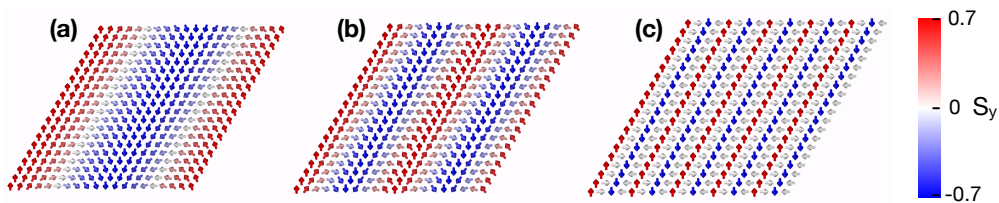


FIG. 2. Spin states corresponding to Eq. 33 for $\psi = \pi/4$ when \mathbf{q} lies along ΓM direction. (a) $q = \pi/10a$, (b) $q = \pi/5a$, (c) $q = \pi/2a$. a is a lattice constant. The color corresponds to y component of the spins. The visualisation was done with OVITO software [36].

TABLE 1. Number of iterations needed in order to reach convergence using three different optimisation algorithms: L-BFGS, Fletcher–Revere conjugate gradients (FR), and steepest descent (SD). Calculations are carried out for different values of the wave number q . The convergence tolerances are $\epsilon = 10^{-8}$, ($\epsilon = 10^{-14}$ in brackets) and $\delta = 10^{-8}$. The initial values of N_i and M_i are 1.4 and 0.44, respectively, and the converged values of N_i and M_i are given in the last two columns.

q	SD	FR	L-BFGS	N_i	M_i
0	30 (58)	52 (401)	24 (29)	1.4271	0.4555
$\pi/10a$	55 (84)	127 (375)	30 (43)	1.4268	0.4556
$\pi/5a$	64 (101)	158 (206)	50 (66)	1.4259	0.4558
$3\pi/10a$	69 (110)	84 (108)	47 (66)	1.4245	0.4562
$4\pi/10a$	73 (119)	43 (536)	25 (38)	1.4225	0.4568
$\pi/2a$	75 (125)	54 (79)	20 (142)	1.4200	0.4581
$6\pi/10a$	77 (128)	372 (174)	26 (39)	1.4170	0.4599
$7\pi/10a$	77 (129)	188 (302)	28 (61)	1.4138	0.4622
$8\pi/10a$	78 (131)	244 (185)	21 (53)	1.4108	0.4646
$9\pi/10a$	78 (134)	140 (211)	32 (41)	1.4086	0.4665
π/a	77 (132)	102 (140)	26 (43)	1.4078	0.4672
average:	68 (113)	142 (247)	30 (56)		

with ψ chosen to be $\pi/4$. If $\psi = \pi/2$, the corresponding spin spirals are stationary states in the NCAA model. The wave vector \mathbf{q} is chosen to lie along ΓM direction in the irreducible two-dimensional Brillouin zone. Different states correspond to different values of q . Three examples are shown in Fig. 2.

The performance of the three minimisation algorithms is summarised in Table 1. Each of the algorithms gives a different search direction during the optimization.

As can be seen from Table 1, the number of iterations needed in the SD calculations systematically grows as the wave number, q is increased. The reason is that the torque acting on the magnetic moments in the initial configuration increases with q and the expectation values of the magnetic moments deviate more from the reference direction. Overall, L-BFGS requires fewer iteration than either SD or FR conjugate gradients algorithm. On average, it requires half as many iterations as SD and 1/5 as many as FR. For one value of q , however, $q = \pi/2a$, and the tight convergence criterion, $\epsilon = 10^{-14}$, L=BFGS requires more iterations than FR and SD (142 vs. 79 and 125).

The poor performance of FR is surprising, but can probably be explained by the fact that the SCF solution does not correspond to a minimum of the NCAA energy, but rather a saddle point. The energy needs to be maximised with respect to N_i and the Lagrange multipliers while being minimised with respect to M_i . Conjugate gradient algorithms require an efficient line search procedure to find the minimum of energy along the search direction. As the extremum is a saddle point in the present case, no line search can be applied and the step taken along the search direction not optimal, thereby reducing the efficiency of the algorithm. This can be the reason why the FR algorithm performs even worse than the SD algorithm in the present case.

TABLE 2. Number of iterations needed in order to obtain the ferromagnetic ground state starting from various initial spiral states with wave vector q and $\psi = \pi/4$. A magnetic field is applied along the y -direction, $H = 10^{-4} \Gamma$. The simulation cell consists of 196 atoms. The first two columns correspond to algorithm M1 involving inner and outer loop iterations, with tolerances $\epsilon = 10^{-3}$ and $\epsilon = 10^{-7}$. In both cases $\delta = 10^{-7}$. The third column corresponds to calculations using a hybrid algorithm where M2 is first used to obtain convergence to a tolerance of $\delta = 10^{-4}$, and then algorithm M1 is used until with tolerances $\epsilon = 10^{-7}$ and $\delta = 10^{-7}$

q	M1($\epsilon = 10^{-3}$)	M1($\epsilon = 10^{-7}$)	M2+M1 ($\epsilon = 10^{-7}$)
0	46	135	110
$\pi/7a$	165	1353	186
$4\pi/14a$	108	1456	153
$6\pi/14a$	197	1459	108
$8\pi/14a$	160	1041	112
$10\pi/14a$	169	894	100
$12\pi/14a$	138	1067	105
π/a	122	750	91
average:	138	1200	120

3.2. Calculations of stationary states

In calculations of energy minima or saddle points on the energy surface, the constraint fields can be set to zero at each iteration during the optimisation as these fields vanish at stationary points. Performance tests were carried out for a 196 atom system where the initial state corresponds to one of the titled spiral states with $\psi = \pi/4$ described in the previous subsection, and the final state corresponds to the uniform, ferromagnetic ground state. A magnetic field of $H = 10^{-4} \Gamma$ is applied along the y -direction. The search direction is calculated using the L-BFGS algorithm.

The results are shown in Table 2. The performance of the M1 algorithm where fast and slow degrees of freedom are treated separately in an inner and outer loop is given for two values of the inner loop convergence tolerance, ϵ . For the outer loop, the tolerance is $\delta = 10^{-7}$ in both cases. In the calculations corresponding to the first column $\epsilon = 10^{-3}$, but since at least one inner loop iteration is taken for each outer loop iteration, the convergence of N and M is actually better than 10^{-3} .

The results in the second column correspond to inner loop tolerance of $\epsilon = 10^{-7}$ and the outer loop tolerance is again $\delta = 10^{-7}$. The number of iterations is significantly larger compared with the results in the first column. The difference in the energy of the system when $\epsilon = 10^{-3}$ and $\epsilon = 10^{-7}$ is around $10^{-4} \Gamma$.

The third column gives results for a hybrid algorithm, where all degrees of freedom are first treated on the same footing using algorithm M2, until convergence corresponding to $\delta = 10^{-4}$ has been reached and then algorithm M1 is used with a tolerance of $\epsilon = 10^{-7}$ in the inner loop and $\delta = 10^{-7}$ in the outer loop. This turns out to be the optimal algorithm, especially when the initial state is far from the minimum energy configuration and the initial values of the gradients are large.

4. Application

The NCAA model has previously been applied in studies of spin density waves and the antiferromagnetic state of BCC Cr [6] and the same approach is used here. A pair of neighboring atoms are included explicitly in order to represent the antiferromagnetic state, but the effect of neighboring atoms in the crystal is included implicitly. The NCAA model parameter values are: $E_0 = -3.37 \Gamma$, $U = 6.745 \Gamma$ and $v = 0.9 \Gamma$. The effective hopping parameter is $V = \sqrt{8}v$ corresponding to the d-d hopping to the eight nearest neighbors in the BCC lattice. The self-consistent NCAA calculations for the antiferromagnetic ground state give magnetic moment of $0.6\mu_B$ and 5.0 d-electrons.

The angle between the prescribed directions of the magnetic moments is denoted by θ , as illustrated in Fig. 3. The deviation from the antiferromagnetic order is $\phi = \pi - \theta$. The angle between the prescribed direction and the calculated magnetic moment and the angle obtained from the self-consistency calculation without constraints is denoted by α . This represents the error due to the lack of constraints on the transverse component of the magnetic moments. A comparison is made between fully self-consistent calculations where constraints are applied and calculations where

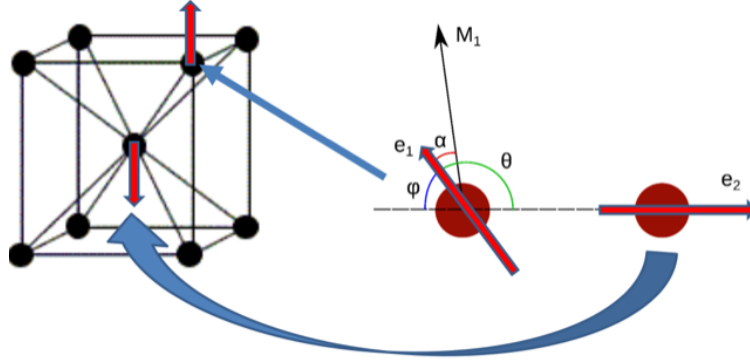


FIG. 3. Illustration of the simulation of a BCC crystal of Cr. Two atoms are included explicitly in the calculations in order to represent the antiferromagnetic order, but the effect of neighbors is included implicitly. The prescribed directions of the magnetic moments are \mathbf{e}_1 and \mathbf{e}_2 . \mathbf{M}_1 is a calculated magnetic moment of atom 1. α is the angle between \mathbf{M}_1 and \mathbf{e}_1 and represents the error in the direction when constraints on the transverse components of the magnetic moments are not included.

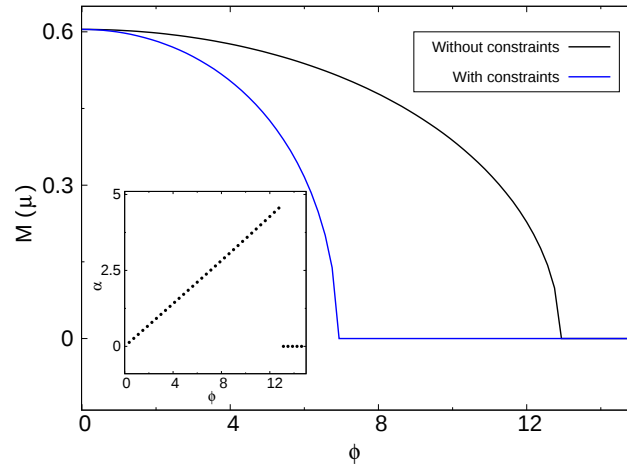


FIG. 4. Magnitude of the magnetic moments as a function of the angle ϕ (see Fig. 3). The blue curve represents calculations including the constraints and the black curve represents the calculations without constraints. Inset: The deviation of the direction of calculated magnetic moment from prescribed directions as functions of angle ϕ when constraints are not included.

the self-consistency calculations only include the average number of d -electrons and the longitudinal component of magnetic moments.

As one of the magnetic moments is rotated with respect to the other, the magnitude of the magnetic moments is reduced as shown in Fig. 4. At a certain angle the magnetic moment vanishes. When the angular constraints are included, the magnitude drops to zero at $\phi \approx 7^\circ$, while it drops to zero at $\phi \approx 13^\circ$ when the constraints are not included. The error that occurs when the constraints are neglected is, therefore, large in this case. The qualitative shape of the curve is similar, but the magnetic moment vanishes at an angle that is nearly twice as large when the constraints are not included.

The inset in Fig. 4 shows the maximum deviation of the direction of the calculated magnetic moments from the prescribed direction when constraints are not included, i.e. the dependence of α on ϕ . The maximum deviation is about 5° obtained right when the magnetic moment vanishes.

The Fig. 5(a) shows the variation of the torques acting on magnetic moments as a function of the angle ϕ . The torques are evaluated using Eq. (14) when the constraints are included, but from Eq. (10) when the constraints are neglected. The torques differ by up to a factor of three in magnitude and the maximum is obtained at different values

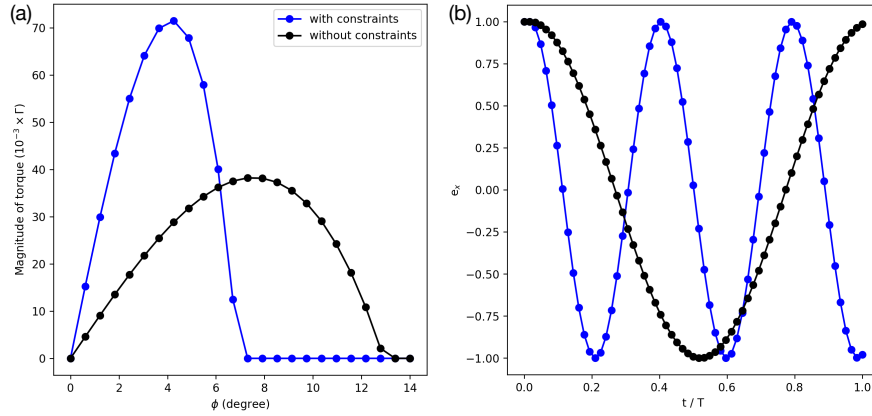


FIG. 5. Comparison of results obtained for Cr crystal with (blue curves) and without (black curves) constraints on the transverse components of the magnetic moments. (a) Torque as a function of ϕ . (b) Projection of the magnetic moment on the x-axis as a function of time in units of the oscillation period obtained without constraints. Here, $\phi = 4^\circ$.

of the angle ϕ . When constraints are not included, the torque rises and falls more gradually than when constraints are included. Both curves level out at zero, corresponding to a non-magnetic solution.

Spin dynamics were simulated by solving numerically the classical Landau-Lifshitz equation of motion for the slow degrees of freedom

$$\frac{d\mathbf{e}_i}{dt} = -\gamma \mathbf{e}_i \times \mathbf{H}_i^{\text{eff}}. \quad (34)$$

The Eq. 14 for torques coincides with what is used in tight-binding and DFT simulations of the spin-dynamics with constraints [17, 19]. Indeed, substitution of Eq. 14 into Eq. 34 gives:

$$\frac{d\mathbf{e}_i}{dt} = \gamma \mathbf{e}_i \times \mathbf{h}_\perp^c(\mathbf{i}). \quad (35)$$

We have used the two step numerical method of Mentink *et al.* [31] to numerically integrate the equation of motion. As the calculated torques are so different, the spin dynamics are also very different. The two sublattices oscillate around a common axis with a frequency that depends directly on the magnitude of the torques. Since the torques differ by almost a factor of three depending on whether the constraints are applied or not, the frequencies in the dynamical motion differ by the same amount, as can be seen from Fig. 5. When the constraints are applied, the frequency is about three times larger.

Effective exchange coupling parameters [15, 32, 33] and pre-exponential factors for estimates of the lifetime of magnetic states [34, 35] can be obtained from the curvature of the energy surface at the minimum. When the curvature is calculated by finite differences, the energy needs to be evaluated at non-stationary points corresponding to small tilts of the magnetic moments away from the ground state, local minimum configurations. Constraints need to be included in order for the angular deviations to be well defined. The second derivative of the energy, $\partial^2 E / \partial \theta_0 \partial \theta_1$, at $\phi = 0$ is calculated with the NCAA model to be $290 \times 10^{-3} \Gamma$ for the Cr crystal when the constraints are included. When the constraints are neglected a significantly smaller curvature is deduced, $87 \times 10^{-3} \Gamma$. This shows the importance of the constraints when the pre-exponential factors and effective exchange parameters are calculated using self-consistency calculations.

Acknowledgements

This work was funded by the Icelandic Research Fund, the University of Iceland doctoral fund (AVI) and the Russian Science Foundation under grant No. 19-72-10138.

Appendix A. Calculation of expectation values

The Green function method is used to calculate expectation values of the number of d -electrons, magnetic moments and the energy of the system. Since the Hamiltonian is quadratic with respect to creation and annihilation operators, the Green function is the resolvent:

$$\left(\omega - \hat{H}^{NCAA}\right) \hat{G} = I \quad (36)$$

In the case of non-collinear magnetism, the density of states is a matrix:

$$\rho_{ij}(\epsilon) = \begin{pmatrix} \rho_{ij}^{\alpha\alpha} & \rho_{ij}^{\alpha\beta} \\ \rho_{ij}^{\alpha\beta*} & \rho_{ij}^{\beta\beta} \end{pmatrix} \quad (37)$$

which can be calculated using the imaginary part of the Green function

$$\rho_{ij}^{\alpha\beta}(\epsilon) = \frac{1}{\pi} \lim_{s \rightarrow 0} \text{Im} G_{ij}^{\alpha\beta}(\epsilon - is) \quad (38)$$

where i, j refer to the atomic sites and α, β refer the spin projection.

The expectation values can be calculated as:

$$\langle \hat{n}_i \rangle = \int_{-\infty}^{\epsilon_f} d\epsilon \text{Tr}_s \rho_{ii}(\epsilon) \quad (39)$$

$$\langle \hat{\mathbf{M}}_i \rangle = \int_{-\infty}^{\epsilon_f} d\epsilon \text{Tr}_s \sigma \rho_{ii}(\epsilon), \quad (40)$$

where the trace operation is carried out with respect to spin degrees of freedom, and $\sigma = (\sigma^x, \sigma^y, \sigma^z)^T$ are the Pauli matrices. To calculate matrix elements of the Green function, an eigendecomposition of the Hamiltonian is used. Let $\{\epsilon_i\}, \{\vec{y}_i\}$ be the eigenvalues and eigenvectors of the NCAA Hamiltonian. Using the eigenvectors as a basis, the Green function is diagonal:

$$G_{km} = \frac{\delta_{km}}{\omega - \epsilon_k - i\Gamma}, \quad k, m = 1..2P \quad (41)$$

where P number of atoms. The Green function in the laboratory basis set can be obtained using the similarity transformation:

$$G_{ij}^{\alpha\beta} = \sum_{k=1}^{2P} \langle x_i^\alpha | y_k \rangle G_{kk}^d \langle y_k | x_j^\beta \rangle \quad i, j = 1..P, \quad (42)$$

where $|x_i^\alpha\rangle$ corresponds to the state on site i with the spin projection α . Using the equation above, one can find expectation values of the operators in terms of eigenvalues and eigenvectors:

$$\langle \hat{n}_i \rangle = \sum_{k=1}^{2P} \left(|\langle x_i^\uparrow | y_k \rangle|^2 + |\langle x_i^\downarrow | y_k \rangle|^2 \right) R_{kk} \quad (43)$$

$$\langle \hat{\mathbf{M}}_i \rangle_x = \sum_{k=1}^{2P} 2\text{Re} \left(\langle x_i^\uparrow | y_k \rangle \langle y_k | x_i^\downarrow \rangle \right) R_{kk} \quad (44)$$

$$\langle \hat{\mathbf{M}}_i \rangle_y = \sum_{k=1}^{2P} -2\text{Im} \left(\langle x_i^\uparrow | y_k \rangle \langle y_k | x_i^\downarrow \rangle \right) R_{kk} \quad (45)$$

$$\langle \hat{\mathbf{M}}_i \rangle_z = \sum_{k=1}^{2P} \left(|\langle x_i^\uparrow | y_k \rangle|^2 - |\langle x_i^\downarrow | y_k \rangle|^2 \right) R_{kk}, \quad (46)$$

where

$$R_{kk} = \frac{1}{\pi} \lim_{s \rightarrow 0} \text{Im} G_{kk}^d = \frac{1}{\pi} \text{arccot} \frac{\epsilon_k}{\Gamma}. \quad (47)$$

and the energy is [5]:

$$E = \frac{1}{\pi} \sum_i \epsilon_i \text{arccot} \left(\frac{\epsilon_i}{\Gamma} \right) + \frac{\Gamma}{2} \ln \left(1 + \frac{\epsilon_i^2}{\Gamma^2} \right) - \frac{U_i}{4} (N_i^2 - M_i^2). \quad (48)$$

References

- [1] Anderson P.W. Localized Magnetic States in Metals. *Phys. Rev.*, 1961, **124**, P. 41.
- [2] Alexander S., Anderson P.W. Interaction Between Localized States in Metals. *Phys. Rev.*, 1964, **133**, P. A1594.
- [3] Uzdin V.M., Yartseva N.S. Periodic Anderson model for the description of noncollinear magnetic structure in low-dimensional 3d-systems. *Comput. Mater. Sci.*, 1998, **10**, P. 211.
- [4] Bessarab P.F., Uzdin V.M., Jónsson H. Calculations of magnetic states and minimum energy paths of transitions using a non-collinear extension of the Alexander-Anderson model and a magnetic force theorem. *Phys. Rev. B*, 2014, **89**, P. 214424.
- [5] Bessarab P.F., Skorodumov A., Uzdin V.M., Jónsson H. Navigation on the Energy Surface of the Noncollinear Alexander-Anderson model. *Nanosystems: physics, chemistry, mathematics*, 2014, **6**, P. 757.
- [6] Uzdin V.M., Demangeat C. Spin-density wave in Cr without the nesting property of the Fermi surface. *J. Phys.: Condens. Matter*, 2006, **18**, P. 2717.
- [7] Uzdin V.M., Vega A. Magnetization reversal process at atomic scale in systems with itinerant electrons. *J. Phys.: Condens. Matter*, 2012, **24**, P. 176002.
- [8] Bessarab P.F., Uzdin V.M., Jónsson H. Navigation on the energy surface of the non-collinear Alexander-Anderson model. *Nanosystems: Physics, Chemistry, Mathematics*, 2014, **5**, P. 757.
- [9] Ivanov A., Bessarab P.F., Uzdin V.M., Jónsson H. Magnetic exchange force microscopy: Theoretical analysis of induced magnetization reversals. *Nanoscale*, 2017, **9**, P. 13320.
- [10] You M.V., Heine V. Magnetism in transition metals at finite temperatures I. Computational model. *J. Phys. F: Met. Phys.*, 1982, **12**, P. 177–94.
- [11] Gyorffy B.L., Pindors A.J., Staunton J., Stocks G.M. and Winter H. A first-principles theory of ferromagnetic phase transitions in metals. *J. Phys. F: Met. Phys.*, 1985, **15**, P. 1337–1386.
- [12] Antropov V.P., Katsnelson M.I., Harmon B.N., M. van Schilfgaarde, Kusnezov D. Spin dynamics in magnets: Equation of motion and finite temperature effects. *Phys. Rev. B*, 1996, **54**, P. 1019.
- [13] Kohn W. Nobel Lecture: Electronic structure of matter wave functions and density functionals. *Rev. Mod. Phys.*, 1999, **71**, P. 1253.
- [14] Harrison W.A. *Elementary Electronic Structure*. Singapore, World Scientific, 2009.
- [15] Bruno P. Exchange Interaction Parameters and Adiabatic Spin-Wave Spectra of Ferromagnets: A Renormalized Magnetic Force Theorem. *Phys. Rev. Lett.*, 2003, **90**, P. 087205.
- [16] Dederichs P.H., Blügel S., Zeller R. and Akai H. Ground States of Constrained Systems: Application to Cerium Impurities. *Phys. Rev. Lett.*, 1984, **53**, P. 2512.
- [17] Small L.M., Heine V. A couple method for calculating interatomic interactions in itinerant electron magnetic systems. *J. Phys. F: Met. Phys.*, 1984, **14**, P. 3041–3052.
- [18] Luchini M.U., Heine V., McMulla G.J. Calculation of longitudinal magnetic fluctuations in iron by a Landau energy and force method. *J. Phys.: Condens. Matter*, 1991, **3**, P. 8647–8664.
- [19] Stocks G.M., Újfalussy B., Xindong Wang, Nicholson D.M.C., Shelton W.A., Yang Wang, Canning A., Gyorffy B.L. Towards a constrained local moment model for first principles spin dynamics. *Philos. Mag.*, 1998, **78**, Nos. 5/6 665–673.
- [20] Kurz Ph., Föster F., Nordstöm L., Bihlmayer G., Blügel S. Ab initio treatment of noncollinear magnets with the full-potential linearized augmented plane wave method. *Phys. Rev. B*, 2004, **69**, P. 024415.
- [21] Singer R., Fähnle M. and Bihlmayer G. Constrained spin-density functional theory for excited magnetic configurations in an adiabatic approximation. *Phys. Rev. B*, 2005, **71**, P. 214435.
- [22] Stocks G.M., Eisenbach M., Újfalussy B., Lazarovits B., Szunyogh L., Weinberger P. On calculating the magnetic state of nanostructures. *Prog. Mater. Sci*, 2007, **52**, P. 371–387.
- [23] Ma P.W., Dudarev S.L. Constrained density functional for noncollinear magnetism. *Phys. Rev. B*, 2015, **91**, P. 054420.
- [24] Wu Q., and T. Van Voorhis. Direct optimization method to study constrained systems within density-functional theory. *Phys. Rev. A*, 2005, **72**, P. 024502.
- [25] Wu Q., and T. Van Voorhis. Constrained Density Functional Theory and Its Application in Long-Range Electron Transfer. *J. Chem. Theory Comput.*, 2006, **2**, P. 765.
- [26] ORegan D.D., Teobaldi G. Optimization of constrained density functional theory. *Phys. Rev. B*, 2016, **94**, P. 035159.
- [27] Nocedal J., Wright S.J. *Numerical Optimization*, 2nd ed. Springer, New York, NY, USA, 2006.
- [28] Hubbard J. Electron correlations in narrow energy bands. *Proc. Roy. Soc. A*, 1963, **276**, P. 238.
- [29] Ivanov A.V., Uzdin V.M., Jónsson H. Fast and Robust Algorithm for the Energy Minimization of Spin Systems Applied in an Analysis of High Temperature Spin Configurations in Terms of Skyrmion Density. arXiv:1904.02669v2 [physics.comp-ph] 2019.
- [30] Bessarab P.F., Uzdin V.M., Jónsson H. Method for finding mechanism and activation energy of magnetic transitions, applied to skyrmion and antivortex annihilation. *Computer Physics Communications*, 2015, **196**, P. 335–347.
- [31] Mentink J.H., Tretyakov M.V., Fasolino A., Katsnelson M.I. and Rasing Th. Stable and fast semi-implicit integration of the stochastic Landau-Lifshitz equation. *J. Phys.: Condens. Matter*, 2010, **22**, P. 176001.
- [32] Liechtenstein A.I., Katsnelson M.I., Antropov V.P., Gubanov V.A. *J. Magn. Magn. Mater.*, 1987, **67**, P. 65–74.
- [33] Katsnelson M.I., Lichtenstein A.I. Magnetic susceptibility, exchange interactions and spin-wave spectra in the local spin density approximation. *J. Phys.: Condens. Matter*, 2004, **16**, P. 7439–7446.
- [34] Bessarab P.F., Uzdin V.M., Jónsson H. Harmonic transition-state theory of thermal spin transitions. *Phys. Rev. B.*, 2012, **85**, P. 184409.
- [35] Bessarab P.F., Uzdin V.M., Jónsson H. Size and shape dependence of thermal spin transitions in nanoislands. *Phys. Rev. Lett.*, 2013, **110**, P. 020604.
- [36] Stukowski A. Visualization and analysis of atomistic simulation data with OVITO the Open Visualization Tool. *Modelling Simul. Mater. Sci. Eng.*, 2010, **18**, P. 015012.

Comparative assessment of antibacterial efficacy for cobalt nanoparticles, bulk cobalt and standard antibiotics: A concentration dependant study

V. Gupta^{1*}, V. Kant², A. K. Sharma¹, M. Sharma¹

¹Department of Chemistry, University of Jammu, J&K, India

²Department of Veterinary Pharmacology & Toxicology, LUVAS, Hisar, India

*vijayta1gupta@gmail.com

DOI 10.17586/2220-8054-2020-11-1-78-85

Synthesis of compounds that can prevent bacterial resistance is of huge interest and gaining immense popularity. Cobalt (Co) is one of the cheaper transition metals and its nano form has not been studied in details for antibacterial actions. Comparative analysis of Co nanoparticles with bulk Co and standard antibacterials are also lacking. In our study, concentration dependent action of Co nanoparticles was observed from 0.125 to 128.0 µg/ml against *S. aureus* and *E. coli*. Zone of inhibition of Co nanoparticles was better against *E. coli* than *S. aureus*. Co nanoparticles were markedly better than bulk Co, oxytetracycline and gentamicin. Activity index and fold increase of Co nanoparticles were higher at most of the concentrations. In conclusion, Co nanoparticles showed better antibacterial action than other tested compounds against *S. aureus* and *E. coli* particularly at lower concentrations, and their use may be extended in different biomedical fields in future.

Keywords: Cobalt nanoparticles, *S. aureus*, *E. coli*, antibacterial activity, activity index, fold increase.

Received: 6 November 2019

Revised: 10 December 2019

1. Introduction

There is a continuous battle throughout history between humans and multiple microorganisms. Major discoveries and developments for antibacterial drugs and other ways of infection control during the middle of the 20th century have occurred, which helped significantly for human being and animals. However, rapid emergence of bacterial resistance become as one of the major concerns of the 21st century. Antimicrobial resistance has become a global problem with the fast increase in multidrug-resistant bacteria. *Staphylococcus aureus* (*S. aureus*) and *Escherichia coli* (*E. coli*) are two common bacteria to which almost every human being and animal has been exposed. Some earlier treatable microorganisms are currently becoming untreatable such as methicillin-resistant *Staphylococcus aureus* (MRSA) and vancomycin-resistant enterococcus (VRE) [1]. Different strategies to address this challenge include the designing of improved version of existing antibacterial classes, combinations therapy etc. have been attempted. These strategies can be quite effective, but a high risk of rapid development of bacterial resistance still remains. Bacteria have the genetic capability to transmit and acquire resistance to antimicrobial drugs. In the last three decades, different pharmaceutical industries have produced a lot of new antibiotics, but the bacterial resistance to these drugs has also increased [2]. In view of the increase of bacterial resistance, synthesis of compounds that may prevent bacterial growth with least cytotoxicity are of huge interest and gaining immense popularity in the area of drug development.

During past decades, applications of nanotechnology have brought many breakthroughs. In recent years, much attention has been given to the applications of nanotechnology in various metals and metal oxides for their different uses. Metal nanoparticles are exceptionally appealing better applications in contrast to mass materials due to their high surface-to-volume proportion. There are many nano metals (such as silver, gold, copper, zinc etc.), which exhibit their own structural properties and important biological activities [3, 4]. Metals have been used in the therapy of several diseases of humans and animals since ancient times. Copper and cobalt (Co) ions have been used for centuries by people to inhibit the growth of harmful microbes. Further, transition metals and their complexes are of current interest from numerous point of view, like their use as antioxidant, antibacterial, antifungal, anticancer, anti-inflammatory agent etc. [5, 6].

Co is one of the cheaper transition metals which have wide applications and also possesses antimicrobial properties. Co nanoparticles are of significant interests due to their exceptional magnetic and catalytic properties, and can be used in super alloys, magnetic fluids, computer hard disks, magnetic sensor, catalyst etc [7]. Moreover, Co nanoparticles are also more focused in healthcare system now days due to its antiseptic action. The concentration dependent studies demonstrating antibacterial potentials of Co nanoparticles are very limited, and the studies on concentration dependent comparative efficacy for antibacterial actions of Co nanoparticles with respect to its bulk form as well as standard antibiotics are completely lacking to the best of our knowledge. In this context, we focused the attention on the synthesis of Co nanoparticles to determine their antibacterial efficacy against *S. aureus* and *E. coli* at different

concentrations, and their comparative analysis of antibacterial potentials with respect to bulk Co, oxytetracycline and gentamicin at different concentrations.

2. Materials and methods

2.1. Materials used

The different chemicals of analytical grade were used for this investigation. Cobalt chloride hexahydrate ($\text{CoCl}_2 \cdot 6\text{H}_2\text{O}$), hydrazine hydrate, sodium hydroxide and ethylene glycol were used for the synthesis of Co nanoparticles/nanofluids and purchased from Sigma Aldrich, USA. Dimethyl sulfoxide (DMSO) was purchased from SRL. Bulk Co powder was purchased from Central Drug House (CDH), New Delhi, India. Oxytetracycline and gentamicin were procured from Hi-media, Mumbai. The Muller-Hinton Agar (MHA), Muller-Hinton Broth (MHB) and nutrient broth (NB) were purchased from Hi-media, Mumbai, India and used for antibacterial studies. The *S. aureus* (MTCC 1430) and *E. coli* (MTCC 2127) were two bacterial strains in used in this study. These were gifted from the Department of Biotechnology, University of Jammu and revived by using the nutrient broth (NB).

2.2. Synthesis and characterization of Co nanoparticles

The synthesis of cobalt nanoparticles was carried out by reducing a cobalt(II) salt using hydrazine hydrate as reducing agent according to the method of Zhu et al. [8] with some modifications. In a typical procedure, cobalt chloride (10 g) was dissolved into 150 ml ethylene glycol and water mixture (2:1). The solution was stirred vigorously until it completely dissolves. The pH of the solution was adjusted to 12 using aqueous NaOH solution. The solution of CoCl_2 was then treated with the mixture of hydrazine hydrate (50 %). After about 30 min, black solid particles appeared. After the completion of reaction, the reaction mixture was centrifuged. The black particles collected were washed several times with triply distilled water and absolute ethanol to remove hydrazine, sodium, and chlorine ions. The final product was then dried in an oven at 60 °C.

The reduction reaction can be expressed as:



The characterization studies of synthesized nanoparticles were conducted by using various standard techniques like particle size analyzer (PSA), transmission electron microscopy (TEM) and scanning electron microscopy (SEM). The particle size distribution (PSD) study of the synthesized nanoparticles was conducted by using Malvern Instruments Zetasizer Nano-ZS instrument. The evaluation of the size and morphology of Co nanoparticles was done by using transmission electron microscope (Hitachi H-7500). The scanning electron microscope (SEM-EDS) using SEM (JEOL JSM – 6390LV) was used for the analysis of surface morphology of the Co nanoparticles.

2.3. Assessment of antibacterial efficacy

All the antimicrobial activity assays were performed in triplicate and confirmed by three independent experiments. The antimicrobial activity of synthesized Co nanoparticles and its comparison with oxytetracycline, gentamicin and bulk Co was investigated against the gram-positive i.e. *S. aureus* and gram-negative i.e. *E. coli* bacterial strains. The *in vitro* antibacterial activity was conducted as per agar well diffusion method by using Muller-Hinton agar. The overnight bacterial cultures (108 cfu/ml) were used for seeding of the autoclaved (at 121 °C and 15 lbs) Mueller Hinton agar medium. Seeded agar was later on poured in glass petri plates (30 ml) and allowed for its solidification. Six wells of 6 mm diameter were created into the agar plates and sealed with one drop of 0.8 % melted agar to prevent the leakage of tested compounds. Oxytetracycline, gentamicin, bulk Co and Co nanoparticles were poured (30 μl of each dilution) in the different wells and incubated at 37 °C for 24 hrs. The sensitivities of the bacterial strains to the different concentrations of tested compounds were indicated by clear zone around the wells. Diameters of zone of inhibition produced by of different concentrations of tested compounds were measured to quantify the antibacterial potentials. In present study, DMSO was used as negative control (NC), and oxytetracycline and gentamicin were used as positive control to compare the efficacy of the nanoparticles. Activity index (AI) and fold increase for the comparison of antibacterial potentials of Co nanoparticles with bulk Co, oxytetracycline and gentamicin was also calculated by using the values of zone of inhibition.

$$\text{Activity Index (AI)} = \frac{\text{Inhibition zone of the Co nanoparticles}}{\text{Inhibition zone of the bulk Co or oxytetracycline or gentamicin}},$$

$$\text{Fold increase (\%)} = \left(\frac{b - a}{a} \right) 100,$$

where, *a* and *b* refer to the inhibition zones of oxytetracycline/gentamicin/bulk Co and Co nanoparticles, respectively.

3. Results and discussion

Figure 1A is representing the PSD of Co nanoparticles. Sample of Co nanoparticles gives an overall z-average size of 145.6 nm with polydispersity index of 0.372, which revealed that the distribution consists of a single size mode without aggregates. TEM (Fig. 1B) and SEM (Fig. 1C) micrographs of Co nanoparticles showed that synthesized Co nanoparticles have spherical morphology and average size of 13 – 25 nm. SEM image also indicated that the prepared nanoparticles are of spherical shape. SEM picture specifies that individual nanoparticles are aggregated and give large sphere like cumulative structure.

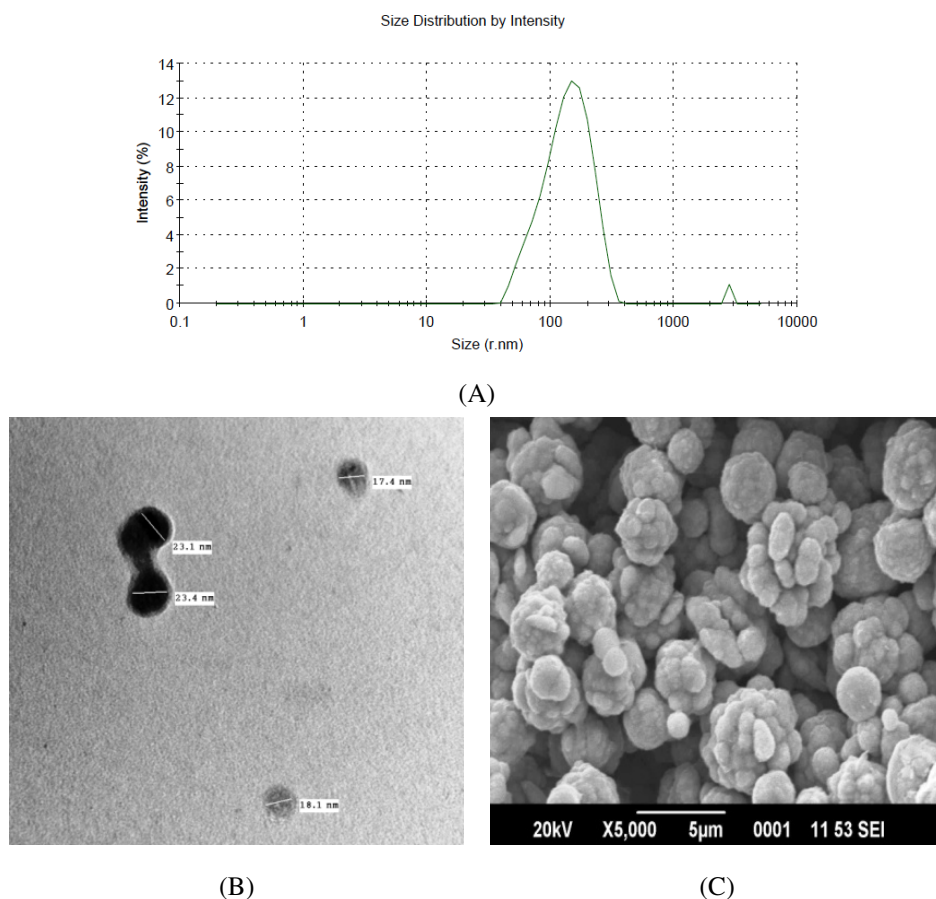


FIG. 1. (A) The particle size distribution (PSD) of Co nanoparticles. Micrograph of TEM (B) and SEM (C) of Co nanoparticles

In this study the synthesis of cobalt nanoparticles was followed as per the Zhu et al. method [8] with some modifications. But, the size of Co nanoparticles in our study was very smaller than the size observed in the study of Zhu et al. [8] i.e. 1 to 2 μm . This variation in size in our and study of Zhu et al. [8] was might be due to the variations in the reaction media. The pure ethylene glycol was used as solvent in the study of Zhu et al. [8], where as ethylene glycol and water mixture (2:1) was used in our study. Previous studies have also reported that solvents usually influence the growth and the morphologies of crystals, and even the formation and the structure of crystals [9–11], because the solvents can selectively control the surface energy of different crystallographic faces [12, 13].

Figure 2 is showing the representative images of bacterial culture plates with zone of inhibition produced by different concentrations of oxytetracycline, gentamicin, bulk Co and Co nanoparticles against *S. aureus* and *E. coli*. Table 1 shows the mean value of diameters of zone of inhibition for oxytetracycline, gentamicin, bulk Co and Co nanoparticles at different concentrations against both bacteria. In many of the earlier studies, both *S. aureus* and *E. coli* are routinely used to evaluate the antimicrobial activities of diverse nanoparticles [14, 15]. We also selected these two bacterial strains and found that synthesized Co nanoparticles produced larger zone of inhibition against *E. coli* than *S. aureus* at the same concentration. This indicated that action of Co nanoparticles is stronger against *E. coli* than *S. aureus*.

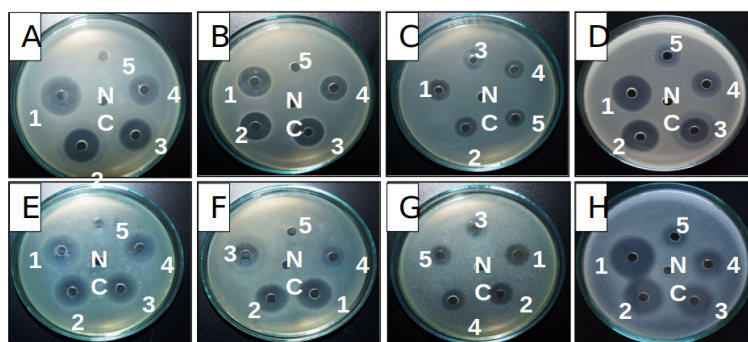


FIG. 2. Zone of inhibitions of oxytetracycline (A & E), gentamicin (B & F), bulk Co (C & G) and Co nanoparticles (D & H) against *S. aureus* (A–D) and *E. coli* (E–H) at different concentrations i.e. (1) 128.0 $\mu\text{g/ml}$, (2) 32.0 $\mu\text{g/ml}$, (3) 8.0 $\mu\text{g/ml}$, (4) 2.0 $\mu\text{g/ml}$, and (5) 0.5 $\mu\text{g/ml}$. NC represents negative control i.e. DMSO

TABLE 1. Zone of inhibition for oxytetracycline, gentamicin, bulk Co and Co nanoparticles (NPs) against *S. aureus* and *E. coli* at different concentrations

Conc. ($\mu\text{g/ml}$)	Zone of inhibition (mm) against <i>S. aureus</i>				Zone of inhibition (mm) against <i>E. coli</i>			
	Oxytetracycline	Gentamicin	Bulk Co	Co NPs	Oxytetracycline	Gentamicin	Bulk Co	Co NPs
128.0	20.92	17.33	9.50	20.17	19.33	16.83	11.33	21.50
64.0	19.17	14.17	9.33	18.00	18.50	13.83	10.67	19.33
32.0	17.17	13.17	9.25	17.00	16.67	12.67	9.83	18.17
16.0	16.17	11.83	9.00	15.83	15.33	11.33	9.50	17.00
8.0	15.42	10.92	8.92	15.33	14.42	10.33	9.33	15.75
4.0	14.17	10.58	8.67	13.67	12.83	9.17	9.25	15.00
2.0	13.00	10.08	8.50	12.83	12.17	8.17	9.00	14.17
1.0	8.50	8.17	8.33	11.75	8.17	7.17	8.92	13.33
0.5	0.00	0.00	8.08	10.67	0.00	0.00	8.67	11.92
0.25	0.00	0.00	7.92	9.33	0.00	0.00	8.50	11.17
0.125	0.00	0.00	7.50	8.50	0.00	0.00	8.25	9.67

Growth and survival of bacteria is also affected by size, morphology and concentration of nanoparticles. Previous studies have suggested that metal and metal oxide nanoparticles having 1 - 100 nm size and different shapes might have promising antimicrobial actions [16]. Thus, size of 13 – 25 nm and spherical shape of our synthesized Co nanoparticles revealed that our Co nanoparticles might be considered a promising antimicrobial candidate. The smaller size of the metal nanoparticles than the pores of bacterial cell membrane helps the easy transmission of nanoparticles across the cell wall to the cytoplasm, which further causes cell death [17]. Thus, the potent antibacterial potentials of Co nanoparticles might be attributed to their relatively smaller sizes and high amount of surface-area-to-volume ratio which facilitated close interaction with the bacterial membranes [18]. Earlier, it has been also reported that inhibition of bacterial growth increases with the increase in concentration of nanoparticles [19]. In our study, concentration dependent increase in diameter of zone of inhibition for Co nanoparticles was observed only up to 128.0 $\mu\text{g/ml}$ against both bacteria, and beyond this concentration, the size of the zone started to decrease. This might be due to the agglomeration of nanoparticles beyond these concentrations. Previously, it has been reported that optimum concentration exist for nanoparticles at which higher effects are noticed in comparison to more or less concentration [20]. Thus, in

this study, 128.0 $\mu\text{g/ml}$ was the optimum concentrations for Co nanoparticles against *S. aureus* and *E. coli*. Oxytetracycline, gentamicin and bulk Co showed increases in diameters of zones of inhibition in concentration dependent manners against both bacteria at all the tested concentrations. Oxytetracycline and gentamicin did not show zone of inhibitions at lower concentrations, i.e., below 1.0 $\mu\text{g/ml}$ against *S. aureus* and *E. coli* (Table 1). Thus, oxytetracycline and gentamicin were considered ineffective at lower concentrations. However, synthesized Co nanoparticles of present study were effective below these concentrations and produced marked zone of inhibition up to 0.125 $\mu\text{g/ml}$. The bulk Co also showed some antibacterial activity at all the tested concentrations, but the sizes of the zones of inhibition produced by it were of smaller size in comparison to its nano form. These results suggested that the range of inhibitory concentration for nano Co was broader with respect to oxytetracycline and gentamicin. Nano form of Co possesses much better antibacterial efficacy in comparison to its bulk form. The markedly better antibacterial effects of nano form of Co particularly at lower concentrations than other tested compounds of present study also revealed that Co nanoparticles may provide antibacterial action for longer duration with less frequency of applications. In the coming years, Co nanoparticles may be considered as a substitute for oxytetracycline, gentamicin and bulk Co in different fields in relation to reduce the occurrence of antibacterial resistance.

Earlier studies have also shown the antibacterial actions of Co nanoparticles prepared by different methods. Environmentally-benign synthesis of Co nanoparticles by using secondary metabolites from *Celosia argentea* plant extract have showed antibacterial activity against *E. coli* and *Bacillus subtilis* (*B. subtilis*) [21]. Studies have revealed that Co nanoparticles possesses potential for the development of antimicrobial nanomedicine. In a recent study, different varieties of Co nanoparticles synthesized by hydrothermal and ultrasonication methods have been found effective against amoeba species like *Acanthamoeba castellanii* (causative agent for threatening *Acanthamoeba* keratitis and granulomatous amoebic encephalitis) [22]. The results of this study revealed that cobalt phosphate $\text{Co}_3(\text{PO}_4)_2$ hexagonal microflakes, and 100 nm large cobalt hydroxide ($\text{Co}(\text{OH})_2$) nanoflakes showed potent amoebicidal activity as compared to granular cobalt oxide (Co_3O_4). Further, other types of Co based nonmaterials have also shown the antimicrobial actions. Cobalt oxide (Co_2O_4) nanoparticles have revealed the concentration (1, 50 and 100 mg/ml) dependent antibacterial activity against different bacterial strains like *E. coli*, *Pseudomonas aeruginosa* (*P. aeruginosa*) and *B. subtilis* [23]. Cobalt ferrite (CoFe_2O_4) nanoparticles have shown antibacterial activity against *E. coli* and its minimum inhibitory concentration was found at 50 mg/L [24]. A comparative study of cobalt ferrite (CoFe_2O_4) and silver-cobalt ferrite ($\text{Ag-CoFe}_2\text{O}_4$) nanoparticles, synthesized by wet ferritization and self-combustion methods using *Hibiscus rosa-sinensis* flower/leaf extracts, showed inhibitory actions against the different strains of bacteria and fungus, and the $\text{Ag-CoFe}_2\text{O}_4$ nanoparticles revealed better inhibitory potentials than CoFe_2O_4 nanoparticles obtained by either of the two methods [25].

The surface of the nanoparticles has a significant effect in their bioactivity and materials made up of nanoparticles have a much greater surface area per unit volume as compared to the materials made up of bigger particles (bulk materials). This makes nanoparticles more reactive and interactive to cell wall/membrane, which leads to their impairment and results in leakage of cellular contents [26]. Previous study has revealed that the antibacterial activity of the nanomaterials increased with an increase in the surface-to-volume ratio due to the decrease in size of nanoparticles, and the size of the nanoparticles might play a role in the antibacterial activity [17]. Although, the exact mechanisms by which the metallic nanoparticles produce antibacterial actions are not clear and still under debate. Some possible mechanisms are supposed by which they produce actions include, interaction of nanoparticles with the cell wall/membrane, formation of reactive oxygen species (ROS), release of metal ions etc. Electrostatic attraction, vander waals forces, receptor – ligand interactions and hydrophobic interactions are considered different ways which promote nanoparticles and bacterial contact [27–30]. Nanoparticles can cross microbe membranes after making contact and interfere with different bacterial metabolic pathways, and also induce changes in membrane shape and permeability. Nanoparticles inside cells interact with the different microbial components and cause inhibition of enzymes, deactivation of proteins, production of oxidative stress, modulate the gene expression and electrolyte imbalance [31]. Previous studies have revealed that different metal nanoparticles produce various types of ROS, which resulted in their antibacterial actions [32]. Different types of ROS are observed to inhibit transcription, translation, enzymatic activity, and the electron transport chain in bacteria [33, 34]. Metal ions also have tendency to attach and destroy the DNA molecule after entry into the bacterial cell [26]. It has been observed that metallic nanoparticles have enhanced potential to combat bacterial infections as compared to their salts, and the size of nanoparticles mostly influences the antibacterial mechanism [33, 35–37]. The fact that small sized nanoparticles tend to be more toxic to bacteria than large nanoparticles and their bulk form is due to the larger surface area to volume ratio of small nanoparticles [38]. So, the antibacterial actions by Co metal nanoparticles in this study might be due through different ways, which could be the reason for its better effects as compared to standard antimicrobials.

The calculated values of activity index (AI) as well as fold increase (%) are used to analyze the comparative antimicrobial efficacy of tested compound with respect to other compound [39]. The tested drug/compound can be

considered better against a particular bacterial strain, if its AI value is more than one. In our study, the AI for Co nanoparticles with respect to (w.r.t.) oxytetracycline, gentamicin and bulk Co against *S. aureus* and *E. coli* were calculated at various concentrations, and the values are presented in Table 2. The AI of Co nanoparticles was higher than 1 w.r.t. oxytetracycline upto 1.0 $\mu\text{g/ml}$ against *S. aureus* and at all the tested concentrations against *E. coli*. The AI of Co nanoparticles w.r.t. gentamicin and bulk Co was higher than 1 at all the tested concentrations against both bacterial strains. The calculation of fold increase (%) is another approach to determine the relative effect of the tested compound in contrast to other compounds. The positive value of fold increase reveals the better potentials of tested compound. However, negative value of fold increase reveals lesser efficacy of the tested compound than other compound against a particular bacterial strain at the same concentration. The Tables 3 presents the values of fold increase for Co nanoparticles w.r.t. oxytetracycline, gentamicin and bulk Co against *S. aureus* and *E. coli* at different concentrations. We observed in this study that the positive values of fold increase of Co nanoparticles w.r.t. other tested compounds against both bacterial strains supported the observations of AI. These findings are suggesting that Co nanoparticles may have better antibacterial potentials, particularly at lower concentrations, than other tested compounds of present study. So, Co nanoparticles may be used for applications/coating of different larger surface area, cellulose bandages, uniforms, bed linen, medical equipment, different utensils of medical fields etc., which may be useful as preventive approach to control microbial infections. This will make a substantial impact to reduce the hospitalized bacterial contamination, mortality, costs of treatment etc.

TABLE 2. Activity index of Co nanoparticles with respect to (w.r.t.) oxytetracycline, gentamicin and bulk Co against *S. aureus* and *E. coli* at different concentrations

Conc. ($\mu\text{g/ml}$)	Activity Index w.r.t. Oxytetracycline		Activity Index w.r.t. Gentamicin		Activity Index w.r.t. bulk Co	
	<i>S. aureus</i>	<i>E. coli</i>	<i>S. aureus</i>	<i>E. coli</i>	<i>S. aureus</i>	<i>E. coli</i>
128.0	0.96	1.11	1.16	1.28	2.12	1.90
64.0	0.94	1.05	1.27	1.40	1.93	1.81
32.0	0.99	1.09	1.29	1.43	1.84	1.85
16.0	0.98	1.11	1.34	1.50	1.76	1.79
8.0	0.99	1.09	1.40	1.52	1.72	1.69
4.0	0.96	1.17	1.29	1.64	1.58	1.62
2.0	0.99	1.16	1.27	1.73	1.51	1.57
1.0	1.38	1.63	1.44	1.86	1.41	1.50
0.5	–	–	–	–	1.32	1.38
0.25	–	–	–	–	1.18	1.31
0.125	–	–	–	–	1.13	1.17

Studies of last few years have showed that the applications of nanoforms of various metals like Ag, Cu, Ti or Zn etc has been augmented due to their bactericidal action against different bacterial strains. Nanoparticles of Ag, Cu, Zn etc. are commonly and widely employed for different purposes like bactericides in catheters, burn wound care, dental practices, antibacterial soaps etc. [40]. However, use of Ag nanoparticles has started to decline due to biological safety of Ag nanoparticles, pigmentation effect of Ag nanoparticles on teeth etc [41]. The Co, metal used in this study, is considered cheaper than silver. In the future, Co nanoparticles may replace the silver nanoparticles for various applications. Additionally, metal nanoparticles are considered better antimicrobial pharmaceuticals in comparison to organic nanoparticles due to their durability, high stability, lower mammalian cell toxicity etc. [42]. The promising antimicrobial efficacy revealed by Co nanoparticles might be very useful for several therapeutic applications in biomedical sciences. Applications of Co nanoparticles may also be extended to food industry, textile industry, nursing homes, water purification, air purifications, paint industry, sewage treatment, etc. There may also be new construction of numerous materials such as antibacterial plastics, antibacterial ceramics, antibacterial clothes, antibacterial stainless steels etc. by using Co nanoparticles. Moreover, applications of Co nanoparticles coated materials in hospitals

TABLE 3. Fold increase (%) of Co nanoparticles with respect to (w.r.t.) oxytetracycline, gentamicin and bulk Co against *S. aureus* and *E. coli* at different concentrations

Conc. ($\mu\text{g/ml}$)	Fold increase (%) w.r.t. Oxytetracycline		Fold increase (%) w.r.t. Gentamicin		Fold increase (%) w.r.t. bulk Co	
	<i>S. aureus</i>	<i>E. coli</i>	<i>S. aureus</i>	<i>E. coli</i>	<i>S. aureus</i>	<i>E. coli</i>
128.0	-3.59	11.21	16.35	27.72	112.28	89.71
64.0	-6.09	4.50	27.06	39.76	92.86	81.25
32.0	-0.97	9.00	29.11	43.42	83.78	84.75
16.0	-2.06	10.87	33.80	50.00	75.93	78.95
8.0	-0.54	9.25	40.46	52.42	71.96	68.75
4.0	-3.53	16.88	29.13	63.64	57.69	62.16
2.0	-1.28	16.44	27.27	73.47	50.98	57.41
1.0	38.24	63.27	43.88	86.05	41.00	49.53
0.5	–	–	–	–	31.96	37.50
0.25	–	–	–	–	17.89	31.37
0.125	–	–	–	–	13.33	17.17

may help reduce the prevalence of nosocomial infections. The utilization of Co nanoparticles coated materials in many industries may also be beneficial to check bacterial deterioration of material. Combination therapy of metal nanoparticles with antibiotics has showed some synergistic effects [43, 44]. Therefore, use of combination therapy of Co nanoparticles with standard antibiotics against simple or mixed type microbial infections may be extended for the formulations of more efficacious preparations.

4. Conclusion

In conclusion, the Co nanoparticles possess much better antibacterial efficacy than its bulk form and are also better than standard antibacterials, particularly at lower concentrations, against *S. aureus* and *E. coli*. In future, the strong antibacterial potentials of Co nanoparticles may extend its applications in different fields and could create a great revolution in the field of health care.

Acknowledgements

We are thankful to Department of Chemistry and Department of Biotechnology, University of Jammu(J&K), for providing essential facilities and support for conducting present investigation. The first author is highly thankful to CSIR UGC, New Delhi, India for providing the Junior Research Fellowship (JRF). The authors also acknowledge the support of SAIF STIC (Kochi), SAIF Chandigarh, CIL Chandigarh for providing the facilities for characterization of nanoparticles.

References

- [1] Henderson D.K. Managing methicillin-resistant staphylococci: a paradigm for preventing nosocomial transmission of resistant organisms. *Am. J. Infect. Control*, 2006, **34**, P. S46–S54, S64–S73.
- [2] Faúndez G., Troncoso M., Navarrete P., Figueroa G. Antimicrobial activity of copper surfaces against suspensions of *Salmonella enterica* and *Campylobacter jejuni*. *BMC Microbiol.*, 2004, **4**, P. 19–26.
- [3] Siddiqi K.S., Rahman A., Tajuddin, Husen A. Properties of Zinc Oxide Nanoparticles and Their Activity against Microbes. *Nanoscale Res. Lett.*, 2018, **13**, P. 2–13.
- [4] Peterson E., Kaur P. Antibiotic Resistance Mechanisms in Bacteria: Relationships between Resistance Determinants of Antibiotic Producers, Environmental Bacteria, and Clinical Pathogens. *Front. Microbiol.*, 2018, **9**, P. 2–21.
- [5] Ghosh A.K., Mitra M., et al. Antibacterial and catecholase activities of Co (III) and Ni (II) Schiff base complexes. *Polyhedron*, 2016, **107**, P. 1.
- [6] Mjos K.D., Orvig C. Metallodrugs in medicinal inorganic chemistry. *Chem. Rev.*, 2014, **114** (8), P. 4540–4563.
- [7] Zhang L., Lan T., et al. Template-free Synthesis of One-dimensional Cobalt Nanostructures by Hydrazine Reduction Route. *Nanoscale Res. Lett.*, 2011, **6**, P. 58.

- [8] Zhu Y., Zheng H., et al. Growth of Dendritic Cobalt Nanocrystals at Room Temperature. *J. Cryst. Growth*, 2004, **260**, P. 427–434.
- [9] Yang Q., Tang K., et al. PVA-Assisted Synthesis and Characterization of CdSe and CdTe Nanowires. *J. Phys. Chem. B*, 2002, **106**, P. 9227–9230.
- [10] Yang Q., Tang K., et al. Wet Synthesis and Characterization of MSe (M = Cd, Hg) Nanocrystallites at Room Temperature. *J. Mater. Res.*, 2002, **17** (5), P. 1147–1152.
- [11] Yang Q., Wang F., et al. The formation of fractal Ag nanocrystallites via γ -irradiation route in isopropyl alcohol. *J. Mater. Chem. Phys.*, 2002, **78**, P. 495–500.
- [12] Lee S.M., Cho S.N., Cheon J. Anisotropic Shape Control of Colloidal Inorganic Nanocrystals. *Adv. Mater.*, 2003, **15** (5), P. 441–444.
- [13] Puntès V.F., Kishnan K.M., Alivisatos A.P. Colloidal nanocrystal shape and size control: the case of cobalt. *Science*, 2001, **291** (5511) P. 2115–2117.
- [14] Yoon K.Y., Byeon J.H., Park J.H., Hwang J. Susceptibility constants of *Escherichia coli* and *Bacillus subtilis* to silver and copper nanoparticles. *Sci. Total Environ.*, 2007, **373**, P. 572–575.
- [15] Ruparelia J.P., Chatterjee A.K., Duttagupta S.P., Mukherji S. Strain specificity in antimicrobial activity of silver and copper nanoparticles. *Acta Biomater.*, 2008, **4**, P. 707–716.
- [16] Hoseinzadeh E., Makhdoomi P., et al. A review on nano-antimicrobials: Metal nanoparticles, methods and mechanisms. *Curr. Drug Metab.*, 2017, **18** (2), P. 120–128.
- [17] Azam A., Ahmed A.S., et al. Antimicrobial activity of metal oxide nanoparticles against Gram-positive and Gram-negative bacteria: a comparative study. *Int. J. Nanomed.*, 2012, **7**, P. 6003–6009.
- [18] Morones J.R., Elechiguerra J.L., et al. The bactericidal effect of silver nanoparticles. *Nanotech.*, 2005, **16** (10), P. 2346–2353.
- [19] Wahab R., Kim Y-S., et al. Formation of ZnO Micro-Flowers Prepared via Solution Process and their Antibacterial Activity. *Nanoscale Res. Lett.*, 2010, **5**, P. 1675–1681.
- [20] Ahamed M., Alhadlaq Hisham A., et al. Synthesis, characterization, and antimicrobial activity of copper oxide nanoparticles. *J. Nanomater.*, 2014, 637858.
- [21] Shahzadi T., Zaib M., et al. Synthesis of Eco-friendly Cobalt Nanoparticles Using *Celosia argentea* Plant Extract and Their Efficacy Studies as Antioxidant, Antibacterial, Hemolytic and Catalytical Agent. *Arab. J. Sci. Eng.*, 2019, **44**, P. 6435–6444.
- [22] Anwar A., Numan A., et al. Cobalt nanoparticles as novel nanotherapeutics against *Acanthamoeba castellanii*. *Parasite. Vector*, 2019, **12** (1), P. 280.
- [23] Raza M.A., Kanwal Z., Riaz S., Naseem S. Synthesis, characterization and antibacterial properties of nano-sized cobalt particles. *The 2016 World Congress on Advances in Civil, Environmental and Materials Research (ACEM'16)*, Jeju Island, Korea, 2016.
- [24] Venkatesan K., Supriya R., et al. Cobalt ferrite (CoFe₂O₄) nanoparticles for evaluation of antibacterial activity. *J. Ind. Chem. Soc.*, 2015, **92**, P. 637–639.
- [25] Gingasu D., Mindru I., et al. Green synthesis methods of CoFe₂O₄ and Ag-CoFe₂O₄ nanoparticles using hibiscus extracts and their antimicrobial potential. *J. Nanomater.*, 2016, 2106756.
- [26] Jung W.K., Koo H.C., et al. Antibacterial activity and mechanism of action of the silver ion in *Staphylococcus aureus* and *Escherichia coli*. *Appl. Environ. Microbiol.*, 2008, **74** (7), P. 2171–2178.
- [27] Li H., Chen Q., Zhao J., Urmila K. Enhancing the antimicrobial activity of natural extraction using the synthetic ultrasmall metal nanoparticles. *Sci. Rep.*, 2015, **5**, P. 11033.
- [28] Armentano I., Arciola C.R., et al. The interaction of bacteria with engineered nanostructured polymeric materials: A review. *Sci. World J.*, 2014, **2014**, 410423.
- [29] Gao W., Thamphiwatana S., Angsantikul P., Zhang L. Nanoparticle approaches against bacterial infections. *Wiley Interdiscip. Rev. Nanomed. Nanobiotechnol.*, 2014, **6**, P. 532–547.
- [30] Luan B., Huynh T., Zhou R. Complete wetting of graphene by biological lipids. *Nanoscale*, 2016, **8**, P. 5750–5754.
- [31] Xu Y., Wei M.T., et al. Exposure to TiO₂ nanoparticles increases staphylococcus aureus infection of HeLa cells. *J. Nanobiotechnol.*, 2016, **14**, P. 34.
- [32] Zhang W., Li Y., Niu J.F., Chen Y.S. Photogeneration of reactive oxygen species on uncoated silver, gold, nickel, and silicon nanoparticles and their antibacterial effects. *Langmuir*, 2013, **29** (15), P. 4647–4651.
- [33] Pelgrift R.Y., Friedman A.J. Nanotechnology as a therapeutic tool to combat microbial resistance. *Adv. Drug Deliv.*, 2013, **65**, P. 1803–1815.
- [34] Raffi M., Hussain F., et al. Antibacterial characterization of silver nanoparticles against *E. coli* ATCC-15224. *J. Mater. Sci. Technol.*, 2008, **24**, P. 192–196.
- [35] Dizaj S.M., Lotfipour F., et al. Antimicrobial activity of the metals and metal oxide nanoparticles. *Mater. Sci. Eng. C*, 2014, **44**, P. 278–284.
- [36] Ivask A., Kurvet I., et al. Size-dependent toxicity of silver nanoparticles to bacteria, yeast, algae, crustaceans and mammalian cells *in vitro*. *PLOS One*, 2014, **9** (7), e102108.
- [37] You C., Han C., et al. The progress of silver nanoparticles in the antibacterial mechanism, clinical application and cytotoxicity. *Mol. Biol. Rep.*, 2012, **39**, P. 9193–9201.
- [38] Mukha I.P., Eremenko A.M., et al. Antimicrobial activity of stable silver nanoparticles of a certain size. *Appl. Biochem. Micro.*, 2013, **49** (2), P. 199–206.
- [39] Selvarani M., Prema P. Evaluation of antibacterial efficacy of chemically synthesized copper and zerovalent iron nanoparticles. *Asian J. Pharm. Clin. Res.*, 2013, **6**, P. 223–227.
- [40] Kim J.S., Kuk E., et al. Antimicrobial effects of silver nanoparticles. *Nanomed.*, 2007, **3**, P. 95–101.
- [41] Sondi I., Salopek-Sondi B. Silver nanoparticles as antimicrobial agent: a case study on *E. coli* as a model for Gram-negative bacteria. *J. Colloid. Interf. Sci.*, 2004, **275**, P. 177–182.
- [42] Deravi L.F., Swartz J.D., Wright D.W. *The biomimetic synthesis of metal oxide nanomaterials*, Wiley, 2010.
- [43] Mu H., Tang J., et al. Potent antibacterial nanoparticles against biofilm and intracellular bacteria. *Sci. Rep.*, 2016, **6**, P. 18877.
- [44] Lai H-Z., Chen W-Y., Wu C-Y., Chen Y-C. Potent antibacterial nanoparticles for pathogenic bacteria. *ACS Appl. Mater. Interfaces*, 2015, **7**, P. 2046–2054.

Optical pathlength enhancement in ultrathin silicon solar cell using decorated silver nanoparticles on aluminium grating

S. Saravanan

Advanced Research Laboratory for Nanomaterials & Devices, Department of Nanotechnology Swarnandhra College of Engineering & Technology, Seetharampuram, Narsapur 534 280, West Godavari, Andhra Pradesh, India
shasa86@gmail.com

PACS 73.50.h, 84.60.Jt

DOI 10.17586/2220-8054-2020-11-1-86-91

In this work, ultrathin silicon solar cell design employed with the aid of periodic silver (Ag) nanoparticles substituted on an aluminium (Al) grating to improve the optical performance by using rigorous coupled-wave analysis (RCWA) method. The enhanced light absorption was observed in the silicon absorber region, due to the photonic and plasmonic modes between the metal and dielectric surface. With the optimal structure, maximum short-circuit current densities were observed at transverse magnetic ($\sim 36.13 \text{ mA/cm}^2$) and electric (31.59 mA/cm^2) modes. Further, we have demonstrated the effectiveness of the different ultrathin silicon solar cells with plasmonic structures and compared.

Keywords: Ultrathin, plasmonic, absorption, grating, nanoparticle, current density.

Received: 28 November 2019

Revised: 25 December 2019

1. Introduction

Nowadays, photovoltaic (PV) industries have been drawn great interest in silicon-based materials due to their natural abundance, low cost, long-term stability with well-equipped technology. These advanced technologies have the capability to yield higher conversion cell efficiency with better stability and researchers are continuously working in that area. Particularly, the nanostructure or thin-film material is appropriate and holding promises to enhance optical performance in PV devices [1]. However, the light trapping mechanism plays a crucial role in the solar cells and improving optical properties due to the various nanostructure such as a nanoparticle, nanorod, distributed Bragg reflector (DBR), nanograting (metal/dielectric) and different refractive indexed nanostructures [2–6]. Among these, noble metal nanoparticles and nanogratings are evidenced by the strong absorption enhancement in the visible and IR spectral region. It can change the optical properties easily by inducing the charge carrier generation. Past few decades, researchers are concentrating on the noble metal nanoparticles (Au, Ag, Al, Cu) in solar cells and excessively studied their performance [7–9]. Sidharthan and Murugesan explored the improved light absorption in the thin-film solar cell using an aluminium (Al) grating and silver (Ag) nanoparticles. The significant improvement noticed in the light absorption due to the combination of metal nanostructures. They have reported $\sim 5.4 \%$ enhanced absorption noticed when compared to the planar metal structure [10]. Zhang and Gu numerically explained the plasmonic light trapping effect in the ultrathin silicon solar cell with metal back reflectors using the finite difference time domain (FDTD) method. The maximum light absorption achieved at longer wavelengths due to the surface excitation and plasmon-coupled guided-mode resonance. The reference cell yields a current density of $\sim 3.55 \text{ mA/cm}^2$ and the silver integrated thin-film silicon solar cells achieved $\sim 6.8 \text{ mA/cm}^2$ within 100 nm thin silicon absorber layers. This investigation generated a significant effect on the plasmonic light-trapping structure-based solar cells [11]. Sathyamoorthy et al. studied the localized surface plasmon on a gold nanoparticles and found optimum thickness. The enhanced plasmonic effects were observed due to the size and shape of the dielectric medium around the gold nanoparticles. They demonstrated the gold nanoparticles were exhibited maximum plasmonic enhancement at 532 nm wavelength range with 60 nm size of the nanoparticles. Further, the Rayleigh scattering study was carried out with their experimental results [12]. Kakavelakis et al. investigated the efficiency and stability of perovskite solar cells by the addition of noble metal nanoparticles. They demonstrated the Ag and Au nanoparticles were providing their maximum power conversion efficiency. Similarly, the Al nanoparticles based solar cell device shown remarkably improved stability as compared others and achieved efficiency up to 13.5 % [13]. Enrichi et al. explored the various plasmonic enhanced solar cells with possible strategies with the results. They reported that the performance of solar cell was determined by the limiting factors, for example, reducing size (layers/particles), acceptance angle of active region, active materials, adopting light trapping schemes and exploiting spectral modification. Furthermore, the plasmonic nanostructure has been boosting by scattering and concentrating the electromagnetic field towards the active region in the device. The different plasmonic approaches were discussed and compared, also provided a few key conclusions

to understand the goal and future perspective of the field [14]. Morawiec et al. investigated the optical properties of localized surface plasmon resonance using self-assembled Ag nanoparticles (NPs) for photovoltaic applications. They fabricated Ag NPs on various substrates by the solid-state dewetting method and demonstrated the structural and optical properties of prepared nanostructures. The obtained spherical and uniform NPs were integrated as plasmonic backside reflector. The parasitic absorption in thin absorber deposited on the backside reflector measured using optoelectronic spectroscopic techniques [15].

In the proposed work, the ultrathin silicon solar cell performance was studied by using plasmonic backside reflectors. In section second, explained the designing approach of the complete solar cell. The current density, absorption spectrum, transverse electric (TE) and magnetic (TM) field analysis of optimal solar cell results were studied in section third. Finally, section fourth concludes the paper.

2. Designing approach

Figure 1 shows the illustration of ultrathin silicon solar cell and investigated using the RCWA method. In this simulation, the work was performed using the RCWA method, which is also known as a simple and fast technique. Initially, 50 nm thick layer of indium-tin-oxide (ITO) acting as an antireflection coating (ARC), silicon absorber with 50 and 100 nm thick aluminium (Al) layer acting as a substrate. On the metal substrate, Al grating added with 50 nm height (Gh) and 100 nm width (Gw) to scatter light at a larger angle. Because the metal nanogratings offer an opportunity for improving the electromagnetic (EM) fields near the surfaces by surface plasmon polariton [16].

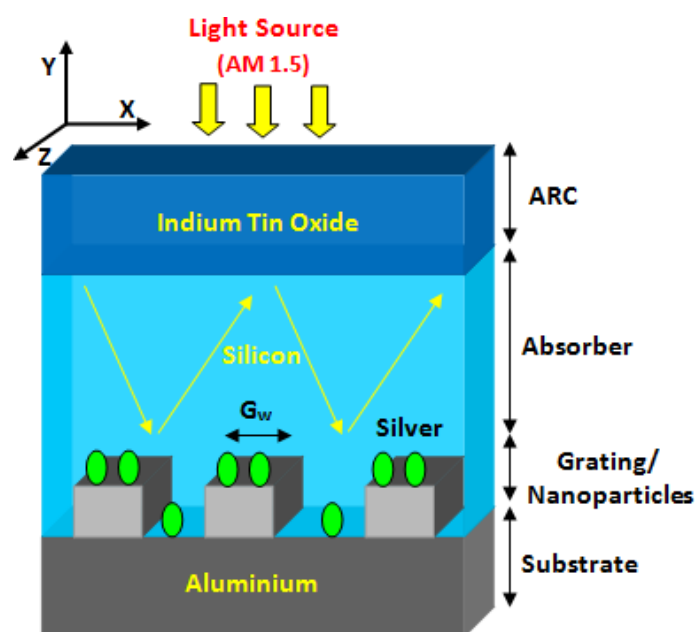


FIG. 1. The schematic diagram of ultrathin silicon solar cell

Furthermore, the 20 nm diameters silver (Ag) nanoparticles periodically substituted on the Al gratings to enhance light trapping mechanism. Shilpa et al. reported the nano-sized (or nanoparticles) structure enhanced the conversion efficiency of silicon thin-film solar cells. They demonstrated the highest absorption achieved by optimal geometrical parameters of Ag nanoparticles than the Au nanoparticles [17]. Probably, the silver nanoparticle is the suitable material to scatter the incident light into the absorber region as compared to other noble metals like gold (Au) and aluminum (Al). The light absorption was expected to be improved due to Al grating and Ag nanoparticles within the solar cell. Recently, various methods are available in the market to study the enhancing optical absorption and the conversion efficiency of PV devices [18]. Our simulation structure was terminated by two boundary conditions, first periodic boundary condition (PBC) is employed (parallel) in x - and y -axis, another perfect matched layer (PML) condition at z -axis and it has perpendicular to the light propagation direction. Here, the smallest spatial grid size (10 nm), harmonics (5) used throughout the simulation to maintain the accuracy of the RCWA calculations. Further, the designed solar cell structure extended and comparative studies are carried out using four different ultrathin film cells.

3. Results and discussion

To compare the performance of various solar cell structures, hereafter named as solar cell A: ARC only, B: ARC+ Substrate, C: ARC+ NPs+ Substrate, D: ARC+ GRA+ Substrate and E: ARC+NPs+GRA+Substrate. Figure 2 depicted the short-circuit current density (J_{sc}) of the different ultrathin film silicon solar cell.

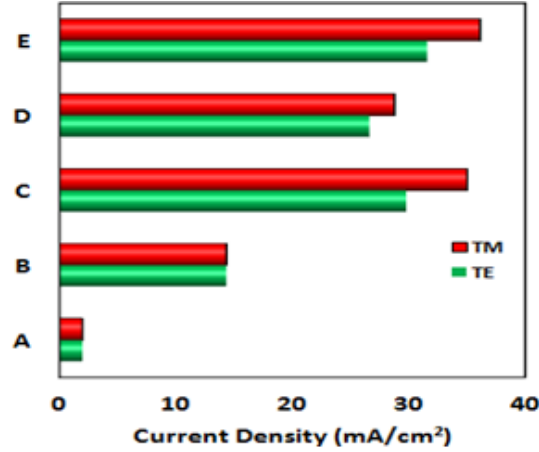


FIG. 2. The types of solar cell vs. short-circuit current density (mA/cm²)

The short-circuit current density (J_{sc}) associated with the number of light photons absorbed by the silicon absorber which could be generating the electron-hole pair combination and the charge carriers contributing the enhancement of current density [19]. Here, the improvement of different solar cell performance noticed with respect to simulated structure. First, solar cell 'A' shows less current density as compared to the other designed cell structure. From the result, cell 'E' reveals the highest current density in both modes such as transverse electric (~ 31.59 mA/cm²) and transverse magnetic (36.13 mA/cm²) fields due to the combination of Ag NPs and Al grating. The incorporation of metal nanostructures, the significant optical performance was noticed by inducing charge carrier generation and acts as a light scattering source [20–23].

Figure 3(a,b) shows the absorption spectrum plotted in both polarizations (TE & TM) conditions against the incident wavelength for five different ultrathin film solar cells. In TE case, Fig. 3(a) represents increased light absorption spectrum in the ascending order like cell A, B, C, D and E. The solar cell 'A' composed of anti-reflection coating (ARC) with absorber shows better absorption from 370 to 400 nm. Solar cell 'B' shows one sharp peak at 390 nm and enhanced broader curve noticed from 670 to 1110 nm due to planar Al substrate. Solar cell 'C' shows shifted the highest peak from 430 to 520 nm and the broader curve obtained significantly from 590 to 900 nm due to added Ag nanoparticles on the planar Al substrate. Similarly, the Ag nanoparticle replaced with Al grating and observed sharp or highest peak shifted at 520 nm but failed to prove a broader curve in longer wavelength region as shown in cell 'D'. Finally, cell 'E' depicts the sharp peak between the cells 'C' and 'D' because of the combined effect of metallic (grating & nanoparticles) nanostructure.

Figure 3(b) depicts various solar cell absorption spectrum under TM polarization. In cell 'A' and 'B' absorption curve not enhanced considerably. However, metal nanoparticle (Cell C) and grating (cell D) based designed structure reveals sharp and broader peaks in visible and infrared wavelength due to plasmonic effects such as LSP and guided-mode resonance (GMR). Solar cell 'E' remarkably enhanced the collection of the photon and observed broader curve in the visible range due to metal grating and nanoparticle, but infrared region reduced the plasmonic effect as compared previous (C and D) two designed solar cell where there is a need for more optimization.

Overall, both polarization causes a significant decrease in the absorption into three modes such as 760, 930 and 1120 nm. Stuart and Hall have demonstrated a smaller number of modes available in absorption spectra because of that enhanced absorption reduced significantly due to some circumstances [1]. However, the required light absorption to be enhanced due to suitable light trapping mechanism within ultrathin materials and it can improve beyond the $4n^2$ limits [12].

Figure 4(a–c) shows the electric field distributions in the designed ultrathin silicon solar cells using the RCWA method. The field has a normal incident angle (0°) and light is parallel to the grating and nanoparticles. Here, the optical concept such as diffraction, scattering, reflection and interference of the light provoked the intensity modulation. The Fabry-Perot resonance and strong guided modes observed at the different incident wavelength (420, 510 & 1160 nm) as shown in Fig. 4(a–c).

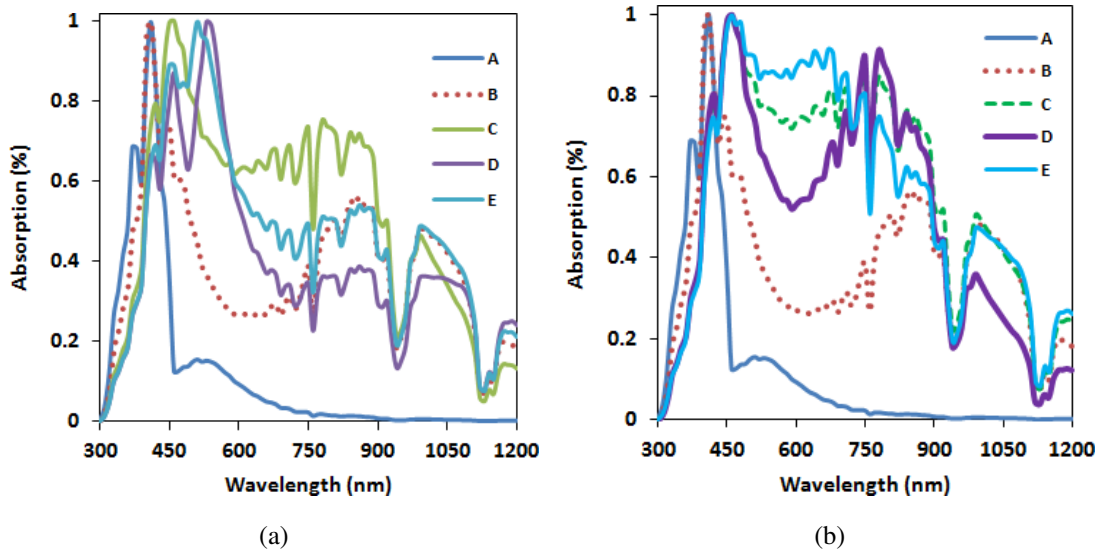


FIG. 3. Light absorption spectrum for TE (a), TM (b) polarization at different cell and comparison with standard solar spectrum ($\text{Wm}^{-2}\text{nm}^{-1}$) on the earth's surface (c)

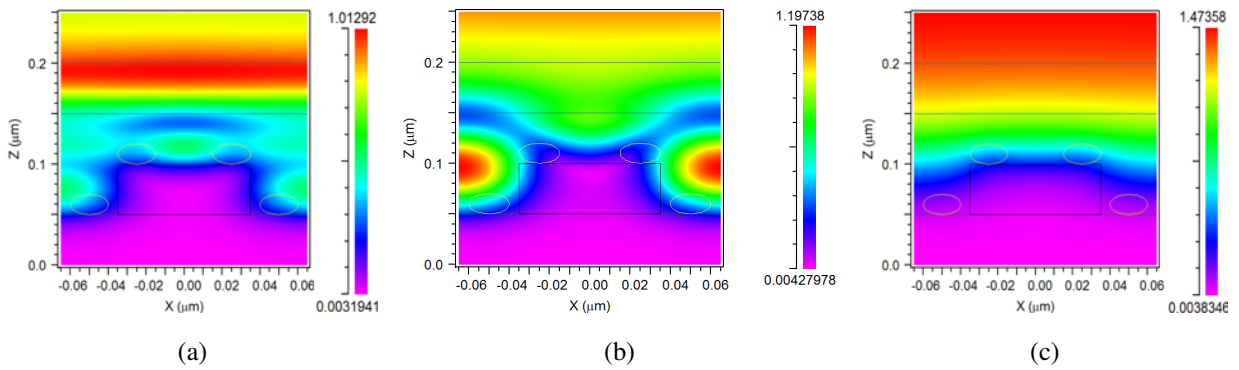


FIG. 4. Electric field intensity distributions with the guided modes at the wavelength (a) 420 nm, (b) 510 nm and (c) 1160 nm with the normal incident

Figure 5 depicts the light interference between the ultrathin silicon solar cells and compared various incident center wavelengths. Here, the metal forces vanishing of the electric field within the tiny distance. For a conductor, the electric field should have a node (grating) with that the coherent (superposition) monochromatic light described as standing wave above the absorber [24]. Fig. 5(a–e) shows the magnetic field distribution of difference shorter and longer wavelength. Fig. 5(a) shows the guided modes in the absorber region and localized surface plasmon on the Ag nanoparticles which generated the maximum number of charge carrier at 420 nm incident wavelength. The visible wavelengths are 460 and 670 nm shows the strongly localized surface plasmon (LSP) appeared on the Al grating and Ag nanoparticles as revealed in Fig. 5(b,c). Remarkably, infrared wavelength (990 and 1120 nm) indicates the strong LSP observed in Fig. 5(d) due to metallic nanostructures. Overall, the strong plasmonic effect shows through bright (red color) regions corresponding to the field intensity. The silver nanoparticles were supporting and boosting the collection of charge carrier absorption within the solar cells [9].

4. Conclusion

In conclusion, we have investigated the light trapping ability of Ag nanoparticle functionalized Al grating as back reflector in ultrathin silicon solar cell using RCWA method. The results shown enhanced optical performance in the visible and infrared region by accompanying the standing wave with in the absorber region. Finally, the optimized ultrathin silicon solar cell yielded the highest current density $\sim 31.59 \text{ mA/cm}^2$ (TE) and $\sim 36.13 \text{ mA/cm}^2$ (TM) within 50 nm silicon absorber region. Further, this work addressing the improved plasmonic effect in ultrathin film solar cells by using metal nanostructures with perfect forward scattering while getting rid of backward scattering.

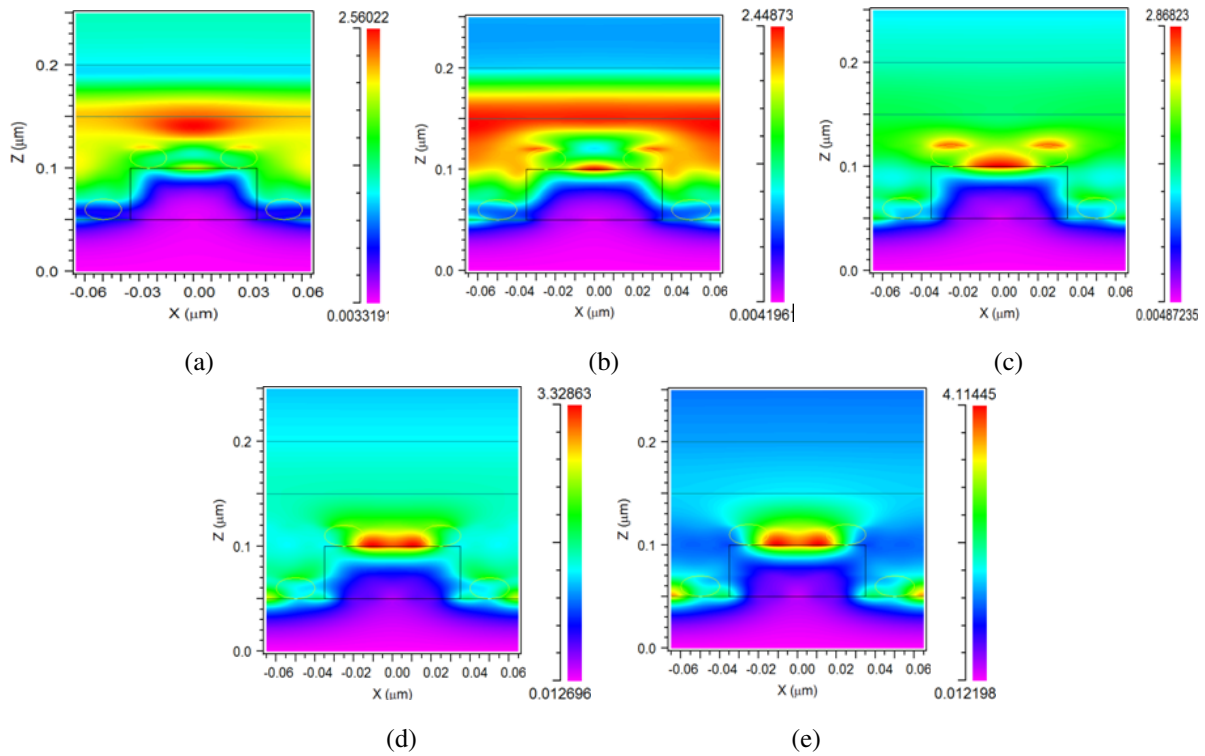


FIG. 5. The magnetic field intensity profiles at (a) 420 nm, (b) 460 nm, (c) 670 nm, (d) 990 nm and (e) 1120 nm

References

- [1] Stuart H.R., Hall D.G. Thermodynamic Limit to Light Trapping in Thin Planar Structures. *Journal of the optical society of America A*, 1997, **14**, P. 3001–3008.
- [2] Saravanan S., Dubey R.S. Optical absorption enhancement in 40 nm ultrathin film silicon solar cells assisted by photonic and plasmonic modes. *Optics Communications*, 2016, **377**, P. 65–69.
- [3] Enes Battal, Taha Alper Yogurt, Levent Erdal Aygun, Okyay Ali K. Triangular metallic gratings for large absorption enhancement in thin film Si solar cells. *Optics express*, 2012, **20**, P. 9458–9464.
- [4] Pillai S., Catchpole K.R., Trupke T., Green M.A. Surface Plasmon Enhanced Silicon Solar Cells. *Journal of Applied Physics*, 2007, **101**, 093105-1-8.
- [5] Saravanan S., Dubey R.S., et al. Design and optimization of ultrathin crystalline silicon solar cells using an efficient back reflector. *AIP Advances*, 2015, **5**, 057160-1-9.
- [6] Mariani G., Wong P.S., et al. Patterend radial GaAs nanopillar solar cells. *Nano Letters*, 2011, **11**, P. 2490–2494.
- [7] Zhang Y., Stokes N., et al. Toward ultra-thin plasmonic silicon wafer solar cells with minimized efficiency loss. *Scientific Reports*, 2014, **4**, P. 1–6.
- [8] Sreekanth K.V., Sidharthan R. Murukeshan V.M. Gap modes assisted enhanced broadband light absorption in plasmonic thin film solar cell. *Journal of Applied Physics*, 2011, **110**, 033107-1-5.
- [9] Zhang Y., Cai B., Jia B. Ultraviolet plasmonic aluminum nanoparticles for highly efficient light incoupling on silicon solar cells. *Nanomaterials*, 2016, **6**, P. 1–10.
- [10] Sidharthan R., Murukeshan V.M. Improved light absorption in thin film solar cell using combination of gap modes and grating back reflector. *Thin Solid Films*, 2013, **548**, P. 581–584.
- [11] Zhang Y., Gu M. Plasmonic light trapping for wavelength-scale silicon solar absorbers. *Frontiers of Optoelectronics*, 2016, **9**, P. 277–282.
- [12] Sathiyamoorthy K., Sreekanth K.V., et al. Surface plasmon enhancement in gold nanoparticles in the presence of an optical gain medium: an analysis. *Journal of Physics D: Applied Physics*, 2014, **44**, 425102-1-9.
- [13] Kakavelakis G., Alexaki K., Stratakis E., Kymakis E. Efficiency and stability enhancement of inverted perovskite solar cells via the addition of metal nanoparticles in the hole transport layer. *RSC Advances*, 2017, **7**, P. 12998–13002.
- [14] Enrichi F., Quandt A., Righini G.C. Plasmonic enhanced solar cells: summary of possible strategies and recent results. *Renewable and Sustainable Energy Reviews*, 2018, **82** (3), P. 2433–2439.
- [15] Morawiec S., Mendes M.J., Priolo F., Crupi I. Plasmonic nanostructure for light trapping in thin-film solar cells. *Materials Science in Semiconductor Processing*, 2019, **92**, P. 10–18.
- [16] Alan X., Wang, Xianming K. Review of Recent Progress of Plasmonic Materials and Nano-Structures for Surface Enhanced Raman Scattering Materials. *Materials*, 2015, **8**, P. 3024–3052.
- [17] Shilpa G.D., Subramanyam T.K., Sreelakshmi K., Uttarakumari. Study and optimization of metal nanoparticles for the enhanced efficiency thin film solar cells. *Materials Science Engineering*, 2016, **149**, 012074-1-6.

- [18] Kim R.S., Zhu J., et al. E-Beam deposited Ag-nanoparticles plasmonic organic solar cell and its absorption enhancement analysis using FDTD-based cylindrical nanoparticle optical model. *Optics Express*, 2012, **20**, P. 12649–12657.
- [19] Pudasaini P.R., Arturo A.A. Nanostructured thin film silicon solar cells efficiency improvement using gold nanoparticles. *Physica Status Solidi A*, 2012, **209**, P. 1475–1480.
- [20] Lim S.P., Pandikumar A., et al. Promotional effect of silver nanoparticles on the performance of N-doped TiO₂ photoanode-based dye-sensitized solar cells. *RSC Advances*, 2014, **4**, P. 48236–48244.
- [21] Lim S.P., Pandikumar A., Huang N.M., Lim H.N. Enhanced photovoltaic performance of silver titania plasmonic photoanode in dye-sensitized solar cells. *RSC Advances*, 2014, **4**, P. 38111–38118.
- [22] Yu B., Leung K.M., et al. Synthesis of Ag–TiO₂ Composite Nano Thin Film for Antimicrobial Application. *Nanotechnology*, 2011, **22**, 115603-1-9.
- [23] Shah S., Noor I.M., et al. Plasmonic effects of quantum size metal nanoparticles on dye-densitized solar cell. *Optical Materials Express*, 2017, **7** P. 2069–2083.
- [24] Shore B.W., Feit M.D., et al. Electric field enhancement in metallic and multilayer dielectric gratings. *SPIE*, 1997, **2633**, P. 709–714.

Synthesis and characterization of bismuth selenide thin films by thermal evaporation technique

H. Sharma^{1,2}, Y. C. Sharma¹

¹Department of Physics, Vivekananda Global University, Jaipur-303012, Rajasthan, India

²Department of Physics, Kanoria P.G College, Jaipur-302017, Rajasthan, India

aks17686@gmail.com

DOI 10.17586/2220-8054-2020-11-1-92-98

In recent years, bismuth selenide has attracted a good deal of attention due to its unique properties. Bismuth selenide is a topological insulator which has surface conductivity that makes it an attractive compound for practical applications. Employing the solid state reaction, bulk bismuth selenide compounds in four different stoichiometric ratios of Bi/Se have been prepared at 850 °C in a muffle furnace. The synthesized bismuth selenide compounds were characterized using XRD. Two most intense peaks were identified, corresponding to the (006) and (0015) planes which conform with the formation of bismuth selenide. Thin films of these compounds were deposited on Soda lime glass substrate by thermal evaporation method. Thin films were characterized by EDAX, SEM and RAMAN. Two clear vibration modes are observed corresponding to E_g^2 and A_{1g}^2 modes. Optical properties of thin films were also studied. Electrical band gap is found to increase with the increment in the amount of Bismuth in thin films.

Keywords: Bismuth selenide, Thin Film (TF), XRD, RAMAN, EDX, SEM, UV-VIS.

Received: 11 November 2019

Revised: 3 December 2019, 20 December 2019

1. Introduction

At present, thermoelectric materials (TE) are considered in many applications such as solid state power generating devices and refrigerating devices [1]. Bi_2Se_3 is a hot area of research because it is topological insulator which is an insulator but has surface conductivity. Bi_2Se_3 is a semiconductor belong to group V-VI [2]. Bismuth Selenide is environmentally friendly because ozone depleting elements like chlorofluorocarbons (CFCs) are not produced by it [3]. Recently by calculations and photoemission spectroscopy measurements on bismuth Selenide it is observed that it is a three dimension topological insulator with nondegenerate spins that makes it a perfect option in electronic and spintronics applications [4]. It is a well-known compound for its unusual anisotropic layered crystal structure, which increases the electrical conductivity of bismuth selenide [5, 6]. Bi_2Se_3 is a compound which has rhombohedral crystal structure. Bi_2Se_3 possess stacked layers of Bismuth and selenium that are held together by weak Van der Waals interactions. Each layer of bismuth selenide is one quintuple layer (QL) and five atoms are covalently bonded with each other along Z axis in the order of Se-Bi-Se-Bi-Se [7]. Bi_2Se_3 have applications in photosensitivity, photoconductivity and thermoelectric power devices because of their fantastic electrical and optical properties [8]. Therefore it is essential to determine the optical properties of bismuth selenide such as light absorption. According to R H Bari, Bi_2Se_3 is a narrow band semiconductor [9]. Band gap of Bi_2Se_3 lies between 0.2–0.3 eV in early report [10, 11]. Thin films of Bismuth Selenide have wide technological applications in solar devices, optoelectronic chemical devices [12], optical recording system and decorating coatings [13]. There are various methods to synthesize thin films including: chemical deposition [14], Magnetron sputtering [15], Successive ionic layer adsorption (SILAR) method [16], Molecular beam epitaxy [17, 18], Thermal evaporation [19] etc. In this communication, we report the synthesis of bulk bismuth selenide of different stoichiometries (0.123 to 0.309) by solid state reaction of bismuth and selenium. The aim of preparing four different samples is to investigate the effect of composition ratio on the structural and optical properties and to find out the best stoichiometry out of four different samples, which could be more applicable in field of photoelectronic and solar application. As in earlier literature only bi-layer thin films of Bi_2Se_3 having elemental ratio of 0.66 have been discussed. But in the present work, bulk bismuth selenide compounds and their thin films deposition by thermal evaporation process have been discussed. Achieved band gap values have been compared with previous literature to determine the best thin film which has lowest band gap, could be used in solar applications. Various characterizations techniques such as EDAX, RAMAN, SEM and optical microscopy were employed to study the films.

2. Experimental Analysis

2.1. Synthesis of Bismuth Selenide solid sample

Elemental precursors of Bi and Se of 99% purity were taken in quartz ampoules. After that ampoules were sealed maintaining the vacuum pressure of 10^{-6} torr. These ampoules were allowed to heat in muffle furnace at $850\text{ }^{\circ}\text{C}$ for 15 minutes and then they were allowed to cool at room temperature. Finally, these ampoules were broken and samples were taken out and chunks were prepared for the preparation of thin films.

2.2. Synthesis of bismuth Selenide thin films

Thermal evaporation method is used for deposition of thin films from the prepared chunks. Thin films have been fabricated on Soda Lime Glass substrates. Prior to the deposition, all the substrates were rinsed in acetone and ultrasonically cleaned to remove the contamination from the surface of the substrates. Then hot bath were given at hot plate at the temperature of $70\text{ }^{\circ}\text{C}$ with 80 rpm and lastly were rinsed in distilled water and were dried. Chunks of bismuth selenide prepared by solid state reaction method were used as a target for the preparation of thin films, employing the thermal evaporation method. The deposition chamber was evacuated to the vacuum of 10^{-6} torr and for uniform deposition substrates were rotated at constant rate of 8 rpm. Deposition has been done at constant rate of $\sim 2\text{ \AA/s}$. Four different thin films of bismuth selenide with the thickness of 100 nm has been synthesized by using the four solid state reacted compounds. Further these thin films have been annealed at the temperature of $200\text{ }^{\circ}\text{C}$. The phase and crystallography structure of solid samples of bismuth selenide have been studied by XRD. RAMAN spectra of thin films were also analysed. SEM and EDX were characterization have been performed to study morphological features and elemental composition respectively. Optical properties of thin films also have been analysed.

3. Result and discussion

3.1. X-Ray diffraction

To identify the crystallography of four solid samples of bismuth selenide, X-ray diffraction technique was used. Fig. 1 shows the XRD pattern of four solid compounds of bismuth selenide. From the XRD data it is clearly seen that two peaks are observed strongly along (006) and (0015) planes.

It means that bismuth selenide nanoparticles have the prominent growth in the direction of (006) and (0015) planes. The observed peaks are approximately matching with standard JCPDS data. The planes (006), (0015) correspond to theoretical data of Bi_2Se_3 (JCPDS file no. 33-214). Researchers observed peak corresponding to (006) plane and found that as bismuth increases in composition ratio, peaks shift towards high theta.

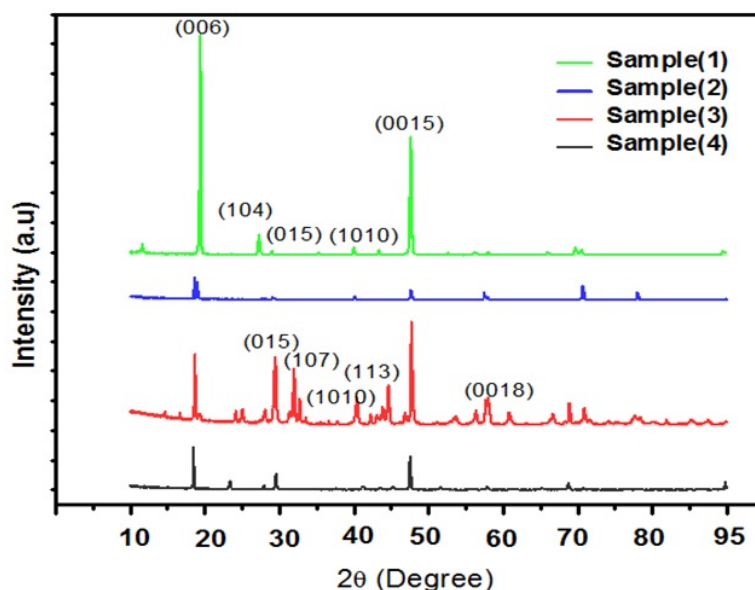


FIG. 1. XRD pattern of four solid compounds of bismuth selenide

3.2. Elemental analysis by EDX (ENERGY DISPERSIVE X-RAY SPECTROSCOPY) of as deposited bismuth selenide thin films

The elemental compositions of thin films were analyzed by energy X-ray spectroscopy (EDAX). Table 1 represents the results of elemental composition of bismuth and selenium present in as-deposited thin films (TF).

TABLE 1. Atomic percent and weight percent of Bismuth and Selenium in thin films

Sample Name	Wt%		At%		Bi/Se
	Bi	Se	Bi	Se	Atomic Ratio
TF-1	24.5	75.5	11.02	88.98	0.123
TF-2	31.57	68.3	14.85	84.15	0.176
TF-3	32.55	67.5	15.42	84.58	0.182
TF-4	45.1	54.9	23.63	76.37	0.309

The EDX results indicate the presence of bismuth and selenium in thin films of different stoichiometry. The ratio of Bi/Se is increases from TF-1 to TF-4.

3.3. SEM (Scanning Electron Microscopy)

The surface morphology of synthesized and annealed thin films of bismuth selenide have been studied against the SEM images. Fig. 2 shows the SEM images of as deposited thin film and annealed thin films. The data is extracted of grain size of five to six particles and presented the mean data of these values.

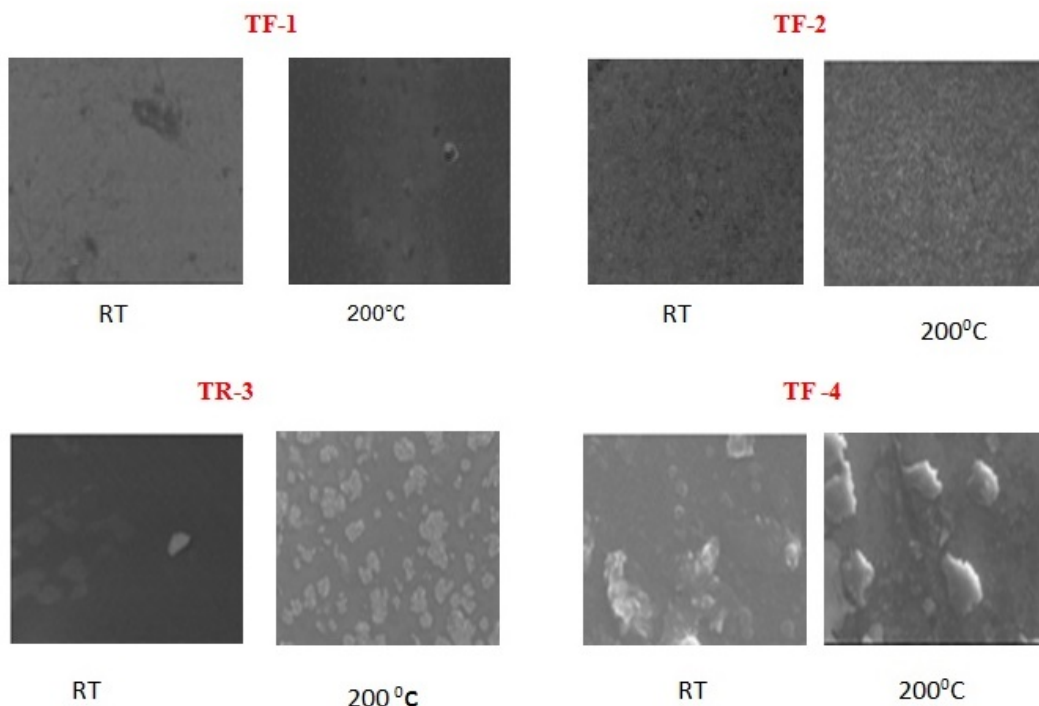


FIG. 2. SEM images of Bismuth Selenide thin films

From the SEM images it is clearly observed that annealing treatment affects the size of particle. It is profound that the grain size of thin films increased with the annealing treatment. A comparative analysis of grain size as a function of stoichiometric variation and annealing treatment has been disclosed in Table 2. The average grain size calculated using of different particle in single film. TF-1 to TF-3 the average grain size goes on decreasing. For films with higher concentration of bismuth ions, the growth occurs with multiple nucleation centers resulting in lower grain size, while for lower concentration of bismuth ions, comparatively lower nucleation centers gives higher grain size (20).

TABLE 2. Average grain size of particle in thin films for as-deposited and annealed thin films

Thin film (TF)	Average grain size RT thin films (nm)	Average grain size annealed thin films (nm)
(1)	41	100
(2)	60	97
(3)	28	54
(4)	124	137

This phenomenon is fully followed for TF-1, 2, 3. But TF-4 showed the higher grain size in comparison to other thin films and which may be due to some the formation of some other phases.

3.4. Raman Spectroscopy

Raman spectrometer is employed to study the vibration modes in thin films with wavelength of 532 nm (diode-pumped frequency doubled Nd:V) with better resolution. Theoretically there are four Raman active modes in bismuth selenide (Bi_2Se_3). There are two A_{1g} modes and two E_g modes in bismuth selenide (Bi_2Se_3). A_{1g} modes represent the atomic vibration along perpendicular to the layer and E_g modes are atomic vibration in plain [21].

Figure 3 shows the Raman spectrum of different four thin films of bismuth selenide. Clear Raman modes were observed at 131 cm^{-1} and 170 cm^{-1} corresponding to E_g^2 and A_{1g}^2 modes of Bi_2Se_3 [22]. The peaks result indicates that annealed thin films of bismuth selenide have better vibration modes than room temperature thin films. In annealed thin films A_{1g} mode is activated but in room temperature thin films it is not observed sharply. The low frequency modes E_g^1 and A_{1g}^1 not observed due to high Rayleigh background. The intense peaks of E_g^2 and A_{1g}^2 in bismuth selenide thin films reveal information of good quality.

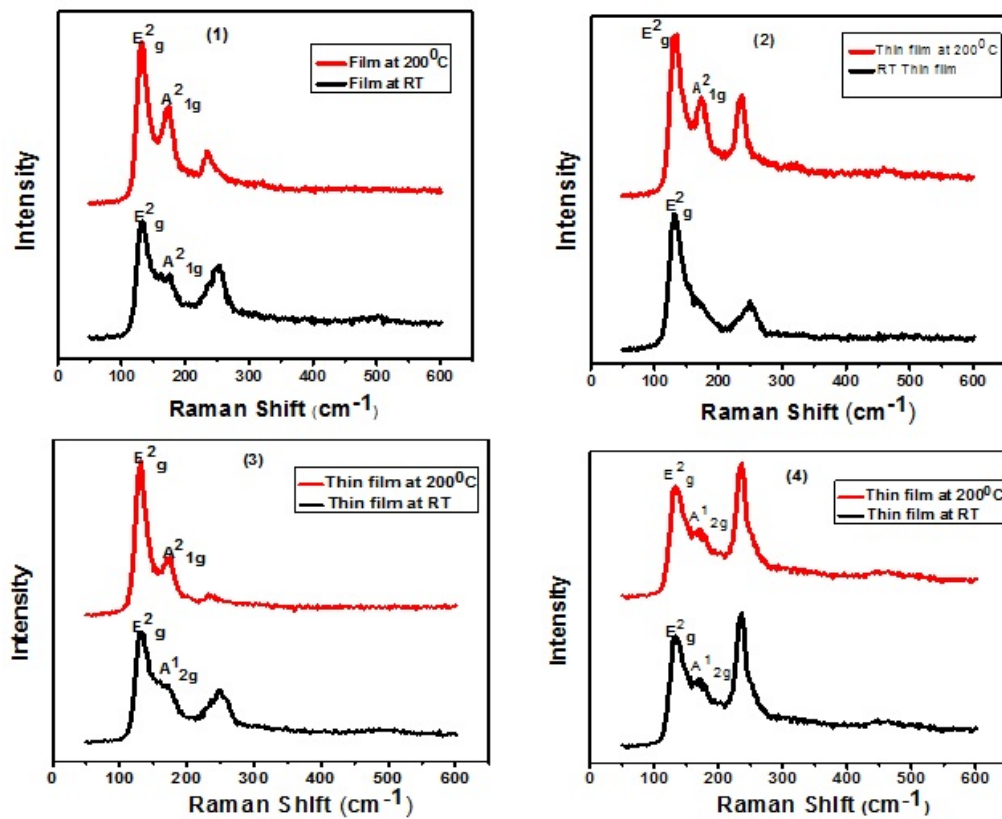


FIG. 3. Raman spectrum for thin films at RT and annealing temperature $200\text{ }^{\circ}\text{C}$ for different four samples

4. Optical Studies

Optical features of bismuth selenide thin films have been investigated by using UV-VIS spectrophotometer [LAMBDA 750 (Perkin Elmer)]. Optical absorption spectra has been recorded at room temperature within the spectral range of 400 to 1600 nm for as- deposited and annealed thin films.

The variation in optical absorbance with wavelength is delineated in Fig. 4. The absorption coefficient (α) is a function of photon energy. The absorption coefficient (α) is calculated using Lambert law [23] as:

$$\alpha = (2.303A)/t,$$

where A is the optical absorbance and t is the thickness of the thin films. Thickness of all thin films is same of 100 nm. Absorption coefficient (α) provides the information about the type of optical transition occurred between conduction band and valence band of the sample.

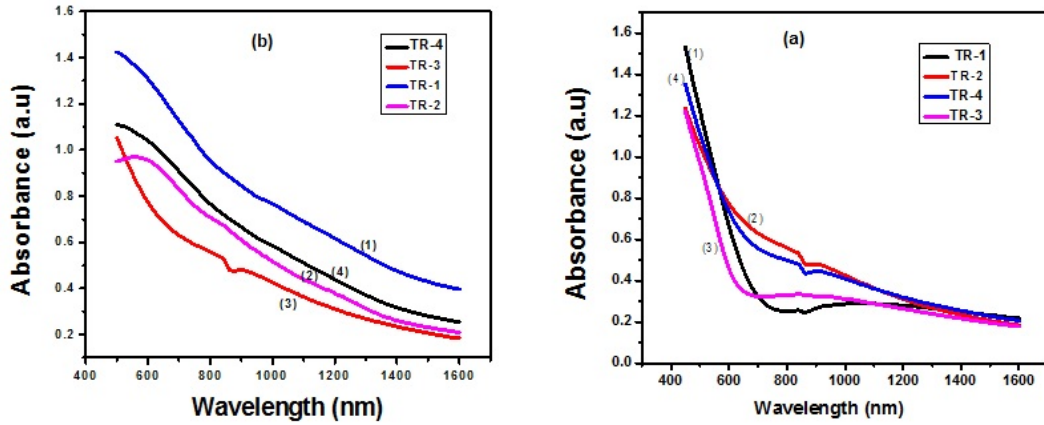


FIG. 4. Optical absorption of bismuth selenide thin films (a) as-deposited (b) annealed at 200 °C

The Tauc's equation for the calculation of direct band gap is given as:

$$\alpha h\nu = A(h\nu - E_g)^n,$$

where A is a constant which is related to the effective masses associated with the bands and E_g is band gap between conduction band and valence band. The index n depends on the type of electronic transitions, for direct transition has $n=1/2$ or $3/2$ while for indirect transition $n=2$ or 3 , whether the transition are allowed or forbidden [24].

Tauc's plot for thin films have been presented in Fig. 5. The optical absorption coefficient is found to be in order of 10^{-6} m supporting the allowed direct band transition of the material. Allowed optical band gap is calculated by extrapolating the edge on energy axis ($h\nu$). The calculated band gap values are found within the range of 1.79–1.94 eV for as-deposited thin films and 1.33–1.4 eV for annealed thin films. The band gap values obtained for fabricated thin films in this work exhibited the lower values in comparison to the earlier data presented by researchers [25, 26]. Annealing treatment caused the decrement in the value of band gap. Further, the effect of stoichiometry variations is also detected in the values of band gap as it goes on decreasing with the increase in at% of Bi in the film composition. It may be due to smaller at% of Se; smaller would be the possibility of formation of localized levels in the forbidden gap. When the dislocation density is fairly high there is an increase in band gap of semiconductor material [27]. TF-1 to TF-3 band gap value decreases. Elemental value of Se in TF-4 is very low in amount in comparison to other. Because selenium is a semiconductor and very low amount of Selenium increase the band gap of TF-4.

The obtained values of band gap of bismuth selenide thin films are near the optimum value for photovoltaic conversion, which suggests that Bismuth Selenide thin films have promising applications in the field of solar energy and photoelectronics [28].

5. Conclusions

In previous work, researchers synthesized Bi_2Se_3 thin films having elemental ratio of 0.66, but in the present work, different thin films with different stoichiometric ratios (0.123 to 0.309) of Bi/Se have been prepared on glass substrate by thermal evaporation method. The foremost aim of the preparation of four different samples is to investigate the effect of compositional variation on the structural and optical properties and to find out the best stoichiometry out of four different samples, which could be more applicable in field of photoelectric and solar application. The EDAX of

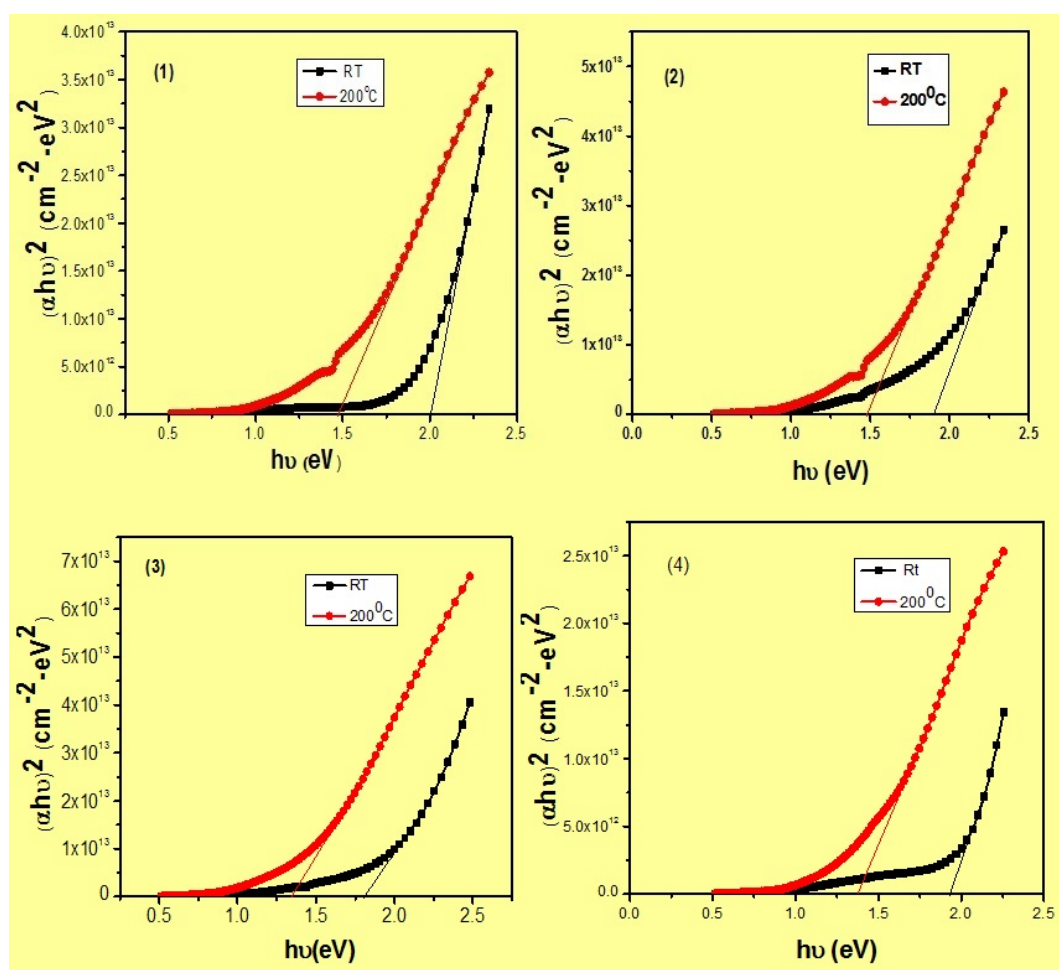


FIG. 5. Variation of $(\alpha h\nu)^2$ Vs $h\nu$ for as-deposited and annealed thin films

thin films indicated that the films were non-stoichiometric. The process of agglomeration becomes more prominent with the increment in of Bi/Se ratio. TF-1 which has elemental ratio 0.123 showed band gap 1.79, further insertion of Selenium in thin films caused a decrement in the band gap of thin films. But TF-4 which has high value of elemental ratio (0.309) of Bi/Se showed higher band gap value because of very low concentration of selenium. Out of four thin films, TF-3 which has elemental ratio 0.182 showed good optical results. Obtained band gap values of thin film reflect that these thin films used in field of solar energy. So that in many applications TF-3 could be used in place of Bi_2Se_3 thin film.

References

- [1] Kadel K., Latha Kumari L., Wz Li, Huang J.Y., Provencio P.P. Synthesis and Thermoelectric properties Bi_2Se_3 . *Nanostructures, Nanoscale Research Letters*, 2010, **6**, Article Number-57.
- [2] Kannan A.G., Manjulavalli T.E. Structural, optical and electrical properties of Bi_2Se_3 thin films prepared by spray pyrolysis technique. *International Journal of Chem Tech Research*, 2015, **8**, P. 599–606.
- [3] Ding Z., Bux S.K., King D.J., Chang F.L., Chen T.-H., Huang S.C., Kaner R.B. Lithium intercalation and exfoliation of layered Bismuth Selenide and Bismuth telluride. *Journal of Material Chemistry*, 2009, **17**, P. 2588–2592.
- [4] Kong D., Randel J.C., Peng H., Cha J.J., Meister S., Yulin C., Shen Z.X., Manoharan H.C., Cui Y. Topological insulator nanowires and nano ribbons. *Nano letters*, 2009, **10**(1), P. 329–333.
- [5] Zhang H., Liu C.X., Qi X.L., Dai, XFang Z., Zhang S.C. *Nature Physics*, 2009, **5**, P. 438–442.
- [6] Ali Z., Butt S., Cao C., Faheem K.B., Tahir M., Tanveer M., Aslam I., Rizwan M., Idrees F., Khalid S. Thermochemically evolved nanoplates of bismuth selenide with enhanced thermoelectric figure of merit, 2014, **4**, P. 117129.
- [7] Sun L., Lin Z., Peng J., Weng J., Huang Y., Luo Z. Preparation of Few-layer Bismuth Selenide by Liquid Phase Exfoliation and its optical absorption properties. *Scientific Report-4*, Article Number-4794, 2014.
- [8] David M. Roae. *CRC Handbook of Thermoelectric*. CRC Press, Boca Raton, FL, 1995.
- [9] Bari R.H., Patil L.A. Synthesis and characterization of bismuth selenide thin films by chemical bath deposition technique. *Indian Journal of Pure and Applied physics*, 2010, **48**, P. 127–132.

- [10] Mishra S.K., Satpathy S., Jepsen O.J. Electronic structure and thermoelectric properties of bismuth telluride and bismuth selenide. *Journal of physics, Condensed Matter*, 1997, **9**, P. 461–470.
- [11] Torane A.P., Bhosle C.H. Preparation and characterization of electrodeposited Bi_2Se_3 thin films from nonaqueous medium. *Material Research Bulletin*, 2001, **36**, P. 1915–1924.
- [12] Xiao C., Yang J., Jhu W., Peng J., Zhang J. Electrodeposition and characterization of Bi_2Se_3 thin films by electrochemical atomic layer epitaxy (ECALE). *Electrochimica Acta*, 2009, **54**, 27, P. 6821–6826.
- [13] Yesugade N.S., Lokhande C.D., Bhosle C.H. Structural and optical properties of electrodeposited Bi_2Se_3 , Sb_2S_3 and As_2S_3 thin films. *Thin Solid Films*, 1995, **263**(2), P. 145–149.
- [14] Meyvel S., Sathya P., Parthibavarman M. Annealing Effect On Structure, Optical and Electrical Properties of Bismuth Selenide Thin Films using Chemical Bath Deposition. *Elixir International Journal*, 2016, **101**, P. 43922–43926.
- [15] Sapkota Y.R., Mazumdar D. Bulk transport properties of bismuth selenide thin films grown by magnetron sputtering approaching the two dimensional limit. *Journal of Applied Physics*, 2018, **124**, P. 105306.
- [16] Sankapal B.R., Pathan H.M., Lokhande C.D. Growth of multilayer Bi_2Se_3 – Sb_2S_3 thin films by SILAR technique. *Indian Journal of Engineering and Material Science*, 2001, **8**, P. 223–227.
- [17] Song C.L., Wang Y.L., Jiang Y.P., Xi Chen, Jia J.F., Wang Y., Dai Z.F.X., Zhang S.C., Kun Q. Topological Insulator Bi_2Se_3 thin films grown on double layer graphene by molecular beam epitaxy. *Applied Physics Letter*, 2010, **97**, P. 143118.
- [18] Kou X.F., He L., Xiu F.X., Lang M.R., Liao Z.M., Wang Y., Fedorov A.V., Yu X.X., Tang J.S., Huang G., Jiang X.W., Zhu J.F., Zou J., Wang K.L. Epitaxial growth of high mobility Bi_2Se_3 thin films on CdS. *Applied Physics letters*, 2011, **98**, P. 242108.
- [19] Augustine S., Anpil Si, Karg J.K., Mathai E. Structural, electrical and optical properties of Bi_2Se_3 and $\text{Bi}_2\text{Se}_{3-x}$ Ternary thin films. *Material Research Bulletin*, 2005, **40**, P. 131.
- [20] Mellnik A.R., Lee J.S., Richardella A., Grab J.L., Mintum P.J., Fischer M.H., Vaez A., Manchon A., Kim E.A., Samarth N. and Ralph D.C. Spin transfer torque generated by a topological insulator. *Nature*, 2014, **511**, P. 449–451.
- [21] Zhang J., Peng Z., Sponi A., Zhao Y., Xiong Y., Peng B., Wang J., Dresselhaus M.S., Xiong Q. Raman spectroscopy of few quintuple layer topological insulator Bi_2Se_3 nanoplates. *Nano Letters*, 2011, **11**, P. 2407.
- [22] Sapkota Y.R., Alkabsh A., Walber A., Samassekou H and Mazumdar D; Optical evidence for blue shift in topological insulator bismuth selenide in the few layer limit. *Applied Physics Letters*, 2017, **110**, P. 181901.
- [23] Kannan A.G., Manjulavalli T.E. Structural, optical and electrical properties of Bi_2Se_3 thin films prepared by spray pyrolysis technique. *Int.J. Chem. Tech. Res.*, 2015, **8**(11), P. 599–606.
- [24] Weast, Robert C. *Hand Book of Chemistry and Physics*, CRC Press, Boca Raton, USA, 1983-1984.
- [25] Subramanian S., Padiyan D.P. Effect of structural, electrical and optical properties of electrodeposited bismuth selenide thin films in polyaniline aqueous medium. *Material, Chemistry and Physics*, 2008, **107**, P. 392–398.
- [26] Pejova B., Grozdanov I. Chemical deposition and characterization of glassy bismuth selenide thin films. *Introducing Applied Surface Science Advances*, 2002, **408**, P. 6–10.
- [27] Mataré H.F. *Defect Electronic in semiconductors*, Wiley, New York, 1971.
- [28] Desai N., Ghanwat V., Kishorkumar V.K., Swanta S.M. Effect of substrate on the nanostructured Bi_2Se_3 thin films for solar cell applications. *Journal of material Science: Mater Electron*, 2015, **27**(3), P. 2385–2393.

Fabrication of CeO₂ nanoparticles embedded in polysaccharide hydrogel and their application in skin wound healing

N. R. Popova¹, V. V. Andreeva², N. V. Khohlov³, A. L. Popov¹, V. K. Ivanov⁴

¹Institute of Theoretical and Experimental Biophysics, Russian Academy of Sciences, Pushchino, Moscow region, 142290, Russia

²Moscow Regional Research and Clinical Institute, Laboratory of Medical and Physics Research, Shchepkina st. 61/2, Moscow, Russia

³I. M. Sechenov First Moscow State Medical University, Bolshaya Pirogovskaya St., 19s1, Moscow, 119146, Russia

⁴Kurnakov Institute of General and Inorganic Chemistry, Russian Academy of Sciences, Moscow, 119991, Russia

nellipopovaran@gmail.com, viktoriasa@yandex.ru, nikolay.khokhlov@gmail.com, antonpopovleonid@gmail.com, van@igic.ras.ru

PACS 68.65.k, 81.20.n, 82.70.Dd, 87.80.-y

DOI 10.17586/2220-8054-2020-11-1-99-109

Nanocrystalline cerium oxide (CeO₂) is considered as one of the most promising inorganic materials for biomedical purposes. The unique redox-activity, high biocompatibility and low toxicity of CeO₂ nanoparticles open great prospects in their biomedical usage as a therapeutic agent, including acceleration of skin regeneration processes after injuries of various etiologies. As part of this work, a hydrogel based on natural polysaccharides modified with CeO₂ nanoparticles was synthesized and its therapeutic efficacy in the treatment of planar full thickness and linear skin wounds in rats was shown. Basing on wound surface area measurements, results of skin wounds tensiometry and histological analysis it was found that polysaccharide hydrogel significantly reduces planar and linear wound healing times. Polysaccharide hydrogel modified with CeO₂ nanoparticles facilitates rapid reduction of wound defect area and the scar formation with complete tissue regeneration in the wound area. Additionally, composite hydrogels reduce the manifestations of non-specific signs of inflammation and intoxication. Thus, polysaccharide hydrogel modified with CeO₂ nanoparticles can be regarded as an effective wound healing substance in the therapy of skin injuries of various etiologies.

Keywords: wound healing, hydrogel, cerium oxide nanoparticles, cutaneous application, regeneration, cell proliferation.

Received: 1 November 2019

Revised: 15 January 2020

1. Introduction

One of the most promising nanomaterials for biomedical applications is nanocrystalline cerium dioxide (i.e., CeO₂ nanoparticles). The unique redox activity of CeO₂ nanoparticles provides its specific activity in a biological microenvironment [1–4] that drastically distinguishes cerium from the other elements of the lanthanides family. CeO₂ nanoparticles are able to inactivate a wide range of reactive oxygen species (ROS), even at nanomolar concentrations, effectively preventing intracellular oxidative stress [5, 6]. The physico-chemical and biological behavior of CeO₂ nanoparticles in the cell is dictated by many factors. To explain the bioactivity of CeO₂ nanoparticles, most authors extrapolate existing data on their activity in catalytic processes (cracking, exhaust gas after burning, organic oxidation) to biological processes, describing CeO₂ nanoparticles as a “biological catalyst”, nanozyme [7, 8]. It is generally accepted that the unique biological activity of CeO₂ nanoparticles is affected by several factors, including the shape, size, crystallinity and surface charge of the particles [9]. The above characteristics depend on the synthesis conditions, the nature of the precursors and surfactants, etc [10].

Earlier, we showed the possibility of using CeO₂ nanoparticles to accelerate the proliferation of human mesenchymal stem cells (MSC) isolated from dental pulp and human Watan jelly, as well as mouse embryonic stem cell culture [11–13]. CeO₂ nanoparticles inhibited intracellular oxidative stress directly by inactivation of ROS and indirectly via modulation of gene expression, which provided natural and microenvironment for cell proliferation and migration. Additionally, it has been shown that polylactide scaffolds modified with CeO₂ nanoparticles can be used as unique material for effective growth and proliferation of human mesenchymal stem cells [14]. Moreover, CeO₂ nanoparticles are capable of enhancing the viability of neuronal cell cultures, including astrocytes, neurons, oligodendrocytes and microglial cells [15, 16]. CeO₂ nanoparticles application into neuronal cell culture leads to prolongation of their life span up to 280 days. Thus, CeO₂ nanoparticles are able to stimulate the growth and proliferation of various types of cell cultures *in vitro* [17]. Meanwhile, all previous studies demonstrate its efficacy in various models only, skipping over the detailed research of the molecular mechanisms of its activity.

In this work, a polysaccharide hydrogel based on carboxymethyl cellulose, chitosan, fucoidan and carrageenan modified with citrate-stabilized CeO₂ nanoparticles was synthesized and its therapeutic efficacy was shown in the treatment of model planar and linear skin wounds in rats.

2. Materials and methods

2.1. Laboratory animals. Animal care and maintenance

Experimental procedures were performed on Wistar white rats. Rats weighing 180 – 190 g at the age of 12 – 13 weeks were used. Animal maintenance was carried out in accordance with the rules adopted by the European Convention for the Protection of Vertebrate Animals (Strasbourg, 1986). The animals were fed twice a day. Animal maintenance was in accordance with the rules of Good Laboratory Practice (GLP) and the Order of the Ministry of Health of the Russian Federation No. 199n “Rules of Good Laboratory Practice”. Animals had unlimited access to water using special drinking bottles for rodents. Preliminary bacteriological analysis and sanitary chemical examination of water was performed. There was no contamination of the bedding, feed and water that could affect the results of the study. During the study each animal was examined daily. The examination included an assessment of overall behavior and systemic condition of animals. When applying test preparations, the examination was carried out approximately 2 hours after the application. Visual characteristics were recorded by photographing the wound on the 2nd, 7th, 14th and 28th days. Wound sizes were recorded by metric methods.

2.2. Vital signs monitoring in laboratory animals

Animal weighing was carried out immediately prior to wound simulation on the 2nd, 7th days, and then once a week to control body weight dynamics and immediately prior to euthanasia to calculate the percentage of organ weight to body weight. Blood samples were collected from animals before the start of the experiment, on the 2nd day after the wound simulation (puncture of the tail vein) and immediately before euthanasia. On the day before blood sampling feed-troughs with food were withdrawn from rat cages. The next day, the animals were sacrificed in a CO₂ chamber and blood samples were collected to analyze the following parameters: hemoglobin, erythrocyte count, leukocyte count, leukogram, platelets, lymphocytes, monocytes, neutrophils. Finally, pathomorphological studies were also performed. The pathomorphological study included necropsy, macroscopic examination, weighing of internal organs, and histological examination of the wound surface of the skin.

2.3. Simulation of skin integument injury

2.3.1. Formation of a planar full-thickness wound. A day prior to the experiment, hair-coat of rats was trimmed at the site of the intended wound infliction. Animals were immobilized by means of ether inhalation anesthesia, a circular flap of skin of $60.0 \pm 1.0 \text{ mm}^2$ was cut off with rounded-end surgical scissors from cervico-occipital region using a stencil. Wounds remained open until the end of the experiment. Levomecol ointment was used as a control medication. Animals were divided into 4 groups of 6 test subjects in each. The first group was intact without wound infliction. The second one was a control group without drug application onto the wound, with spontaneous wound healing. In the third group, Levomecol ointment was applied onto the wound. In the fourth group, a CeO₂ containing hydrogel was applied onto the wound. Immediately after the operation and then daily for 14 days experimental groups of animals were treated with hydrogels in an amount of 0.2 g. The hydrogel was preheated in a water bath to 38 – 40 °C and then applied with a glass rod onto the wound surface. Thereafter, the animals were placed for 2 hours into special individual plastic containers to restrict locomotor activity and to prevent gel licking. After releasing of rats from the containers, the excess of the gel was removed from the skin with filter paper. The change in wound surface area was recorded once a day by measuring the wound diameter using the vernier caliper (length = 125 mm, accuracy = 0.01 mm). The wound surface area was then calculated:

$$S = \frac{\pi \times D^2}{4},$$

where S is the wound area, D is the wound diameter, $\pi = 3.14$.

2.4. Formation of a linear wound

A day prior to the experiment, hair-coat of rats was trimmed at the dorso-lumbar area. The animals were anesthetized with diethyl ether by inhalation. A linear full-thickness skin wound 5.0 cm long was created in the skin of the depilated rat's back applying the stencil using a surgical scalpel, the wound edges were brought together and sutures were applied at an equal distance. Sutures were applied so that the epithelium of the lateral edges of the wound did not come into contact, and the epithelization took place from the terminal edges of the wound. The suture material used was sterilized silk filament #0, which was removed on the 5th day of the experiment. Wounds remained open

until the end of the experiment. During the experiment the body temperature of the animals was measured. Blood samples were collected prior to the experiment, on the 2nd and 7th days after linear wound formation, morphological parameters of blood and leukocyte formula were determined. The total duration of observations was 7 days. The efficacy of pharmaceutical agents used was evaluated basing on the observations of linear wounds healing dynamics, the performance status of the animals was assessed as well as the presence or absence of an inflammatory process. On the 7th day after wound formation animals were euthanized by sacrificing in a CO₂ chamber followed by the withdrawal of wound area full-thickness skin flap of 2 cm × 3 cm. According to the recommendations of the guide to preclinical trials of pharmaceutical agents the scar-breaking strength was determined using wound tensiometer [18].

2.5. Polysaccharide hydrogel synthesis and modification

The hydrogels were made from citrate-stabilized cerium oxide nanoparticles prepared according to [19], pectin, fucoidan, sodium alginate, water-soluble derivatives of cellulose (carboxymethyl cellulose) and purified water. Briefly, 1.0 g fucoidan, 1.0 g sodium alginate, 8.0 g carboxymethyl cellulose were dissolved in 100 ml distilled water. The solution was mixed at 25 °C and then left at 4 °C for 96 h until the formation of a homogeneous gel. Then 100 μl of the CeO₂ sol (CeO₂ concentration in the sol was 10⁻² M) was added and the mixture was vigorously homogenized. Before application, the gel was sterilized in an autoclave.

2.6. Statistical data treatment

Statistical treatment of the results was performed using STATISTICA 8.0 software to evaluate the Student's *t*-criterion. Data are presented as the sample mean *M*, the standard error of the mean *m*, and the achieved level of significance *p*. Accepted minimum significance level of differences was taken as $p \leq 0.05$. In some cases, especially when there is a natural trend of indicators (e.g. animal body weight gain over the observation period, etc.), the methods of dispersion analysis were used.

3. Results

Data obtained indicate that CeO₂-containing hydrogel is well tolerated by the animals, has no irritating effect, does not cause hyperemia and skin edema, and does not affect the level of physical activity in test animals. During the observation period, no cases of death, wound abscess or complicated course of wound process were registered. The gel could easily be applied onto the wounds, adsorbing wound excretions, not drying wound bottom, and maintaining a wet environment in the wound. The results of comparative assessment of wound healing activity of hydrogel and Levomecol ointment on a model planar full-thickness wound are presented in Table 1.

Analysis of the experimental study results showed that throughout the test period a gradual decrease in the wound surface area at all stages of the wound process was observed in the control group. In the group of animals treated with Levomecol ointment, the wound area is reduced on the 9th day by 16.38 % relative to the control ($p < 0.05$).

In the experimental group, where wounds were treated with hydrogel, there was an acceleration in wound healing by 3 days; on the 8th and 11th days wound surface area decreased by 40.51 % and 39.99 %, respectively, relative to the control ($p < 0.05$).

The maximum effect is observed in a group of animals treated with hydrogel at all stages of wound healing process (Fig. 1).

In histological sections of the skin of the intact group of animals, the epidermis is characterized by a classical histological structure (Fig. 2(a1)). Cells of epithelial tissue of ectodermal origin of basal layer have a regular cubic shape and are arranged in line abreast, there are very few mitotic cells. In the depth of the spinous layer, the cells are cubic, while near the next layer, they become flatter (Fig. 2(a2)). The corneum layer is formed by several layers of corneal cells comprising keratin. The papillary layer is formed by a loose fibrous connective tissue consisting of collagen, elastin and reticulin fibers randomly interconnected with each other (Fig. 2(a3)). Up to seven hair follicles fall within one field of vision, forming complexes together with sebaceous glands (Fig. 2(a3)). In histological sections, the identified dermal papillae are very few, being randomly arranged. Fibroblasts are located mainly in subepidermal layers. The vessels are few, small and well evident.

In the control group of animals, a thin scar is formed with complete recovery of the epidermis in the wound region. On day 14, the epidermis is significantly enlarged, cells of all skin layers have a variety of sizes and shapes (Fig. 2(b1)). Cellular vacuolization is observed in the spinous layer of the epidermis (Fig. 2(b2)). The papillary layer of dermis is poorly resolved (Fig. 2(b1, b2)). Vascular blood filling is uneven, some blood vessels are collapsed, in the form of "cellular chorda", the other ones are moderately filled with blood together with weak leukocyte infiltration. Epithelium growth occurs across the surface of the granulation tissue and loose connective tissue that is formed during dermal regeneration. Granulation tissue cells proliferate around the blood vessels in the form of small clusters. Proliferative processes are dominated in regenerating tissue resulting in formation of focal cell infiltrates with the proliferation of

TABLE 1. Wound healing activity of ceria-containing hydrogel and levomecol ointment on planar full thickness skin wound model in rats

Day	Surface area of planar full-thickness wound, cm ²		
	Control	Levomecol ointment	CeO ₂ Hydrogel
0	0.65 ± 0.03	0.62 ± 0.03	0.63 ± 0.05
1	0.58 ± 0.07	0.57 ± 0.05	0.58 ± 0.08
2	0.58 ± 0.07	0.58 ± 0.04	0.56 ± 0.08
3	0.56 ± 0.07	0.54 ± 0.06	0.48 ± 0.03*
4	0.57 ± 0.05	0.54 ± 0.07	0.43 ± 0.05* **
5	0.56 ± 0.05	0.54 ± 0.07	0.36 ± 0.03* **
6	0.53 ± 0.07	0.52 ± 0.06	0.37 ± 0.04* **
7	0.49 ± 0.07	0.47 ± 0.06	0.33 ± 0.03* **
8	0.48 ± 0.07	0.43 ± 0.05	0.21 ± 0.06* **
9	0.40 ± 0.06	0.28 ± 0.08*	0.16 ± 0.08* **
10	0.34 ± 0.07	0.21 ± 0.04*	0.10 ± 0.05* **
11	0.26 ± 0.04	0.17 ± 0.04*	0.01 ± 0.01* **
12	0.14 ± 0.04	0.07 ± 0.05*	0
13	0.09 ± 0.07	0.03 ± 0.04*	0
14	0.09 ± 0.07	0.01 ± 0.05*	0

* – significant difference of parameters from control ($p < 0.05$)

** – significant difference of parameters from reference preparation (at $p < 0.05$)

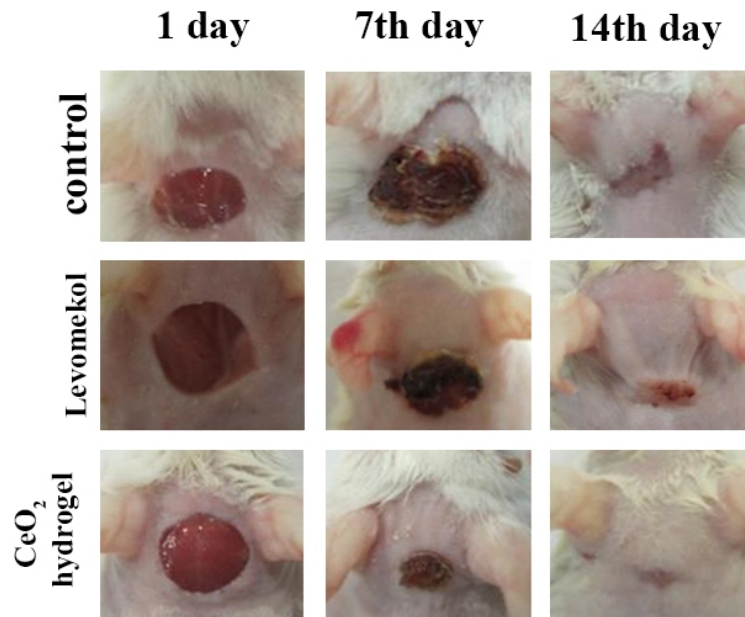


FIG. 1. Appearance of planar full-thickness wound in rats

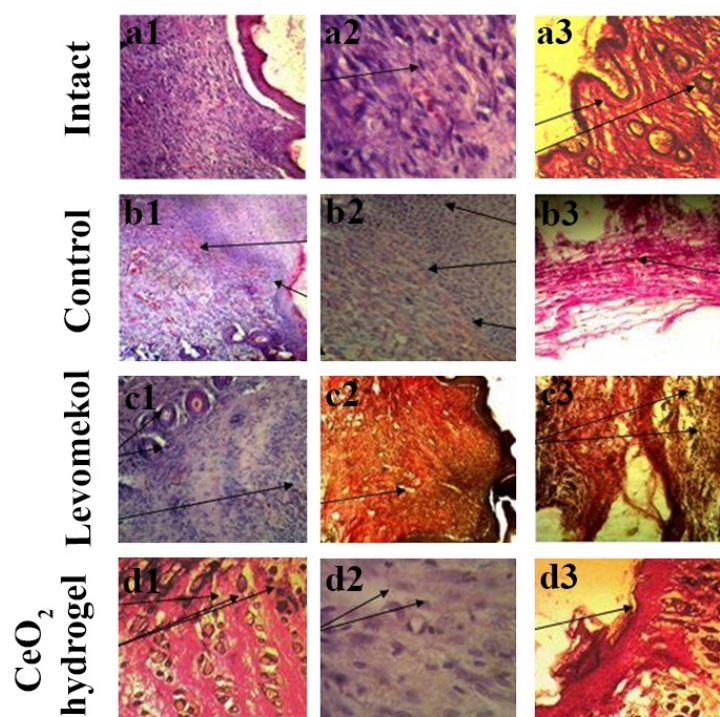


FIG. 2. Histological analysis of the epidermis of the skin of rats treated with various substances

granulation tissue and fibrous connective tissue (Fig. 2(b3)). Strands of collagen fibers are located in parallel to skin surface. Neither hair follicles nor sebaceous glands were found.

In the group of animals treated with Levomecol ointment, the epidermis is moderately or significantly thickened, elongated cell nuclei are horizontally oriented (Fig. 2(c1)). In the underlying dermis, macrofocal profound homogenization is registered, moderate basophilia of dermal collagen fibers could be observed, the blood vessels of the dermis are congested with blood (Fig. 2(c2)). In adjacent skin, there is microfocal weakly expressed epidermal cell swelling in the form of translucent perinuclear spaces. Newly formed blood vessels of different diameters with expanded lumen could be distinguished, they are congested with blood with erythrocytes, diapedetic microhemorrhages (Fig. 2(c3)), the formation of sporadic hair follicles is observed (Fig. 2(c3)), and sebaceous glands were not found.

In the group of animals where the wounds were treated with CeO₂-containing hydrogel, scar formation occurs with complete recovery of the epidermis in the wound region. The scarring zone is visually smaller in area as compared to control groups. There is a proliferation of granulation tissue that fills the entire wound defect region and has a typical structure (Fig. 2(d1)). Among cells of developing tissue, cells of circulatory bed as well as of tissular origin were revealed, including fibroblasts located around small capillaries (Fig. 2(d2)). Epithelial sheets of regenerating tissue are formed from the edges of wound defect as two arrays towards each other and cover the wound. In the animals, on day 14 after wound infliction, the epithelium is almost completely restored in the region of skin injury. The epithelial cells of the basal layer proliferate deep into the dermis, forming intergrowths. As the wound heals, a cornea layer of the epidermis is formed (Fig. 2(d3)). Collagenization processes occur at the site of the tissue defect. Mature connective tissue is formed, and the generation of hair follicles and sebaceous glands take place inside it (Fig. 2(d1)).

Thus, the use of the hydrogel reduces inflammatory changes, activates macrophagal response, restores impaired intercellular interactions, enhances angiogenesis, proliferation and differentiation of fibroblasts, synthesis and secretion of collagen, fibrillogenesis processes, maturation, and remodeling of granulation tissue and its epithelization.

Our studies indicate that treatment with cerium-containing hydrogel accelerates regeneration of the planar full-thickness wound of rat skin that is expressed in the formation of hair follicles and sebaceous glands in the wound area, as well as in remarkable reduction in the scarring area, without causing reorganization of the scarring structure.

Animals were observed within 14 days after wound simulation. Observation of the overall condition and behavior, weighing, monitoring of feed and water consumption were carried out daily. After 14 days, all animals in the test groups were euthanized in a CO₂ chamber and dissected. Hematological studies, macroscopic description and the

evaluation of mass coefficients of internal organs, histological studies were carried out. The results of animal body weight measurements are shown in Table 2.

Table 2 shows that the body weight of animals is reduced after injury. Subsequently, the weight growth rates of control animals and Levomecol-treated animals are lower than the results of the intact group. When the hydrogel is used, these body weight values are not significantly different from intact control. The revealed changes are not statistically significant. No significant differences in body weight dynamics were found in the groups of animals treated with Levomecol and CeO₂-containing hydrogel.

2 hours after drug epicutaneous application, rats were relocated into exchange cages for 24 hours to evaluate water and food consumption. The results are shown in Tables 3, 4.

TABLE 2. Body weight dynamics of male white rats (g , $M \pm m$) during the treatment of planar full-thickness skin wound

	Test group			
	Intact animals	Control	Levomecol ointment	CeO ₂ Hydrogel
Initially	189.0 ± 4.8	187.2 ± 2.1	185.1 ± 4.4	180.7 ± 3.0
2-nd day	191.3 ± 3.6	180.2 ± 3.1	182.4 ± 4.7	178.0 ± 3.8
7-th day	196.2 ± 4.3	182.7 ± 2.9	187.4 ± 5.5	195.7 ± 3.3
14-th day	204.4 ± 4.3	188.4 ± 3.8	192.6 ± 5.1	201.5 ± 2.8

TABLE 3. Water consumption dynamics (ml/day) by rats during the treatment of planar full-thickness skin wound ($M \pm m$)

	Test group			
	Intact animals	Control	Levomecol ointment	CeO ₂ Hydrogel
Initially	20.2 ± 1.5	19.0 ± 0.3	19.8 ± 1.3	21.7 ± 0.5
2-nd day	19.0 ± 0.4	14.1 ± 1.5*	15.2 ± 0.9*	13.7 ± 0.2*
7-th day	19.4 ± 1.2	19.4 ± 0.3	21.1 ± 1.0	17.9 ± 0.7
14-th day	19.7 ± 0.9	18.9 ± 0.6	18.3 ± 0.3	18.5 ± 0.2

* – Significant differences from initial values and results of the intact group ($p < 0.05$)

TABLE 4. Food consumption dynamics (g/day) by rats during the treatment of planar full-thickness skin wound ($M \pm m$)

	Test group			
	Intact animals	Control	Levomecol ointment	CeO ₂ Hydrogel
Initially	19.2 ± 2.2	19.9 ± 0.8	20.1 ± 2.3	19.6 ± 2.3
2-nd day	20.9 ± 2.8	10.2 ± 3.0*	11.8 ± 2.5*	10.4 ± 3.5*
7-th day	21.4 ± 1.3	18.9 ± 2.1	21.5 ± 1.4	22.1 ± 1.2
14-th day	20.2 ± 2.4	23.7 ± 1.7	21.7 ± 1.4	20.9 ± 1.8

* – Significant differences from initial values and results of the intact group ($p < 0.05$)

As it could be seen from Tables 3 and 4, in the control group and the groups of animals treated with the tested preparations, on the 2nd day after administration the amount of water consumed is statistically reduced and the food consumption is reduced considerably in comparison with the initial level and with the intact group. Subsequently, the results of the evaluation of water and food consumption in the control and intact groups did not vary. There were no significant differences in these values in the groups of animals receiving the tested preparations.

As a non-specific sign of inflammation during the treatment of planar full-thickness skin wound using Levomecol ointment and CeO₂-containing hydrogel, the body temperature of rats was determined. Rectal temperatures were measured using an electronic medical thermometer (permissible intrinsic error for the range of measured temperatures ± 1 %) 2 hours after drug epicutaneous application. The data obtained are shown in Table 5.

TABLE 5. Rectal temperature of rats during the treatment of planar full-thickness skin wound ($^{\circ}\text{C}$, $M \pm m$)

	Test group			
	Intact animals	Control	Levomecol ointment	CeO ₂ Hydrogel
Initially	37.6 \pm 0.2	37.3 \pm 0.3	37.3 \pm 0.2	36.9 \pm 0.4
2-nd day	36.8 \pm 0.3	38.9 \pm 0.4*	38.9 \pm 0.4*	38.1 \pm 0.3*
7-th day	36.8 \pm 0.2	38.1 \pm 0.3*	38.0 \pm 0.2*	37.1 \pm 0.6
14-th day	36.8 \pm 0.3	38.0 \pm 0.3*	37.6 \pm 0.3	37.3 \pm 0.4

* – Significant differences from initial values and results of the intact group ($p < 0.05$)

It was found that on the 2nd day after planar full-thickness wound infliction the body temperature in animals of the control group is increased relative to the initial values. On the 7th and 14th days of observation, body temperature remains elevated. In the Levomecol ointment treated group, the results are not significantly different from the control ($p < 0.05$). In the CeO₂-containing hydrogel treated group, a reduction in rectal temperature to the initial level was observed on day 7 after the wound infliction.

Hematological studies were carried out prior to wound simulation and after 2 and 14 days of daily drug application in all groups. Blood samples were collected by puncture of the tail vein, and at the end of the experiment – after euthanasia of the animals.

The data obtained are shown in Tables 6, 7.

On the 2nd and 14th day, the control group showed an increase in ESR by 166.3 and 77.2 % as well as in leukocytes by 43.6 and 21.0 %, respectively, compared to the initial values ($p < 0.05$) that indicates an inflammatory process in animals. Levomecol ointment showed a significant decrease in ESR and number of leukocytes on day 2. In the group of animals treated with CeO₂-containing hydrogel, on day 2 there was a significant decrease in ESR and a decrease in leukocytosis relative to control, on day 14 there was a decrease in ESR and the number of leukocytes returns to the initial level.

No statistically significant differences were found in the values of other indicators

The ratio of leukocyte forms (Table 7) in animals in the intact group prior to the start of the experiment corresponds to the normal values typical to the healthy rats. Initial values in the control and all test groups are within normal limits and indicate the absence of inflammatory processes in animals prior to the start of the experiment.

In the control group, on the 2nd and 14th days after the wound simulation there was a decrease in the percentage of lymphocytes by 5.0 and 3.3 %, respectively, compared to initial values. On day 2, an increase in the number of segmentonuclear and banded neutrophils compared to intact group and initial values was observed, indicating the presence of neutrophilic leukocytosis and an inflammatory process.

Application of Levomecol ointment onto a linear wound for 14 days resulted in a slight increase in the relative number of lymphocytes compared to the control. The number of segmentonuclear and banded neutrophils did not differ significantly from the control, which indicated the inability of Levomecol ointment to prevent the leucogram deviation. When using CeO₂-containing hydrogel, on day 14 there was an increase in lymphocyte count compared to the data for the control group, as well as a decrease in the number of segmentonuclear and banded neutrophils compared to the control. These values did not differ statistically from the initial ones. This indicates the ability of CeO₂-containing hydrogel to reduce the severity of the inflammatory process. No statistically significant changes in other leucogram parameters were found. At the end of the experiment, all the animals of control and test groups, as well as intact animals, were subjected to pathomorphological studies. Animals were withdrawn from the experiment

TABLE 6. The effect of drug epicutaneous application on peripheral blood morphological composition of white rats during the treatment of planar full-thickness wound ($M \pm m$)

	Test group			
	Intact animals	Control	Levomecol ointment	CeO ₂ Hydrogel
Hemoglobin, g/dl				
Initially	13.9 ± 0.2	13.2 ± 0.1	13.1 ± 0.2	14.7 ± 0.1
2-nd day	12.7 ± 0.1	12.2 ± 0.3	12.2 ± 0.4	12.8 ± 0.4
14-th day	13.8 ± 0.2	12.7 ± 0.2	12.4 ± 0.3	13.7 ± 0.2
Hematocrit, %				
Initially	53.0 ± 2.6	51.4 ± 1.5	53.8 ± 1.0	51.9 ± 2.0
2-nd day	49.1 ± 1.3	58.7 ± 2.6	48.0 ± 1.5	49.4 ± 1.5
14-th day	50.7 ± 2.6	54.8 ± 1.3	52.3 ± 1.6	51.7 ± 2.1
Erythrocytes, ×10 ¹² /l				
Initially	6.6 ± 0.2	6.6 ± 0.2	7.2 ± 0.2	7.3 ± 0.3
2-nd day	6.9 ± 0.1	7.3 ± 0.1	6.4 ± 0.3	6.5 ± 0.2
14-th day	7.2 ± 0.1	6.4 ± 0.2	6.8 ± 0.3	6.9 ± 0.2
Blood colour index, pg				
Initially	18.9 ± 0.4	17.5 ± 0.4	17.9 ± 0.1	17.9 ± 0.4
2-nd day	17.9 ± 0.5	18.2 ± 0.6	18.6 ± 0.7	18.5 ± 0.5
14-th day	18.7 ± 0.6	17.5 ± 0.5	18.0 ± 0.4	17.3 ± 0.8
Leucocytes, ×10 ⁹ /l				
Initially	9.2 ± 0.2	9.5 ± 0.4	10.1 ± 0.2	10.2 ± 0.3
2-nd day	10.3 ± 0.3	13.6 ± 0.2*	11.9 ± 0.5*	11.2 ± 0.4*
14-th day	9.7 ± 0.4	11.5 ± 0.7*	10.3 ± 0.4	10.3 ± 0.3
Thrombocytes, ×10 ⁹ /l				
Initially	759 ± 47	721 ± 30	752 ± 75	725 ± 44
2-nd day	770 ± 34	748 ± 40	736 ± 38	715 ± 26
14-th day	783 ± 31	783 ± 70	749 ± 21	785 ± 34
ESR, mm/h				
Initially	4.5 ± 0.2	4.8 ± 0.4	4.5 ± 0.1	4.2 ± 0.1
2-nd day	4.0 ± 0.3	12.7 ± 1.2*	9.4 ± 2.6* **	7.9 ± 1.2* **
14-th day	5.2 ± 0.2	8.5 ± 1.1*	4.8 ± 3.7**	4.9 ± 3.6**

* – Significant difference from initial values (at $p < 0.05$)** – Significant difference from the results of the control group (at $p < 0.05$)

TABLE 7. The effect of drug epicutaneous application on peripheral blood leucogram of white rats during the treatment of planar full-thickness wound ($M \pm m$)

	Test group			
	Intact animals	Control	Levomecol ointment	CeO ₂ Hydrogel
Banded neutrophils, %				
Initially	2.4 ± 0.2	2.1 ± 0.1	2.2 ± 0.2	2.3 ± 0.2
2-nd day	2.2 ± 0.1	3.7 ± 0.4*	3.4 ± 0.2*	3.1 ± 0.1*
14-th day	2.4 ± 0.1	3.0 ± 0.2*	3.1 ± 0.1*	2.2 ± 0.1
Segmentonuclear neutrophils, %				
Initially	35.4 ± 1.0	35.0 ± 0.6	32.5 ± 1.1	35.6 ± 0.8
2-nd day	34.1 ± 0.6	41.4 ± 0.6*	39.5 ± 0.9*	40.6 ± 1.1*
14-th day	33.4 ± 0.4	40.9 ± 0.4*	36.1 ± 0.3**	31.5 ± 0.8**
Basophils, %				
Initially	0	0	0	0
2-nd day	0	0	0	0
14-th day	0	0	0	0
Eosinophils, %				
Initially	4.4 ± 0.1	2.6 ± 0.1	3.0 ± 0.2	2.9 ± 0.1
2-nd day	3.9 ± 0.1	2.7 ± 0.4	3.8 ± 0.2	3.3 ± 0.1
14-th day	4.6 ± 0.1	4.7 ± 0.1	3.8 ± 0.2	4.0 ± 0.2
Monocytes, %				
Initially	5.3 ± 0.1	5.1 ± 0.2	6.3 ± 0.2	5.7 ± 0.2
2-nd day	5.5 ± 0.4	5.9 ± 0.7	5.2 ± 0.1	6.8 ± 0.4
14-th day	5.7 ± 0.1	5.4 ± 0.4	5.4 ± 0.1	5.6 ± 0.3
Lymphocytes, %				
Initially	52.4 ± 1.1	57.3 ± 1.1	56.1 ± 0.7	53.3 ± 1.2
2-nd day	54.3 ± 0.7	46.4 ± 1.2*	48.1 ± 0.3	46.2 ± 0.8*
14-th day	53.9 ± 0.7	46.1 ± 0.5*	51.4 ± 0.7*	56.6 ± 0.5**
Plasmacytes, %				
Initially	0.1 ± 0.1	0.1 ± 0.1	0.1 ± 0.1	0.1 ± 0.1
2-nd day	0.1 ± 0.1	0.1 ± 0.1	0.2 ± 0.1	0.2 ± 0.1
14-th day	0.2 ± 0.1	0.1 ± 0.1	0.1 ± 0.1	0.1 ± 0.1

* – Significant difference from initial values (at $p < 0.05$)** – Significant difference from the results of the control group (at $p < 0.05$)

by sacrificing in a CO₂ chamber. Pathomorphological study included necropsy, macroscopic examination, internal organ weighing, and histological examination of the wound skin.

Table 8 shows the mass coefficients of organs of white rats from all experimental groups. It has been found that thymus mass coefficients in all experimental groups are significantly lower than the results of the intact group. The greatest differences with intact animals have been revealed in the case of Levomecol ointment use. The use of CeO₂-containing hydrogel partially normalizes these values, but the difference with control is unreliable.

TABLE 8. Mass coefficients of rat's internal organs during the treatment of planar full-thickness skin wound ($M \pm m$)

Organ	Test group			
	Intact animals	Control	Levomecol ointment	CeO ₂ Hydrogel
Heart	4.2 ± 0.2	3.1 ± 0.1*	3.2 ± 0.3*	3.4 ± 0.3*
Lungs with a trachea	6.8 ± 0.2	6.9 ± 0.3	7.1 ± 0.2	7.0 ± 0.4
Timus	1.30 ± 0.12	1.03 ± 0.06*	1.01 ± 0.21*	1.18 ± 0.09*
Liver	36.0 ± 1.4	31.0 ± 1.4	36.3 ± 2.0	36.5 ± 2.5
Spleen	4.7 ± 0.2	4.2 ± 0.3	4.3 ± 0.2	4.5 ± 0.4
Kidney (left)	6.1 ± 0.3	6.0 ± 0.5	5.9 ± 0.5	5.9 ± 0.2
Adrenal gland (left)	0.11 ± 0.01	0.10 ± 0.01	0.09 ± 0.02	0.09 ± 0.01
Brain	7.5 ± 0.2	7.7 ± 0.2	7.6 ± 0.1	7.8 ± 0.1
Testicles	12.14 ± 0.36	12.30 ± 0.25	12.26 ± 0.35	11.98 ± 0.33

* – Significant differences from the results for the intact group ($p < 0.05$)

The heart mass coefficient is significantly reduced in all types of traumatic exposure relative to intact control, although there are no significant differences in this indicator among the test groups.

Traumatic exposure itself and traumatic exposure with further Levomecol treatment reduce the spleen mass coefficient; however, differences with the results for the intact group are not statistically significant at $p < 0.05$. The use of CeO₂-containing hydrogel restores the indicators to values that are not statistically distinguishable from those of the intact group.

The liver mass coefficient in different groups did not give reliable differences. The mass distribution of the remaining internal organs in the groups was consistent with the normal values for intact animals.

Analysis of the mass coefficient values did not reveal any significant differences both between the groups of animals treated with Levomecol ointment or CeO₂-containing hydrogel as well as with respect to the control group.

4. Conclusions

Thus, the experimental data obtained show that CeO₂-containing hydrogel reduces the healing time of a planar full-thickness skin wound in rats in comparison with control and reference preparation, provides rapid reduction of wound defect area and formation of a complete scar. The CeO₂-containing hydrogel has a greater effect than Levomecol ointment on non-specific signs of the inflammatory process. Thus, CeO₂-containing hydrogel normalizes body temperature, improves morphological composition of peripheral blood, leukocyte formula, and mass coefficients of internal organs of experimental animals.

Acknowledgements

This research has been supported by the Russian Science Foundation (project 19-13-00416).

References

- [1] Shcherbakov A.B., Zholobak N.M., et al. Cerium fluoride nanoparticles protect cells against oxidative stress. *Materials Science and Engineering: C*, 2015, **50**, P. 151–159.
- [2] Walkey C., Das S., et al. Catalytic properties and biomedical applications of cerium oxide nanoparticles. *Environ Sci Nano.*, 2015, **2** (1), P. 33–53.
- [3] Pilar V.M., Montserrat M. Antitumor activities of metal oxide nanoparticles. *Nanomaterials*, 2015, **5**, P. 1004–1021.
- [4] Khaksar M., Rahimifard M., et al. Protective effects of cerium oxide and yttrium oxide nanoparticles on reduction of oxidative stress induced by sub-acute exposure to diazinon in the rat pancreas. *J. Trace Elem. Med. Biol.*, 2017, **41**, P. 79–90.
- [5] Pezzini I., Marino A., et al. Cerium oxide nanoparticles: the regenerative redox machine in bioenergetic imbalance. *Nanomedicine (Lond.)*, 2017, **12** (4), P. 403–416.
- [6] Wei H., Wang E. Nanomaterials with enzyme-like characteristics (nanozymes): next-generation artificial enzymes. *Chem. Soc. Rev.*, 2013, **42** (14), P. 6060–6093.
- [7] Singh S., Dosani T., et al. A phosphate-dependent shift in redox state of cerium oxide nanoparticles and its effects on catalytic properties. *Biomaterials*, 2011, **32** (28), P. 6745–6753.
- [8] Shin D.S., Didonato M., et al. Superoxide dismutase from the eukaryotic thermophile *Alvinella pompejana*: structures, stability, mechanism, and insights into amyotrophic lateral sclerosis. *J. Mol. Biol.*, 2009, **385** (5), P. 1534–1555.
- [9] Ould-Moussa N., Safi M., et al. In vitro toxicity of nanocerium: effect of coating and stability in biofluids. *Nanotoxicology*, 2014, **8** (7), P. 799–811.
- [10] Asati A., Santra S., et al. Surface-charge-dependent cell localization and cytotoxicity of cerium oxide nanoparticles. *ACS Nano*, 2010, **4** (9), P. 5321–5331.
- [11] Popov A.L., Ermakov A.M., et al. Citrate-stabilized nanoparticles of CeO₂ stimulate proliferation of human mesenchymal stem cells in vitro. *Int. J. Nanomech. Sci. and Technol.*, 2016, **7** (3) P. 1–12.
- [12] Popov A.L., Ermakov A.M., et al. Biosafety and effect of nanoparticles of CeO₂ on metabolic and proliferative activity of human mesenchymal stem cells in vitro. *Int. J. Nanomech. Sci. and Technol.*, 2016, **7** (2), P. 165–175.
- [13] Popov A.L., Popova N.R., et al. Cerium oxide nanoparticles stimulate proliferation of primary mouse embryonic fibroblasts in vitro. *Materials Science and Engineering: C*, 2016, **68**, P. 406–413.
- [14] Mandoli C., Pagliari F., et al. Stem cell aligned growth induced by CeO₂ nanoparticles in PLGA scaffolds with improved bioactivity for regenerative medicine. *Tissue Engineering*, 2010, **20** (10), P. 1617–1624.
- [15] Rzigalinski B.A., Carfagna C.S., et al. Cerium Oxide Nanoparticles in Neuroprotection and Considerations for Efficacy and Safety. *Wiley Interdiscip Rev Nanomed Nanobiotechnol.*, 2017, **9** (4), 10.1002/wnan.1444.
- [16] Passacantando M., Lozzi L., et al. Retinal long term neuroprotection by Cerium Oxide nanoparticles after an acute damage induced by high intensity light exposure. *Experimental Eye Research*, 2019, **182**, P. 30–38.
- [17] Pesaraklou A., Mahdavi-Shahri N., et al. Use of cerium oxide nanoparticles: a good candidate to improve skin tissue engineering. *Biomed Mater.*, 2019, **14** (3), 035008.
- [18] Gorbounov S.M., Zaikonnikova I.V., Abdrakhmanova N.G. The device for measurements the tensile strength of healing wounds. *Pharmacological regulation of regenerative processes in experiment and clinic*, 1979, P. 100–104 (in Russian).
- [19] Ermakov A.M., Popov A.L., et al. The first inorganic mitogens: Cerium oxide and cerium fluoride nanoparticles stimulate planarian regeneration via neoblastic activation. *Mater. Sci. Eng. C*, 2019, **104**, 109924.

Modification of nanoscale thermal oxide films formed on indium phosphide under the influence of tin dioxide

I. Ya. Mittova, V. F. Kostryukov, N. A. Ilyasova, B. V. Sladkopevtsev, A. A. Samsonov

Voronezh State University, Universitetskaya pl., Voronezh, 394018, Russia

imittova@mail.ru, vc@chem.vsu.ru, ilyasova_1997@mail.ru, dp-kmins@yandex.ru, samsonjr@mail.ru

DOI 10.17586/2220-8054-2020-11-1-110-116

The kinetic parameters and the limiting stage of the defining process were established by studying the thermal oxidation of SnO₂/InP heterostructures (thickness of SnO₂ layer ~ 50 nm). It was established that SnO₂ does not have a chemical stimulating effect on the film growth rate; however, it is effective as a modifier of their structure and properties. SnO₂ provides the formation of nanoscale films with semiconductor properties.

Keywords: indium phosphide, nanoscale films, thermal oxidation, tin dioxide.

Received: 8 November 2019

Revised: 16 January 2020

1. Introduction

The high transparency and conductivity of tin dioxide films allows them to be used as transparent conductive layers, and the sensitivity of their properties to surface conditions – as resistive sensors in gas sensors [1–3]. However, the application of SnO₂ as a material for gas sensors is limited by low selectivity due to a large number of active centers on the surface that can interact with the molecules of many gases [4]. On the other hand, doping SnO₂ with various elements, for example, antimony, allows one to increase the selectivity [5]. The chemical nature of the dopant and its acid-base and redox properties play key roles in determining the response to a detected gas. The selection of a suitable dopant modifier is based on an analysis of the chemical properties of detectable gases and the eventual interactions of the gas with a surface.

Pure stoichiometric SnO₂ is an insulator, however pure but nonstoichiometric SnO₂ is oxygen deficient and it is an n-type semiconductor with high conductivity at room temperature [6]. Although there are two stable tetragonal modification oxides, in the tin-oxygen system, SnO and SnO₂, SnO does not find such widespread application due to its lower thermodynamic stability than SnO₂ [7].

Due to its combination with InP components, the mixed indium-tin oxide (ITO structure) has several outstanding properties: almost metallic conductivity, good transparency in the visible range of electromagnetic radiation and the simplicity for formation of a nanoscale thin film. The optical and electrical properties are explained by the following: replacing the indium atom, tin supplies an additional electron to the conduction band, and such doping effectively increases the electron concentration [8].

ITO is widely used as transparent conductive coatings in the production of liquid crystal displays, laptop monitors, electroluminescent lamps, electrodes of photoconductive cells, fuel cells (including high-temperature ones), etc. [9, 10].

ITO are most often obtained by sputtering from ceramic targets, but since target regeneration is a rather complex and lengthy process, there are both traditional, reagent processing methods and methods based on cathode and anode processing [11].

It is known that by controlling the content of tin dioxide, it is possible to obtain ITO films with crystalline and amorphous structures and certain electrical and optical properties [12].

The deposition of metals such as Mo and Ni on the ITO structure can improve the mechanical properties and increase its corrosion resistance [13], while the deposition of copper-based conductive pastes on the ITO surface can increase the lifetime of electronic devices [14].

ITO structures are widely used as elements of recording devices. In particular, organic recording devices with an active layer located between two electrodes are becoming more popular. The use of ITO is determined by the low power consumption of these devices and simplicity of its production [15]. Today, there are recording devices, the basis of which is amorphous ITO, allowing extending the lifetime of such devices [16].

The thermodynamic calculation of the corresponding reactions using data [17] shows that SnO₂ can theoretically transfer oxygen to the InP components, in other words it is a chemical stimulator of the semiconductor thermal oxidation [18]. Good reconcilability of oxide components, in particular, during the formation of ITO films, can serve as the basis for the modifying effect of tin dioxide [19] on the structure and electrophysical properties of thermal oxide films

on InP. Accordingly, the purpose of this study was establishment of the effect of SnO₂ as a possible chemostimulator and modifier of the structure and properties of nanoscale films grown by InP thermal oxidation.

2. Experimental

Nanoscale thin films grown on two-sided polished single-crystal (100)-oriented indium phosphide, doped with tin, the concentration of the main charge carriers at 300 K is more than $5 \cdot 10^{16} \text{ cm}^{-3}$, intrinsic n-type conductivity, pretreated with an etchant of H₂SO₄ composition (chemical grade GOST-4204-77, 92.80 %): H₂O₂ (OSCh TU 6-02-570-750, 56 %): H₂O = 2:1:1 for 10 min were studied. After repeated washing in distilled water and air-drying the plates, SnO₂/InP heterostructures were formed in a Covap II vacuum ion sputter by the magnetron sputtering. The sputtering process was performed in a chamber with a pressure of $2 \cdot 10^{-5} \text{ mm Hg}$. The source material was Sn with a purity of 99.99 %, and the ion source was O₂ + Ar gases with a purity of 99.99 %. In order to obtain the SnO₂ crystal structure on the InP surface, the semiconductor substrate was heated to 200°C during magnetron sputtering [20]. According to laser ellipsometry (LE), the thickness of the SnO₂ layer on the InP surface was 50 nm.

Thermal oxidation of SnO₂/InP samples was carried out in an MTP-2M-50-500 resistance heating furnace. The volumetric oxygen flow rate was 30 L/h (the corresponding linear speed is 10 cm/min) at 475, 500, 530, and 550 °C. The total thermal oxidation time was 60 min. The sample was perpendicular to the oxygen flow. The temperature in the reactor was maintained constant ($\pm 1 \text{ }^\circ\text{C}$) by a TRM-10 PID controller. The thickness of the formed film was determined by laser ellipsometry (LEF-754, $\lambda = 632.8 \text{ nm}$, absolute error $\pm 1 \text{ nm}$) and spectral ellipsometry (SE) (Ellipse-1891, operating in a range of wave lengths from 250 to 1100 nm) every 10 minutes before the process time limit of 60 minutes was reached.

The need to use two methods for measuring the film thickness is due to the fact that only their combination allows obtaining the most accurate result [21–23], which is especially important when studying the considered nanoscale systems.

The composition of the films grown by thermal oxidation was determined by the XRD method on an ARL X'TRA X-ray diffractometer. The X-ray diffraction patterns were recorded in the geometry of a sliding beam (with a fixed position of the arm of the X-ray tube). The several samples were studied by this method: SnO₂/InP (oxidation at 475 °C), SnO₂/InP (oxidation at 500 °C) and SnO₂/InP (oxidation at 530 °C). The starting angle for the samples oxidized at 475 and 530 °C was $-2\theta = 10^\circ$, the last $-2\theta = 70^\circ$ scan step -0.05° . The starting angle for the samples oxidized at 500 °C was $-2\theta = 20^\circ$, the last $-2\theta = 80^\circ$ scan step -0.06° .

The surface morphology of the samples was examined by scanning tunnelling microscopy (STM) using the complex of nanotechnological equipment UMKA in direct current mode and atomic force microscopy (AFM) on an SolverP47 Pro scanning probe microscope.

According to the value of resistivity, it is possible to draw the corresponding conclusions about the properties of the formed films: whether they have the ohmic conductivity, possess semiconductor or dielectric properties [24]. For this, aluminium contacts were magnetron sputtered on the surface of the synthesized samples in vacuum through a mask with holes with an area of $5 \cdot 10^{-3} \text{ cm}^2$ and the resistivity ρ (Ohm-cm) of the formed structures was determined using an Agilent 344 10A universal multimeter. In the process of measuring ρ , the thickness of the formed film was taken into account.

3. Results and discussion

Figure 1 shows kinetic curves (LE) for the thermal oxidation in double logarithmic coordinates of SnO₂/InP heterostructures at 475 – 550 °C for 60 minutes.

The kinetic data were analysed using the power law equation:

$$d = (k \cdot t)^n, \quad (1)$$

where d (nm) is the film thickness, τ (min) is the oxidation time, n is a formal kinetic parameter, and k ($\text{nm}^{1/n}/\text{min}$) is the rate constant of the process [20].

The value of the effective activation energy (EAE) was determined from the Arrhenius dependence of the averaged process rate constant $\ln k_{cp} = f(10^3/RT)$. The exponent n , considered together with the EAE, gives information about the nature of the determining process and its limiting stage [26].

The calculated value of n_{av} , 0.05, indicates that in the temperature range 475 – 550 °C the determining process is the mutual diffusion of the film components [18]. The value of the EAE is 48 kJ/mol, and even taking into account an error (of the order of 10 %), it cannot be equal to the EAE of the indium phosphide oxidation ($\sim 170 \text{ kJ/mol}$), for which the limiting stage of the process is a solid-phase reaction limited by diffusion of the substrate components (In) to the outer interface [24]. Such a low value of the EAE of the thermal oxidation process of SnO₂/InP heterostructures,

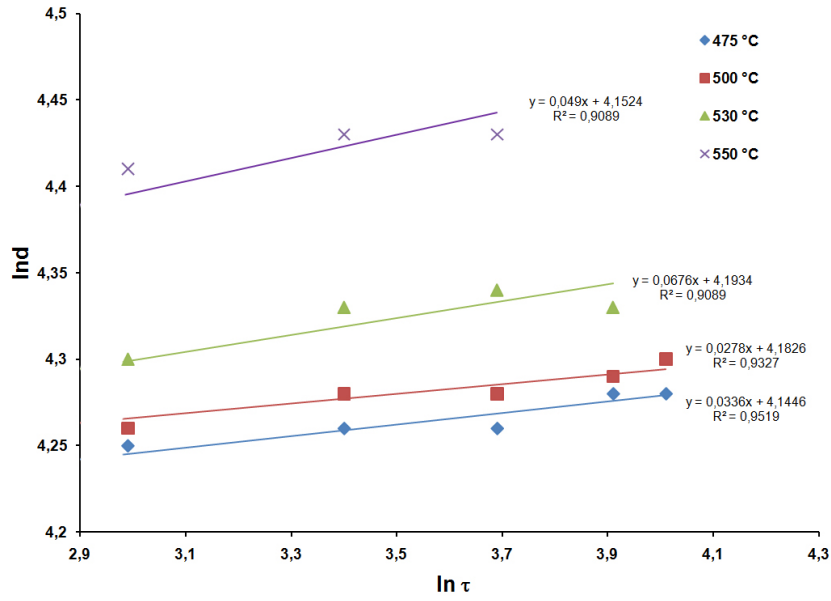


FIG. 1. Loglog plots of kinetic isotherms for the SnO₂/InP heterostructures thermal oxidation process at 475 – 550 °C during 60 minutes

as well as a very small value of n_{av} , just confirms the “diffusion mixing” as a limiting stage of the whole process (Table 1).

TABLE 1. Kinetic parameters of the thermal oxidation process of the SnO₂/InP heterostructures at 475 – 550 °C

Kinetic parameters		$n \pm \Delta n, \text{nm}^{1/n} \text{min}^{-1}$	EAE, kJ/mol
$T, ^\circ\text{C}$	$\ln k_{cp.}$		
475	91.39	0.03 ± 0.023	48
500	92.23	0.03 ± 0.021	
530	91.56	0.05 ± 0.013	
550	92.47	0.07 ± 0.014	
n_{av}	0.045 ± 0.018		

In order to evaluate the chemical stimulating effect of the nanosized SnO₂ layer on the InP thermal oxidation process, we calculated the values of the relative change in the film thickness b compared to the reference using the formula (2)

$$b = \frac{d_{\text{SnO}_2/\text{InP}} - d_{\text{SnO}_2/\text{InP}}^*}{\Delta d_{\text{InP}}}, \quad (2)$$

where Δd_{InP} is the change in the thickness of the oxide film during oxidation of indium phosphide (reference standard), $d_{\text{SnO}_2/\text{InP}}$ is the value of the thickness of the oxide film during oxidation of SnO₂ at a certain oxidation time, and $d_{\text{SnO}_2/\text{InP}}^*$ is the thickness of deposited layer (without oxidation) [25].

However, the film thickness values obtained by the LE method (80 nm), even taking into account the error, do not coincide with the SE data (60 nm). This may be due to the fact that the Cauchy model allows one to obtain only an approximate film thickness [26]. In this regard, the results obtained by laser ellipsometry can be considered more reliable.

At all temperatures (475 – 550 °C) (see Table 2), there is no acceleration of film growth over the entire time. Small values of the corresponding Gibbs free energies of reactions ($\Delta G = -273 - -211$ kJ/mol) of oxygen transfer from tin dioxide to the substrate components in combination with the data of Table 2, indicate a slowing effect of tin dioxide on the InP oxidation rate and the certain barrier function of the deposited layer, serving as an obstacle for the oxidation of the components of the substrate.

TABLE 2. The values of the relative change of the film thickness formed in the process of thermal oxidation of SnO₂/InP heterostructures at 475 – 550 °C, calculated by the formula (2)

Relative change of film thickness, times						
$T, ^\circ\text{C}/\tau, \text{min.}$	10	20	30	40	50	60
475	0.18	0.26	0.32	0.3	0.32	0.32
500	0.94	0.76	0.68	0.61	0.58	0.59
530	0.14	0.21	0.26	0.25	0.22	0.38
550	0.48	0.55	0.53	0.48	0.54	0.71

We can now make a conclusion that SnO₂ is not a chemical stimulator of the InP thermal oxidation process.

According to the results of X-ray phase analysis (Fig. 2), we can conclude that the thermal oxidation of SnO₂/InP heterostructures at 475 – 530 °C, metal tin does not form, as in the process of a transit interaction.

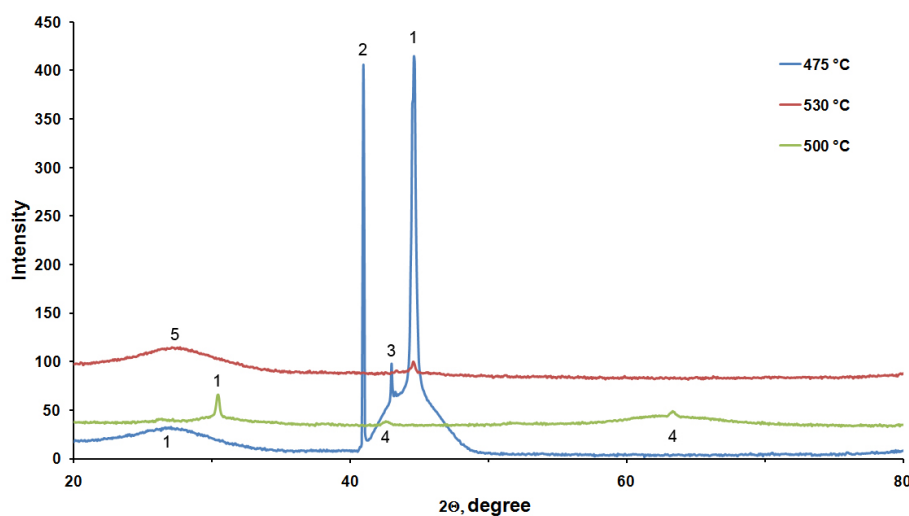


FIG. 2. X-ray diffraction patterns of the SnO₂/InP heterostructures after thermal oxidation for 60 minutes at 475 – 530 °C, where 1 – In(PO₃)₃, 2 – P₂O₅, 3 – In₂O₃, 4 – SnO₂, 5 – Sn₃(PO₄)₂

Based on the presented diffractograms, we can conclude that the thermal oxidation of SnO₂/InP heterostructures requires a relatively high temperature, from which SnO₂ will interact with the substrate components. The presence of peaks corresponding to the compound Sn₃(PO₄)₂ indicates the interaction of the SnO₂ layer deposited on the surface with the oxidation products of the substrate components, in particular phosphorus, and, therefore, a change in the composition of the film and its surface. Thus, we can speak about the modifying properties of SnO₂. In this case, it is necessary to take into account the fact that the modification of nanoscale films with a thickness not exceeding 100 nm can ultimately lead to a noticeable change in the surface topography. For a number of practical applications, this is unacceptable, therefore, the study of the surface morphology of nanoscale films formed by the thermal oxidation of SnO₂/InP heterostructures is a necessary task.

Films, formed during thermal oxidation of SnO₂/InP heterostructures, have a fairly smooth surface (Figs. 3 and 4) at all oxidation temperatures, which is confirmed by AFM and STM methods. A feature of the InP surface is

the presence of vacancy defects and a residual oxide phase, which leads to the formation of active centers. The growth of an oxide film during the oxidation of indium phosphide without chemical stimulators begins at these active centers [29].

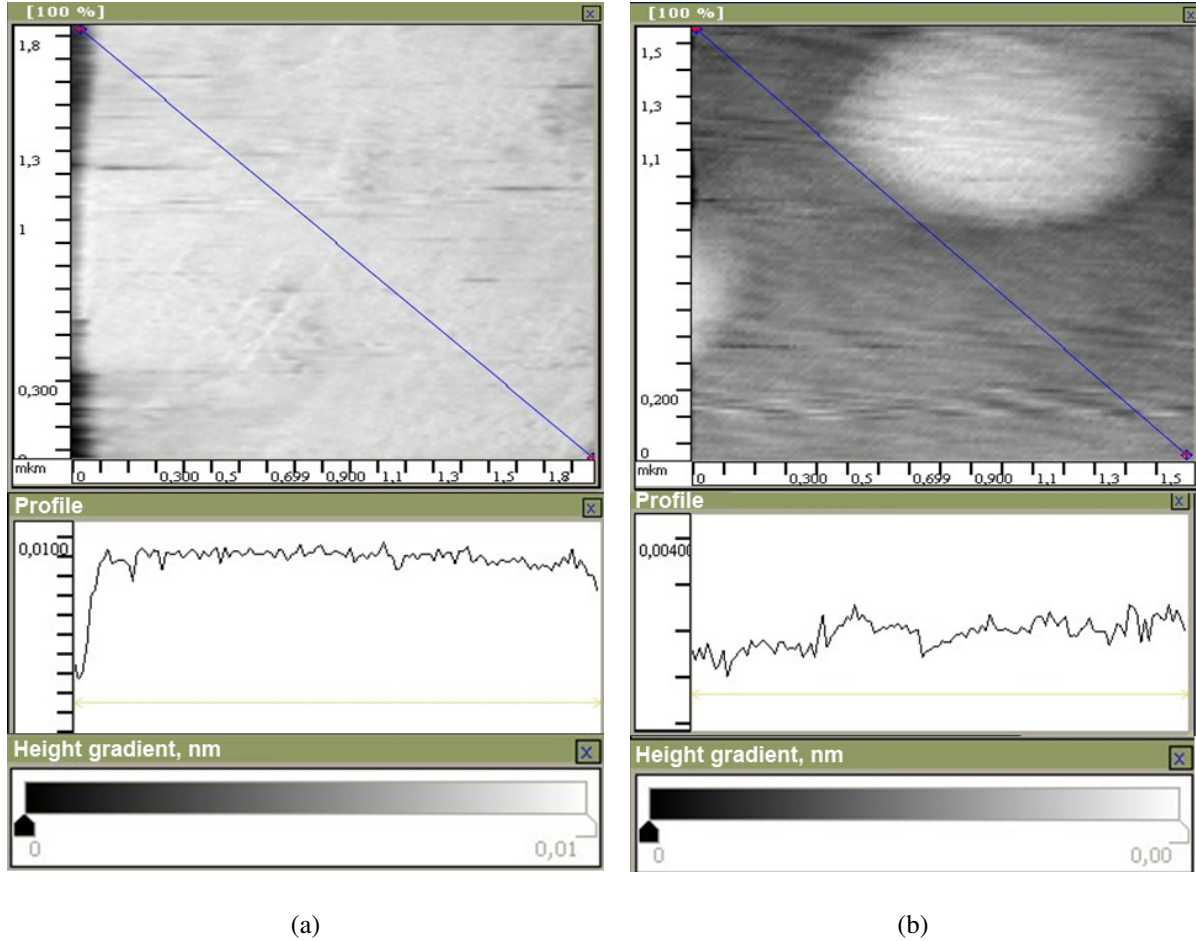


FIG. 3. STM images of SnO_2/InP samples and their surface profile after oxidation at 500 (a) and at 550 °C (b) for 60 minutes. The scanning area was 1.8×1.8 and $1.5 \times 1.5 \mu\text{m}^2$, respectively

According to the AFM data, the average roughness of the film is $S_a = 1.065 \text{ nm}$, that also confirms the smoothness of the films formed during the thermal oxidation process.

The resistivity of pure film SnO_2 is $3.4 \cdot 10^3 \text{ Ohm}\cdot\text{cm}$ [30]. The investigations of the electrophysical characteristics showed that films synthesized as a result of thermal oxidation of SnO_2/InP heterostructures have a higher electrical resistivity ($\rho = 9 \cdot 10^6 \text{ Ohm}\cdot\text{cm}$), indicating an improvement electrophysical properties. The semiconductor properties can be explained by the fact that no metal indium is released during the oxidation of SnO_2/InP heterostructures; SnO_2 promotes its chemical binding to phosphorus, as a result the formation of the corresponding phosphates occur. As a result, the suppression of ohmic conductivity was observed.

4. Conclusion

Thus, it was found that SnO_2 is not a chemical stimulator of the InP thermal oxidation process. This was confirmed by the LE method that correlate with the data of thermodynamic calculations of the corresponding reactions. At the same time, SnO_2 has a modifying effect on the composition and properties of nanoscale (thickness not more than 80 – 90 nm) films synthesized by thermal oxidation, as evidenced by the presence of $\text{Sn}_3(\text{PO}_4)_2$ (XRD) phases in the films. When InP is thermally oxidized, conductive films, enriched with metallic indium and characterized by a very developed surface relief are formed. At the same time, during the oxidation of SnO_2/InP heterostructures, semiconductor films are formed (the specific electrical resistance is $9 \cdot 10^6 \text{ Ohm}\cdot\text{cm}$), the average roughness of which is 1.065 nm.

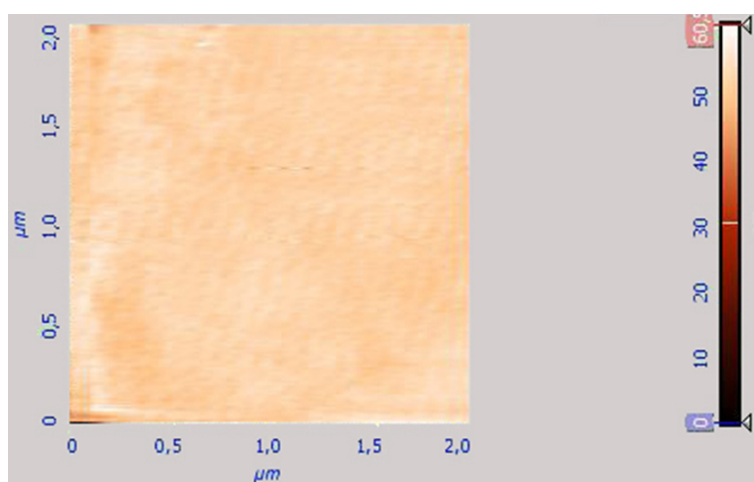


FIG. 4. FM image of the SnO₂/InP heterostructure after thermal oxidation for 60 min at 530 °C. The scan area was $2 \times 2 \mu\text{m}^2$

Acknowledgements

This research was supported by the Russian Foundation for Basic Research, grant No. 18-03-00354a. The research results were partially obtained on the equipment of the Collective Use Centre of Voronezh State University. URL: <http://ckp.vsu.ru>.

References

- [1] Shikova T.G., Kholodkov I.V., Talanov E.N. An investigation of the properties of tin oxide films produced by thermal oxidation of the metal films. *Physics and chemistry of materials processing*, 2011, **3** (6), P. 88–92.
- [2] Krivetskiy V.V., Rumyantseva M.N., et al. Materials based on Modified SnO₂ for Selective Gas Sensors. *Inorganic Materials*, 2010, **46** (10), P. 1218–1224.
- [3] Povarov V.G., Lopatnikov A.I. A simple multisensor detector based on tin dioxide in capillary gas chromatography. *Journal of Analytical Chemistry*, 2016, **71** (9), P. 940–945.
- [4] Rumyantseva M.N., Makeeva E.A., Gaskov A.M. The effect on the chemisorption of oxygen on their surface the microstructure of semiconductor sensors materials. *Russian Journal of General Chemistry*, 2008, **52** (2), P. 122–129.
- [5] Zhukova A.A., Rumyantseva M.N., et al. Influence of antimony doping on structure and conductivity of tin oxide whiskers. *Thin Solid Films*, 2009, **518**, P. 1359–1362.
- [6] Nasheksky A.Ya. *IIIbV semiconductor phosphides and solid solutions based on it*. Mir, Moscow, 1974, 154 p.
- [7] Turishchev S.Yu., Yurakov Yu.A., et al. Synchrotron Investigations of Oxides Formation in Tin Nanolayers. *Journal of Surface Investigation: X-Ray, Synchrotron and Neutron Techniques*, 2007, **1**, P. 66–70.
- [8] Drozdov K.A., Krylov I.V., et al. Effect of the tin impurity on the energy spectrum photoelectric properties of nanostructured In₂O₃ films. *Semiconductors*, 2014, **48** (4), P. 467–470.
- [9] Amosova L.P. Electrooptical properties and structural features of amorphous ITO. *Semiconductors*, 2015, **49** (3), P. 414–418.
- [10] Yoon-Heung Tak, Ki-Beom Kim, et al. Criteria for ITO (indium–tin–oxide) thin film as the bottom electrode of an organic light emitting diode. *Thin Solid Films*, 2002, **411**, P. 12–16.
- [11] Belobaba A.G., Zelinsky A.G., Gusev A.A., Masliy A.I. Electrochemical Stability of Indium–Tin Oxides. *Chemistry for Sustainable Development*, 2014, **22** (4), P. 417–422.
- [12] Rembeza S.I., Rembeza E.S., Voronov P.E., Sinelnikov B.M. Synthesis, structure and electrical properties of (SnO₂)_x(In₂O₃)_{1-x} ($x = 0.5-1$) nanocomposites. *Semiconductors*, 2011, **45** (11), P. 1538–1541.
- [13] Ramasundari P., Ganeshan S., Vijayalakshmi R. Characterization studies on the novel mixed thin films. *Nanosystems: Physics, Chemistry, Mathematics*, 2016, **7** (4), P. 683–686.
- [14] Begletsova N.N., Al-Alwani A.J.K., et al. Influence of copper nanoparticle film processing temperature on their structure and electrical properties. *Nanosystems: Physics, Chemistry, Mathematics*, 2018, **9** (5), P. 586–596.
- [15] Gayathri A.G., Joseph C.M. Bistable electrical switching and performance of a pentacene-based write once/read many memory device. *Nanosystems: Physics, Chemistry, Mathematics*, 2016, **7** (4), P. 643–646.
- [16] Wang Yaqin, Tang Wu. Surface-dependent conductivity, transition type, and energy band structure in amorphous indium tin oxide films. *Solid State Electronics*, 2017, **138**, 10.1016/j.sse.2017.09.007.
- [17] Glushko V.P. *Thermodynamic properties of individual substances*. **4**. Nauka, Moscow, 1978, 386 p.
- [18] Mittova I.Ya. Influence of the Physicochemical Nature of Chemical Stimulators and the Way They are Introduced into a System on the Mechanism of the Thermal Oxidation of GaAs and InP. *Inorganic Materials*, 2014, **50** (9), P. 948–955.
- [19] Mittova I.Ya., Sladkoptsev B.V., et al. Growth and Properties of Nanofilms Produced by the Thermal Oxidation of MnO₂/InP under the Effect of Mn₃(PO₄)₂. *Inorganic Materials*, 2019, **55** (9), P. 969–974.

- [20] Kim T.W., Lee D.U., Lee J.H., Yoon Y.S. Surface and microstructural properties of SnO₂ thin films grown on p-InP (100) substrates at low temperature. *Solid State Communications*, 2000, **115**, P. 503–507.
- [21] Shvets V.A., Spesivtsev E.V., Rykhliitskii S.V., Mikhailov N.N. Ellipsometry as a high-precision technique for subnanometer-resolved monitoring of thin-films structures. *Nanotechnologies in Russia*, 2009, **4** (3–4), P. 91–102.
- [22] Aspnes D.E. Optical properties of thin films. *Thin solid films*, 1982, **89**, P. 249–262.
- [23] Tomina E.V., Mittova I.Ya., Zelenina L.S. Thermal Oxidation as a Method of formation of Nanoscale Functional Films on A^{III}B^V Semiconductors: Influence of Deposited Metal Layers. Overview. *Condensed Matter and Interphases*, 2018, **20** (1), P. 6–24.
- [24] Mittova I.Ya., Tomina E.V., et al. High-speed determination of the thickness and spectral ellipsometry investigation of films produced by the thermal oxidation of InP and VxOy/InP structures. *Inorganic Materials*, 2013, **49** (2), P. 173–179.
- [25] Mittova I.Ya., Sladkopevtsev B.V., et al. Formation of nanoscale films of the (Y₂O₃–Fe₂O₃) on the monocrystal InP. *Condensed Matter and Interphases*, 2019, **21** (3), P. 406–418.
- [26] Synowicki R.A. Spectroscopic ellipsometry characterization of indium tin oxide film microstructure and optical constants. *Thin Solid Films*, 1998, **46** (20), P. 394–397.
- [27] Mittova I.Ya., Borzakova G.V., et al. Growth of Oxide Layers on Indium Phosphide. *Inorganic Materials*, 2012, **48** (2), P. 161–168.
- [28] Thilakan P., Kumar J. Reactive thermal oxidation of indium oxide and tin-doped indium oxide thin films on InP substrates. *Thin Solid Films*, 1997, **292**, P. 50–54.
- [29] Mittova I.Ya., Tomina E.V., Tretyakov N.N., Sladkopevtsev B.V. Dependence of the Mechanism of V₂O₅ Chemostimulating Action from the Method of its Introduction into the System during InP Thermal Oxidation. *Condensed Matter and Interphases*, 2013, **15** (3), P. 305–311.
- [30] Kovtunenکو P.V., Nesterova I.L., Knunyants I.L. *Chemical Encyclopedia*. Great Russian Encyclopedia, Moscow, 1992, 639 p.

Microwave synthesis and studies room temperature optical properties of LaF₃: Ce³⁺, Pr³⁺, Nd³⁺ nanocrystals

Sidheshwar G Gaurkhede

Department of Physics, Bhavan's College of Science, Andheri (W) Mumbai – 400058, India

s.gaurkhede@gmail.com

PACS 61.05.cp, 77.22.d

DOI 10.17586/2220-8054-2020-11-1-117-122

Lanthanum fluoride (LaF₃:Ce³⁺, Pr³⁺, Nd³⁺) was synthesized by water soluble LaCl₃ + CeCl₃ + PrCl₃ + NdCl₃ and NH₄F as starting materials in de-ionized water as solvent using microwave assisted technique. The structure of LaF₃:Ce³⁺, Pr³⁺, Nd³⁺ nanocrystals analyzed by XRD and TEM analysis is found to be in hexagonal structure and average crystalline particle size is 20 nm (JCPDS standard card (32-0483) of pure hexagonal LaF₃ crystals). The absorption edge in UV spectra is found at 250 nm corresponding to energy of 4.9 eV. It further shows a wide transparent window lying between 200 nm–800 nm. For LaF₃: Ce³⁺, Pr³⁺, Nd³⁺ nanocrystals emission of blue color (458 nm) has been observed with at an excitation wavelength of 254 nm. The measured relative second harmonic generation (SHG) efficiency of LaF₃: Ce³⁺, Pr³⁺, Nd³⁺ in de-ionized water with respect to KDP crystal is 0.186.

Keywords: Microwave radiation, Hexagonal shape, X-ray diffraction, Luminescent, SHG.

Received: 23 January 2020

1. Introduction

LaF₃ is an ideal host material for various phosphors to its low phonon energy and the consequent minimal multi phonon relaxation of its excited states [1, 2]. Lanthanum fluoride is an excellent F⁻ ionic conductor among other rare earth fluorides [3]. Lanthanum fluoride based chemical sensors widely used in potential application in sensing the fluorine, oxygen, and carbon monoxide due to its high chemical stability and ionic conductivity [4]. Ion conducting nature of the rare earth fluorides (solid electrolyte) is exploited as sensor materials to construct various electrochemical sensors like gas sensor, biosensor, and ion selective electrode [5]. Miura et al. reported the use of lanthanum fluoride film in biosensor and room-temperature oxygen sensor based on its high F⁻ ion-conducting property. The working principle of LaF₃ based biosensor and oxygen sensors is explained as the movement of F⁻ ion conduction [6, 7]. Fedorov P.P. [8] et al. review the major aspects of inorganic chemistry of nanofluorides, methods of synthesis including nanochemical effects, preparation of 1D, 2D, and 3D nanostructures, surface modification of the nanoparticles, fluoride nanocomposites and applications of nanofluorides. The orthorhombic β -YF₃ structure and ionic conductivity of rare earth fluorides and of tysonite-structured were investigated by Trnovcova et al. [9, 10].

Hai Guo et al. [11] have reported water-soluble LaF₃: Ce³⁺, Tb³⁺ nanodiskettes having particle size of 25 nm synthesized by ionic liquid-based hydrothermal process. The luminescent properties of LaF₃: Ce³⁺, Tb³⁺ nanodiskettes show intense green emission (541 nm) at 254 nm excited wavelength both in solid state and dispersed in solution. A simple and straightforward method was developed by Yong Zhang et al. [12, 13] to produce water-dispersible LaF₃: Ce³⁺, Tb³⁺ nanocrystals and to grow these nanocrystals on silica microspheres which show a raspberry-like structure with LaF₃ nanocrystals. The nanocrystals were 25 nm in size and exhibited strong green fluorescence for excited wavelength of 254 nm. There is a report by Cong-Cong Mi et al. [14] on Polyethyleneimine (PEI) functionalized multicolor luminescent LaF₃: Ce³⁺, Tb³⁺ nanoparticles which were synthesized via a novel microwave-assisted method and nanoparticles possessed a pure hexagonal structure with an average size of was 12 nm and green fluorescence was observed when sample was excited with 252 nm wavelength. The lanthanide series of trivalent ions is Ce³⁺, Pr³⁺, Nd³⁺ having ultra violet (UV) and visible luminescence spectra consisting of many narrow lines whose half-widths reach only several nm⁻¹. It was found that the in Nd³⁺ UV and visible luminescence depend on the excitation wavelength [15].

The synthesized LaF₃:Ce³⁺, Pr³⁺, Nd³⁺ nanoparticles exhibit hexagonal shape and exhibit blue luminescence. In the present case LaF₃:Ce³⁺, Pr³⁺, Nd³⁺ nanoparticles have been synthesized using a conventional microwave radiation technique for first time.

2. Experimental

2.1. Synthesis of nanocrystals

Synthesis of $\text{LaF}_3:\text{Ce}^{3+}$, Pr^{3+} , Nd^{3+} nanocrystals follows an aqueous route and uses a microwave heating at low power range. The method is simple and cost effective. Water soluble $\text{LaCl}_3 + \text{CeCl}_3 + \text{PrCl}_3 + \text{NdCl}_3$ and NH_4F are mixed to obtain a solution in 1:3 molar proportions [16]. A 10 ml homogenous mixture (in the ionized water) in a 100 ml beaker using 0.064 mol of each $\text{LaCl}_3 + \text{CeCl}_3 + \text{PrCl}_3 + \text{NdCl}_3$ allowed a 10 ml solution of 0.768 mol NH_4F to drip into this solution uniformly through a funnel attached with a stopper to facilitate control of dripping, and placed the whole set up inside a conventional microwave set at low power range (in on-off mode set at 30 sec) for around 30 min. The low power range setting largely helped us avoid spill off of the solution. A white crystalline precipitate identified as doped LaF_3 nanocrystals appears almost instantly having settled down to the bottom of the beaker. White precipitate is then washed several times with de-ionized water and then drying it in microwave oven for about 15 min. The dried sample was then stored in sealed ampoules for further characterization and analysis.

3. Characterization

Powder X-ray diffraction (XRD) measurements have been performed using a PANALYTICAL X'PERT PROMPD diffractometer model using $\text{CuK}\alpha$ radiation $\lambda = 1.5405 \text{ \AA}$ with a scanning rate of 20 per min in the 2° range from 0° to 80° . Transmission electron microscope (TEM) analysis has been carried out for different magnification by PHILIPS (CM 200) 0.24 nm resolution, operating at 200 kV. The UV-visible spectrum of the samples was recorded in the spectral range of 200 nm–800 nm using a double beam (Perkin Elmer Corp.) spectrophotometer. The fluorescence spectrum was measured on LS 45 luminescence spectrometer (Perkin Elmer Corp.) using a high energy pulsed Xenon source for excitation and FL Win Lab software. NLO studies for the measurements of SHG efficiency are obtained through the crystalline powder sample by using Kurtz and Perry technique.

4. Result and discussion

The XRD pattern obtained from the $\text{LaF}_3:\text{Ce}^{3+}$, Pr^{3+} , Nd^{3+} nanocrystals shown in Fig. 1. The results of the XRD are in good agreement with the hexagonal LaF_3 structure as described in the reports LaF_3 (JCPDS card No. 32-0483) [17]. The average crystallite size estimated from the Scherrer equation, $D = 0.90\lambda/\beta \cos \theta$, where D is the average crystallite size, λ is the x-ray wavelength (0.15405 nm), θ and β being the diffraction angle and full width at half maximum of an observed peak, respectively. The strongest peak (111) at $2\theta=27.84^\circ$ for $\text{LaF}_3:\text{Ce}^{3+}$, Pr^{3+} , Nd^{3+} samples have been used to calculate the average crystallite size (D) of the nanoparticles [18]. The average crystallite sizes of $\text{LaF}_3:\text{Ce}^{3+}$, Pr^{3+} , Nd^{3+} nanoparticles are in the range of 15 nm–20 nm, which is in agreement with the TEM and SEM results. The XRD pattern of the LaF_3 nanoparticles is nearly similar to that of $\text{LaF}_3:\text{Ce}^{3+}$, Tb^{3+} [19]. No XRD signals are observed for impurity phases.

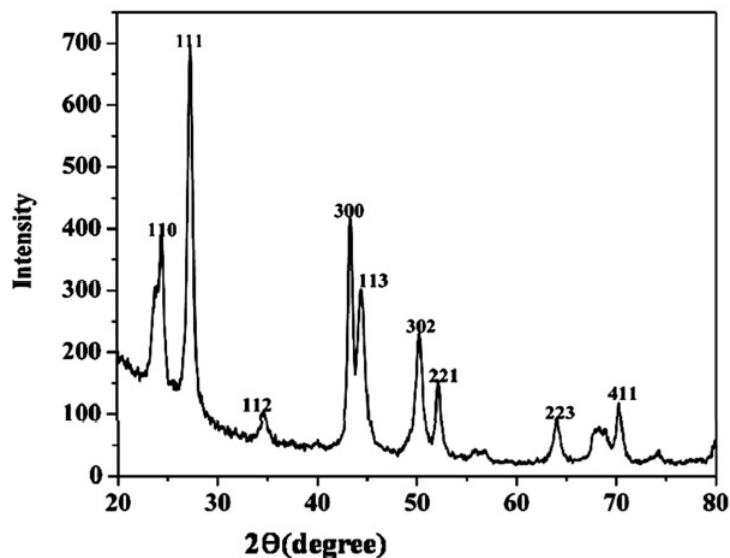


FIG. 1. X-ray diffraction pattern of $\text{LaF}_3:\text{Ce}^{3+}$, Pr^{3+} , Nd^{3+} nanocrystals

Figure 2 shows the transmission electron microscopy (TEM) image of $\text{LaF}_3: \text{Ce}^{3+}, \text{Pr}^{3+}, \text{Nd}^{3+}$ nanocrystals. It is seen that most of the nanocrystals are in the form of hexagon, sphere and nanorods. Most of the nanorods of $\text{LaF}_3: \text{Ce}^{3+}, \text{Pr}^{3+}, \text{Nd}^{3+}$ are found to be well separated with some instances of agglomeration with average particle size of 20 nm are found. Fig. 3 shows the selected area electron diffraction (SAED) pattern. Three strong diffraction rings corresponding to the (002), (111) and (300) reflections, have been observed which is in close agreement with the hexagonal LaF_3 structure [20]. This shows that the original structure of LaF_3 may be retained even after modification.

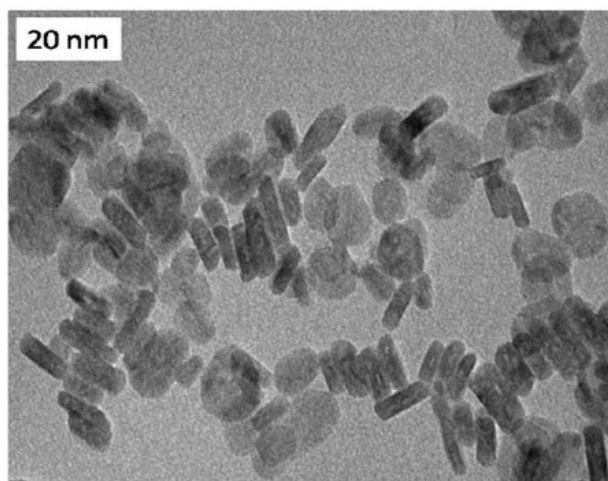


FIG. 2. TEM image of $\text{LaF}_3: \text{Ce}^{3+}, \text{Pr}^{3+}, \text{Nd}^{3+}$ nanocrystals

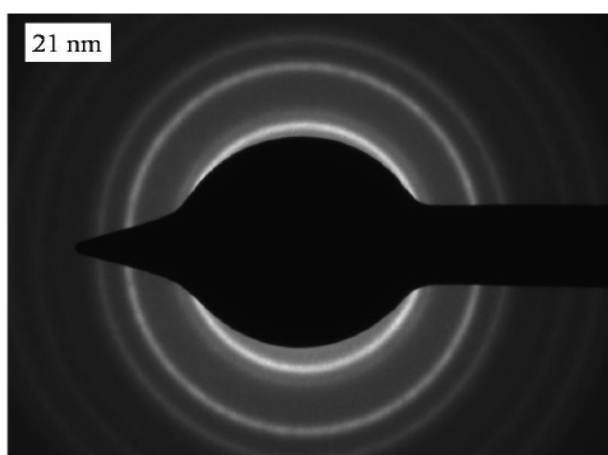


FIG. 3. Selected area electron diffraction (SAED) pattern image of $\text{LaF}_3: \text{Ce}^{3+}, \text{Pr}^{3+}, \text{Nd}^{3+}$ nanocrystals

Figure 4 shows the optical absorption spectrum of the nanocrystallites with an absorption edge at 250 nm in the UV region, with corresponding energy band gap lying at 4.9 eV. Absorption against wavelength values was used to determine the band gap energy. The band gap energy was calculated by determining the ' $h\nu$ ' value. A wide transparent window is present between 200 – 800 nm suggesting its use in optoelectronics devices.

The emission spectra of synthesized $\text{LaF}_3: \text{Ce}^{3+}, \text{Pr}^{3+}, \text{Nd}^{3+}$ ion is shown in Fig. 5. The emission spectra was obtained by monitoring (254 nm) 4f to 5d transition of Ce^{3+} ions. The broadband emission is located at 458 nm due to the electronic transitions from 5d to 4f state of Ce^{3+} ions [21]. The sharp emission peaks originates from the 4f5d - 4f² transitions of Pr^{3+} ions [$^3\text{H}_4 \rightarrow ^3\text{P}_2$ (458 nm), $^3\text{H}_4 \rightarrow ^3\text{P}_0$ (497 nm), $^3\text{H}_4 \rightarrow ^1\text{D}_2$ (608 nm)]. The quenching of Ce^{3+} emissions and the enhancement of Pr^{3+} emissions is strong evidence of efficient energy transfer from Ce^{3+} to Pr^{3+} and Nd^{3+} . The emission spectrum is mainly located in the region corresponding to blue colour. Here, the doping Ce^{3+} ions act as sensitizers and the doping ions $\text{Pr}^{3+}, \text{Nd}^{3+}$ can be considered as luminescent centers. It is well known fact that the luminescent spectra of trivalent lanthanide ions in crystals come mainly from two types of electronic transitions: 4f-4f transition and 5d-4f transition. The excited electronic configuration of Ce^{3+} is $^5\text{D}_1$. The

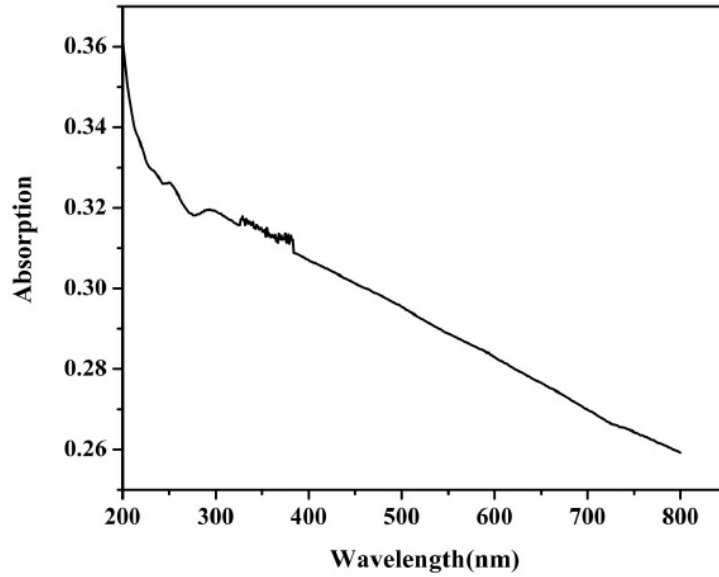


FIG. 4. UV-VIS absorption spectra of LaF_3 doped Ce^{3+} , Pr^{3+} Nd^{3+} nanocrystals in ionized water

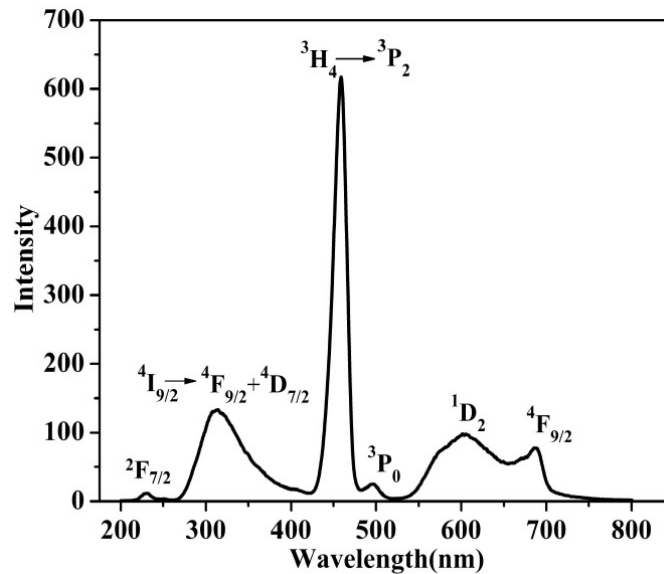
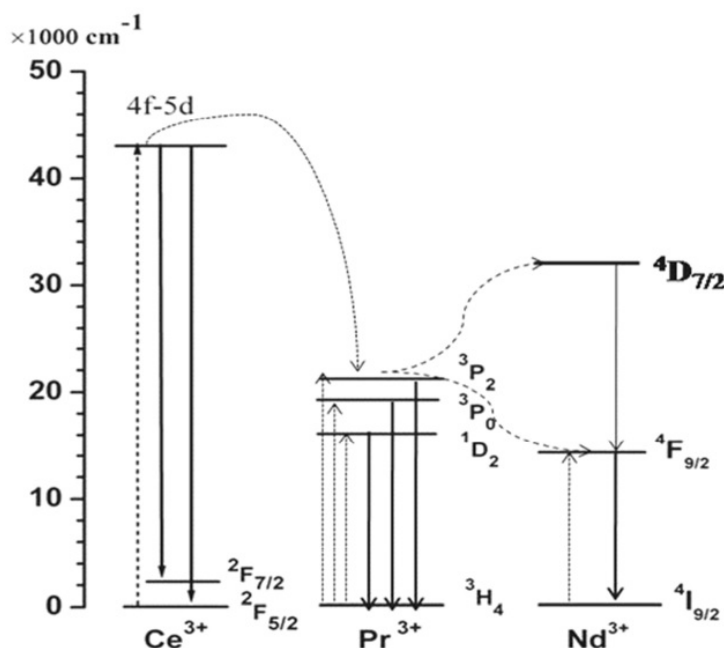


FIG. 5. Excitation ($\lambda_{em}=458$ nm) and Emission ($\lambda_{ex}=254$ nm) spectra of LaF_3 nanocrystals doped Ce^{3+} , Pr^{3+} , Nd^{3+} ions in deionized water

5d electron has a strong interaction with the neighboring anion ligands in the compounds and results in broadband emissions. The 4f orbital is shielded from the surroundings by the filled 5s² and 5p⁶ orbital. Therefore, the influence of the host lattice on the optical transitions within the 4fⁿ configuration is small [15, 22].

Figure 6 shows the energy level scheme of LaF_3 ; Ce^{3+} , Pr^{3+} Nd^{3+} , with optical transitions and energy transfer processes. The Ce^{3+} ion excited at 254 nm absorbs one photon and is pumped to the 5d level. Then, it relaxes to the ground state by radiative process with emission of photons; and transfers its energy to a nearby Pr^{3+} ion in the ground state, promoting this Pr^{3+} ion to excited state. Then, the excited Pr^{3+} ion relaxes to the $^3\text{P}_2$, $^3\text{P}_0$, and $^1\text{D}_2$ levels by non-radiative process. The Pr^{3+} ion excited by 254 nm is pumped to the $^3\text{P}_2$, $^3\text{P}_0$, and $^1\text{D}_2$ states. As mentioned above, $^3\text{H}_4 \rightarrow ^3\text{P}_2$ (458 nm), $^3\text{H}_4 \rightarrow ^3\text{P}_0$ (497 nm), $^3\text{H}_4 \rightarrow ^1\text{D}_2$ (608 nm) transitions have been observed only for low Pr^{3+} doped samples. Blue fluorescence from the higher energy $^3\text{P}_2$ level has been observed for high Pr^{3+} doped samples [23].


 FIG. 6. Energy level scheme for $\text{LaF}_3: \text{Ce}^{3+}, \text{Pr}^{3+}, \text{Nd}^{3+}$ nanocrystals

The nonlinear optical property of $\text{LaF}_3: \text{Ce}^{3+}, \text{Pr}^{3+}, \text{Nd}^{3+}$ in de-ionized water was tested by passing the output of Nd: YAG Quanta ray laser emitting 1064 nm, generating about 6mJ / pulse through the samples. SHG is a key technology as frequency doublers of laser light. The SHG efficiency of $\text{LaF}_3: \text{Ce}^{3+}, \text{Pr}^{3+}, \text{Nd}^{3+}$ nanocrystals were determined in de-ionized water by modified Kurtz and Perry technique [24]. Crystalline powder of Potassium dihydrogen phosphate (KDP) taken as the reference material. The measured relative SHG efficiency of $\text{LaF}_3: \text{Ce}^{3+}, \text{Pr}^{3+}, \text{Nd}^{3+}$ in de-ionized water with respect to KDP crystal is 0.186.

5. Conclusions

LaF_3 nanocrystals successfully have been synthesized using $\text{LaCl}_3 + \text{CeCl}_3 + \text{PrCl}_3 + \text{NdCl}_3$ and NH_4F in deionized water. Elongated and assorted size hexagonal geometry of LaF_3 nanocrystals has been observed. XRD and TEM studies indicate that the average particle size is 20 nm. The conductivity at room temperature for LaF_3 sample prepared in deionized water is found to be in close agreement with reported values. The absorption edge in UV spectra is found at 250 nm corresponding to energy of 4.9 eV. It further shows a wide transparent window lying between 200 nm–800 nm. For $\text{LaF}_3: \text{Ce}^{3+}, \text{Pr}^{3+}, \text{Nd}^{3+}$ nanocrystals emission of blue color (458 nm) has been observed with an excitation wavelength of 254 nm. The SHG property was tested by using Nd: YAG laser. The second harmonic efficiency of $\text{LaF}_3: \text{Ce}^{3+}, \text{Pr}^{3+}, \text{Nd}^{3+}$ nanocrystals is found to be 0.186 in deionized water using KDP as standard material.

References

- [1] Zheng H.R. Up-converted emission in Pr^{3+} doped fluoride nanocrystals-based oxyfluoride glass ceramics. *Journal of Luminescence*, 2004, **108**(1), P. 395–399.
- [2] Nogami M. Enhanced fluorescence of Eu^{3+} induced by energy transfer from nanosized SnO_2 crystals in glass. *Journal of Luminescence*, 2002, **97**(3), P. 147–152.
- [3] Schoonman J., Oversluizen G., Wapennar K.E.D. Solid electrolyte properties of LaF_3 . *Solid State Ionics*, 1980, **1**(3), P. 211–221.
- [4] Yamazoe N., Miura N. Environmental gas sensing. *Sensors Actuators*, 1994, **B20**(2), P. 95–102.
- [5] Fergus J.W. The Application of Solid Fluoride Electrolytes in Chemical Sensors. *Sensors Actuators*, 1997, **B42**(2), P. 119–130.
- [6] Miura N., Hisamoto J., Yamazoe N., Kuwata S. LaF_3 sputtered film sensor for detecting oxygen at room temperature. *Applied Surface Science*, 1988, **33/34**, P. 1253–1259.
- [7] Miura N., Hisamoto J., Yamazoe N., Kuwata S., Salardenne J., Solid-state oxygen sensor using sputtered LaF_3 film. *Sensors Actuators*, 1989, **B16**(4), P. 301–310.
- [8] Fedorov P.P., Luginina A.A., Kuznetsov S.V., Osiko V.V. Nanofluorides. *Journal of Fluorine Chemistry*, 2011, **132**(12), P. 1012–1039.
- [9] Trnovcova V., Garashina L.S., Skubla A., Fedorov P.P., Cicka R., Krivandina E.A., Sobolev B.P. Structural aspects of fast ionic conductivity of rare earth fluorides. *Solid State Ionics*, 2003, **157**(1-4), P. 195–201.
- [10] Trnovcova V., Fedorov P.P., Furara I. Fluoride Solid Electrolytes. *Russian Journal of Electrochemistry*, 2009, **45**(6), P. 630–639.

- [11] Guo H., Zhang T., Qiao Y.M., Zhao L.H., Z. Quan Li. Ionic Liquid-Based Approach to Monodisperse Luminescent LaF₃: Ce, Tb Nanodiskettes: Synthesis, Structural and Photoluminescent Properties. *Journal Nanoscience and Nanotech*, 2010, **10**(3), P. 1913–1919.
- [12] Zhang Y., Lu M. Labelling of silica microspheres with fluorescent lanthanide-doped LaF₃ nanocrystals. *Nanotechnology*, 2007, **18**(27), P. 275603.
- [13] Zhu X., Zhang Q., Li Y., Wang H. Redispersible and water-soluble LaF₃: Ce, Tb nanocrystals via a microfluidic reactor with temperature steps. *Journal Material Chemistry*, 2008, **18**(42), P. 5060–5062.
- [14] Mi C.C., Tian Z.H., Han B.F., Mao C., Xu S.K. Microwave-assisted one-pot synthesis of water-soluble rare-earth doped fluoride luminescent nanoparticles with tunable colors. *Journal Alloys Compound*, 2012, **525**, P. 154–158.
- [15] Pieterse L.V., Wegh R.T., Meijerink A. Emission spectra and trends for $4f^{n-1}5d \leftrightarrow 4f^n$ transitions of lanthanide ions: Experiment and theory. *The Journal of Chemical Physics*, 2001, **115**(20), P. 9382.
- [16] Meng J., Zhang M., Liu Y. Hydrothermal preparation and luminescence of LaF₃:Eu³⁺ nanoparticles. *Spectroscopic Acta part A*, 2007, **66**(1), P. 81–85.
- [17] Daihua T., Liu X., Zhen Z. Oleic acid (OA)-modified LaF₃: Er, Yb nanocrystals and their polymer hybrid materials for potential optical-amplification applications. *Journal of Material Chemistry*, 2007, **17**(1), P. 1597–1601.
- [18] Daqin C., Yuansheng W., En Ma, Yunlong Y. Influence of Yb³⁺ content on microstructure and fluorescence of oxyfluoride glass ceramics containing LaF₃ nano-crystals. *Material Chemistry Physics*, 2007, **101**(9), P. 464–469.
- [19] Pi D., Wang F., Fan X., Wang M., Zhang Y. Polyol-mediated synthesis of water-soluble LaF₃:Yb,Er upconversion fluorescent nanocrystals. *Materials Letters*, 2007, **61**(6), P. 1337–1340.
- [20] Yuanfang L., Wei C. Shaopeng W. Alan G.J. Sarah W. Boon K.W. X-ray Luminescence of LaF₃: Tb and LaF₃: Ce, Tb Water Soluble Nanoparticles. *Journal of Applied Physics*, 2008, **103**(6), P. 1–7.
- [21] Wang Z.L., Quan Z.W., Jia P.Y., Lin C.K., Luo Y., Chen Y., Fang J., Zhou W., Connor C.J.O., Lin. A Facile Synthesis and Photoluminescent Properties of Redispersible CeF₃, CeF₃:Tb³⁺, and CeF₃:Tb³⁺ / LaF₃ (Core / Shell) Nanoparticles. *Chemistry of Materials*, 2006, **18**(8), P. 2030–2037.
- [22] Li C., Liu X., Yang P., Zhang C., Lian H., and Lin. LaF₃, CeF₃, CeF₃:Tb³⁺, and CeF₃:Tb³⁺ @ LaF₃ (Core/Shell) Nanoplates: Hydrothermal Synthesis and Luminescence Properties. *The Journal of Physical Chemistry C*, 2008, **112**(8), P. 2904–2910.
- [23] Guo H. Photoluminescent properties of CeF₃:Tb³⁺ nanodiskettes prepared by hydrothermal microemulsion. *Applied Physics B-Lasers Optics*, 2006, **84**(1-2), P. 365–369.
- [24] Kurtz S.K., Perry T.T. A powder technique for the evaluation of nonlinear optical materials. *Journal of Applied Physics*, 1968, **39**(8), P. 3798–3813.



NANOSYSTEMS:

PHYSICS, CHEMISTRY, MATHEMATICS

INFORMATION FOR AUTHORS

The journal publishes research articles and reviews, and also short scientific papers (letters) which are unpublished and have not been accepted for publication in other magazines. Articles should be submitted in English. All articles are reviewed, then if necessary come back to the author to completion.

The journal is indexed in Web of Science Core Collection (Emerging Sources Citation Index), Chemical Abstract Service of the American Chemical Society, Zentralblatt MATH and in Russian Scientific Citation Index.

Author should submit the following materials:

1. Article file in English, containing article title, the initials and the surname of the authors, Institute (University), postal address, the electronic address, the summary, keywords, MSC or PACS index, article text, the list of references.
2. Files with illustrations, files with tables.
3. The covering letter in English containing the article information (article name, MSC or PACS index, keywords, the summary, the literature) and about all authors (the surname, names, the full name of places of work, the mailing address with the postal code, contact phone number with a city code, the electronic address).
4. The expert judgement on possibility of publication of the article in open press (for authors from Russia).

Authors can submit a paper and the corresponding files to the following addresses: nanojournal.ifmo@gmail.com, popov1955@gmail.com.

Text requirements

Articles should be prepared with using of text editors MS Word or LaTeX (preferable). It is necessary to submit source file (LaTeX) and a pdf copy. In the name of files the English alphabet is used. The recommended size of short communications (letters) is 4-6 pages, research articles– 6-15 pages, reviews – 30 pages.

Recommendations for text in MS Word:

Formulas should be written using Math Type. Figures and tables with captions should be inserted in the text. Additionally, authors present separate files for all figures and Word files of tables.

Recommendations for text in LaTeX:

Please, use standard LaTeX without macros and additional style files. The list of references should be included in the main LaTeX file. Source LaTeX file of the paper with the corresponding pdf file and files of figures should be submitted.

References in the article text are given in square brackets. The list of references should be prepared in accordance with the following samples:

- [1] Surname N. *Book Title*. Nauka Publishing House, Saint Petersburg, 2000, 281 pp.
- [2] Surname N., Surname N. Paper title. *Journal Name*, 2010, **1** (5), P. 17-23.
- [3] Surname N., Surname N. Lecture title. In: Abstracts/Proceedings of the Conference, Place and Date, 2000, P. 17-23.
- [4] Surname N., Surname N. Paper title, 2000, URL: <http://books.ifmo.ru/ntv>.
- [5] Surname N., Surname N. Patent Name. Patent No. 11111, 2010, Bul. No. 33, 5 pp.
- [6] Surname N., Surname N. Thesis Title. Thesis for full doctor degree in math. and physics, Saint Petersburg, 2000, 105 pp.

Requirements to illustrations

Illustrations should be submitted as separate black-and-white files. Formats of files – jpeg, eps, tiff.



NANOSYSTEMS:

PHYSICS, CHEMISTRY, MATHEMATICS

Журнал зарегистрирован

Федеральной службой по надзору в сфере связи, информационных технологий и массовых коммуникаций

(свидетельство ПИ № ФС 77 - 49048 от 22.03.2012 г.)

ISSN 2220-8054

Учредитель: федеральное государственное автономное образовательное учреждение высшего образования

«Санкт-Петербургский национальный исследовательский университет информационных технологий, механики и оптики»

Издатель: федеральное государственное автономное образовательное учреждение высшего образования

«Санкт-Петербургский национальный исследовательский университет информационных технологий, механики и оптики»

Отпечатано в Учреждении «Университетские телекоммуникации»

Адрес: 197101, Санкт-Петербург, Кронверкский пр., 49

Подписка на журнал НФХМ

На первое полугодие 2020 года подписка осуществляется через

ОАО Агентство «Роспечать»

Подписной индекс 57385 в каталоге «Издания органов научно-технической информации»